Application of Gaussian Moment Closures to Three-Dimensional Micro-Scale Flows

by

Christopher Lam

A thesis submitted in conformity with the requirements
for the degree of Doctor of Philosophy
Graduate Department of Aerospace Engineering
University of Toronto

Copyright © 2016 by Christopher Lam

Abstract

Application of Gaussian Moment Closures to Three-Dimensional Micro-Scale Flows

Christopher Lam

Doctor of Philosophy

Graduate Department of Aerospace Engineering

University of Toronto

2016

A parallel, implicit, adaptive mesh refinement (AMR), finite-volume scheme is described for the solution of the standard and regularized Gaussian moment closures on three-dimensional, multi-block, body-fitted, hexahedral meshes. The standard Gaussian closure has been shown to accurately predict non-equilibrium phenomena at moderate Knudsen numbers through an anisotropic treatment of pressure. The regularized closure builds on these advantages and includes the effects of non-equilibrium heat transfer by means of a first-order correction to the standard Gaussian closure. The combined moment closure treatment / numerical method is applied to the prediction of three-dimensional, non-equilibrium, micro-scale, gaseous flows. Unlike other regularized moment closures, the underlying closure is the standard maximum-entropy Gaussian closure which provides a fully-realizable and strictly hyperbolic description of non-equilibrium gaseous flows that is valid from the continuum limit, through the transition regime, and up to the free-molecular flow limit. The proposed finite-volume scheme uses Riemann-solver-based flux functions and limited linear reconstruction to provide accurate and monotonic solutions, even in the presence of large solution gradients and/or under-resolved solution content. A rather effective and highly scalable parallel implicit time-marching scheme based on a Jacobian-free inexact Newton-Krylov-Schwarz (NKS) approach with additive Schwarz preconditioning and domain partitioning following from the multi-block AMR mesh is used to obtain solutions to the non-linear ordinary-differential equations that result from finite-volume spatial discretization procedure. Details are given of the standard and regularized Gaussian closure, extensions for diatomic gases, and slip-flow boundary treatment. Numerical results for several canonical flow problems demonstrate the potential of the closures, that when combined with an

efficient parallel solution method, provide an effective means for accurately predicting a range of fully three-dimensional non-equilibrium gaseous flow behavior.

Acknowledgements

I've been fortunate enough to undertake studies at the University of Toronto's Institute for Aerospace Studies under the direction of Professor C.P.T. Groth. I have him to thank for spurring my continued interest in this field of study and for the guidance he has provided for me. I would also like to thank James McDonald for assistance in understanding the group code framework and the intricacies of the Gaussian moment closure.

I would like to thank my parents for their caring and nurturing over all these years. I would not be here today without their encouragement.

Thanks also goes out to all my friends both here at UTIAS and beyond. Your company has been much appreciated and I hope to partake of it even more in the future.

Computational resources for performing all of the calculations reported herein were provided by the SciNet High Performance Computing Consortium at the University of Toronto and Compute/Calcul Canada through funding from the Canada Foundation for Innovation (CFI) and the Province of Ontario, Canada.

Toronto, 2015 *Chris Lam*

Contents

List of Tables

List of Figures

Chapter 1

Introduction

1.1 Motivation

Gaseous flow behaviour is commonly described in computational fluid dynamics (CFD) by the Navier-Stokes equations and this macroscopic mathematical model has proven itself to be extremely useful in describing fluid flows in problems frequently encountered in the aerospace industry. Fluid flows in these problems are treated in a continuous, near-equilibrium manner, with intermolecular collisions occurring frequently enough to warrant such an assumption. At the other end of the spectrum, the modelling of highly-rarefied gases and slip flows usually requires the use of microscopic particle simulation methods, such as the Direct Simulation Monte Carlo (DSMC) developed by Bird [1]. While these particle techniques are successful in modelling both continuous and slip flows, their computational expense increases dramatically as more simulation particles are needed for progressively nearer equilibrium flows approaching the continuum regime. Recent scientific technologies, such as micro-electromechanical systems (MEMS) [2], encounter flow regimes that occupy a transitional area between these two extremes, where the fluid cannot be assumed to be sufficiently close to near-equilibrium to warrant the use of the Navier-Stokes equations, but the number of particles involved is high enough to make particle simulation methods quite impractical. Developments in modelling the behaviour of this transitional regime efficiently with suitable extensions to both the continuous and slip-flow regimes would not only provide invaluable information about the flow physics, but would also aid in the development of future micro-scale technologies.

1.2 Background

Continuum models, such as those based on the Navier-Stokes equations, make the assumption that the fluid remains in or in close proximity to local thermodynamic equilibrium. The thermal state can then be described by a single temperature that fully describes the translational, rotational and vibrational energy modes of the fluid particles. Energy transfer through particle collisions must occur sufficiently frequently to maintain local thermodynamic equilibrium. The dimensionless parameter used to gauge the nearness to equilibrium for a given flow is provided by the Knudsen number Kn, defined as

$$\mathrm{Kn} = \frac{\lambda}{\mathrm{L}} \tag{1.1}$$

where λ is the mean free path between interparticle collisions and L is the characteristic length scale of the problem of interest. Continuum-limit flows are dominated by interparticle collisions with very short mean free paths, with Knudsen numbers in the range $\mathrm{Kn} < 0.01$. Conversely, non-equilibrium flows may occur due to low gas densities and thus large mean free paths (as in rarefied flows) or for problems having very small length scales, where particle collisions are infrequent for the length scales of interest. In both of these cases, the Knudsen number in these flows exceeds 0.01 and becomes large as the deviation from equilibrium conditions becomes significant. The collisionless regime is taken to occur for $\mathrm{Kn} > 10 - 100$. The focus of this thesis lies in the modelling of flows in a transitional regime lying somewhere within $0.01 < \mathrm{Kn} < 1$ where the Navier-Stokes and particle simulation techniques experience difficulties. The ability to seamlessly treat the continuum regime with the same model is also deemed to be a desirable feature.

The use of moment methods for non-equilibrium gases was first hypothesized by Maxwell [3] through the use of an equilibrium phase-space distribution function. Later, Boltzmann provided a means with which to study the evolution of non-equilibrium phase-space distribution functions, which in turn could be used to derive generalized transport equations for macroscopic properties of interest [4]. However, the construction of the resulting moment equations is such that each transport equation relies on the flux of the next higher-order velocity moment, *ad infinitum*. One approach to closing off this set of equations for practical purposes is to assume a particular form for the non-equilibrium distribution function having a fixed number of free parameters in such a way that the higher-order closing velocity moment can be expressed solely in terms of lower ones. Grad [5] considered moment closures based on truncated polynomial power series expansions for the approximate distribution function and this technique generated first-order systems of hyperbolic partial differential equations (PDEs) describing the time evolution of the macroscopic moments. However, hyperbolicity of the Grad moment equations is

not guaranteed for all flow conditions leading to closure breakdown. Furthermore, the assumed form for the distribution function is not always physically plausible and certainly not strictly positive valued.

More recently, alternative hierarchies of maximum-entropy moment closures has been proposed by Dreyer [6], Müller and Ruggeri [7], and Levermore [8]. In particular, Levermore [8] points out that the maximum-entropy hierarchies have a number of desirable mathematical properties including strict hyperbolicity, thus the possibility of closure breakdown in this sense is avoided. The lowest order of the Levermore hierarchy of closures is the 5-moment closure that corresponds to the Euler equations, while the next member results in the 10-moment closure, also known as the Gaussian closure (the latter will be of primary interest herein). While a full guarantee of hyperbolicity, moment realizability, and breakdown avoidance applies only to these two lowest-order closures in the hierarchy as described by Junk [9], the usefulness of the 10-moment Gaussian closure is evident from a computational standpoint. Being purely hyperbolic with only first-order derivatives, the solution is guaranteed to have finite speeds of propagation. Moreover, numerical solutions can be readily obtained using the highly successful class of Godunov-type finite-volume schemes developed for hyperbolic conservation laws without excessive modification [10]. These schemes are robust, accurate, and can preserve the conservation properties of the solution at the discrete level. They can also be applied using a large variety of boundary conditions and meshing techniques and, for first-order systems, provide solutions that are generally insensitive to irregularities in the mesh.

It should be noted that recent advances in the field of interpolated closures, based on maximum-entropy ideas, proposed McDonald and Groth [11] and McDonald and Torrilhon [12] have sought to reintroduce higher-order moments to the Levermore system without incurring the closure-breakdown penalties described by Junk [9]. These closures have been investigated in recent work for two-dimensional flows by Tensuda *et al.* [13, 14] and have shown promise in accurately modelling non-equilibrium flows, but such closures are beyond the scope of this thesis.

The Gaussian closure is a somewhat simplified or reduced mathematical model as it does not incorporate the effects of heat transfer. Nevertheless, it has been shown to accurately describe non-equilibrium momentum transport for a range of micro-scale flows and is very representative of other higher-order closures that would potentially include the effects of non-equilibrium thermal transport [15–18]. The numerical solution and application of the Gaussian closure for two-dimensional micro-scale flows has been studied extensively by McDonald and Groth, with considerations for diatomic gases following the approach devised by Hittinger [19].

The lack of heat transfer in the Gaussian closure becomes an issue that cannot be ignored given

its otherwise attractive computational properties. Work by Struchtrup and Torrilhon [20–23] has explored the regularization of the Grad moment closure for describing higher order effects through a Chapman-Enskog-type perturbative expansion about the moment equations to allow for small deviations from the assumed form of the distribution function. The regularized forms of the Grad 13-moment and 26-moment closures have been shown to be accurate in the prediction of non-equilibrium phenomena such as velocity and temperature slip at solid boundaries, and the accurate modelling of one-dimensional shock structures that deviate significantly from thermodynamical equilibrium. While promising, the underlying hyperbolic moment system can still suffer from those of the original Grad moment closure mentioned above, namely the loss of hyperbolicity even for small deviations from equilibrium. McDonald and Groth [16, 18] have recently applied a similar regularization procedure on the Gaussian closure for two-dimensional, heat-conducting flow directly based on the anisotropic pressure tensor. While the regularization process adds additional terms of an elliptic nature term to the otherwise hyperbolic set of equations, the underlying first-order moment system remains hyperbolic for the full range of physically realizable moments. The computational advantages and modelling potential for this approach to non-equilibrium flows has now prompted its advancement for the modelling of fully three-dimensional flows.

The development of general purpose solution methods for the Gaussian closure in two dimensions has been considered previously by McDonald and Groth and Brown *et al.* [15, 16, 24, 25] for which Godunov-type finite-volume schemes were proposed. A discontinuous Galerkin finite-element solution procedure of the Gaussian closure has also been proposed by Barth [26]. Additional research by Levermore *et al.* [27] investigated solutions of the Gaussian closure for one-dimensional shock structures. From these studies, the Gaussian closure was shown to be a computationally robust method for describing flow in a variety of regimes, and its extension to three dimensions would make it even more attractive for academic and industrial uses. Nevertheless, the explicit nature of the above-mentioned solution schemes, while useful in exploring the computational potential of the closure system, require small time steps that result in long computational times, especially for highly rarefied flow regimes. Implicit schemes, such as those based on the Newton-Krylov method, allow for larger time steps and fewer iterations at the expense of a higher cost per iteration. The increased time step size allows for fully converged steady state flow solutions to be acquired in very few iterations compared to an explicit scheme. Newton-Krylov solution methods have already seen significant use in the field in computational fluid dynamics [28–31]. The coupling of the Gaussian closures with this implicit solver would allow low-cost steady state solutions for rarefied flow regimes. This would provide researchers with a useful tool for exploring both the physics of the flow regime and the mathematical

properties of the closure. Reduced computational costs and physical accuracy would also be of great benefit in an industrial setting, where the current design of MEMS devices are still firmly entrenched in physical experimentation.

1.3 Objectives

In this study, the extension of the previous work by McDonald and Groth [15–18] for two-dimensional micro-channel flows to the three-dimensional flow case is considered. A parallel, semi-implicit, adaptive mesh refinement (AMR), upwind, finite-volume scheme is described for the solution of the 10-moment standard Gaussian closure and the regularized Gaussian closure that includes the effects of heat transfer through additional elliptic terms. An implicit Newton-Krylov method with Schwarz preconditioning is employed for accelerated convergence and robustness for steady flows. The combined modelling treatment/numerical method is applied to the prediction of three-dimensional, non-equilibrium, micro-scale, gaseous flows.

Beginning with an review of the kinetic theory of gases in Chapter 2, the 10-moment Gaussian closure is defined with suitable approximations for treating diatomic gases. A description of the resulting eigenstructure shows the hyperbolic characteristics that makes the Gaussian closure computationally attractive. Details are also given concerning the regularization of the standard Gaussian closure to allow for the modelling of heat transfer. Solid wall boundaries for the transport equations in the Gaussian closure are then defined.

In Chapter 3, the proposed finite-volume method used for the solution of the Gaussian closure is described. As in the previous studies, the proposed upwind scheme makes use of Riemann-solver-based flux functions and limited linear reconstruction to provide accurate and monotonic solutions, even in the presence of large solution gradients and/or under-resolved solution content on three-dimensional, multi-block, body-fitted, hexahedral mesh. A block-based AMR strategy is used here to allow for local refinement of the computational mesh based on the procedure of Gao and Groth [32–34]. The focus here is on micro-scale flows as the Reynolds numbers in these regimes tend to be very small and this allows for a comparison with standard laminar fluid flows. The proposed parallel finite-volume scheme with block-based AMR on hexahedral mesh is then used to assess the predictive capabilities of the Gaussian closure for three-dimensional micro-scale flows and demonstrate the computational advantages offered by the closure.

A description of the implicit Newton-Krylov solution method with an additive Schwarz preconditioner then follows in Chapter 4. An implicit Newton-Krylov method with Schwarz preconditioning is developed for both the standard and regularized Gaussian closures based on

a framework used for the prediction of two and three-dimensional Navier-Stokes equations by Charest *et al.* [29] and Northrup and Groth [28]. The performance of the fully-implicit solver is compared to those from a semi-implicit solver developed by McDonald and Groth [15–18] extended to three dimensions. The convergence qualities of both methods are analyzed for a number of non-equilibrium micro-scale flows and the benefits of the fully implicit treatment are explored.

Numerical results for the standard and regularized Gaussian closure are then presented in Chapter 5 and Chapter 6, respectively. A comparison of predicted results with those from the continuum-based Navier-Stokes equations and free molecular flow theory for the same problems will be made to show how the Gaussian closure performs in various regimes, from the continuum limit to the free-molecular regime. Concluding remarks are then made about the use of the Gaussian closures and its future development in Chapter 7. It should be noted that to the best knowledge of the author, this study represents the first numerical study of three-dimensional solutions of the Gaussian closure for rarefied flow applications.

Chapter 2

Gaussian and Regularized Gaussian Moment Closures

2.1 Brief Review of Gaskinetic Theory

The kinetic theory of gases begins by treating the gas as a collection of discrete microscopic particles that interact with each other and the walls of its container through collisional processes to create perceived macroscopic properties such as density and pressure. Energy transfer between particles and its container are solely described by classical mechanics subject to Newton's laws of motion. However, constructing a set of equations describing the motion of individual particles becomes computationally prohibitive for all but the most rarefied of flow conditions.

Treatment of the particles in kinetic theory is done instead through a statistical description, and the evolution of this probability density function is correlated directly to the macroscopic properties of the fluid medium [35]. As particle position and velocity are independent of each other, a complete statistical description can be given by a six-dimensional phase space distribution spanning three-dimensional physical space, x_i, and velocity space, v_i, at a particular moment in time, t. The resulting probability density function, $\mathcal{F}(t, x_i, v_i)$, describes the number of particles occupying an elemental volume in the six-dimensional physical-velocity space at a particular moment in time.

2.1.1 Phase Space Distribution Function and Macroscopic Properties

The time evolution of $\mathcal{F}$ is governed by the Boltzmann equation [35–37], an integro-differential equation having the form

$$\frac{\partial \mathcal{F}}{\partial t} + v_i \frac{\partial \mathcal{F}}{\partial x_i} + a_i \frac{\partial \mathcal{F}}{\partial v_i} = \frac{\delta \mathcal{F}}{\delta t}\,, \tag{2.1}$$

where a_i is the acceleration due to external forces and is taken to be zero in the present work. The term on the right-hand side of the equation, $\delta\mathcal{F}/\delta t$, is the Boltzmann collision operator representing the time rate of change of the distribution function produced by binary inter-particle collisions. This term involves a multi-dimensional integral over both velocity space and solid angle, and is given by

$$\frac{\delta \mathcal{F}}{\delta t} = \iiint_{\infty} \mathrm{d}^3\mathbf{v} \int_0^{2\pi} \mathrm{d}\epsilon \int_0^{\pi} \mathrm{d}\chi \sin\chi \frac{\mathrm{d}\sigma}{\mathrm{d}\Omega} \left|\overrightarrow{g}\right| \left[\mathcal{F}\left(\vec{v}\,'\right)\mathcal{F}\left(\vec{v_2}'\right) - \mathcal{F}\left(\vec{v}\right)\mathcal{F}\left(\vec{v_2}\right)\right] \tag{2.2}$$

where $\vec{v}, \vec{v_2}$ and $\vec{v}\,', \vec{v_2}'$ are the pre-collision and post-collision velocities of the two particles involved in the collision, respectively.

Macroscopic properties of the gas can be obtained by taking appropriate velocity moments of $\mathcal{F}$. This is done by multiplying the distribution function by a velocity-dependent weight, $M(v_i)$, and integrating over all velocity space as follows:

$$\langle M(v_i)\mathcal{F}\rangle = \iiint_{\infty} M(v_i)\mathcal{F}(t, x_i, v_i)\, \mathrm{d}^3 v\,. \tag{2.3}$$

If the gas particle mass, m, is chosen as the weight (i.e., $M(v_i) = m$), the corresponding velocity moment yields the fluid density given by

$$\rho(t, x_i) = \iiint_{\infty} m\mathcal{F}(t, x_i, v_i)\, \mathrm{d}^3 v = \langle m\mathcal{F}\rangle\ . \tag{2.4}$$

Other moments of interest include the bulk velocity ($M(v_i) = mv_i$),

$$u_i(t, x_\alpha) = \frac{< mv_i\mathcal{F} >}{\rho}\,, \tag{2.5}$$

and second-order anisotropic pressure tensor ($M(v_\alpha) = mc_ic_j$),

$$P_{ij}(t, x_\alpha) = < mc_ic_j\mathcal{F} >\,, \tag{2.6}$$

where here $c_i = v_i - u_i$ is the random component of particle velocity. The deviatoric or fluid stress tensor, τ_{ij}, is related to the pressure tensor as $\tau_{ij} = \delta_{ij}p - P_{ij}$, where p is the thermodynamic pressure. Using the ideal gas equation of state, the pressure, p, is given by

$$p = \rho RT\,, \tag{2.7}$$

where T is the gas temperature and R is the gas constant. For a monatomic gas, τ_{ij} is traceless (i.e., $\tau_{kk}=0$) such that $P_{kk}=3p$ and T is a measure of the energy of the random translational motion of the gaseous particles. However, for non-equilibrium diatomic and polyatomic gases, this relationship does not generally hold and $\tau_{kk} \neq 0$ and $P_{kk} \neq 3p$. For the latter, $P_{kk} = 3p - \tau_{kk}$ and T will be taken to be the temperature of the translational modes, which are not necessarily in equilibrium with the other internal energy modes of the particle (i.e. rotational and vibrational modes).

In the derivation of the equilibrium distribution function, Maxwell makes several assumptions about the gas that are held to be true throughout this work which are also applicable for any general non-equilibrium distribution function. Combined with notions from classical mechanics, these assumptions can be summarized as:

1. Molecular Hypothesis
    - Matter is composed of discrete small, hard and perfectly elastic spherical particles.
    - All molecules of a given substance are alike and are the smallest quantity of the substance that retains its unique chemical properties.
2. Ideal Gases
    - Particles are point-like structures with no internal structure or internal degrees of freedom (monatomic gas assumption). Note that this assumption will be challenged later to expand the applicability of this work for diatomic gases.
    - Particles exert inter-particle forces on each other over a sphere of influence with a radius much smaller than the mean free path λ, and are governed purely by the laws of classical mechanics elsewhere.
    - Particles undergo binary collisions only. Tertiary and higher-order collision processes are taken to be rare and have little to no impact on the general evolution of the state of the gas.
3. Statistical Theory
    - The individual motion of each particle is not tracked. Only the probability that particles at a given location have a given velocity is of interest. The velocity distribution at any spatial location is also independent of time.
    - Post-collision directions are distributed with equal probability over all solid angles.
    - The orthogonal components of the particle velocities becomes statistically independent after a large number of intermolecular collisions.

- The isotropic nature of the distribution function holds in the absence of external forces.

4. Molecular Chaos

- Colliding particles are uncorrelated and undergo many collisions with other particles before re-colliding, and is responsible for the irreversibility of the system.

2.1.2 Maxwell-Boltzmann Distribution Function

For a monatomic gas in thermodynamic equilibrium, the solution to the Boltzmann's equation (2.1) is given by $\mathcal{F} = \mathcal{M}$ where $\mathcal{M}$ is the Maxwell-Boltzmann distribution function given by

$$\mathcal{F}(t, x_i, c_i) = \mathcal{M}(t, x_i, c_i) = \frac{(\rho/m)}{(2\pi)^{3/2} (p/\rho)^{3/2}} \exp\left(-\frac{1}{2}\frac{\rho}{p}c^2\right) , \tag{2.8}$$

which is fully defined in terms of the conserved macroscopic moments or collisional invariants ρ, ρu_i, and p. This collision operator in Eq. (2.2) will force all non-equilibrium solutions of the distribution function towards this equilibrium solution, and, once in this state, the collision operator will produce no further net changes to the distribution function. This entropy maximization property of the collision operator is well established by Boltzmann's H theorem [35].

While the Maxwellian distribution function, $\mathcal{M}$, fully defines the equilibrium behavior of the gas, it is generally a poor description of the gas under non-equilibrium conditions. This is partially due to the assumption of spatial uniformity used in its early derivation, but Boltzmann later showed that the distribution function holds even under the condition of dynamic equilibrium. Nevertheless, the Maxwell-Boltzmann distribution function, coupled with the method of moments, is an alternate method for deriving a description of a system equivalent to Euler equations of compressible gas dynamics.

2.1.3 Transport Equations for Macroscopic Properties and Maxwell's Equation of Change

Transport equations governing the time evolution of general sets of macroscopic quantities can be derived by evaluating velocity moments of the Boltzmann equation given above, Eq. (2.1). This yields the so-called Maxwell's equation of change [35] describing the transport of the moment $\langle M(v_\alpha)\mathcal{F}\rangle$, which can be expressed in weak conservation form as

$$\frac{\partial}{\partial t}\langle M(v_\alpha)\mathcal{F}\rangle + \frac{\partial}{\partial x_i}\langle v_i M(v_\alpha)\mathcal{F}\rangle = \Delta\left(\langle M(v_\alpha)\mathcal{F}\rangle\right) , \tag{2.9}$$

where the acceleration is now taken to be zero, $M(v_\alpha)$ is the appropriate velocity dependent weight, and $\Delta(\langle M(v_\alpha)\mathcal{F}\rangle) = \langle M(v_\alpha)(\delta\mathcal{F}/\delta t)\rangle$ represents the effect of collisions on the moment quantity. This collision term assumes that only binary collisions occur, as the probability of collisions involving more than two collision partners at exactly the same instance in time and space are rare and will therefore not contribute significantly to the transport and evolution of macroscopic properties.

2.2 Approximate Solutions via Moment Methods

In developing solutions to the Boltzmann equation and subsequently Maxwell's equation of change, the collision term given in Eq. (2.2) poses significant challenges. The evaluation of the collision term in its current form turns the Boltzmann equation into a seven-variable, integro-differential equation which is difficult to evaluate computationally or analytically even for the simplest of problems. While solutions to the Boltzmann equation can be found for the simplest of flow conditions [38,39], if computationally efficient ways to evaluate this expression for more complex flows are not found, the effect of molecular collisions on moment evolution cannot be investigated.

A problem of closure also becomes apparent for moment method techniques when the transport equations for each moment defined from Maxwell's equation of change in Eq. (2.9) are written out. Evaluating the time evolution of a moment $\langle M(v_\alpha)\mathcal{F}\rangle$ requires finding the spatial divergence of the next higher order moment $\langle v_i M(v_\alpha)\mathcal{F}\rangle$. The transport equation describing this next higher order moment similarly depends on an even higher order moment, *ad infinitum*. A complete and exact description of a non-equilibrium gas using this moment method directly would therefore require the solution of an infinite number of coupled moment equations, which is obviously not practical. In order to close off the number of required number of transport equations that need to be evaluated, the non-equilibrium distribution function is assumed to take on a certain form that contains a finite set of moments representative of a specified set of macroscopic quantities. The result is that the highest order moment of interest can be expressed solely in terms of lower order ones, thus providing a closed set of conservation equations. This closing off of the equations, while making the closure computationally manageable, is also necessarily responsible for the approximate nature of the moment method. Choosing a form of the distribution function that contains more moments will theoretically increase the accuracy of the model, but the computational expense may be beyond practicality. Research on moment method techniques has therefore concentrated on finding a suitable balance between computational efficiency and modelling accuracy.

2.2.1 Bhatnager-Gross-Krook Collision Operator

For many engineering applications, the complexity of the collision operator can be replaced by suitable model, provided that it mimics some basic properties of the original operator. The entropy-increasing property outlined in Boltzmann's H-Theorem should be upheld, such that for any collision model, $\mathbf{C}(\mathcal{F})$, should satisfy

$$\langle \log(\mathcal{F})\, \mathbf{C}(\mathcal{F}) \rangle \leqslant 0. \tag{2.10}$$

A well-known model that simplifies the treatment of the collision term and satisfies the entropy condition above was proposed by Bhatnagar *et al.* [40], known as the BGK model, that can be written as

$$\frac{\delta \mathcal{F}}{\delta t} \approx \mathbf{C}(\mathcal{F}) = -\frac{1}{\tau} \left(\mathcal{F} - \mathcal{M} \right) , \tag{2.11}$$

where τ is a relaxation time scale characteristic of the collisional processes, whereupon the non-equilibrium distribution function $\mathcal{F}$ relaxes towards the Maxwell-Boltzmann equilibrium distribution function $\mathcal{M}$. As the gas becomes increasingly rarefied, this relaxation time increases, which in turn drives the collision term towards zero. This behaviour is in line with what is expected in free-molecular flow. It is also evident that if the gas is already in equilibrium such that $\mathcal{F} = \mathcal{M}$, additional collisions between particles will impart no physical change to the average measurement of any macroscopic property, as the collision term is again equivalent to zero.

2.2.2 Ellipsoidal Statistical Collision Operator

One of the most serious drawbacks to using the BGK collision operator described above is the assumption that all non-equilibrium processes relax on the same time scale, τ, regardless of the gas properties. This single relaxation time is responsible for the non-equilibrium behaviour of both the momentum and thermal energy, and as a result will always predict a Prandtl number, Pr, equal to unity. This result is not ideal for the purposes of this study, given the need to model Prandtl numbers that realistically depict heat transfer for monatomic and diatomic gases that will appear in the regularized Gaussian closure.

The approximate collision operator originally developed by Holway [41], now commonly known as the ellipsoidal statistical model, is used in place of the original BGK collision operator to allow for variable Prandtl numbers and preserves much of the simplicity of the original BGK approximation. For a monatomic gas, the ellipsoidal statistical collision operator can be written

as

$$\frac{\delta \mathcal{F}}{\delta t} = -\frac{1}{\tau_{\mathrm{ES}}} \left(\mathcal{F} - \mathcal{G}_{\mathrm{ES}} \right) , \tag{2.12}$$

where

$$\mathcal{G}_{\mathrm{ES}}(t, x_i, c_i) = \frac{(\rho/m)}{(2\pi)^{3/2} \left(\det \mathbf{T} \right)^{1/2}} \exp \left(-\frac{1}{2} T_{ij}^{-1} c_i c_j \right) . \tag{2.13}$$

The distribution, $\mathcal{G}_{\mathrm{ES}}$, is a Gaussian distribution function that possesses a modified pressure tensor such that the second-order tensor, T_{ij}, is defined as

$$T_{ij} = (1-\nu)\frac{p}{\rho}\delta_{ij} + \nu \Theta_{ij} = (1-\nu)\frac{p}{\rho}\delta_{ij} + \nu \frac{P_{ij}}{\rho} , \tag{2.14}$$

where Θ_{ij} is a symmetric 'temperature' tensor given by $\Theta_{ij} = P_{ij}/\rho$ and P_{ij} is again the generalized pressure tensor. For monatomic gases, the ellipsoidal statistical collision model's adherence to Boltzmann's H theorem was first demonstrated by Andries and Perthame [42]. Andies *et al.* [43] have also considered extensions of the ellipsoidal statistical collision model to both diatomic and polyatomic gases and demonstrated that these extensions also satisfy the H theorem.

It can be shown that if the parameters τ_{ES} and ν associated with the ellipsoidal collision operator are chosen such that

$$\tau_{\mathrm{ES}} = (1-\nu)\frac{\mu}{p} = (1-\nu)\tau , \qquad 1 - \nu = \frac{1}{\mathrm{Pr}} , \tag{2.15}$$

then the model will predict the correct values for fluid viscosity and thermal conductivity in the continuum limit. It is important to note that the relaxation times for both the relaxation-time BGK and ellipsoidal statistical models, τ and τ_{ES}, differ by just a factor of the Prandtl number (i.e., $\tau_{\mathrm{ES}} = \tau/\mathrm{Pr}$). The moment equations and analyses to follow will be written in terms of the relaxation time for the standard BGK model, τ, and Prandtl number, Pr, for consistency with traditional forms of these equations and other previous analyses.

2.2.3 Moment Closure Techniques

The method of moments was developed to attain approximate solutions to the Boltzmann equation. It is, of course, possible to solve the Boltzmann equation directly and thus eliminate the need for any closure expressions. Suitable boundary conditions for the physical and velocity space can be developed, but difficulties can arise from the high dimensionality of the collision term. The equation itself contains seven independent variables (time, three-dimensional physical and velocity space). At each point in the phase space, the five-dimensional collision operator must also be evaluated. When properly calculated, this method can be very accurate, but is extremely expensive to implement. When additional physical effects such as multi-species

mixtures are considered, evaluating the Boltzman equation directly becomes a purely academic exercise.

The assumed form of the non-equilibrium distribution function can give rise to a large variety of closure methods, each with its own distinct characteristics. Grad [5] proposed a set of moment closures based on a truncated polynomial power series expansion about the Maxwell-Boltzmann distribution function of the form

$$\mathcal{F}_{\text{Grad}} \approx \mathcal{M}\left[1 + A_i c_i + B_{ij} c_i c_j + D_{ijk} c_i c_j c_k + \cdots\right] \tag{2.16}$$

where the coefficients A_i, B_{ij} and D_{ijk} are derived by matching the resulting moments with those known from a finite number of velocity moments. The polynomial can be truncated at any point to provide expressions for consecutively higher order moments, generating a set of quasi-linear, first order, hyperbolic PDEs. These equations, however, have been shown to break down and lose their hyperbolicity at times even under simple flows as shown by McDonald and Groth [15]. The truncated polynomial can also potentially provide a mathematically sound, but physically unrealistic distribution function.

In contrast to the Grad moment closure system, the Chapman-Enskog perturbative expansion technique offers approximate solutions to a 'scaled' form of the Boltzmann equation in the form

$$\frac{\partial \mathcal{F}}{\partial t} + v_i \frac{\partial \mathcal{F}}{\partial x_i} = -\frac{\mathcal{F} - \mathcal{M}}{\epsilon \tau}, \tag{2.17}$$

where the BGK collision operator has been implemented. A small perturbative parameter, $\epsilon \propto$ Kn, is introduced to simulate the effects of small deviations from the equilibrium distribution. Solutions to this scaled expression can be written as

$$\mathcal{F}_{\text{CE}} \approx \mathcal{M}\left[f^{(0)} + \epsilon f^{(1)} + \epsilon^2 f^{(2)} + \epsilon^3 f^{(3)} + \cdots\right] \tag{2.18}$$

where $f^{(n)}$ represents an nth order perturbative correction to the Maxwell-Boltzmann distribution function, with contributions that become increasingly small with increasing powers of ϵ. Substituting this perturbed distribution function into the scaled kinetic equation 2.17 and

collecting like terms in powers of ϵ yields

$$\begin{aligned}
&\mathcal{M}\left(\frac{f^{(0)}-1}{\tau}\right)\\
&+\epsilon\left[\frac{\partial\left(f^{(0)}\mathcal{M}\right)}{\partial t}+v_i\frac{\partial\left(f^{(0)}\mathcal{M}\right)}{\partial x}+\frac{f^{(1)}\mathcal{M}}{\tau}\right]\\
&+\epsilon^2\left[\frac{\partial\left(f^{(1)}\mathcal{M}\right)}{\partial t}+v_i\frac{\partial\left(f^{(1)}\mathcal{M}\right)}{\partial x}+\frac{f^{(2)}\mathcal{M}}{\tau}\right]\\
&+\epsilon^3\left[\frac{\partial\left(f^{(2)}\mathcal{M}\right)}{\partial t}+v_i\frac{\partial\left(f^{(2)}\mathcal{M}\right)}{\partial x}+\frac{f^{(3)}\mathcal{M}}{\tau}\right]\\
&+\cdots=0\,.
\end{aligned}\tag{2.19}$$

Non-trivial solutions can be obtained by equating each term in powers of ϵ to zero. Higher order moments can be evaluated by taking into account ever higher order perturbations to the Maxwellian. It is important to note that while the solution content for higher order moments in the Grad closures is embedded within all the coefficients in the truncated polynomial, the Chapman-Enskog perturbative expansion technique simply adds additional corrective terms to account for the higher order moments. The drawback to this method is that these corrective terms involve high-order derivatives resulting in a loss of hyperbolicity that can produce unrealistic infinite propagation speeds for infinitesimal disturbances. This method of perturbative expansions is used later to introduce higher-order moment contributions that would otherwise be inaccessible for the moment closures considered in this thesis.

More recently, a hierarchy of maximum-entropy moment closures has been proposed by Dreyer [6], Müller and Ruggeri [7], and Levermore [8]. The entropy of a system of particles can be directly related to the number of possible arrangements of the particles in phase space as described by some chosen distribution function. Assuming each particle arrangement occurs at the same frequency, in the absence of complete information regarding the exact nature of the system, choosing a distribution function with limited information that maximizes physical entropy would provide the most likely distribution for the system. Deriving moment closures based on this idea, the assumed form of the distribution function in the Levermore hierarchy takes on a simple exponential form similar to the Maxwell-Boltzmann distribution function. The lowest order, 5-moment member of this hierarchy recovers the Maxwell-Boltzmann distribution function, generating the transport equations found in the Euler equations. The next higher-order member is a 10-moment closure with a similar structure to that found in the equilibrium distribution function with the exception of an anisotropic description of pressure. These moment closures possess significant advantages over those found from the Grad hierarchy and a Chapman-Enskog technique. The exponential nature of the distribution function guarantees that it is strictly positive

for all points in velocity space, eliminating the moment realizability problem found in the Grad closures. The transport equations derived from these low order members of the Levermore hierarchy are also strictly hyperbolic, unlike the elliptic terms generated in the Chapman-Enskog perturbative expansion technique. In addition to producing finite speeds of information propagation associated with physical processes, hyperbolicity and its associated first order derivatives also provide many computational advantages in flux evaluation and time step size.

Unfortunately, higher order members of the Levermore hierarchy encounter difficulties. Expressions for the closure coefficients derived from the moments become impossible to express analytically and must be found numerically. A numerical application of these closures would require large computational resources to perform these operations. A more serious problem lies in the assumption that a maximum-entropy istribution function always exists for any given set of moments. Junk [9, 44] has shown this to be false for members of the Levermore hierarchy above the Gaussian closure. Higher order members of the hierarchy have been shown to fail in the near-equilibrium regime, where the problem of calculating the maximum entropy becomes ill-posed as the equilibrium point is unfortunately located exactly between the realizable and unrealizable moment space. The inability to account for even small deviations from equilibrium makes the higher order members of the Levermore hierarchy unattractive, while the lowest order Maxwellian member provides nothing new. The Gaussian closure, however, contains the computational advantages of the Levermore closures while offering a more detailed analysis of the flow compared to the Euler equations. The numerical solutions of the original and regularized forms of the Gaussian closure are explored in this thesis.

2.3 10-Moment Gaussian Closure

2.3.1 Maximum Entropy Gaussian Closure for a Monatomic Gas

The lowest order members of the Levermore hierarchy of moment closures [8] result in the local equilibrium Maxwellian closure leading to the 5-moment Euler equations, and the Gaussian distribution that leads to a 10-moment closure. For a monatomic gas, the velocity weights associated with constructing the 10-moment Gaussian closure are

$$\mathbf{M}(v_\alpha) = [m,\ mv_i,\ mv_iv_j]^{\mathrm{T}}\ , \tag{2.20}$$

which correspond to the macroscopic moments

$$\langle \mathbf{M}(v_\alpha)\mathcal{F}\rangle = [\rho,\ \rho u_i,\ \rho u_iu_j + P_{ij}]^{\mathrm{T}}\ . \tag{2.21}$$

The assumed form of the distribution function can be derived through analytical means, based on entropy maximization concepts [8], and results in the Gaussian distribution function, $\mathcal{G}$, given by

$$\mathcal{F}(t,x_i,c_i) = \mathcal{G}(t,x_i,c_i) = \frac{(\rho/m)}{(2\pi)^{3/2}\left(\det\boldsymbol{\Theta}\right)^{1/2}} \exp\left(-\frac{1}{2}\Theta_{ij}^{-1}c_ic_j\right), \tag{2.22}$$

where $\Theta_{ij}=P_{ij}/\rho$ is an anisotropic "temperature" tensor written as

$$\boldsymbol{\Theta} = \begin{bmatrix} \frac{P_{xx}}{\rho} & \frac{P_{xy}}{\rho} & \frac{P_{xz}}{\rho} \\ \frac{P_{xy}}{\rho} & \frac{P_{yy}}{\rho} & \frac{P_{yz}}{\rho} \\ \frac{P_{xz}}{\rho} & \frac{P_{yz}}{\rho} & \frac{P_{zz}}{\rho} \end{bmatrix}, \tag{2.23}$$

with a determinant defined as

$$\det\boldsymbol{\Theta} = \frac{1}{\rho^3}\left[P_{xx}P_{yy}P_{zz} + 2P_{xy}P_{yz}P_{xz} - P_{xz}^2P_{yy} - P_{yz}^2P_{xx} - P_{xy}^2P_{zz}\right] \tag{2.24}$$

and an inverse, Θ^{-1}, found to be

$$\Theta^{-1} = \frac{1}{\rho^2\det\boldsymbol{\Theta}} \begin{bmatrix} \left(P_{yy}P_{zz} - P_{yz}^2\right) & -\left(P_{xy}P_{zz} - P_{xz}P_{yz}\right) & \left(P_{xy}P_{yz} - P_{xz}P_{yy}\right) \\ -\left(P_{xy}P_{zz} - P_{xz}P_{yz}\right) & \left(P_{xx}P_{zz} - P_{xz}^2\right) & -\left(P_{xx}P_{yz} - P_{xz}P_{xy}\right) \\ \left(P_{xy}P_{yz} - P_{xz}P_{yy}\right) & -\left(P_{xx}P_{yz} - P_{xz}P_{xy}\right) & \left(P_{xx}P_{yy} - P_{xy}^2\right) \end{bmatrix}. \tag{2.25}$$

The non-equilibrium distribution function possesses a Gaussian-like distribution for each of the principal strain axes, and physically corresponds to a non-equilibrium state with different temperatures in each direction. The form of the Gaussian distribution function was first suggested by Maxwell [3] as a probable and more general form of the widely known Maxwell-Boltzmann equilibrium distribution function with consideration towards particle velocity anisotropies, though no further attempt was made at the time to discover the nature of the velocity distributions. Independent work by Schlüter [45,46] and Holway [41,47–49] seems to have rediscovered this form of the distribution function for use in describing flows with significant anisotropic pressure effects.

The moment equations arising from the Gaussian closure can be found using Maxwell's equation of change in Eq. (2.9), with $\mathcal{F}=\mathcal{G}$ and the ellipsoidal statistical approximation described in Section 2.2.2 for the collision term after substituting the velocity moments in Eq. (2.20). The transport equations from the Gaussian closure can then be summarized as follows:

$$\frac{\partial}{\partial t}(\rho) + \frac{\partial}{\partial x_i}(\rho u_i) = 0, \tag{2.26}$$

$$\frac{\partial}{\partial t}(\rho u_i) + \frac{\partial}{\partial x_j}(\rho u_iu_j + P_{ij}) = 0, \tag{2.27}$$

$$\frac{\partial}{\partial t}(\rho u_iu_j + P_{ij}) + \frac{\partial}{\partial x_k}(\rho u_iu_ju_k + u_iP_{jk} + u_jP_{ik} + u_kP_{ij} + Q_{ijk}) = -\frac{1}{\tau}(P_{ij} - p\delta_{ij}). \tag{2.28}$$

The first two equations, Eqs. (2.26) and (2.27), describe the well-known conditions for the conservation of mass and momentum, while the third equation, Eq. (2.28) describes the transport of the symmetric non-equilibrium tensor for the total energy in the flow including random and bulk kinetic energy components. Due to the assumed exponential form of the distribution function, integration of the third-order velocity moment, Q_{ijk}, is always zero. The generalized energy equation can then be simplified to give

$$\frac{\partial}{\partial t}\left(\rho u_i u_j + P_{ij}\right) + \frac{\partial}{\partial x_k}\left(\rho u_i u_j u_k + u_i P_{jk} + u_j P_{ik} + u_k P_{ij}\right) = -\frac{1}{\tau}\left(P_{ij} - p\delta_{ij}\right) . \tag{2.29}$$

The next higher order moment, when subject to Maxwell's equation of change, gives

$$Q_{ijk} = \langle m c_i c_j c_k \mathcal{G} \rangle = 0 \,, \qquad q_i = \frac{1}{2}\langle m c_i c_j c_j \mathcal{G} \rangle = 0 \,, \tag{2.30}$$

due to the assumed exponential form of the distribution function. Its equivalence to zero provides closure to the system as the transport equation for the total energy is now only dependent on the lower order moments $\langle m\mathcal{G}\rangle$ and $\langle m c_i \mathcal{G}\rangle$. However, Q_{ijk} is the third-order generalized heat flux tensor and q_i is the usual fluid-dynamic heat flux vector. Its absence means that the use of the Gaussian closure for modelling non-equilibrium flows automatically assumes negligible heat flux.

2.3.2 Maximum Entropy Gaussian Closure for a Diatomic Gas

The description of the Gaussian closure to this point has been limited to monatomic particles. Extending the validity of the closure to diatomic or even polyatomic particles would allow for the modelling of a larger class of physically interesting flows and would bring the use of the Gaussian closure closer towards engineering and industrial-relevant applications. The modelling of polyatomic particles must take into account the energy associated with the internal rotational degrees of freedom. Given that particles with more than two atoms will possess an increasingly large number of geometric configurations and internal rotational degrees of freedom, it seems prudent at this time to begin with diatomic molecules.

Diatomic particles are treated in a classical sense as two rigid bodies rotating about a common center of mass. The dumbbell-like configuration for the diatomic molecule includes three rotational degrees of freedom. Rotation about the axis joining the two atoms has a moment arm equivalent to the radius of the atom, and the treatment of the atoms as point masses reduces the moment of inertia about this arm to zero, leaving two significant rotational degrees of freedom to manage. The net effect of these rotational degrees of freedom on the average angular momentum of the fluid is assumed to be zero, along with the assumption that external forces and

torques applied to the fluid do not directly affect the internal rotational modes. The treatment of diatomic particles in the non-equilibrium distribution function, $\mathcal{F}$, remains largely the same as for monatomic particles, except for an additional dependence on the angular velocity of the particle, ω_α. The resulting maximum-entropy Gaussian distribution takes the form

$$\mathcal{G}_{\mathrm{D}}(t, x_i, c_i, \omega_\alpha) = \frac{(\rho/m)\,(I/m)}{(2\pi)^{5/2}\,(\det \boldsymbol{\Theta})^{1/2}\,(p/\rho)\,(T_{\mathrm{r}}/T)} \exp\left[-\frac{1}{2}\left(\Theta^{-1}_{ij} c_i c_j + R^{-1}_{\alpha\beta}\omega_\alpha\omega_\beta\right)\right], \quad (2.31)$$

where I is the moment of inertia of a gas molecule, p is again the usual thermodynamic pressure, T is now the temperature associated with the translational energy, T_{r} is the rotational temperature, and

$$R_{\alpha\beta} = \left(\frac{mp}{I\rho}\right)\left(\frac{T_{\mathrm{r}}}{T}\right)\delta_{\alpha\beta} = \left(\frac{me_{\mathrm{r}}}{I}\right)\delta_{\alpha\beta} \quad (2.32)$$

where specific rotational energy of the gas, e_{r}, is then given by $e_{\mathrm{r}} = (p/\rho)(T_{\mathrm{r}}/T)$. The corresponding Maxwellian distribution function for equilibrium conditions for a diatomic gas is then given by

$$\mathcal{M}_{\mathrm{D}}(t, x_i, c_i, \omega_\alpha) = \frac{(\rho/m)\,(I/m)}{(2\pi)^{5/2}\,(p/\rho)^{5/2}} \exp\left[-\frac{1}{2}\frac{\rho}{p}\left(c^2 + \frac{I}{m}\omega^2\right)\right]. \quad (2.33)$$

Taking moments about a non-equilibrium distribution function for diatomic gases to find the macroscopic properties of the fluid proceeds in a similar fashion to the method described previously for monatomic gases. General velocity weights that can be applied can now be a function of both the translation velocity, v_i, and rotational velocity, ω_α, and the resulting moments will take the form

$$\langle M(v_i, \omega_\alpha)\mathcal{F}\rangle = \iiint\limits_{\infty} M(v_i, \omega_\alpha)\mathcal{F}(t, x_i, v_i, \omega_\alpha)\,\mathrm{d}^3v\,\mathrm{d}^2\omega\,, \quad (2.34)$$

which requires an integration over five-dimensional space. The moments constructed up to this point have all been formed from translational velocity functionals only. Their integration through this new five-dimensional space will not bring about any additional terms in the mass and momentum transport equations, but will have an effect on the energy transport equations. Of interest are the moments found from the velocity weight $I\omega_\alpha\omega_\beta$ which describes the rotational energy tensor, or, since the rotational energy is invariant over the two internal rotational degrees of freedom, $I\omega^2/2$, which describes the scalar rotational energy. Their respective moments can be written as

$$\iiint\limits_{\infty} I\omega_\alpha\omega_\beta\mathcal{G}_{\mathrm{D}}(t, x_i, v_i, \omega_\delta)\,\mathrm{d}^3v\,\mathrm{d}^2\omega = \langle I\omega_\alpha\omega_\beta\mathcal{G}_{\mathrm{D}}\rangle = p\left(\frac{T_{\mathrm{r}}}{T}\right)\delta_{\alpha\beta} = \rho(t, x_i)e_{\mathrm{r}}(t, x_i)\delta_{\alpha\beta}\,, \quad (2.35)$$

$$\iiint\limits_{\infty} \frac{I}{2}\omega^2\mathcal{G}_{\mathrm{D}}(t, x_i, v_i, \omega_\alpha)\,\mathrm{d}^3v\,\mathrm{d}^2\omega = \left\langle\frac{I}{2}\omega^2\mathcal{G}_{\mathrm{D}}\right\rangle = \rho(t, x_i) = p\left(\frac{T_{\mathrm{r}}}{T}\right) = \rho(t, x_i)e_{\mathrm{r}}(t, x_i)\,, \quad (2.36)$$

An extended treatment of the collision model is also required for diatomic gases. It is assumed that the relaxation times required to reach equilibrium in the translational velocities only will be shorter than those required to reach complete equilibrium in both the translational and rotational velocities. This is in contrast to the single relaxation time used for monatomic gases and its effect must be incorporated into the collision term operator. Using the ellipsoidal collision operator described in the previous section, the collision term accounting for diatomic gases can be written as

$$\frac{\delta \mathcal{F}}{\delta t} = -\frac{1}{\tau_{\mathrm{t}}} \left(\mathcal{F} - \mathcal{G}_{\mathrm{ID}} \right) - \frac{1}{\tau_{\mathrm{r}}} \left(\mathcal{G}_{\mathrm{ID}} - \mathcal{G}_{\mathrm{ESD}} \right) , \tag{2.37}$$

where it is assumed that the general non-equilibrium distribution relaxes first toward an intermediate ellipsoidal Gaussian distribution, $\mathcal{G}_{\mathrm{ID}}$, given by

$$\mathcal{G}_{\mathrm{ID}}(t, x_i, c_i) = \frac{(\rho/m)\,(I/m)}{(2\pi)^{5/2} \left(\det \boldsymbol{\Upsilon}\right)^{1/2} (p/\rho)\,(T_{\mathrm{r}}/T)} \exp\left[-\frac{1}{2} \left(\Upsilon_{ij}^{-1} c_i c_j + R_{\alpha\beta}^{-1} \omega_\alpha \omega_\beta \right) \right] , \tag{2.38}$$

whereupon equilibrium is achieved for the translational degrees of freedom, but not necessarily for the rotational degrees of freedom, on some time scale τ_{t}. This distribution function then further relaxes towards the modified ellipsoidal distribution function for diatomic gases, $\mathcal{G}_{\mathrm{ESD}}$, having the form

$$\mathcal{G}_{\mathrm{ESD}}(t, x_i, c_i) = \frac{(\rho/m)\,(I/m)}{(2\pi)^{5/2} \left(\det \mathbf{T}\right)^{1/2} (p/\rho)\left[(1-\nu) + \nu\,(T_{\mathrm{r}}/T)\right]} \exp\left[-\frac{1}{2} \left(T_{ij}^{-1} c_i c_j + S_{\alpha\beta}^{-1} \omega_\alpha \omega_\beta \right) \right] , \tag{2.39}$$

on some time scale τ_{r}, where both the translational and rotational degrees of freedom are in equilibrium. The pseudo-temperature tensor in the intermediate ellipsoidal Gaussian distribution, Υ_{ij}, is defined as

$$\Upsilon_{ij} = (1-\nu)\frac{P_{kk}}{3\rho}\delta_{ij} + \nu\Theta_{ij} = (1-\nu)\frac{P_{kk}}{3\rho}\delta_{ij} + \nu\frac{P_{ij}}{\rho} . \tag{2.40}$$

The tensor appearing in the equilibrium ellipsoidal Gaussian distribution, $S_{\alpha\beta}$, takes the form

$$S_{\alpha\beta} = (1-\nu)\frac{mp}{I\rho}\delta_{ij} + \nu R_{\alpha\beta} = \frac{mp}{I\rho}\left[(1-\nu) + \nu\frac{T_{\mathrm{r}}}{T}\right]\delta_{ij} . \tag{2.41}$$

The remaining tensors appearing in these distribution functions, T_{ij} and $R_{\alpha\beta}$, have been defined earlier in Eqs. (2.14) and (2.32) respectively.

This three-scale relaxation time approximation incorporates two time scales related to the equilibrium processes in the translational and rotational modes. These can be defined using a similar process as those shown for monatomic gases in Eq. (2.15) such that

$$\tau_{\mathrm{t}} = (1-\nu)\tau , \qquad \tau_{\mathrm{r}} = (1-\nu)\tau_{\mathrm{v}} , \qquad 1-\nu = \frac{1}{\mathrm{Pr}} , \tag{2.42}$$

where μ is the fluid viscosity, μ_{v} is the bulk or volume viscosity. To define the characteristic relaxation times for the collisional processes, the bulk and dynamic viscosities for the fluid are used. In the near-equilibrium limit for perfect gases, rotational relaxation exhibits itself as a major source of bulk viscosity. Through a perturbative expansion about a small parameter, Hittinger [19] has shown that the relaxation times can be related to the dynamic viscosity μ and the bulk viscosity μ_B through the expressions

$$\tau \sim \frac{\mu}{p}, \quad \tau_{\mathrm{v}} \sim \frac{15\mu_B}{4p}. \tag{2.43}$$

Using the three-scale relaxation-time approximation defined above, the moment equations of the maximum-entropy Gaussian closure for a diatomic gas can thus be obtained by substituting appropriate weights into Maxwell's equation of change yielding

$$\frac{\partial}{\partial t}\left(\rho\right) + \frac{\partial}{\partial x_i}\left(\rho u_i\right) = 0\,, \tag{2.44}$$

$$\frac{\partial}{\partial t}\left(\rho u_i\right) + \frac{\partial}{\partial x_j}\left(\rho u_i u_j + P_{ij}\right) = 0\,, \tag{2.45}$$

$$\begin{aligned} \frac{\partial}{\partial t}\left(\rho u_i u_j + P_{ij}\right) \quad &+ \quad \frac{\partial}{\partial x_k}\left(\rho u_i u_j u_k + u_i P_{jk} + u_j P_{ik} + u_k P_{ij}\right) \\ &= \quad -\frac{1}{\tau}\left(P_{ij} - \frac{P_{kk}}{3}\delta_{ij}\right) - \frac{2}{15\tau_{\mathrm{v}}}\left(P_{kk} - 3\rho e_{\mathrm{r}}\right)\delta_{ij}\,, \end{aligned} \tag{2.46}$$

$$\frac{\partial}{\partial t}\left(\rho e_{\mathrm{r}}\right) + \frac{\partial}{\partial x_i}\left(\rho u_i e_{\mathrm{r}}\right) = -\frac{1}{5\tau_{\mathrm{v}}}\left(3\rho e_{\mathrm{r}} - P_{kk}\right)\,, \tag{2.47}$$

As with the monatomic closure, the moment equations of the diatomic closure are also strictly hyperbolic and do not incorporate a description of heat transfer and predicts zero heat flux. Note that the transport equations for diatomic gases are similar to those for monatomic gases given in Eqs. (2.26)–(2.28), with the exception of an additional source term in the energy transport accounting for a rotational energy relaxation time, and an additional transport equation describing the evolution of rotational energy. This similarity allows for the construction of a unified computational solution scheme with minimal specializations for managing fluids with varying molecular structure.

2.3.3 Eigenstructure for Diatomic Gases

The eigenstructure of the Gaussian closure is of interest here not only because of its heavy use in various flux functions used in Godunov-type finite volume schemes, but also to demonstrate the hyperbolicity of the system and the propagation characteristics of various macroscopic properties. While the structure for diatomic gases is given here, the eigenstructure for monatomic

gases can be obtained by simply removing the rotational energy transport equation and the rotational energy contribution to the energy transport source term. Equations (2.44)–(2.47) can be written in weak conservation form by

$$\frac{\partial \mathbf{U}}{\partial t} + \frac{\partial \mathbf{E}}{\partial x} + \frac{\partial \mathbf{F}}{\partial y} + \frac{\partial \mathbf{G}}{\partial z} = \mathbf{S}, \tag{2.48}$$

where $\mathbf{U}$ is the vector of conserved variables, $\mathbf{S}$ is the source vector, and $\mathbf{E}$, $\mathbf{F}$, and $\mathbf{G}$ are the flux vectors in the x, y, and z directions respectively. The vectors are defined as

$$\mathbf{U} = \begin{bmatrix} \rho \\ \rho u \\ \rho v \\ \rho w \\ \rho u^2 + P_{xx} \\ \rho uv + P_{xy} \\ \rho uw + P_{xz} \\ \rho v^2 + P_{yy} \\ \rho vw + P_{yz} \\ \rho w^2 + P_{zz} \\ E_{rot} \end{bmatrix}, \quad \mathbf{S} = \begin{bmatrix} 0 \\ 0 \\ 0 \\ 0 \\ -\frac{1}{3\tau}\left(2P_{xx} - P_{yy} - P_{zz}\right) - \frac{2}{15\tau_{\mathrm{v}}}\left(P_{xx} + P_{yy} + P_{zz} - 3E_{rot}\right) \\ -\frac{P_{xy}}{\tau} \\ -\frac{P_{xz}}{\tau} \\ -\frac{1}{3\tau}\left(-P_{xx} + 2P_{yy} - P_{zz}\right) - \frac{2}{15\tau_{\mathrm{v}}}\left(P_{xx} + P_{yy} + P_{zz} - 3E_{rot}\right) \\ -\frac{P_{yz}}{\tau} \\ -\frac{1}{3\tau}\left(-P_{xx} - P_{yy} + 2P_{zz}\right) - \frac{2}{15\tau_{\mathrm{v}}}\left(P_{xx} + P_{yy} + P_{zz} - 3E_{rot}\right) \\ -\frac{1}{5\tau_{\mathrm{v}}}\left(3E_{rot} - P_{xx} - P_{yy} - P_{zz}\right) \end{bmatrix}$$

$$\mathbf{E} = \begin{bmatrix} \rho u \\ \rho u^2 + P_{xx} \\ \rho uv + P_{xy} \\ \rho uw + P_{xz} \\ \rho u^3 + 3uP_{xx} \\ \rho u^2 v + 2uP_{xy} + vP_{xx} \\ \rho u^2 w + 2uP_{xz} + wP_{xx} \\ \rho uv^2 + uP_{yy} + 2vP_{xy} \\ \rho uvw + uP_{yz} + vP_{xz} + wP_{xy} \\ \rho w^2 u + uP_{zz} + 2wP_{xz} \\ uE_{rot} \end{bmatrix}, \quad \mathbf{F} = \begin{bmatrix} \rho v \\ \rho uv + P_{xy} \\ \rho v^2 + P_{yy} \\ \rho vw + P_{yz} \\ \rho u^2 v + 2uP_{xy} + vP_{xx} \\ \rho uv^2 + uP_{yy} + 2vP_{xy} \\ \rho uvw + uP_{yz} + vP_{xz} + wP_{xy} \\ \rho v^3 + 3vP_{yy} \\ \rho v^2 w + 2vP_{yz} + wP_{yy} \\ \rho vw^2 + vP_{zz} + 2wP_{yz} \\ vE_{rot} \end{bmatrix},$$

$$\mathbf{G} = \begin{bmatrix} \rho w \\ \rho uw + P_{xz} \\ \rho vw + P_{yz} \\ \rho w^2 + P_{zz} \\ \rho u^2 w + 2uP_{xz} + wP_{xx} \\ \rho uvw + uP_{yz} + vP_{xz} + wP_{xy} \\ \rho uw^2 + uP_{zz} + 2wP_{xz} \\ \rho v^2 w + 2vP_{yz} + wP_{yy} \\ \rho vw^2 + vP_{zz} + 2wP_{yz} \\ \rho w^3 + 3wP_{zz} \\ wE_{rot} \end{bmatrix}.$$

The conservative form of Eq. (2.48) can also be written with flux Jacobians as

$$\frac{\partial \mathbf{U}}{\partial t} + \mathbf{A}\frac{\partial \mathbf{U}}{\partial x} + \mathbf{B}\frac{\partial \mathbf{U}}{\partial y} + \mathbf{C}\frac{\partial \mathbf{U}}{\partial z} = \mathbf{S}, \tag{2.49}$$

where $\mathbf{A} = \partial\mathbf{F}/\partial\mathbf{U}$, $\mathbf{B} = \partial\mathbf{E}/\partial\mathbf{U}$, and $\mathbf{C} = \partial\mathbf{G}/\partial\mathbf{U}$.

Taking the x-direction as an example, the eigenvalues of the Jacobian matrix $\mathbf{A}$ in three dimensions are found to be

$$\lambda_{1-11} = \left(u - \sqrt{3}c_{xx}, u - c_{xx}, u - c_{xx}, u, u, u, u, u, u + c_{xx}, u + c_{xx}, u + \sqrt{3}c_{xx}\right) \tag{2.50}$$

where $c_{xx} = \sqrt{P_{xx}/\rho}$ is representative of an x-directional 'sound' speed. These eigenvalues are representative of the propagation speeds of small disturbances in this system, and are all real when $\rho > 0$ and $P_{xx} > 0$. Eigensystem and dispersion analyses of this system have been performed previously by Brown [25] for monatomic gases, and Hittinger [19] for diatomic gases. The right eigenvectors show the hydrodynamic properties affected by each of these wave speeds

and are written as

$$\mathbf{r_{c1}} = \begin{bmatrix} 1 \\ u - \sqrt{3}c_{xx} \\ v - \frac{\sqrt{3}P_{xy}}{c_{xx}\rho} \\ w - \frac{\sqrt{3}P_{xz}}{c_{xx}\rho} \\ 3c_{xx}^2 - 2\sqrt{3}uc_{xx} + u^2 \\ \frac{\rho u v c_{xx} - u\sqrt{3}P_{xy} - \sqrt{3}c_{xx}^2\rho v + 3c_{xx}P_{xy}}{c_{xx}\rho} \\ \frac{\rho u w c_{xx} - u\sqrt{3}P_{xz} - \sqrt{3}c_{xx}^2\rho w + 3c_{xx}P_{xz}}{c_{xx}\rho} \\ \frac{\rho^2 v^2 c_{xx}^2 - 2\sqrt{3}P_{xy}c_{xx}\rho v + \rho c_{xx}^2 P_{yy} + 2P_{xy}^2}{\rho^2 c_{xx}^2} \\ \frac{c_{xx}\rho\left(-\sqrt{3}(wP_{xy} + vP_{xz}) + c_{xx}(P_{yz} + \rho v w)\right) + 2P_{xz}P_{xy}}{\rho^2 c_{xx}^2} \\ \frac{-2\sqrt{3}\rho c_{xx} w P_{xz} + \rho^2 c_{xx}^2 w^2 + P_{zz}c_{xx}^2\rho + 2P_{xz}^2}{\rho^2 c_{xx}^2} \\ \frac{E_{rot}}{\rho} \end{bmatrix}, \mathbf{r_{c2}} = \begin{bmatrix} 0 \\ 0 \\ 1 \\ 0 \\ 0 \\ u - c_{xx} \\ 0 \\ \frac{2(vc_{xx}\rho - P_{xy})}{c_{xx}\rho} \\ \frac{wc_{xx}\rho - P_{xz}}{c_{xx}\rho} \\ 0 \\ 0 \end{bmatrix}, \mathbf{r_{c3}} = \begin{bmatrix} 0 \\ 0 \\ 0 \\ 1 \\ 0 \\ 0 \\ u - c_{xx} \\ 0 \\ \frac{(vc_{xx}\rho - P_{xy})}{c_{xx}\rho} \\ \frac{2(wc_{xx}\rho - P_{xz})}{c_{xx}\rho} \\ 0 \end{bmatrix},$$

$$\mathbf{r_{c4}} = \begin{bmatrix} 1 \\ u \\ v \\ w \\ u^2 \\ uv \\ uw \\ v^2 \\ vw \\ w^2 \\ 0 \end{bmatrix}, \mathbf{r_{c5}} = \begin{bmatrix} 0 \\ 0 \\ 0 \\ 0 \\ 0 \\ 0 \\ 0 \\ 1 \\ 0 \\ 0 \\ 0 \end{bmatrix}, \mathbf{r_{c6}} = \begin{bmatrix} 0 \\ 0 \\ 0 \\ 0 \\ 0 \\ 0 \\ 0 \\ 0 \\ 1 \\ 0 \\ 0 \end{bmatrix}, \mathbf{r_{c7}} = \begin{bmatrix} 0 \\ 0 \\ 0 \\ 0 \\ 0 \\ 0 \\ 0 \\ 0 \\ 0 \\ 1 \\ 0 \end{bmatrix}, \mathbf{r_{c8}} = \begin{bmatrix} 0 \\ 0 \\ 0 \\ 0 \\ 0 \\ 0 \\ 0 \\ 0 \\ 0 \\ 0 \\ 1 \end{bmatrix},$$

$$\mathbf{r_{c9}} = \begin{bmatrix} 0 \\ 0 \\ 0 \\ 1 \\ 0 \\ 0 \\ u + c_{xx} \\ 0 \\ \frac{(vc_{xx}\rho + P_{xy})}{c_{xx}\rho} \\ \frac{2(wc_{xx}\rho + P_{xz})}{c_{xx}\rho} \\ 0 \end{bmatrix}, \mathbf{r_{c10}} = \begin{bmatrix} 0 \\ 0 \\ 1 \\ 0 \\ 0 \\ u + c_{xx} \\ 0 \\ \frac{2(vc_{xx}\rho + P_{xy})}{c_{xx}\rho} \\ \frac{wc_{xx}\rho + P_{xz}}{c_{xx}\rho} \\ 0 \\ 0 \end{bmatrix}, \mathbf{r_{c11}} = \begin{bmatrix} 1 \\ u + \sqrt{3}c_{xx} \\ v + \frac{\sqrt{3}P_{xy}}{c_{xx}\rho} \\ w + \frac{\sqrt{3}P_{xz}}{c_{xx}\rho} \\ 3c_{xx}^2 + 2\sqrt{3}uc_{xx} + u^2 \\ \frac{\rho uvc_{xx} + u\sqrt{3}P_{xy} + \sqrt{3}c_{xx}^2\rho v + 3c_{xx}P_{xy}}{c_{xx}\rho} \\ \frac{\rho uwc_{xx} + u\sqrt{3}P_{xz} + \sqrt{3}c_{xx}^2\rho w + 3c_{xx}P_{xz}}{c_{xx}\rho} \\ \frac{\rho^2 v^2 c_{xx}^2 + 2\sqrt{3}P_{xy}c_{xx}\rho v + \rho c_{xx}^2 P_{yy} + 2P_{xy}^2}{\rho^2 c_{xx}^2} \\ \frac{c_{xx}\rho\left(\sqrt{3}(wP_{xy} + vP_{xz}) + c_{xx}(P_{yz} + \rho vw)\right) + 2P_{xz}P_{xy}}{\rho^2 c_{xx}^2} \\ \frac{2\sqrt{3}\rho c_{xx}wP_{xz} + \rho^2 c_{xx}^2 w^2 + P_{zz}c_{xx}^2\rho + 2P_{xz}^2}{\rho^2 c_{xx}^2} \\ \frac{E_{rot}}{\rho} \end{bmatrix}$$

The left eigenvectors can be interpreted as the strength of each wave, and when expressed in primitive variables are found to be

$$l_{p1} = \left[0, -\frac{\sqrt{3}\rho}{6c_{xx}}, 0, 0, \frac{1}{6c_{xx}^2}, 0, 0, 0, 0, 0, 0\right], \quad l_{p2} = \left[0, -\frac{P_{xy}}{2c_{xx}^2}, \frac{\rho}{2}, 0, \frac{P_{xy}}{2c_{xx}^3\rho}, -\frac{1}{2c_{xx}}, 0, 0, 0, 0, 0\right],$$

$$l_{p3} = \left[0, -\frac{P_{xz}}{2c_{xx}^2}, 0, \frac{\rho}{2}, \frac{P_{xz}}{2c_{xx}^3\rho}, 0, -\frac{1}{2c_{xx}}, 0, 0, 0, 0\right],$$

$$l_{p4} = \left[1, 0, 0, 0, -\frac{1}{3c_{xx}^2}, 0, 0, 0, 0, 0, 0\right], \quad l_{p5} = \left[0, 0, 0, 0, \frac{4P_{xy}^2 - \rho c_{xx}^2 P_{yy}}{3\rho^2 c_{xx}^4}, -\frac{2P_{xy}}{c_{xx}^2\rho}, 0, 1, 0, 0, 0\right],$$

$$l_{p6} = \left[0, 0, 0, 0, \frac{4P_{xz}P_{xy} - \rho c_{xx}^2 P_{yz}}{3\rho^2 c_{xx}^4}, -\frac{P_{xz}}{c_{xx}^2\rho}, -\frac{P_{xy}}{c_{xx}^2\rho}, 0, 1, 0, 0\right],$$

$$l_{p7} = \left[0, 0, 0, 0, \frac{4P_{xz}^2 - \rho c_{xx}^2 P_{zz}}{3\rho^2 c_{xx}^4}, 0, -\frac{2P_{xz}}{c_{xx}^2\rho}, 0, 0, 1, 0\right], \quad l_{p8} = \left[0, 0, 0, 0, -\frac{E_{rot}}{3\rho c_{xx}^2}, 0, 0, 0, 0, 0, 1\right]$$

$$l_{p9} = \left[0, -\frac{P_{xz}}{2c_{xx}^2}, 0, \frac{\rho}{2}, -\frac{P_{xz}}{2c_{xx}^3\rho}, 0, \frac{1}{2c_{xx}}, 0, 0, 0, 0\right],$$

$$l_{p10} = \left[0, -\frac{P_{xy}}{2c_{xx}^2}, \frac{\rho}{2}, 0, -\frac{P_{xy}}{2c_{xx}^3\rho}, \frac{1}{2c_{xx}}, 0, 0, 0, 0, 0\right], \quad l_{p11} = \left[0, \frac{\sqrt{3}\rho}{6c_{xx}}, 0, 0, \frac{1}{6c_{xx}^2}, 0, 0, 0, 0, 0, 0\right]$$

Provided that P_{xx} and ρ remain real and greater than zero, this system of equations has real eigenvalues and linearly independent eigenvectors and is therefore strictly hyperbolic, as shown in the work of McDonald and Groth [15], Brown *et al.* [24], and Hittinger [19]. This condition holds in any Cartesian reference frame as the x-direction chosen for the calculations here were chosen arbitrarily and no direction-specific anomalies are seen. Returning to the assumed form of the non-equilibrium distribution function for the Gaussian closure, the condition of hyperbolicity is maintained when $\rho > 0$ and the symmetric tensor Θ_{ij} is positive definite.

2.4 Regularized Gaussian Closure

The regularized Gaussian closures were first introduced by McDonald and Groth [16, 17] as an alternative to including heat transfer effects into the standard Gaussian closure described

previously. A more rigorous presentation of the material with full derivations is found in a subsequent publication by these authors [50], complete with their application to a number of two-dimensional flows. The regularization procedure for both monatomic and diatomic gases described here is based on that description and is included here for the purposes of completeness.

As noted previously, due to the assumed form of the non-equilibrium distribution function, the third order velocity moments representative of the heat flux in the system are equivalently zero. This is an essential feature of the Gaussian distribution function that gives the system closure, so any direct introduction of higher-order velocity moments through a change to the assumed form of the distribution function would alter the closure, if closure in that sense can be even attained at all. Junk [9] has shown that higher-order members of the Levermore maximum-entropy hierarchy of closures cannot guarantee hyperbolicity for all physically realizable moments. Moment closures with alternate assumed forms for the distribution function such as those of Grad [5], could incorporate these higher-order moments, but do not have many of the attractive mathematical and computational features of the Gaussian closure.

McDonald and Groth [16, 17] have found that by adding a small perturbative correction to the moment closure itself, in the same spirit as that found in the well-known Chapman-Enskog perturbative expansion technique, a higher-order velocity moment describing heat flux can be reintroduced into the moment closure system without severely affecting many of the desirable properties of the closure. McDonald and Groth [16, 17] have also rigorously demonstrated that the perturbative treatment is equally applicable to the moment equations directly as well as the original kinetic equation and results in the same corrective term accounting for non-equilibrium heat flux. These heat flux terms are of an elliptic nature that is directly dependent only on lower order moments and provides smooth regularized solutions. The moment system, though formally more elliptic in nature, is based on an underlying strictly hyperbolic, first-order set of equations with the attractive computational qualities of the standard Gaussian closure for all realizable moments of interest.

2.4.1 Regularized Gaussian Closure for a Monatomic Gas

Derivation of the regularized closure for a monatomic gas proceeds as follows. A general transport equation for energy as derived by taking second-order velocity moments about some arbitrary non-equilibrium distribution function, $\mathcal{F}$, with the ellipsoidal statistical collision approximation for a monatomic gas takes the form

$$\frac{\partial}{\partial t}\left(\rho u_i u_j + P_{ij}\right) + \frac{\partial}{\partial x_k}\left(\rho u_i u_j u_k + u_i P_{jk} + u_j P_{ik} + u_k P_{ij} + Q_{ijk}\right) = -\frac{1}{\tau}\left(P_{ij} - p\delta_{ij}\right) . \quad (2.51)$$

When $\mathcal{F} = \mathcal{G}$, the form of the distribution forces the third-order tensor Q_{ijk} to zero and closure to the coupled set of equations is achieved, giving us the energy equation derived from the Gaussian closure shown earlier in Eq. (2.28). Assuming once again the use of any general non-equilibrium distribution function $\mathcal{F}$, a transport equation derived from Maxwell's Equation of Change for the third-order velocity moment requires the macroscopic quantity $m\langle v_i v_j v_k \mathcal{F}\rangle$, already evaluated within the spatial divergence in Eq. (2.51), and also introduces the fourth-order velocity moment $m\langle v_i v_j v_k v_l \mathcal{F}\rangle$ defined as

$$\begin{aligned} m\langle v_i v_j v_k v_l \mathcal{F}\rangle &= m\langle (u_i + c_i)(u_j + c_j)(u_k + c_k)(u_l + c_l)\mathcal{F}\rangle \\ &= \rho u_i u_j u_k u_l + u_i u_j P_{kl} + u_i u_k P_{jl} + u_i u_l P_{jk} + u_j u_k P_{il} + u_j u_l P_{ik} + u_k u_l P_{ij} \\ &\quad + u_i Q_{jkl} + u_j Q_{ikl} + u_k Q_{ijl} + u_l Q_{ijk} + R_{ijkl}. \end{aligned} \tag{2.52}$$

The random velocity moments have been simplified such that $m\langle c_\alpha c_\beta \mathcal{F}\rangle = P_{\alpha\beta}$, $m\langle c_\alpha c_\beta c_\gamma \mathcal{F}\rangle = Q_{\alpha\beta\gamma}$, and $m\langle c_\alpha c_\beta c_\gamma c_\epsilon \mathcal{F}\rangle = R_{\alpha\beta\gamma\epsilon}$. Using the ellipsoidal statistical collision operator, the complete weak-conservation form of the transport equation describing the evolution of the third-order velocity moments takes the form

$$\begin{aligned} &\frac{\partial}{\partial t}\left(\rho u_i u_j u_k + u_i P_{jk} + u_j P_{ik} + u_k P_{ij} + Q_{ijk}\right) \\ &+ \frac{\partial}{\partial x_l}\Big(\rho u_i u_j u_k u_l + u_i u_j P_{kl} + u_i u_k P_{jl} + u_i u_l P_{jk} + u_j u_k P_{il} + u_j u_l P_{ik} + u_k u_l P_{ij} \\ &\qquad + u_i Q_{jkl} + u_j Q_{ikl} + u_k Q_{ijl} + u_l Q_{ijk} + R_{ijkl}\Big) \\ &= -\frac{1}{(1-\nu)\,\tau} Q_{ijk}\,. \end{aligned} \tag{2.53}$$

Written in primitive form, the transport of the third-order generalized heat flux tensor, Q_{ijk}, can be derived from the above equation through an expansion and simplification of terms, yielding

$$\begin{aligned} &\frac{\partial Q_{ijk}}{\partial t} + \frac{\partial}{\partial x_l}\left(u_l Q_{ijk}\right) + Q_{jkl}\frac{\partial u_i}{\partial x_l} + Q_{ikl}\frac{\partial u_j}{\partial x_l} + Q_{ijl}\frac{\partial u_k}{\partial x_l} + P_{kl}\frac{\partial}{\partial x_l}\left(\frac{P_{ij}}{\rho}\right) \\ &+ P_{jl}\frac{\partial}{\partial x_l}\left(\frac{P_{ik}}{\rho}\right) + P_{il}\frac{\partial}{\partial x_l}\left(\frac{P_{jk}}{\rho}\right) + \frac{\partial \mathcal{K}_{ijkl}}{\partial x_l} = -\frac{1}{(1-\nu)\tau} Q_{ijk} = -\frac{\mathrm{Pr}}{\tau} Q_{ijk}\,, \end{aligned} \tag{2.54}$$

where, in the expression above, $\mathcal{K}_{ijkl}$ is a fourth-order deviatoric tensor comprised of the terms

$$\mathcal{K}_{ijkl} = \langle m c_i c_j c_k c_l \mathcal{F}\rangle - \langle m c_i c_j c_k c_l \mathcal{G}\rangle = R_{ijkl} - \frac{1}{\rho}\left[P_{ij}P_{kl} + P_{ik}P_{jl} + P_{il}P_{jk}\right], \tag{2.55}$$

The formal Chapman-Enskog-like perturbative expansion technique of McDonald and Groth [16, 17] expresses the general non-equilibrium distribution function as a series of small perturbations about a Maxwellian distribution, upon which progressively higher-order approximations to the

Boltzmann Equation shown in Eq. (2.1) can be found. A similar treatment is used here for Q_{ijk} and $\mathcal{K}_{ijkl}$, such that when applied to Eq. (2.54) estimates can be made for the corrective values to Q_{ijk}. In this case, the two tensors can be expressed as a perturbative expansion about their values that result from the Gaussian closure, $Q^{(G)}_{ijk}$ and $K^{(G)}_{ijkl}$, such that

$$Q_{ijk} = Q^{(G)}_{ijk} + Q^{(1)}_{ijk} + Q^{(2)}_{ijk} + Q^{(3)}_{ijk} + \cdots , \tag{2.56}$$

$$K_{ijkl} = K^{(G)}_{ijkl} + K^{(1)}_{ijkl} + K^{(2)}_{ijkl} + K^{(3)}_{ijkl} + \cdots , \tag{2.57}$$

where the superscript (n) represents an nth-order correction. Note that again, due to the construction of the non-equilibrium distribution function and the nature of the Gaussian solution, $Q^{(G)}_{ijk} = K^{(G)}_{ijkl} = 0$. Introducing a smallness or scaling parameter, ϵ, the contribution of these higher-order corrections can be scaled to give

$$Q_{ijk} = \epsilon^0 Q^{(G)}_{ijk} + \epsilon^1 Q^{(1)}_{ijk} + \epsilon^2 Q^{(2)}_{ijk} + \epsilon^3 Q^{(3)}_{ijk} + \cdots , \tag{2.58}$$

$$K_{ijkl} = \epsilon^0 K^{(G)}_{ijkl} + \epsilon^1 K^{(1)}_{ijkl} + \epsilon^2 K^{(2)}_{ijkl} + \epsilon^3 K^{(3)}_{ijkl} + \cdots , \tag{2.59}$$

with the assumption that $\epsilon \ll 1$. The transport equation for the generalized heat flux tensor can also then be scaled to yield

$$\begin{aligned} \frac{\partial Q_{ijk}}{\partial t} \quad &+ \quad \frac{\partial}{\partial x_l}\left(u_l Q_{ijk}\right) + Q_{jkl}\frac{\partial u_i}{\partial x_l} + Q_{ikl}\frac{\partial u_j}{\partial x_l} + Q_{ijl}\frac{\partial u_k}{\partial x_l} + P_{kl}\frac{\partial}{\partial x_l}\left(\frac{P_{ij}}{\rho}\right) \\ &+ \quad P_{jl}\frac{\partial}{\partial x_l}\left(\frac{P_{ik}}{\rho}\right) + P_{il}\frac{\partial}{\partial x_l}\left(\frac{P_{jk}}{\rho}\right) + \frac{\partial \mathcal{K}_{ijkl}}{\partial x_l} = -\frac{1}{\epsilon(1-\nu)\tau}Q_{ijk}\,. \end{aligned} \tag{2.60}$$

Substituting the expressions of Eqs. (2.58) and (2.59) and collecting like terms in powers of ϵ, the transport equation for Q_{ijk} can be rearranged as

$$\begin{aligned} &\epsilon^0\left[Q^{(G)}_{ijk}\right] \\ &+\epsilon^1\left[Q^{(1)}_{ijk} + (1-\nu)\tau\left(\frac{\partial Q^{(G)}_{ijk}}{\partial t} + P_{kl}\frac{\partial}{\partial x_l}\left(\frac{P_{ij}}{\rho}\right) + P_{jl}\frac{\partial}{\partial x_l}\left(\frac{P_{ik}}{\rho}\right) + P_{il}\frac{\partial}{\partial x_l}\left(\frac{P_{jk}}{\rho}\right) + \frac{\partial K^{(G)}_{ijkl}}{\partial x_l}\right)\right] \\ &+\epsilon^2\left[Q^{(2)}_{ijk} + (1-\nu)\tau\left(\frac{\partial Q^{(1)}_{ijk}}{\partial t} + \frac{\partial}{\partial x_l}\left(u_l Q^{(1)}_{ijk}\right) + Q^{(1)}_{jkl}\frac{\partial u_i}{\partial x_l} + Q^{(1)}_{ikl}\frac{\partial u_j}{\partial x_l} + Q^{(1)}_{ijl}\frac{\partial u_k}{\partial x_l} + \frac{\partial K^{(1)}_{ijkl}}{\partial x_l}\right)\right] \\ &+\epsilon^3\left[Q^{(3)}_{ijk} + (1-\nu)\tau\left(\frac{\partial Q^{(2)}_{ijk}}{\partial t} + \frac{\partial}{\partial x_l}\left(u_l Q^{(2)}_{ijk}\right) + Q^{(2)}_{jkl}\frac{\partial u_i}{\partial x_l} + Q^{(2)}_{ikl}\frac{\partial u_j}{\partial x_l} + Q^{(2)}_{ijl}\frac{\partial u_k}{\partial x_l} + \frac{\partial K^{(2)}_{ijkl}}{\partial x_l}\right)\right] \\ &+\cdots = 0\,. \end{aligned} \tag{2.61}$$

Non-trivial solutions require that each term in powers of ϵ in the above expression be equal to zero. The zeroth-order correction returns the expected zero heat flux tensor predicted from the Gaussian closure. Corrections of order ϵ^2 and higher require unavailable knowledge concerning

high-order gradients of the perturbations of the tensors of interest, and their contribution becomes increasingly small for higher powers of ϵ. This leaves a non-zero first-order correction dependent purely on lower order moments, as by definition $\partial Q_{ijk}^{(G)}/\partial t = \partial K_{ijkl}^{(G)}/\partial x_l = 0$. These quantities are either already available or can be derived from the application of the flow problem on a finite-volume mesh. Rearranging to solve for the first-order correction to the generalized heat flux tensor results in

$$\begin{aligned} Q_{ijk}^{(1)} &= -(1-\nu)\tau\left[P_{kl}\frac{\partial}{\partial x_l}\left(\frac{P_{ij}}{\rho}\right) + P_{jl}\frac{\partial}{\partial x_l}\left(\frac{P_{ik}}{\rho}\right) + P_{il}\frac{\partial}{\partial x_l}\left(\frac{P_{jk}}{\rho}\right)\right] \\ &= -\frac{\tau}{\mathrm{Pr}}\left[P_{kl}\frac{\partial}{\partial x_l}\left(\frac{P_{ij}}{\rho}\right) + P_{jl}\frac{\partial}{\partial x_l}\left(\frac{P_{ik}}{\rho}\right) + P_{il}\frac{\partial}{\partial x_l}\left(\frac{P_{jk}}{\rho}\right)\right]. \end{aligned} \tag{2.62}$$

Assuming that $Q_{ijk} \approx Q_{ijk}^{(1)}$, this first-order correction can be substituted into Eq. (2.51), such that the complete set of transport equations for monatomic fluids governing the conservation of mass, momentum and energy in this regularization of the Gaussian closure in conservative form can be expressed as

$$\frac{\partial}{\partial t}(\rho) + \frac{\partial}{\partial x_i}(\rho u_i) = 0\,, \tag{2.63}$$

$$\frac{\partial}{\partial t}(\rho u_i) + \frac{\partial}{\partial x_j}(\rho u_i u_j + P_{ij}) = 0\,, \tag{2.64}$$

$$\begin{aligned} &\frac{\partial}{\partial t}(\rho u_i u_j + P_{ij}) + \frac{\partial}{\partial x_k}(\rho u_i u_j u_k + u_i P_{jk} + u_j P_{ik} + u_k P_{ij}) \\ &\qquad + \frac{\partial}{\partial x_k}\left\{-\frac{\tau}{\mathrm{Pr}}\left[P_{kl}\frac{\partial}{\partial x_l}\left(\frac{P_{ij}}{\rho}\right) + P_{jl}\frac{\partial}{\partial x_l}\left(\frac{P_{ik}}{\rho}\right) + P_{il}\frac{\partial}{\partial x_l}\left(\frac{P_{jk}}{\rho}\right)\right]\right\} \\ &\qquad = -\frac{1}{\tau}(P_{ij} - p\delta_{ij})\,. \end{aligned} \tag{2.65}$$

2.4.2 Regularized Gaussian Closure for a Diatomic Gas

It has been well established that an increase in the degrees of freedom of a molecule results in a corresponding increase in the specific heat capacity of that fluid. The energy stored within the gas can no longer be attributed only to the translational kinetic energy of the molecules (as measured by temperature), and is instead also influenced by the energy distributed throughout the degrees of freedom of each molecule. As addressed in Section 2.3.2, the rotational energy within a diatomic gas contributes significantly to the transport of the total energy, and is likewise affected by a corresponding energy flux.

For diatomic gases, an additional equation describing the transport of rotational energy using the Gaussian closure is given by Eq. (2.47). For a general non-equilibrium distribution function,

$\mathcal{F}$, the full form of this transport equation is given as

$$\frac{\partial}{\partial t}\left(\rho e_{\mathrm{r}}\right)+\frac{\partial}{\partial x_i}\left(\rho u_i e_{\mathrm{r}}+h_i\right)=-\frac{1}{5\tau_{\mathrm{v}}}\left(3\rho e_{\mathrm{r}}-P_{kk}\right)\,, \tag{2.66}$$

where h_i is the heat flux vector associated with the transport of rotational energy defined by the moment quantity

$$h_i=\left\langle Ic_i\omega^2\mathcal{F}\right\rangle\,. \tag{2.67}$$

This third-order velocity moment is once again equivalent to zero when using the Gaussian closure for a diatomic gas. The conservative transport equation for this third-order velocity moment for any general non-equilibrium distribution function can be shown to take the form

$$\begin{aligned}\frac{\partial}{\partial t}\left(\rho u_i e_{\mathrm{r}}+h_i\right) \quad &+ \quad \frac{\partial}{\partial x_j}\left(\rho u_i u_j e_{\mathrm{r}}+u_i h_j+u_j h_i+P_{ij}e_{\mathrm{r}}+r_{ij}\right)\\ &= \quad -\frac{1}{(1-\nu)\tau}h_i-\frac{1}{5\tau_{\mathrm{v}}}u_i\left(3\rho e_{\mathrm{r}}-P_{kk}\right)\,.\end{aligned} \tag{2.68}$$

Note that once again, due to the construction of the Boltzmann equation, an additional higher-order velocity moment is introduced in the spatial divergence term. This second-order deviatoric tensor, r_{ij}, can be written as

$$r_{ij}=\left\langle Ic_ic_j\omega^2\mathcal{F}\right\rangle-\left\langle Ic_ic_j\omega^2\mathcal{G}_{\mathrm{D}}\right\rangle=\left\langle Ic_ic_j\omega^2\mathcal{F}\right\rangle-P_{ij}e_{\mathrm{r}}\,. \tag{2.69}$$

Similar to the Chapman-Enskog-like method used to describe first-order correction terms for the Q_{ijk} and K_{ijkl} in the previous section, a perturbative expansions for h_i and r_{ij} can be postulated and used to determine a first-order correction to the Gaussian solution purely in terms of lower-order moment quantities. The perturbative expansions for h_i and r_{ij} in terms of a small parameter ϵ take the form

$$h_i=\epsilon^0h_i^{(G)}+\epsilon^1h_i^{(1)}+\epsilon^2h_i^{(2)}+\epsilon^3h_i^{(3)}+\cdots\,, \tag{2.70}$$

$$r_{ij}=\epsilon^0r_{ij}^{(G)}+\epsilon^1r_{ij}^{(1)}+\epsilon^2r_{ij}^{(2)}+\epsilon^3r_{ij}^{(3)}+\cdots\,, \tag{2.71}$$

where once again, $h_i^{(G)}=r_{ij}^{(G)}=0$ as stipulated by their values arising from the Gaussian closure. The scaled version of the non-conservative transport equation for this rotational energy heat flux vector is given by

$$\frac{\partial h_i}{\partial t}+\frac{\partial}{\partial x_j}\left(u_jh_i\right)+h_j\frac{\partial u_i}{\partial x_j}+P_{ij}\frac{\partial e_{\mathrm{r}}}{\partial x_j}+\frac{\partial r_{ij}}{\partial x_j}=-\frac{1}{(1-\nu)\epsilon\tau}h_i\,. \tag{2.72}$$

Substituting Eqs. (2.70)–(2.71) into this tranport equation and grouping like-orders of ϵ results

in

$$\begin{aligned}
&\epsilon^0 \left[h_i^{(G)} \right] \\
&+ \epsilon^1 \left[h_i^{(1)} + (1-\nu)\tau \left(\frac{\partial h_i^{(G)}}{\partial t} + P_{ij} \frac{\partial e_r}{\partial x_j} + \frac{\partial r_{ij}^{(G)}}{\partial t} \right) \right] \\
&+ \epsilon^2 \left[h_i^{(2)} + (1-\nu)\tau \left(\frac{\partial h_i^{(1)}}{\partial t} + \frac{\partial}{\partial x_j} \left(u_j h_i^{(1)} \right) + h_j^{(1)} \frac{\partial u_i}{\partial x_j} + \frac{\partial r_{ij}^{(1)}}{\partial t} \right) \right] \\
&+ \epsilon^3 \left[h_i^{(3)} + (1-\nu)\tau \left(\frac{\partial h_i^{(2)}}{\partial t} + \frac{\partial}{\partial x_j} \left(u_j h_i^{(2)} \right) + h_j^{(2)} \frac{\partial u_i}{\partial x_j} + \frac{\partial r_{ij}^{(2)}}{\partial t} \right) \right] \\
&+ \cdots = 0 \,. \qquad (2.73)
\end{aligned}$$

With the stipulation that all terms in powers of ϵ must be equivalent to zero for non-trivial solutions, and that $\partial h_i^{(G)}/\partial t = \partial r_{ij}^{(G)}/\partial t = 0$, the first-order corrective term describing the heat flux due to the transport of rotational energy is found to be

$$h_i^{(1)} = -(1-\nu)\tau \left(P_{ij} \frac{\partial e_\mathrm{r}}{\partial x_j} \right) = -\frac{\tau}{\mathrm{Pr}} P_{ij} \frac{\partial e_\mathrm{r}}{\partial x_j} \,. \qquad (2.74)$$

The heat flux associated with the transport of translational energy derived for monatomic gases is equally applicable for diatomic gases. Again assuming that $h_i \approx h_i^{(1)}$ and substituting the derived expression for Q_{ijk} shown earlier into the original set of moment equations from the Gaussian closure for diatomic gases described in Eqs. (2.44)–(2.47), the complete set of moment equations resulting from a regularization of the Gaussian closure as applied to diatomic gases can be summarized as

$$\frac{\partial}{\partial t} (\rho) + \frac{\partial}{\partial x_i} (\rho u_i) = 0 \,, \qquad (2.75)$$

$$\frac{\partial}{\partial t} (\rho u_i) + \frac{\partial}{\partial x_j} (\rho u_i u_j + P_{ij}) = 0 \,, \qquad (2.76)$$

$$\begin{aligned}
&\frac{\partial}{\partial t} (\rho u_i u_j + P_{ij}) + \frac{\partial}{\partial x_k} (\rho u_i u_j u_k + u_i P_{jk} + u_j P_{ik} + u_k P_{ij}) \\
&\qquad + \frac{\partial}{\partial x_k} \left\{ -\frac{\tau}{\mathrm{Pr}} \left[P_{kl} \frac{\partial}{\partial x_l} \left(\frac{P_{ij}}{\rho} \right) + P_{jl} \frac{\partial}{\partial x_l} \left(\frac{P_{ik}}{\rho} \right) + P_{il} \frac{\partial}{\partial x_l} \left(\frac{P_{jk}}{\rho} \right) \right] \right\} \\
&\qquad = -\frac{1}{\tau} \left(P_{ij} - \frac{P_{kk}}{3} \delta_{ij} \right) - \frac{2}{15\tau_\mathrm{v}} (P_{kk} - 3\rho e_\mathrm{r}) \, \delta_{ij} \,, \qquad (2.77)
\end{aligned}$$

$$\frac{\partial}{\partial t} (\rho e_\mathrm{r}) + \frac{\partial}{\partial x_i} (\rho u_i e_\mathrm{r}) + \frac{\partial}{\partial x_i} \left(-\frac{\tau}{\mathrm{Pr}} P_{ij} \frac{\partial e_\mathrm{r}}{\partial x_j} \right) = \frac{1}{5\tau_\mathrm{v}} (3\rho e_\mathrm{r} - P_{kk}) \,. \qquad (2.78)$$

This extended fluid-dynamic description is used herein for all diatomic fluid flow problems addressed in this thesis. The validity of the regularized formulation for incorporating heat transfer effects into the Gaussian closure will be thoroughly analyzed as part of this thesis in Chapter 6.

2.5 Solid-Wall Boundary Conditions

In the continuum regime, the commonly-used no-slip boundary conditions assume that the velocity of the fluid is at rest relative to the reference frame of the wall, with a similar assumption on equivalency made on the temperature of the fluid adjacent to the wall and the temperature of the wall. At moderate Knudsen numbers, increased intermolecular collision distances extends both the time and the distance needed for molecules to reach an equilibrium state. Aside from producing thickened boundary layers, the lack of intermolecular collisions also produces a slip effect at solid wall boundaries, affecting both the velocity and temperature profiles of the flow of interest. This effect must be taken into account when developing suitable boundary conditions for the Gaussian closures. Applying continuum-regime techniques for slip regime flows requires some description of these slip effects at solid wall boundaries that rely on corrective parameters derived separately either from kinetic theory [51] or from physical experiments [52]. It will be shown in this section that the boundary conditions necessary for modelling slip effects falls naturally from the construction of the Gaussian closure, providing a smooth transition between the continuum and slip flow regimes.

2.5.1 Velocity Slip

The construction of appropriate boundary conditions for the Gaussian closure used in this thesis is based on a classical method proposed by Grad [5]. Similar approaches were developed and used by McDonald and Groth [16, 18] and Torrilhon *et al.* [23]. An infinitesimally thin layer of particles, known as the Knudsen layer, is assumed to exist next to the surface of the wall, and its distribution function is affected by particles from the interior flow field and those that have reflected off the wall. Reflected particles may reach thermodynamic equilibrium with the wall prior to being released back into the Knudsen layer (diffuse reflection), in which case the particles adopt a Maxwell-Boltzmann distribution function dependent only on the wall temperature and wall velocity. Particles can also be reflected back into the Knudsen layer still retaining its original incoming particle distribution function with only a change in particle direction (specular reflection). The fraction of diffuse reflections versus specular reflections can be described with an accommodation coefficient, α, where $\alpha = 1$ describes diffuse or fully accommodated reflection, and $\alpha = 0$ describes specular reflection. The true physical behavior of solid walls will depend on material and finish, with $0 < \alpha < 1$. The remainder of this study will focus on fully diffuse reflections only, though specular reflection will be considered when examining the limiting behavior of the boundary conditions. For the sake of computational simplicity, fluxes are computed by first rotating the two cell states into the $+x$ frame of reference,

solving the Riemann problem in that frame, and subsequently rotating the updated cell states back into their original orientation. This simplifies the Riemann solver and boundary condition problem to one in which the wall normal extends in the $+x-$direction only.

The particle distribution function for the Knudsen layer, $\mathcal{F}_{\mathrm{Kn}}$, is then formulated as a linear combination of both the incoming and reflected distributions, $\mathcal{F}_{-}$ and $\mathcal{F}_{+}$ respectively. For a wall normal extending into the flow in the $+x-$direction,

$$\mathcal{F}_{\mathrm{Kn}} = \mathcal{F}_{-} + \mathcal{F}_{+}\,, \tag{2.79}$$

where $\mathcal{F}_{-}$ and $\mathcal{F}_{+}$ are given by

$$\mathcal{F}_{-} = \begin{cases} \mathcal{G}_{\mathrm{e}}(v_x, v_y, v_z) & \text{for} \quad v_x < 0\,, \\ 0 & \text{for} \quad v_x > 0\,, \end{cases} \tag{2.80}$$

$$\mathcal{F}_{+} = \begin{cases} \alpha\mathcal{M}_{\mathrm{w}}(v_x, v_y, v_z) + (1-\alpha)\mathcal{G}_{\mathrm{e}}(-v_x, v_y, v_z) & \text{for} \quad v_x > 0\,, \\ 0 & \text{for} \quad v_x < 0\,, \end{cases} \tag{2.81}$$

where $\mathcal{G}_{\mathrm{e}}$ represents the Gaussian particle distribution at the interior edge of the boundary and $\mathcal{M}_{\mathrm{w}}$ is a Maxwell-Boltzmann distribution defined by the solid wall properties.

Armed with this proposed distribution function, the properties of the gaseous particles in the Knudsen layer can be found through the same integrating methods outlined in Section 2.1.3, with the exception of a change in the limits of the integration due to the presence of the wall. A cursory look at the number of moment equations involved reveals that blindly integrating all eleven flow variables from the system will yield too many boundary conditions. The number of required conditions can be reduced by considering the geometry of the flow problem. For an $+x-$direction wall normal, only variables that generate a flux across the wall-fluid interface are needed, and the list of moments reduces to $\{c_x, c_{xx}, c_{xy}, c_{xz}\}$. Grad [5] and Torrilhon and Struchtrup [23] have further observed that if the accommodation coefficient α is set to zero, velocity functionals of even degree in c_x create non-zero boundary conditions that cannot be controlled. To preserve the continuity of the boundary conditions as α approaches zero, the list of moments is restricted to only odd degrees of c_x, yielding $\{c_x, c_{xy}, c_{xz}\}$. The first moment c_x corresponds to the bulk velocity of the fluid normal to the walls and is required to be zero to ensure the impermeability of the solid wall. Together with expressions for the remaining shear

pressures defined by the moments c_{xy} and c_{xz}, the boundary conditions can be summarized as

$$
\begin{aligned}
u_{x\,\mathrm{Kn}} &= 0 \quad , && (2.82)\\
P_{xy\,\mathrm{Kn}} &= m \int_0^\infty dv_x \int_{-\infty}^\infty dv_y \int_{-\infty}^\infty dv_z v_x \left(v_y - \overline{u}_y\right) \left[(1-\alpha)\,\mathcal{G}\left(-v_x, v_y, v_z\right) + \alpha \mathcal{M}\left(v_x, v_y, v_z\right)\right] \\
&\quad + m \int_0^\infty dv_x \int_{-\infty}^\infty dv_y \int_{-\infty}^\infty dv_z v_x \left(v_y - \overline{u}_y\right) \left[\mathcal{G}\left(v_x, v_y, v_z\right)\right] \\
&= m \int_0^\infty dv_x \int_{-\infty}^\infty dv_y \int_{-\infty}^\infty dv_z v_x \left(v_y - \overline{u}_y\right) \left[-\alpha\mathcal{G}\left(-v_x, v_y, v_z\right) + \alpha \mathcal{M}\left(v_x, v_y, v_z\right)\right] \\
&= \alpha \left[\frac{P_{xy}}{2} - \sqrt{\frac{\rho P_{xx}}{2\pi}}\left(u_y - \overline{u}_y\right)\right] + \alpha\sqrt{\frac{P_{xx}\rho}{2\pi}}\left(u_{y_\mathrm{w}} - \overline{u}_y\right), && (2.83)\\
P_{xz\,\mathrm{Kn}} &= \alpha \left[\frac{P_{xz}}{2} - \sqrt{\frac{\rho P_{xx}}{2\pi}}\left(u_z - \overline{u}_z\right)\right] + \alpha\sqrt{\frac{P_{xx}\rho}{2\pi}}\left(u_{z_\mathrm{w}} - \overline{u}_z\right), && (2.84)
\end{aligned}
$$

where u_{y_w} and u_{z_w} are the $y-$ and $z-$ direction velocities of the wall respectively, and $\overline{u}_y$ and $\overline{u}_z$ are the bulk velocities of the Knudsen layer velocity distribution given by

$$
\begin{aligned}
\overline{u}_y &= \frac{\rho}{\rho_\mathrm{Kn}}\left[(2-\alpha)\left[\frac{u_y}{2} - \frac{P_{xy}}{\sqrt{2\pi\rho P_{xx}}}\right] + \frac{\alpha}{2}\sqrt{\frac{mP_{xx}}{\rho k T_\mathrm{w}}}u_{y_\mathrm{w}}\right] && (2.85)\\
\overline{u}_z &= \frac{\rho}{\rho_\mathrm{Kn}}\left[(2-\alpha)\left[\frac{u_z}{2} - \frac{P_{xz}}{\sqrt{2\pi\rho P_{xx}}}\right] + \frac{\alpha}{2}\sqrt{\frac{mP_{xx}}{\rho k T_\mathrm{w}}}u_{z_\mathrm{w}}\right] && (2.86)
\end{aligned}
$$

where ρ_Kn is the density within the Knudsen layer found from a similar half-Maxwellian integration with $\mathbf{M}(v_\alpha) = m$, given by

$$
\rho_\mathrm{Kn} = \frac{\rho}{2}\left((2-\alpha) + \alpha\sqrt{\frac{mP_{xx}}{\rho k T_w}}\right) \tag{2.87}
$$

with all properties being those from the incoming Gaussian except for u_{y_w}, u_{z_w}, and T_w which define the Maxwellian distribution of accommodated particles from the wall. By placing boundary conditions on the shear pressure, it is possible to recover the no-shear-stress condition for the Euler equations in the equilibrium limit with no accommodation at the wall, as can be seen in Eqs. (2.83) and (2.84) with $\alpha = 0$. A full description on the procedure performed to find the Knudsen layer properties through half-Maxwellian type integrations can be found in Appendix A of the thesis.

2.5.2 Additional Boundary Conditions for Temperature Slip

Temperature slip at wall boundaries is one of the most significant physical characteristics present in high Knudsen number flows. Since the standard Gaussian closure cannot account for heat flux regardless of boundary conditions, the implementation of temperature slip phenomena is

limited to the the regularized Gaussian closure. The velocity slip boundary conditions discussed above, however, are used for both closure systems. The effects of thermal transpiration are not included within the velocity slip boundary conditions, as heat flux is not treated as a moment quantity and does not appear naturally within the derivation for the velocity slip boundary conditions. Expressions for this term can be derived from higher-order moment systems, but the Gaussian closure alone cannot model this effect. The lack of thermal transpiration in the boundary conditions prevents the regularized Gaussian closure from modelling counter-gradient heat flux behaviour in the near-wall region, and remains a significant source of error when using this closure for non-equilibrium flows.

Boundary conditions used up till this point involves rotating the Knudsen layer boundary state and the first interior cell into the $x-$direction and performing a series of half-Maxwellian integrations to find the appropriate velocity moments. However, temperature slip cannot be modelled with these boundary conditions alone, even with the regularization procedure described in the previous section, as the heat flux becomes dependent only on the pressure gradients through the wall, creating a corresponding smooth transition in temperature at the wall.

A method of introducing temperature slip into the boundary conditions has been proposed by Smoluchowski [53] and implemented for the two-dimensional regularized Gaussian closure by McDonald and Groth [16, 18]. The Knudsen layer temperature T is adjusted such that

$$T = T_{\mathrm{w}} + \Delta T_{\mathrm{s}} = T_{\mathrm{w}} + f_{\mathrm{s}} \lambda \frac{\partial T}{\partial n_i}\,, \tag{2.88}$$

where T is the temperature of the fluid at the Knudsen layer, T_{w} is the temperature of the wall introduced earlier, ΔT_{s} is the temperature slip across the Knudsen layer, and n_i is the unit vector normal to the wall. The idea is to take the no-slip temperature gradient along an outward-drawn normal to the wall, $\partial T/\partial n_i$, and evaluate the temperature along this gradient at a slip distance factor, f_{s}, given by Smoluchowski [53] as

$$f_{\mathrm{s}} = \frac{10\pi}{16\mathrm{Pr}} \left(\frac{2 - \alpha_t}{\alpha_t} \right) \frac{\gamma}{\gamma + 1}\,, \tag{2.89}$$

and where α_t is the thermal accommodation coefficient. Thermal accommodation coefficients are typically empirically derived and depend largely on gas properties, surface materials and smoothness. For the purposes of this study, the thermal accommodation coefficient is set to unity, such that the incoming gas is fully accommodated to the wall temperature upon collision. This newly calculated temperature is then used in Eqs. (2.82)–(2.87) to calculate updated boundary conditions for the corresponding pressure tensor and rotational energy within the Knudsen layer, which in turn is used to calculate the heat flux corrections in Eqs. (2.62) and (2.74). These temperature slip boundary conditions are equally amenable for monatomic and

diatomic gases as the rotational energy is coupled only through the source terms in the energy equation and is easily separable.

It is important to note that while the slip temperature is approximate, there are no boundary conditions on the heat flux at the wall, as the regularized Gaussian closure treats the heat flux as function of the pressure gradient, and not as a separate macroscopic property derived from taking moments about the non-equilibrium distribution function. Higher-order moment techniques, such as the regularized 13-moment equations of Struchtrup and Torrilhon [21], treat heat flux directly as moments of the non-equilibrium distribution function, with which half-Maxwellian-type boundary conditions can be formed. The regularization of the 13-moment closure treats the even higher order moments representative of the Burnett equations in the same manner as the heat flux used in the regularized Gaussian. For the regularized Gaussian closure, producing the correct slip temperature is expected to give some insight into the correct non-equilibrium behaviour in the near-wall region.

Chapter 3

Finite-Volume Spatial Discretization Scheme

In this study, a parallel, implicit, AMR, finite-volume scheme is proposed and developed for the solution of the moment equations of the standard and regularized Gaussian moment closure described in Chapter 2 for both monatomic and diatomic gases. For the three-dimensional flows of interest here, the finite-volume discretization is applied to multi-block body-fitted meshes with hexahedral volume elements. The multi-block mesh and spatial discretization procedure readily allow for the application of solution-directed block-based AMR as developed previously by Gao *et al.* [32, 34, 54–57] for three space dimensions. In this block-based AMR scheme, a flexible block-based hierarchical octree data structure is used to facilitate automatic, solution-directed, and local adaptation of the mesh according to physics-based refinement criteria. The local refinement and coarsening of the mesh is carried out by division and merging of solution blocks, respectively. In the proposed finite-volume procedure, the hyperbolic fluxes at cell boundaries will be evaluated using a Riemann-solver based flux function by Roe, though an approximate Harten-van Leer-Lax-Einfeldt (HLLE) solver is also implemented. A Newton-Krylov-Schwarz (NKS) algorithm implemented for two and three-dimensional Navier-Stokes equations by Charest *et al.* [29] and Northrup and Groth [28] is employed for steady-state solutions. The elliptic heat transfer terms from the regularized Gaussian closure are incorporated using the technique implemented by Gao [34] with a centrally-weighted method for cell face gradients described by Mathur and Murphy [58]. The multi-block, body-fitted, AMR and Newton schemes are well suited to the parallel implementation of the implicit finite-volume AMR scheme on distributed-memory multi-processor architectures via domain decomposition. Because of the self-similar nature of the grid blocks, domain decomposition is a achieved by

simply distributing the blocks making up the computational mesh equally among available processors and/or processor cores, with more than one block permitted per core. The use of NKS with the proposed parallel, implicit, AMR, finite-volume scheme has been applied successfully for a number of complex flow problems in computational combustion, including unsteady, fully compressible reactive flows [59] and radiative heat transfer [60]. To the best of the author's knowledge, the Newton-Krylov approach is applied here for the first time to the solution of three-dimensional non-equilibrium micro-scale flows using the Gaussian closures.

This thesis focuses on the application of an implicit NKS scheme to the Gaussian closures for the solution of steady-state, three-dimensional flows. This is in contrast to the semi-implicit approach of McDonald and Groth [15, 16] applied to the Gaussian closures for two-dimensional flows. Based on this approach, the semi-implicit solver was extended for solutions to the standard Gaussian closure in three dimensions in the thesis of Lam [61]. While its use is not the focus of this thesis, its performance is nevertheless used as a benchmark for the Newton-Krylov implicit solver implemented for all examined flow problems. Details on the Newton-Krylov method with Schwarz preconditioning are described in Chapter 4 with reference to its application to the two and three-dimensional Navier-Stokes equations by Charest *et al.* [29] and Northrup and Groth [28].

The proposed block-based AMR solution scheme is similar to that described in Gao and Groth [34,55] for the prediction of three-dimensional turbulent non-premixed combustion flames, and those used in the prediction of MHD flows by Ivan *et al.* [62–65]. Aspects of the mesh adaptation scheme and computer code developed as part of this previous work were re-used in the current development of the approach for the Gaussian closure. An overview of the finite-volume AMR scheme for multi-block, body-fitted meshes using hexahedral cells is presented here, including special consideration for the source terms associated with the Gaussian moment closure. The reader is referred to the above-mentioned papers for full details of the block-based AMR algorithm for multi-block hexahedral mesh.

3.1 Godunov-Type Finite-Volume Methods

The purely hyperbolic and first-order quasi-linear nature of maximum-entropy moment closures present several numerical advantages which extend into both the transition and continuum regimes as discussed by Groth and McDonald [66]. These hyperbolic systems are less sensitive to grid irregularities, making them well suited to to AMR and complex geometries. They also only require the evaluation of first derivatives, which means that an extra order of spatial

accuracy, relative to a mixed hyperbolic-parabolic system such as the Navier-Stokes, can be gained using the same stencil. Hyperbolic equations describing a system of conservation laws, such as the moment equations derived from the Gaussian closures, are well suited to solution by Godunov-type finite-volume methods. In such finite-volume methods, the domain of interest is divided into subvolumes wherein the transport of macroscopic properties are solved from cell to cell. Evolving the solution in each cell produces a Riemann problem at each of the cell interfaces that translates into a net flux at that interface. The proper accounting of these fluxes over each interface in each cellular control volume, its effect on the average solution in each cell over time, and the incorporation of source terms become the primary areas of concern for finite-volume methods.

In differential form, the general form of the governing equations for the Gaussian closures from Eqn. (2.48) can be expressed using matrix-vector notation as

$$\frac{\partial \mathbf{U}}{\partial t} + \overrightarrow{\nabla} \cdot \overrightarrow{\mathbf{F}} = \mathbf{S}, \tag{3.1}$$

where $\mathbf{U}$ is the vector of conserved flow solution variables, F is the total solution flux dyad, and S is the source vector. Integrating this expression throughout three-dimensional physical space and applying the divergence theorem, the integral form of the conservation equations can then be written as

$$\frac{\mathrm{d}}{\mathrm{d}t} \iiint_V \mathbf{U} \, \mathrm{d}V + \oiint_\Omega \overrightarrow{\mathbf{F}} \cdot \overrightarrow{n} \, \mathrm{d}\Omega = \iiint_V \mathbf{S} \, \mathrm{d}V \tag{3.2}$$

where V is the control volume of interest, Ω is the closed surface of the control volume, and $\overrightarrow{n}$ is the outward-facing unit normal vector of the closed surface Ω. This integral equation is enforced over each three-dimensional cell that spatially-discretizes the domain of interest. The conserved properties in each cell are then subject to change through the net solution flux through the surface of each cell and through the source terms. Due to the spatially-discretized nature of the finite-volume scheme, the solution content within each cell is averaged over the cell, such that

$$\overline{\mathbf{U}} \equiv \frac{1}{V} \iiint_V \mathbf{U} \, \mathrm{d}V \tag{3.3}$$

and

$$\overline{\mathbf{S}} \equiv \frac{1}{V} \iiint_V \mathbf{S} \, \mathrm{d}V, \tag{3.4}$$

where $\overline{\mathbf{U}}$ and $\overline{\mathbf{S}}$ represent the averaged solution vector and source term within each cell respectively. The solution within each cell, however, is assumed to be piecewise constant in Godunov's original method, while higher-order methods allow for a polynomial variation of the solution within each cell. The reader is directed to the texts of Lomax *et al.* [67] and Hirsch [68, 69] for

detailed discussions regarding conservation equations and their properties as applied towards finite-volume methods.

General Godunov-type methods involve three major steps: reconstruction, flux function evaluation, and time marching. The original method developed by Godunov [10] uses a piecewise constant reconstruction, an exact Riemann solver for the flux function evaluation, and a time-marching scheme that reduces to an explicit Euler scheme. The following sections expand on these ideas to create a higher-order scheme that provide greater computational efficiency and accuracy.

3.2 Semi-Discrete Form

The preceding moment equations for the Gaussian closure are solved herein by applying an upwind finite-volume method in which the conservation equations are integrated over hexahedral cells of a body-fitted, multi-block mesh. By applying the geometric properties of a sample hexahedral cell depicted in Figure 3.1 to the integral form of the conservation equations given in Eq. (3.2), the finite-volume formulation applied to some cell (i, j, k) of the body-fitted grid can be expressed as

$$\frac{\mathrm{d}\overline{\mathbf{U}}_{i,j,k}}{\mathrm{d}t} = -\frac{1}{V_{i,j,k}} \sum_{m} \left(\vec{\mathbf{F}} \cdot \vec{n} \, \Delta A \right)_{i,j,k.m} + \overline{\mathbf{S}} \left(\overline{\mathbf{U}}_{i,j,k} \right)_{i,j.k} \tag{3.5}$$

where $\overline{\mathbf{U}}$ is the vector of conserved solution variables averaged over the cell, $\vec{\mathbf{F}} = (\mathbf{F}, \mathbf{G}, \mathbf{H})$ is the hyperbolic solution flux dyad, $\overline{\mathbf{S}}$ is the cell-averaged source term associated with the collisional processes, $V_{i,j,k}$ is the volume of cell (i, j, k), and ΔA and $\vec{n}$ are the area and unit outward normal vector of the cell face m respectively. Definitions for the flux vectors $\mathbf{F}$, $\mathbf{G}$, $\mathbf{H}$ and the source term $\mathbf{S}$ can be found in Sections 2.3.1 and 2.4.1 of Chapter 2 for the Gaussian closure and the regularized Gaussian closure, respectively. Equation (3.5) then describes the evolution of the averaged solution over a computational cell and forms a non-linear system of first-order ordinary differential equations. The numerical fluxes at the faces of each cell are determined using the least-squares piecewise limited linear solution reconstruction procedure of Barth [70] and Riemann solver based flux functions. The limiter of Venkatakrishnan [71] and an extension of the approximate linearized Riemann solver of Roe [72] for the Gaussian moment equations are both used. Details of the numerical flux functions and solution reconstruction procedure follow below.

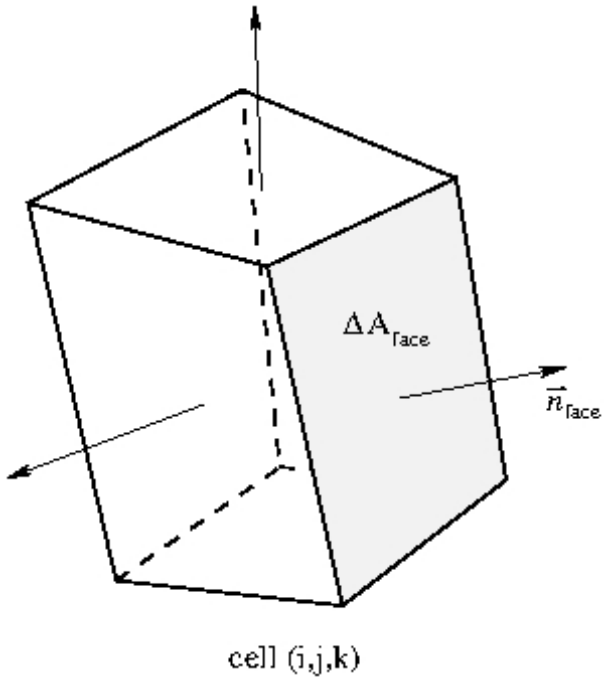

Figure 3.1: An example of a three-dimensional hexahedral cell for the finite volume formulation used in this thesis. Image from Northrup [59].

3.3 Approximate Riemann Solvers

Godunov [10] initially evaluated the solution to the Riemann problem or extended 'shock tube' problem at each interface using the Rankine-Hugonoit relations and Riemann invariant formulations to extract an exact flux through the interface, defined by the initial conditions as

$$\mathbf{F} = \bar{\mathbf{F}}\left(\mathbf{R}\left(\mathbf{U_L}, \mathbf{U_R}, x/t = 0\right)\right) \tag{3.6}$$

where $\mathbf{U_L}$, $\mathbf{U_R}$ are the solutions from the left and right sides of the interface respectively, $\mathbf{R}(\mathbf{U_L}, \mathbf{U_R}, x/t = 0)$ is the solution of the Riemann problem using these initial conditions, and the flux is evaluated at $x/t = 0$.

The usefulness of this exact flux is diminished by the fact that Godunov's scheme, based on a piecewise constant representation of the solution within each cell makes the entire scheme only first-order accurate. Solving the Riemann problem exactly can also become computationally expensive due to its iterative procedure and limitations to simple equations of state. Although a very efficient solution algorithm has been devised by Gottlieb and Groth [73] for polytropic gases, these issues spurred the development of approximate Riemann solvers that provide the numerical flux with the necessary degree of accuracy. While the reduction in computational

cost may not be significant for simple systems such as the Euler equations, the lack of an exact solution for general hyperbolic systems, including the Gaussian closures, generally necessitates the use of an approximate solver.

3.3.1 Roe's Approximate Riemann Solver

Roe [72] developed a linearized approximate Riemann solver, taking advantage of the fact that a linear system's solution can be easily obtained through an eigensystem decomposition. The simplicity of solving such systems can be employed by using a local linearization of the Euler equations. The governing equations for the system from Eq. (3.1) can be rewritten as

$$\frac{\partial \mathbf{U}}{\partial t} + \mathbf{A}\frac{\partial \mathbf{U}}{\partial x} = 0 \tag{3.7}$$

with the Jacobian matrix given by $\mathbf{A} = \partial\mathbf{F}/\partial\mathbf{U}$. Roe replaces this Jacobian with a constant matrix, $\bar{\mathbf{A}}$, dependent on some intermediate state $\mathbf{U}_*$, which in turn is a function of the initial states $\mathbf{U_L}$ and $\mathbf{U_R}$. This procedure generates a linear system of constant coefficients which is then solved exactly. The approximate nature of the Roe solver comes from replacing the original non-linear conservation laws and its associated Jacobian with this linearized system.

The creation of this replacement matrix for the flux Jacobian is subject to a number of stipulations in order to accurately mimic the behaviour of the original Jacobian. They are:

1. In the limit that $\mathbf{U_L} = \mathbf{U_R} = \mathbf{U}$, $\bar{\mathbf{A}}$ should be able to recover the same system as the original Jacobian such that

$$\bar{\mathbf{A}}\left(\mathbf{U_L}, \mathbf{U_R}\right) = \bar{\mathbf{A}}\left(\mathbf{U}, \mathbf{U}\right) = \mathbf{A}\left(\mathbf{U}\right) = \frac{\partial \mathbf{F}}{\partial \mathbf{U}} \tag{3.8}$$

2. An exact solution for an isolated discontinuity between $\mathbf{U_L}$ and $\mathbf{U_R}$, such that

$$\Delta\mathbf{F} = \bar{\mathbf{A}}\left(\mathbf{U_L}, \mathbf{U_R}\right)\Delta\mathbf{U} \tag{3.9}$$

3. The constant coefficient matrix $\bar{\mathbf{A}}$ has real eigenvalues and a complete set of linearly independent eigenvectors to retain the hyperbolic nature of the original system of equations.

Roe [72] developed the original approximate solver for the Euler equations of compressible gas dynamics; however, extensions are possible for other hyperbolic systems such as the moment equations found from the Gaussian closure, as demonstrated by Brown *et al.* [24] and McDonald and Groth [15]. The construction of the intermediate state, $\mathbf{U}_*$, is done here through a corrected

average approach as proposed by Brown [25]. Applied to the Gaussian closure, with $W_{ij} = P_{ij}/\rho$, the primitive variables for this state are found to be

$$\hat{\rho} = \sqrt{\rho_L \rho_R} \tag{3.10a}$$

$$\hat{u}_i = \frac{\sqrt{\rho_L}u_{iL} + \sqrt{\rho_R}u_{iR}}{\sqrt{\rho_L} + \sqrt{\rho_R}} \tag{3.10b}$$

$$\hat{W}_i = \frac{\sqrt{\rho_L}W_{ijL} + \sqrt{\rho_R}W_{ijR}}{\sqrt{\rho_L} + \sqrt{\rho_R}} + \frac{1}{3}\frac{\sqrt{\rho_L\rho_R}}{\left(\sqrt{\rho_L} + \sqrt{\rho_R}\right)^2}\Delta u_i \Delta u_j \tag{3.10c}$$

$$\hat{E}_{rot} = \frac{\sqrt{\rho_L}E_{rotL} + \sqrt{\rho_R}E_{rotR}}{\sqrt{\rho_L} + \sqrt{\rho_R}} \tag{3.10d}$$

The final form of the flux function is then found to be

$$\mathcal{F} = \frac{1}{2}(\bar{\mathbf{F}}_{\mathbf{L}} + \bar{\mathbf{F}}_{\mathbf{R}}) - \frac{1}{2}\sum_{k=1}^{n} |\lambda_{*,k}|\alpha_{*,k}\bar{\mathbf{r}}_{c*,k} \tag{3.11}$$

where $\bar{\mathbf{F}}_{\mathbf{L}}$, $\bar{\mathbf{F}}_{\mathbf{R}}$ are the left and right states of the interface, n is the number of conserved variables, and $\lambda_{*,k}$, $\alpha_{*,k}$ and $\bar{\mathbf{r}}_{c*,k}$ are the eigenvalues, wave strengths, and the right eigenvectors associated with each conserved variable. The computational advantages of the Gaussian closure can be seen here, as the eigenvectors and eigenvalues of the constant coefficient matrix, $\bar{\mathbf{A}}$, can be easily generated to satisfy the hyperbolicity requirement needed to use this approximate flux function.

The linearization process applied to the Riemann problem works well for contact and shock waves where the discontinuity of the problem is modelled, albeit with errors associated with the size of the jump. However, the continuous change in flow properties in rarefaction waves is oversimplified by the linearizing process where the averaging procedure models all the propagating waves using only their eigenvalues, leading to an inability to distinguish between shock waves and rarefaction waves. The two nonlinear acoustic waves, λ_1 and λ_{11}, for the diatomic Gaussian closure are prone to this problem and are incorrectly modelled as rarefaction shocks. An entropy fixing term proposed by Harten [74] is added to Roe's solver and corrects the eigenvalues to avoid this problem. The positive and negative parts of the eigenvalues, $\lambda_k^{\pm}$, are replaced by a corrected value, $\hat{\lambda}_k^{\pm}$, such that

$$\hat{\lambda}_{*,k}^{\pm} = \frac{1}{2}\left(\lambda_{*,k} \pm |\lambda_{*,k}|\right) \pm \frac{\delta_{*,k}}{2}, \tag{3.12}$$

where

$$\delta_{*,k} = \begin{cases} \frac{1}{2}\left[\frac{|\lambda_{*,k}|^2}{\Theta_{*,k}} + \Theta_{*,k}\right] - |\lambda_{*,k}| & \text{if } |\lambda_{*,k}| \leq \Theta_{*,k} \\ 0 & \text{if } |\lambda_{*,k}| > \Theta_{*,k} \end{cases} \tag{3.13}$$

and

$$\Theta_{*,k} = \max\left[0, 2\left(\lambda_{R,k} - \lambda_{L,k}\right)\right]. \tag{3.14}$$

3.3.2 HLLE and HLLL Flux Functions

Originally developed by Harten, van Leer and Lax and expanded on by Einfeldt [75], the HLLE flux function postulates the presence of a single intermediate state between the left and right states of the interface. The maximum and minimum signal velocities are found by comparing signal velocities taken from the eigenvalues of a Roe's scheme linearization, and those from the exact Riemann solution using the left and right states. The final form of the HLLE flux function can be expressed as

$$\mathcal{F} = \frac{\lambda^+ \mathbf{F_L} - \lambda^- \mathbf{F_R}}{\lambda^+ - \lambda^-} + \frac{\lambda^+ \lambda^-}{\lambda^+ - \lambda^-}(\mathbf{U_R} - \mathbf{U_L}) \tag{3.15}$$

where $\mathbf{F_L}$, $\mathbf{F_R}$ are the left and right flux contributions, and λ^+, λ^- are the maximum and minimum signal velocities respectively. The lack of the intermediate wave can be problematic in modelling shear waves and introduces excess dissipation in the boundary layer. To account for this phenomenon, a formulation by Linde [76] based on the HLL flux function introduces an intermediate wave in the presence of isolated contacts and discontinuities. Note that while both flux functions are able to model the evolution of the shock and rarefaction waves, the Roe flux function generates slightly steeper profiles at discontinuities. The HLLE flux function is not without its merits, however, as the flux function of Roe can sometimes lead to negative internal energies for highly rarefied flows.

3.3.3 Reconstruction and Slope Limiting

Godunov's original method assumes that the solution is piecewise constant in each cell. Adopting a piecewise linear representation or higher order scheme to model a varying solution within the cell would increase the global accuracy of the method. For second-order accuracy, linear reconstruction can be used in which the solution inside the cell is modelled with a linear function. This results in a different initial solution on either side of the cell's interfaces, and the resulting Riemann problem on the interfaces would be changed. For a uniformly spaced one-dimensional mesh, the slope of the solution within a cell i can be found through a second-order centred derivative using the solutions from the two adjacent cells. The solution at each of the two interfaces are then evaluated. The flux function evaluation is then carried out at each interface and the average solution in each cell can then be updated

Employing a linear reconstruction procedure as is carries with it the risk of continuously fluctuating slopes in a cell, resulting in undesirable oscillations near shocks. The use of slope limiters helps to enforce montonicity by adjusting the slope based on the maximum and minimum averaged solutions in adjacent cells. As an example, slope limiters are applied to the

one-dimensional problem such that the calculation of the solution at interface $i + \frac{1}{2}$ in cell i is given by

$$\mathbf{U}_{i+\frac{1}{2}} = \mathbf{U}_i + \phi : \left.\frac{\partial \mathbf{U}}{\partial x}\right|_i (x_{i+\frac{1}{2}} - x_i) \tag{3.16}$$

where $\partial \mathbf{U}/\partial x\big|_i$ is the slope in cell i, x_i is the position vector of the centre of cell i, and ϕ is a slope limiter (one value of the limiter for each variable). Various slope limiters are available, with the Barth-Jespersen [77] and the Venkatakrishnan [71] slope limiters studied here. The use of a linear reconstruction dramatically increases the resolution of the shock, while the use of a slope limiter limits the size of oscillations near discontinuities. The Barth-Jespersen and Venkatakrishnan slope limiters behave similarly, with the only difference lying in the way the slope limiters vary when encountering nearly smooth areas of the solution.

3.3.4 Treatment of Elliptic Fluxes

The regularization procedure applied to the Gaussian closure outlined in Section 2.4 of Chapter 2 introduces fluxes having an elliptic nature that are not addressed directly in the Godunov scheme described above. The treatment of these terms in two dimensions, as performed by McDonald and Groth [16–18], used a diamond-path reconstruction technique using the solution state at a cell and the gradients at the cell interfaces. An application of the Green-Gauss theorem on the diamond-shaped polygon bounded by the cell centers of the cell of interest and its neighbouring cell, and the vertices of the cell that form the interface between the two cells.

In three dimensions, a direct application of this method becomes rather expensive. The edges formed from the diamond-path reconstruction are replaced by surfaces instead. The octahedron formed by a similar joining of cell centers and vertices requires an extensive storage of geometric data, such as the face tangential vectors, which is not readily available for most hexahedral meshes. Instead using the technique implemented by Gao [34] with a centrally-weighted method for cell face gradients as proposed by Mathur and Murphy [58], the cell face gradients in three dimensions for some cell and its i-direction neighbour can be expressed and evaluated as

$$\overrightarrow{\nabla}\mathbf{W}|_{i+\frac{1}{2},j,k} = \frac{\mathbf{W}|_{i+\frac{1}{2},j,k} - \mathbf{W}|_{i,j,k}}{ds} \frac{\overrightarrow{n}}{\overrightarrow{n} \cdot \overrightarrow{e_s}} + \left(\overline{\overrightarrow{\nabla}\mathbf{W}|_{i+\frac{1}{2},j,k}} - \overline{\overrightarrow{\nabla}\mathbf{W}|_{i+\frac{1}{2},j,k}} \cdot \overrightarrow{e_s} \frac{\overrightarrow{n}}{\overrightarrow{n} \cdot \overrightarrow{e_s}} \right), \tag{3.17}$$

where $\mathbf{W}$ is the primitive solution vector, ds is the centroid distance, $\overrightarrow{n}$ is the face norm unit vector, and $\overrightarrow{e_s}$ is the unit vector joining the two cell centroids. The weighted average of the cell-centered gradient at the cell interface, $\overline{\overrightarrow{\nabla}\mathbf{W}|_{i+\frac{1}{2},j,k}}$ is given by

$$\overline{\overrightarrow{\nabla}\mathbf{W}|_{i+\frac{1}{2},j,k}} = \alpha \overrightarrow{\nabla}\mathbf{W}|_{i,j,k} + (1-\alpha)\, \overrightarrow{\nabla}\mathbf{W}|_{i+1,j,k} \tag{3.18}$$

where the weighting factor, α, is based on the respective volumes of the cells, V, such that

$$\alpha = \frac{V_{i,j,k}}{V_{i,j,k} + V_{i+1,j,k}} \tag{3.19}$$

3.3.5 Semi-Implicit Time Marching Scheme

While the focus of this thesis is the development of a fully implicit Newton-Krylov solver, a semi-implicit time marching scheme for the Gaussian closures developed by McDonald and Groth [15, 16] for the solution of two-dimensional flows is used as a comparison to highlight the computational advantages provided by the Newton-Krylov solution scheme. The details of this semi-implicit time marching scheme are provided forthwith.

As the relaxation times, τ_t and τ_r, become very small under near-equilibrium conditions, the numerical stiffness of the system increases. To handle these difficulties, the explicit solver uses a point-implicit finite-volume formulation with second-order semi-implicit time-marching is used to integrate the set of differential equations that results from the spatial discretization. Returning to the three-dimensional semi-discrete form of the problem presented in Eq. (3.5), a fully discrete solution scheme can be formed from the semi-discrete equations by introducing a two-stage, second-order accurate, semi-implicit time marching scheme with implicit treatment of the source terms, resulting in a solution update for some cell (i, j, k) that takes the form

$$\tilde{\mathbf{U}}^{n+1}_{i,j,k} = \mathbf{U}^{n}_{i,j,k} - \frac{\Delta t}{V_{i,j,k}} \left(\sum_m \left(\vec{\mathbf{F}} \cdot \vec{n} \Delta A \right)^{n}_{i,j,k,m} \right) + \Delta t \tilde{\mathbf{S}}^{n+1}_{i,j,k} \tag{3.20a}$$

$$\mathbf{U}^{n+1}_{i,j,k} = \mathbf{U}^{n}_{i,j,k} - \frac{\Delta t}{2V_{i,j,k}} \left(\sum_m \left(\vec{\mathbf{F}} \cdot \vec{n} \Delta A \right)^{n}_{i,j,k,m} + \sum_m \left(\tilde{\vec{\mathbf{F}}} \cdot \vec{n} \Delta A \right)^{n+1}_{i,j,k,m} \right) + \Delta t \left(\frac{\mathbf{S}^{n}_{i,j,k} + \tilde{\mathbf{S}}^{n+1}_{i,j,k}}{2} \right) \tag{3.20b}$$

where $\mathbf{U}^{n}_{i,j,k}$ and $\mathbf{S}^{n}_{i,j,k}$ are the vector of conserved variables and the source terms at time level n respectively, $V_{i,j,k}$ is the volume of the cell, and $\left(\vec{\mathbf{F}} \cdot \vec{n} \Delta A \right)^{n}_{i,j,k,m}$ is the numerical flux through the m-face of the hexahedral cell with area A to be solved with the approximate Riemann solver described in the previous section, resulting in a second-order accurate scheme over smooth sections of the solution.

A matrix $\mathbf{K}$ can be constructed such that the source terms can be expressed in the form $\mathbf{S}^n = \mathbf{K}^n \mathbf{U}^n$ where

$$\mathbf{K} = \begin{bmatrix} 0 & 0 & 0 & 0 & 0 & 0 & 0 & 0 & 0 & 0 & 0 \\ 0 & 0 & 0 & 0 & 0 & 0 & 0 & 0 & 0 & 0 & 0 \\ 0 & 0 & 0 & 0 & 0 & 0 & 0 & 0 & 0 & 0 & 0 \\ 0 & 0 & 0 & 0 & 0 & 0 & 0 & 0 & 0 & 0 & 0 \\ au^2+bv^2+bw^2 & -2au & -2bv & -2bw & a & 0 & 0 & b & 0 & b & \frac{2}{5\tau_r} \\ -\frac{uv}{\tau_t} & \frac{v}{\tau_t} & \frac{u}{\tau_t} & 0 & 0 & -\frac{1}{\tau_t} & 0 & 0 & 0 & 0 & 0 \\ -\frac{uw}{\tau_t} & \frac{w}{\tau_t} & 0 & \frac{u}{\tau_t} & 0 & 0 & -\frac{1}{\tau_t} & 0 & 0 & 0 & 0 \\ bu^2+av^2+bw^2 & -2bu & -2av & -2bw & b & 0 & 0 & a & 0 & b & \frac{2}{5\tau_r} \\ -\frac{vw}{\tau_t} & 0 & \frac{w}{\tau_t} & \frac{v}{\tau_t} & 0 & 0 & 0 & 0 & -\frac{1}{\tau_t} & 0 & 0 \\ bu^2+bv^2+aw^2 & -2bu & -2bv & -2aw & b & 0 & 0 & b & 0 & a & \frac{2}{5\tau_r} \\ \frac{u^2+v^2+w^2}{5\tau_r} & \frac{-2u}{\tau_r} & \frac{-2v}{\tau_r} & \frac{-2w}{\tau_r} & \frac{1}{5\tau_r} & 0 & 0 & \frac{1}{5\tau_r} & 0 & \frac{1}{5\tau_r} & -\frac{3}{5\tau_r} \end{bmatrix}$$

$$a = -\frac{2}{3\tau_t} - \frac{2}{15\tau_r}, \quad b = \frac{1}{3\tau_t} - \frac{2}{15\tau_r}$$

The update scheme in Eqs. (3.20) can then be rewritten and rearranged as

$$\tilde{\mathbf{U}}^{n+1}_{i,j,k} - \left(\check{\mathbf{K}}\tilde{\mathbf{U}}\right)^{n+1}_{i,j,k} = \mathbf{U}^{n}_{i,j,k} - \frac{\Delta t}{V_{i,j,k}}\left(\sum_m \left(\vec{\mathbf{F}}\cdot\vec{n}\Delta A\right)^{n}_{i,j,k,m}\right) \tag{3.21a}$$

$$\mathbf{U}^{n+1}_{i,j,k} - \frac{\Delta t}{2}\left(\mathbf{K}\mathbf{U}\right)^{n+1}_{i,j,k} = \mathbf{U}^{n}_{i,j,k} - \frac{\Delta t}{2V_{i,j,k}}\left(\sum_m \left(\vec{\mathbf{F}}\cdot\vec{n}\Delta A\right)^{n}_{i,j,k,m} + \sum_m \left(\tilde{\vec{\mathbf{F}}}\cdot\vec{n}\Delta A\right)^{n+1}_{i,j,k,m}\right) + \Delta t\left(\frac{\mathbf{S}^{n}_{i,j,k}}{2}\right) \tag{3.21b}$$

Defining a matrix $\mathbf{B} = \mathbf{I} - \Delta t/\Omega\mathbf{K}$, where Ω is the internal stage of the update scheme, a further simplification of the scheme is possible. The inverse of this matrix preconditions the stages to account for the, in many cases, stiff source terms and can be evaluated analytically due to the local nature of the source terms and by assuming that the relaxation times do not vary over the time step. In this case, the fully-discrete finite-volume scheme can then be written as

$$\tilde{\mathbf{U}}^{n+1}_{i,j,k} = \mathbf{B}^{-1}\left[\mathbf{U}^{n}_{i,j,k} - \frac{\Delta t}{V_{i,j,k}}\left(\sum_m \left(\vec{\mathbf{F}}\cdot\vec{n}\Delta A\right)^{n}_{i,j,k,m}\right)\right] \tag{3.22a}$$

$$\mathbf{U}^{n+1}_{i,j,k} = \mathbf{B}^{-1}\left[\mathbf{U}^{n}_{i,j,k} - \frac{\Delta t}{2V_{i,j,k}}\left(\sum_m \left(\vec{\mathbf{F}}\cdot\vec{n}\Delta A\right)^{n}_{i,j,k,m} + \sum_m \left(\tilde{\vec{\mathbf{F}}}\cdot\vec{n}\Delta A\right)^{n+1}_{i,j,k,m}\right) + \Delta t\left(\frac{\mathbf{S}^{n}_{i,j,k}}{2}\right)\right] \tag{3.22b}$$

3.4 Parallel Adaptive Mesh Refinement

Groth and co-researchers [28, 55–57, 66, 78, 79] have developed block-based AMR finite-volume schemes for the solution of a range of physically complex flows on multi-block body-fitted meshes with second-order accuracy. The application of these methods has included laminar flames [57, 79] and high-pressure soot prediction [80–82], turbulent non-premixed flames [55–57] as well as turbulent multi-phase rocket core flows [78,83], micro-scale flows [15,66], and radiation transport [84]. Extensions of the multi-block methods for embedded boundaries not aligned with the mesh [85] and for use with an anisotropic refinement strategy [86, 87] are also possible and have been developed. This adaptive multi-block approach was extended to cubed sphere grids (with second-order accuracy) and magnetohydrodynamics (MHD) flow problems by Ivan *et al.* [62–65]. Application of this block-based AMR scheme for the Gaussian closures has been performed by McDonald and Groth [15, 66] for a variety of two-dimensional micro-scale flows, and highlights the computational benefits of the mesh refinement scheme. In this thesis, a three-dimensional AMR scheme based on the work of Gao and Groth [34, 55] has now been extended for use with the standard and regularized Gaussian closure with an implicit Newton-Krylov method for the solution of fully three-dimensional steady flow micro-scale problems.

High mesh resolution allows for a more accurate numerical solution of various flow problems, but this comes at the expense of increasingly larger computational costs. In order to minimize these costs, an adaptive mesh refinement algorithm proposed by Gao and Groth [34, 55] for the modelling of turbulent non-premixed combustion flames in three dimensions is used herein with a body-fitted hexahedral mesh leading to an efficient distribution of computational loads suitable for implementation on large-scale distributed-memory computing clusters. By changing the mesh according to physics-based criteria during the computation, areas of interest are resolved with high mesh densities, while areas with smaller solution changes are evaluated with larger cells. When used in conjunction with the finite-volume scheme above, the entire technique can be used to treat flows with disparate length scales commonly present in shear and boundary layers with reduced computational costs.

The mesh is divided into a number of body-fitted blocks dependent on the initial geometries of the problem. At regular points during the computation, physics-based refinement criteria are evaluated in each block to determine if a higher or lower mesh resolution is desired. To ensure that gradual changes in the overall solution are depicted, mesh refinement ratios between adjacent blocks are limited to 1:2 and the minimum resolution is limited to the initial mesh resolution. An octree data structure such as the one in Figure 3.2 emerges from this three-dimensional algorithm, where ‘parent’ blocks in need of refinement are divided into eight equally-

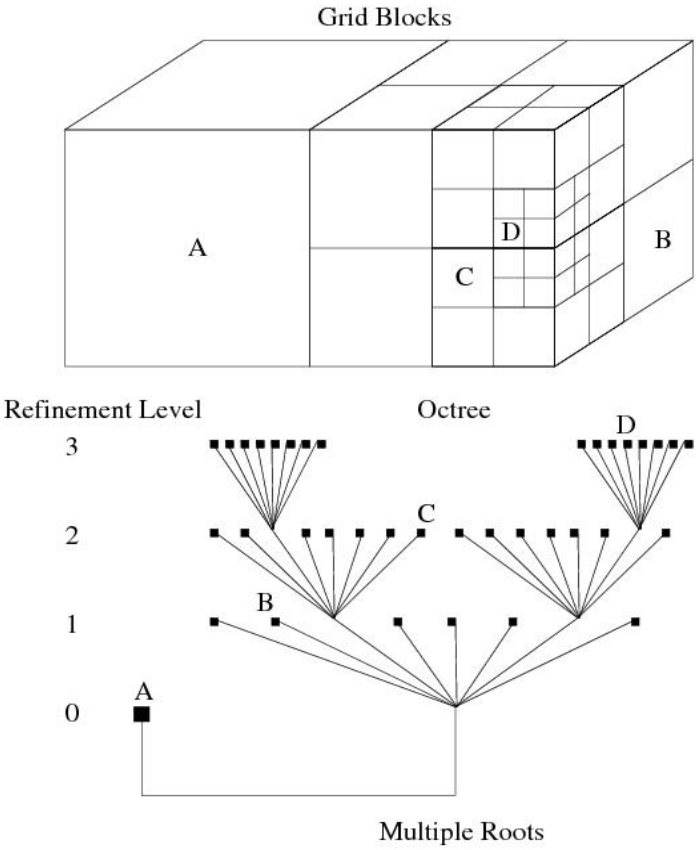

Figure 3.2: Octree data structure and block connectivity for an AMR multi-block hexahedral mesh.

sized 'child' blocks, each with the same mesh resolution as its parent, effectively doubling the resolution in the parent block. Coarsening is done in the same manner with the joining of 8 child blocks to form a parent block. The computational costs for each block from this data structure are equal, and a redistribution of the child blocks amongst available processors in the parallel cluster ensures load balancing. Two layers of ghost cells form an overlapping layer between adjacent blocks that provide a transparent passing of information between blocks and are also used to impose boundary conditions, an illustration of which can be seen in Figure 3.3. An example of the application of the overall AMR algorithm can be seen in Figure 3.4, where refined grid blocks can be seen in areas of interest in the vicinity of a small cylindrical flow tube embedded in a surrounding cylindrical flow. Refer to the paper by Gao and Groth [34, 55] for further details of the AMR method used here.

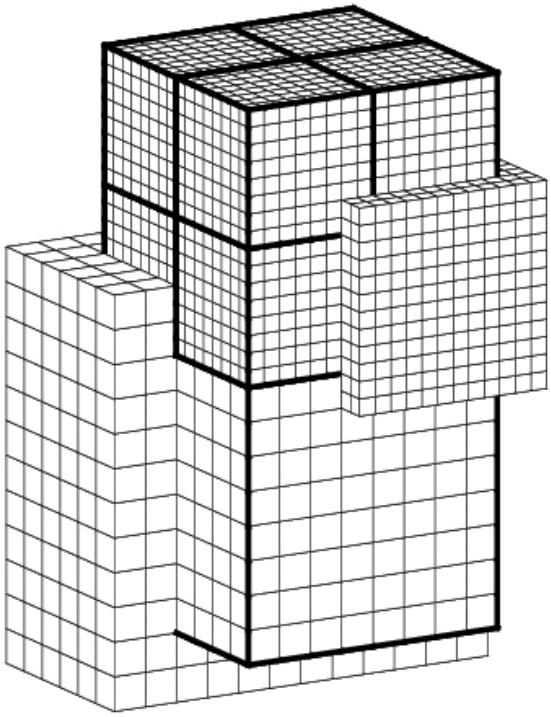

Figure 3.3: Two layers of overlapping ghost cells responsible for passing information between neighbouring three-dimensional blocks on a hexahedral mesh.

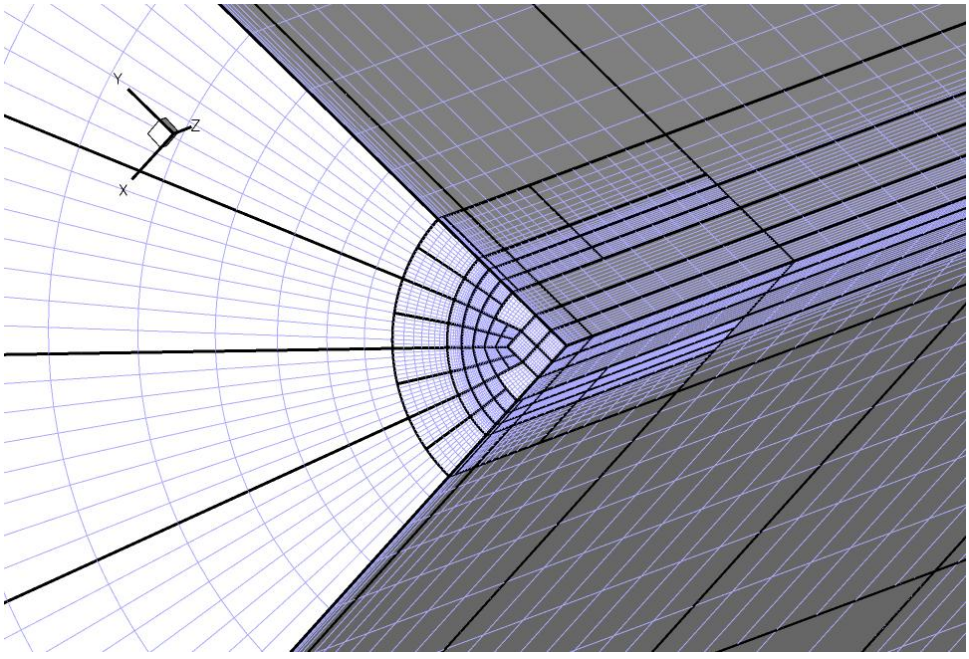

Figure 3.4: Sample 3D AMR for multiblock body-fitted hexahedral mesh for internal flow of a fuel line.

Chapter 4

Newton-Krylov-Schwarz Solution Method for Steady Flows

The NKS solution algorithm for the set of non-linear algebraic equations that result from the spatial discretization procedures of the finite-volume procedure defined in Chapter 3 uses Newton's method with a Krylov subspace approach for the solution of the linear system at each Newton step. An additive Schwarz preconditioner is used in the parallel implementation of the Krylov subspace method, and is fully compatible with the block-based AMR and domain decomposition procedure used in the parallel implementation of the solution method. The application of this implicit non-linear iterative solver to the standard and regularized Gaussian closures aims to replicate the advantageous parallel performance of the NKS method for reactive flows as previously investigated by Northrup [59] for a range of laminar flames.

4.1 Overview

Time marching methods seek fo find a solution to the coupled set of non-linear ordinary differential equations given in Eq. (3.5), and can be broadly categorized as either explicit or implicit schemes [67]. Explicit schemes, such as the Runge-Kutta methods, are easily programmable with a low computational cost per iteration. However, these methods tend to suffer from strict stability limits that restrict the size of the time steps that can be taken. As a result, a very large number of iterations with very small time steps is required to produce meaningful insight on the temporal evolution of the conservative system of equations. Numerical stiffness puts further restrictions on the size of the time step, such that the overall computational cost of an explicit scheme can become astronomical. Advancements in algorithm development have

introduced explicit methods of increasing efficiency, such as multi-grid techniques [88], local time-stepping [89], and implicit residual smoothing [90]. Implicit time marching methods can typically employ larger time steps and are not limited by the numerical stiffness of the system. They can therefore potentially reach a converged solution in far fewer iterations compared with its explicit counterpart. The computational cost per iteration is significantly higher than those from the explicit scheme, as a linear system of equations must be stored and solved at each iteration. While the complexity of the implicit schemes requires more effort to implement during algorithm development, the ability to use time steps orders of magnitude larger than those from explicit methods is highly desirable, and can lead to significant savings in computational cost.

For steady flows, it is also possible to eschew the use of time-marching altogether since by definition the contribution of the time-derivative terms to the conservation equations reduces to zero under steady state conditions. By removing the time derivative terms, the remaining set of non-linear algebraic equations can be solved in an iterative manner using Newton's method. While Newton's method alone reduces the algebraic equations of a semi-discrete approach into a slightly more manageable coupled set of linear equations, an efficient solution to this linear system is required at each Newton iteration. Exploiting the relatively sparse nature of this linear system, an accelerated version of Newton's method known as Newton-Krylov method is used herein as an alternative to traditional time-marching methods for steady state flows. They can also be applied to time-dependent problems using a dual-timestepping approach as discussed by Northrup [59], but this is beyond the scope of this thesis.

The class of Newton-Krylov methods are so named by the use of Newton's method for solutions to a non-linear set of equations, with a Krylov subspace method used to find a solution for the coupled set of linear equations generated within Newton's method. As an iterative technique, the internal linear system is only solved to within a certain tolerance before performing another Newton iteration, so practical implementations of such methods are more accurately classified as inexact Newton methods. Dembo *et al.* [91] have shown that the iterative treatment of inexact Newton methods have significant advantages over exact Newton methods while retaining the attractive quadratic convergence rates of Newton's method.

The use of the Krylov subspace methods for use with Newton's method was first proposed by Brown and Saad [92]. A large variety of Krylov methods have been developed but many require that the system of equations to be symmetric, such as the Conjugate Gradient method [93], a condition that is impossible to satisfy for the Gaussian closure due to constraints in geometry and the structure of the solution vector. The specific Krylov method used in this thesis is the the Generalized Minimum RESidual (GMRES) method developed by Saad and Schultz [94].

McHugh and Knoll [95] have shown that GMRES outperforms many other Krylov subspace methods in the matrix-free implementation of Newton-Krylov methods applied to the steady, incompressible Naview-Stokes equations in terms of convergence behaviour and robustness.

As an added acceleration technique, preconditioning is implemented on the Newton-Krylov scheme in the form of a domain-decomposition method proposed by Schwarz [96]. The domain-decomposition aspect of Schwarz preconditioning is an attractive feature, as the division of the domain of interest is already performed by the multi-block, parallel, AMR scheme used in this thesis. The additive nature of the preconditioning also leads to a fully parallel implicit scheme as with no global serial computations. With additive Schwarz preconditioning applied to the inexact Newton method described above, the entire scheme is referred to as the Newton-Krylov-Schwarz (NKS) method in this thesis. The robustness of this combination of methods has been shown in applications towards flow problems including aerodynamic optimization [30, 31] and computational combustion [28, 29]. The successful implementation of the NKS solution scheme for such a diverse range of flow problems has prompted an investigation on its applicability for the Gaussian closures considered in this thesis. A brief review the fundamentals of the NKS method and its application specifically for the Gaussian closures is presented in this chapter.

4.2 Newton's Method

The semi-discrete form of the governing equations used in the finite volume method form a coupled set of non-linear ordinary differential equations. However, steady-state solutions (the primary focus here), can be computed directly by solving the nonlinear algebraic equations such that the residual vector satisfies

$$\mathbf{R}\left(\mathbf{U}\right) = \frac{\mathrm{d}\mathbf{U}_{i,j,k}}{\mathrm{d}t} = 0 \tag{4.1}$$

using Newton's method. Given an estimate to the solution to $\mathbf{R}(\mathbf{U}) = 0$ at iteration level n, the following system of linear equations can be solved in Newton's method to obtain an improved estimate for the solution at the $n+1$ iteration level, $\mathbf{U}^{(n+1)}$, satisfying $\Delta\mathbf{U}^{(n+1)} = \mathbf{U}^{(n+1)} - \mathbf{U}^{(n)}$:

$$\left(\frac{\partial \mathbf{R}}{\partial \mathbf{U}}\right)^{n+1} \Delta\mathbf{U}^{n+1} = \mathbf{J}\Delta\mathbf{U}^{n+1} \approx -\mathbf{R}\left(\mathbf{U}^{n+1}\right) \tag{4.2}$$

Given an initial estimate for the steady-state solution, $\mathbf{U}^0$, successively improved estimates for the solution $\mathbf{U}^{n+1}$ are obtained by solving Equation (4.2) at each step, n, of the Newton method, where $\mathbf{J} = \partial\mathbf{R}/\partial\mathbf{U}$ is the residual Jacobian. Newton's method is then applied in an iterative fashion until a selected L_2 residual norm (usually density) is reduced beyond a

specified tolerance, ϵ, such that

$$\|\mathbf{R}\left(U^n\right)\|_2 \leq \epsilon \left\|\mathbf{R}\left(U^0\right)\right\|_2 . \tag{4.3}$$

The sparse nature of this linear system lends itself well to a number of accelerated solution methods, such as the iterative Krylov method used in this thesis. The result is that within each Newton iteration another set of iterations is performed to find the solution to the coupled linear system. This nesting of iterations, while seemingly expensive, provides excellent convergence properties that make the method much more attractive than algorithmically-simple explicit schemes.

When the initial estimate of the problem is far from the desired converged solution, the nonlinear nature of Eq. (4.1) can cause the solution method to converge slowly. To address this problem, a finite-time step approach reminiscent of an implicit application of the Euler method with switched evolution/relaxation (SER) is used, as proposed by van Leer and Mulder [97] and incorporated in the NKS solver using the Navier-Stokes for reactive flows by Northrup [59]. The linear system given in Eq. (4.2) is modified to include an additional term in the diagonal entries in Jacobian, such that

$$\left(\frac{\partial \mathbf{R}}{\partial \mathbf{U}} - \frac{\mathbf{I}}{\Delta t}\right)^n \Delta \mathbf{U}^n \approx -\mathbf{R}\left(\mathbf{U}^n\right) \tag{4.4}$$

where $\mathbf{I}$ is an identity matrix of the same dimensions as $\partial\mathbf{R}/\partial\mathbf{U}$. A small time step, Δt, is chosen at the first Newton step, and is then allowed to increase gradually depending on the ratio between the current Newton iteration residual norm and the starting residual norm. The diagonal dominance of the Jacobian matrix reduces the implicitness of the system and aids in the convergence rate during the initial Newton iterations. As the residual norm decreases, Δt increases, and its contribution to the linear system is reduced until the original linear system in Eq. (4.2) is recovered when $\Delta t = \infty$. The initial and final time step is not controlled directly upon startup, but is instead done so by specifying an initial and final CFL number to avoid handling variations in time step due to mesh spacing.

4.3 Krylov Subspace Linear Solver

Krylov subspace methods [93] focus on the solution to linear systems of the form

$$\mathbf{A}\mathbf{x} = \mathbf{b} \tag{4.5}$$

1.	Compute $\mathbf{r}_0 = \mathbf{b} - \mathbf{A}\mathbf{x}_0$, $\beta = \|\mathbf{r}_0\|_2$, and $\mathbf{v}_1 = \mathbf{r_0}/\beta$
2.	Define the $m \times m$ matrix $\mathbf{H}_m = \{h_{ij}\}_{1 \le i \le m+1, 1 \le j \le m}$. Set $\mathbf{H}_m = 0$
3.	For $j = 1, 2, \cdots, m$ Do:
4.	Compute $\mathbf{w}_j = \mathbf{A}\mathbf{v}_j$
5.	For $i = 1, \cdots, j$ Do:
6.	$h_{ij} = (\mathbf{w}_j, \mathbf{v}_i)$
7.	$\mathbf{w}_j = \mathbf{w}_j - h_{ij}\mathbf{v}_i$
8.	EndDo
9.	Compute $h_{j+1,j} = \|\mathbf{w}_j\|_2$. If $h_{j+1,j} = 0$ set $m = j$ and Goto 12
10.	Compute $\mathbf{v}_{j+1} = \mathbf{w}_j / h_{j+1,j}$.
11.	EndDo
12.	Compute $\mathbf{y}_m$ the minimizer of $\|\beta\mathbf{e}_1 - \mathbf{H}_m\mathbf{y}\|$ and $\mathbf{x}_m = \mathbf{x}_0 + \mathbf{V}_m\mathbf{y}_m$

Table 4.1: The GMRES algorithm, from Saad [93]

where, for the system in Eq. (4.2), $\mathbf{x} = \Delta\mathbf{U}^n$, $\mathbf{b} = -\mathbf{R}(\mathbf{U}^n)$ and $\mathbf{A} = \mathbf{J}(\mathbf{U}^n)$. A Krylov subspace for this non-singular system is a linear subspace defined as

$$\mathrm{K}_m(\mathbf{A}, \mathbf{b}) = \mathrm{span}\left\{\mathbf{b}, \mathbf{A}\mathbf{b}, \mathbf{A}^2\mathbf{b}, ..., \mathbf{A}^{m-1}\mathbf{b}\right\} \tag{4.6}$$

The usefulness of this subspace comes from the fact that the solution to the linear system can be expressed as a linear combination of basis vectors spanning this subspace. As discussed earlier, the Krylov method used in this thesis is the GMRES method developed by Saad and Schultz [94], which will define the spanning vectors and initiate a search through this subspace for a solution vector $\mathbf{z}$ that solves $\min_{\mathbf{z} \in \mathrm{K}_j(\mathbf{A},\mathbf{b})} \|\mathbf{b} - \mathbf{A}\mathbf{z}\|$. GMRES constructs a set of orthonormal basis vectors for the Krylov subspace using Arnoldi's method, which in turn is an extension of the Gram-Schmidt process adapted to Krylov subspaces. Table 4.1 summarizes the basic GMRES algorithm.

Starting with the normalized vector, $\mathbf{v}_1 = \mathbf{r_0}/\beta$, and some initial solution vector, $\mathbf{x}_0$, each iteration j through the Arnoldi algorithm recursively builds an orthonormal basis vector, $\mathbf{v}_{j+1}$, by a matrix-vector multiplication of the matrix $\mathbf{A}$ and the basis vector generated in the previous iteration, $\mathbf{A}^{j-1}\mathbf{b}$. Upon completion of each iteration, a vector of the computed basis vectors, $\mathbf{V}_{j+1}$, and a Hessenberg matrix, $\mathbf{H}_j$, consisting of dot products used in the basis vector calculations (Line 6. from Table 4.1) can be extracted. The decomposition process for each Arnoldi method iteration can be written as

$$\mathbf{A}\mathbf{V}_j = \mathbf{V}_{j+1}\mathbf{H}_j \tag{4.7}$$

with

$$\mathbf{V}_{j+1} = \begin{pmatrix} \mathbf{V}_j & \mathbf{v}_{j+1} \end{pmatrix}, \quad \mathbf{H}_j = \begin{pmatrix} \mathbf{H}_{j-1} & \mathbf{h}_j \\ 0 & h_{j+1,j} \end{pmatrix} \tag{4.8}$$

where $h_{j+1,j}$ is the magnitude of the newly-found non-normalized basis vector $\mathbf{v}_{j+1}$. Upon completion of the interior loops, a solution vector $\mathbf{z}$ can be defined as a member of the Krylov subspace $\mathrm{K}_j(\mathbf{A}, \mathbf{b})$ and thus can be written as a linear combination of the orthonormal basis vectors as $\mathbf{z} = \mathbf{V}_m \mathbf{y}$, where $\mathbf{y}$ is some vector. With this relation, the minimization problem can be rewritten with

$$\mathbf{A}\mathbf{z} = \mathbf{A}(\mathbf{V}_m \mathbf{y}) = (\mathbf{V}_{m+1}\mathbf{H}_m)\mathbf{y}, \quad \mathbf{b} = \beta \mathbf{v}_1 = \beta \mathbf{V}_{m+1}\mathbf{e}_1 \tag{4.9}$$

$$\min_{\mathbf{z} \in \mathrm{K}_j(\mathbf{A},\mathbf{b})} \|\mathbf{b} - \mathbf{A}\mathbf{z}\| = \min_{\mathbf{y}} \|\beta \mathbf{V}_{m+1}\mathbf{e}_1 - \mathbf{V}_{m+1}\mathbf{H}_m\mathbf{y}\| = \min_{\mathbf{y}} \|\beta \mathbf{e}_1 - \mathbf{H}_m\mathbf{y}\| \tag{4.10}$$

where $\mathbf{e}_1$ is the first column of the identity matrix. Once the minimized vector is obtained, denoted here as $\mathbf{y}_m$, the updated approximate solution is then found as $\mathbf{x}_j = \mathbf{x}_0 + \mathbf{V}_m \mathbf{y}_m$.

Additional iterations of the GMRES algorithm will expand the number of basis vectors in the Krylov subspace until j is equal to the size of the system, N, at which point the exact solution of the system in Eq. (4.5) will be found. However, searching through the entire Krylov subspace can be computationally expensive. Krylov methods therefore in general are instead used as iterative methods to accelerate solution convergence by prematurely terminating the number of iterations under two conditions: a maximum number of iterations $m < N$ as specified by the user, or if the residual norm $\|\mathbf{b} - \mathbf{A}\mathbf{x}\|$ is sufficiently small. In a restarted GMRES algorithm, also known as GMRES(m), further computational improvements can be seen if modifications are made to the linear system through global and local preconditioning to encourage an accurate approximation within a small number of iterations, m, and will be discussed later in Section 4.5 of Chapter 4.

4.4 Approximate Jacobian Matrix and Application to the Gaussian Closure

The residual vector, $\mathbf{R}(\mathbf{U})$, can be defined as the change in the solution state with respect to time, which the finite volume formulation defines as

$$\mathbf{R}(\mathbf{U}) = \frac{\mathrm{d}\mathbf{U}_{i,j,k}}{\mathrm{d}t} = -\frac{1}{V_{i,j,k}} \sum_m (\mathbf{F} \cdot \vec{n}\, \Delta A)_{i,j,k.m} + \mathbf{S}_{i,j.k}. \tag{4.11}$$

Newton's method requires the Jacobian of this residual vector with respect to the solution state, $\partial \mathbf{R}/\partial \mathbf{U}$, which in turn requires an evaluation of $\partial(\mathbf{F} \cdot \vec{n})/\partial \mathbf{U}$ and the Jacobian acting on the

source terms, $\partial\mathbf{S}/\partial\mathbf{U}$. The source vector itself is clearly defined from the collisional processes in the Gaussian closure. The source vector found from the regularized Gaussian closure for diatomic gases can be taken to be the right hand side expressions given in Eqs. (2.75)–(2.78). The evaluation of the source term Jacobian is a straightforward exercise as it is not dependent on the face normal. The same cannot be said for the remaining flux Jacobian.

To reduce the computational complexity regarding arbitrarily-oriented face normals, the intermediate Jacobian $\partial\left(\mathbf{F}\cdot\vec{n}\right)/\partial\mathbf{U}$ is computed on a reference frame generated by aligning the face normal to the $+x$-axis. The transformation of this Jacobian into and out of this reference frame can be written as

$$\frac{\partial\left(\mathbf{F}\cdot\vec{n}\right)}{\partial\mathbf{U}_{ij}}=\frac{\partial\mathbf{F}}{\partial\mathbf{F}_{*}}\frac{\partial\mathbf{F}_{*}}{\partial\mathbf{U}_{*}}\frac{\partial\mathbf{U}_{*}}{\partial\mathbf{U}_{ij}}, \tag{4.12}$$

where $\partial\mathbf{F}_{*}/\partial\mathbf{U}_{*}$ is the Jacobian of the rotated flux vector in the rotated reference frame. The Jacobian $\partial\mathbf{U}_{*}/\partial\mathbf{U}_{ij}$ describes the rotation of the cell state into the $+x$-axis, while the Jacobian $\partial\mathbf{F}/\partial\mathbf{F}_{*}$ describes the inverse of this rotation. Due to the structure of the terms in the conservative form of the state vector, the Jacobian of the flux with respect to this conservative state vector is further broken down via the chain rule to use the primitive form of the state vector instead, resulting in

$$\frac{\partial\left(\mathbf{F}\cdot\vec{n}\right)}{\partial\mathbf{U}_{ij}}=\frac{\partial\mathbf{F}}{\partial\mathbf{F}_{*}}\left(\frac{\partial\mathbf{F}}{\partial\mathbf{W}}\frac{\partial\mathbf{W}}{\partial\mathbf{U}}\right)_{*}\frac{\partial\mathbf{U}_{*}}{\partial\mathbf{U}_{ij}}, \tag{4.13}$$

where $\mathbf{W}$ is the primitive variable solution state.

The method described here is applicable to both the standard Gaussian closure and its regularized counterpart, though additional consideration is required when incorporating the elliptic fluxes in the regularized closure. As applied to Eq. (4.11), the flux vector is now defined as a sum of the hyperbolic flux from the Gaussian closure and the elliptic flux from the regularization. This necessitates the construction of an additional 'viscous' flux Jacobian, but otherwise the solution method remains the same. Expressions for the structure of the above-mentioned Jacobians as applied to both forms of the Gaussian closure can be found in Appendix B.

4.5 Global and Local Preconditioning Strategies

Preconditioning a system of linear equations represents any strategy of implicit or explicit modifications done to a linear system that will make it easier to solve. Saad and Schultz [94] have shown that the size of the Krylov subspace is dependent on the minimal polynomial of $\mathbf{A}$. This phenomenon suggests that preconditioning the matrix into a more diagonal form has the potential to reduce the size of the searched subspace. Highly scalable parallel algorithms

have been developed with this technique by Charest *et al.* [29] for the solution of radiative heat transfer and by Northrup and Groth [98] for unsteady laminar flames.

A right-preconditioning, additive Schwarz scheme is applied here to the linear system in the form

$$\left(\mathbf{J}\mathbf{M}^{-1}\right)\left(\mathbf{M}\mathbf{x}\right) = \mathbf{b} \tag{4.14}$$

where $\mathbf{M}$ is the preconditioning matrix. An additive Schwarz global preconditioner is a domain decomposition method where the solution in each subdomain is updated only when the cycle of updates is completed for all subdomains. The domain decomposition aspect of the additive Schwarz and the independence of subdomain communication during temporal updates is exactly what is used in the parallel, block-based AMR scheme. A further block incomplete lower upper (BILU) local preconditioner is used in each subdomain as described by Saad [93]. The preconditioner with both global Schwarz and local BILU can be written in the form

$$\mathbf{M}^{-1} = \sum_{k=1}^{N_b} \mathbf{B}_k^T \mathbf{M}_k^{-1} \mathbf{B}_k, \tag{4.15}$$

where N_b is the number of blocks, and $\mathbf{B}_k$ is a gather operator matrix for the k^{th} block, with the BILU preconditioning appearing in the local preconditioner, $\mathbf{M}_k$. Small overlaps between subdomains can be performed by a suitable exchange of data between blocks to increase the overall implicitness of the scheme, but care must be made to ensure that the cost of computing the preconditioner does not exceed the cost of not using a preconditioner at all.

Solving the right-preconditioned system in (4.14), the matrix-vector product $\mathbf{J}\mathbf{M}^{-1}\mathbf{x}$ is required. Numerical differentiation based on Fréchet derivatives yields an approximation to this product as

$$\mathbf{J}\mathbf{M}^{-1}\mathbf{x} \approx \frac{\mathbf{R}\left(\mathbf{U} + \varepsilon\mathbf{M}^{-1}\mathbf{x}\right) - \mathbf{R}\left(\mathbf{U}\right)}{\varepsilon}, \tag{4.16}$$

where ε is a small scalar quantity representing a small perturbation in the solution state. The value for ε used here is derived from Neilsen *et al.* [99], and is presented as $\varepsilon = \varepsilon_o / \left\|\mathbf{x}\right\|_2^{1/2}$, where $\varepsilon_o \approx 10^{-8} - 10^{-7}$. Using this expression, the GMRES algorithm does not require an explicit definition of a global Jacobian $\partial\mathbf{R}/\partial\mathbf{U}$.

4.6 Selection of Newton-Krylov Solution Parameters for the Gaussian Closures

Sufficiently converged solutions to the Gaussian closures using the NKS method are sensitive to various adjustable parameters within the solver. In addition to the small perturbative quantity

Flow Regime	Initial CFL	Final CFL	ε
Continuum (Kn < 0.01)	$10^1 - 10^3$	$10^6 - 10^7$	$10^{-6} - 10^{-7}$
Transition ($0.01 \leq$ Kn < 1)	$10^2 - 10^4$	$10^7 - 10^{10}$	$10^{-7} - 10^{-9}$
Free-Molecular (Kn ≥ 1)	$10^0 - 10^2$	$10^2 - 10^4$	$10^{-9} - 10^{-11}$

Table 4.2: NKS Initial/Final CFL parameters and ε values for various flow regimes using the standard and regularized Gaussian closures.

for the first-order Frechet derivative discussed earlier, the time step used in the SER implicit Euler startup procedure outlined in Eq. (4.4) can be started at low value and slowly ramped up to a specified final value to recover Newton's method. This time step is controlled via an initial and final CFL value that takes into account the mesh density of the computed problem. It is certainly possible to set this time step to be a constant throughout the computation, but this has been found to negatively impact the convergence rate for all problems considered in this thesis. While the optimal NKS solution parameters will vary depending on the geometries of the mesh, some conclusions can be drawn about their general behaviour in relation to the non-equilibrium nature of the flow problem.

Table 4.2 shows the initial and final CFL values and the corresponding values for ε used in the Frechet derivative for problems within the continuum, transition, and free-molecular regimes, respectively. These general parameter settings hold for both the standard and regularized Gaussian closures. In the continuum regime, increased stiffness of the equations due to the short relaxation times in the source terms requires smaller initial time steps in the implicit Euler startup procedure, but as the solution progresses larger time steps can be easily accommodated. Strictness in the accuracy of the Frechet derivative through the selection of ε for continuum flow tends to lead to stalled solutions. In transition regime flow, tightening the accuracy of the Frechet derivative tends to increase the convergence rate, but lower accuracies can still lead to converged solutions. Transition regime flows also seem less sensitive to the initial and final time step values in the implicit Euler startup and operate under a large range of values. Flows within the free-molecular regime pose significant restrictions on the NKS parameters. The initial and final time steps tend to much smaller than those for the continuum and transition regimes, and a highly-accurate Frechet derivative was also required. It should be noted that the smaller time steps needed for free-molecular flows are still orders of magnitude larger than those need for the semi-implicit method, as will be shown in the convergence histories of problems discussed in Chapters 5 and 6.

Another adjustable parameter in the NKS method is the GMRES convergence tolerance, which effectively governs how accurately the linear system is solved within each Newton iteration.

High tolerances, while mathematically favourable, may require a large number of GMRES iterations and become computationally expensive. Low tolerances, however, can negatively impact the performance of subsequent Newton updates. Due to the iterative nature of the NKS method and the inexact implementation of the restarted GMRES algorithm, tolerances within the GMRES algorithm do not need to be too strict. For the standard and regularized Gaussian closure, tolerances of 0.3 have been found to be sufficient, though for highly rarefied flows, tolerances were tightened to 0.1.

Other adjustable NKS parameters and their effects on convergence are discussed by Northrup [59], however these parameters have not been found to be dependent on the collisional nature of the flow. Parameters such as the local BILU preconditioner fill level and domain overlap for the additive Schwarz global preconditioner have been found to provide little improvement on the convergence qualities of the standard and regularized Gaussian closures, and is similar to results reported by Northrup [59]. Higher levels of fill in the local BILU preconditioner allows the approximate inverse to retain more non-zero entries at the expense more computational work. For the flow problems considered in this thesis, a fill level of 2 was found to be sufficient. Domain overlap can help overcome the loss of implicitness in the Schwarz preconditioner, which becomes evident when the number of domains becomes large. Northrup [59] has reported that while domain overlap can reduce the number of GMRES iterations, the overall computational cost increases due to the extra block communication required. A similar behaviour was also observed for the three-dimensional Gaussian closures, and therefore no domain overlap is used for all flow problems considered herein.

Chapter 5

Three-Dimensional Numerical Results for the Gaussian Closure

5.1 Overview

The standard Gaussian closure for both monatomic and diatomic gases and the proposed solution method for three-dimensional non-equilibrium flows are applied here to various flow problems to demonstrate their ability to model commonly-encountered flow phenomena, including drag, boundary layer evolution, and slip flow behaviour. The flow problems considered are mainly all three-dimensional extensions of similar two-dimensional cases considered previously by McDonald and Groth [15–18]. Three-dimensional subsonic flow past a sphere is also considered. The numerical predictions are compared to available analytical solutions, experimental data, and previous numerical solutions where applicable. The solid-wall boundary conditions derived in Section 2.5 of Chapter 2 are used exclusively here.

For the cases considered here, the definition of mean free path, λ, used for all of the flow problems considered here is that as given by Bird [1] and has the form

$$\lambda = \frac{16\mu}{5\left(2\pi\rho p\right)^{\frac{1}{2}}}, \tag{5.1}$$

where μ is the dynamic viscosity of the fluid, and the gas particles are assumed to behave as hard spheres during collision processes.

5.2 Manufactured Solution

The finite-volume scheme developed here for the Gaussian closure is similar to that used in previous two-dimensional studies by McDonald and Groth [15–17]. A spatial accuracy assessment for the finite-volume scheme applied to the solution of the Euler equations on two-dimensional multi-block quadrilateral mesh has been performed by Sachdev and Groth [85, 100], and more recently for the two-dimensional Gaussian closure with embedded boundaries by Mcdonald *et al.* [50]. As the second-order spatial accuracy of the scheme has been demonstrated for the moment equations of interest here, the task that remains is to demonstrate that the spatial accuracy is also achieved in the current implementation for three-dimensional multi-block hexahedral grids. As practical situations with exact analytical solutions for the variants of the three-dimensional Gaussian closure of interest here are not available, the accuracy of the proposed scheme is instead verified with the method of manufactured solutions [101]. This accuracy assessment mirrors closely the analysis carried out previously by Mcdonald *et al.* [50] for the two-dimensional case.

The method of manufactured solutions permits the construction of an analytical solution over the computational domain of interest by driving the solution of the governing PDEs towards the selected analytical results through the addition of source terms. This chosen analytical solution for the Gaussian closure, $\widehat{\mathbf{U}}$, can be used to determine its associated solution residual vector, $\widehat{\mathbf{R}}$, based on a re-expression of Eqs. (2.44)–(2.47) in weak conservation form such that

$$\widehat{\mathbf{R}} = \frac{\partial \widehat{\mathbf{U}}}{\partial t} + \frac{\partial \mathbf{F}(\widehat{\mathbf{U}})}{\partial x} + \frac{\partial \mathbf{G}(\widehat{\mathbf{U}})}{\partial y} + \frac{\partial \mathbf{H}(\widehat{\mathbf{U}})}{\partial z} - \mathbf{S}(\widehat{\mathbf{U}}) \tag{5.2}$$

where $\mathbf{F}$, $\mathbf{G}$, and $\mathbf{H}$ are the flux vectors of the analytical solution in the $x-$, $y-$, and $z-$ directions respectively, and $\mathbf{S}$ is the associated source term. This residual vector is then added as an additional source term to the original set of equations in the form

$$\frac{\partial \mathbf{U}}{\partial t} + \frac{\partial \mathbf{F}(\mathbf{U})}{\partial x} + \frac{\partial \mathbf{G}(\mathbf{U})}{\partial y} + \frac{\partial \mathbf{H}(\mathbf{U})}{\partial z} = \mathbf{S}(\mathbf{U}) + \widehat{\mathbf{R}} \tag{5.3}$$

such that the computed solution vector, $\mathbf{U}$, is driven towards the prescribed solution, $\widehat{\mathbf{U}}$, once a converged steady-state solution is achieved. The spatial accuracy of the solution method (i.e. the discretization error) can then be evaluated by comparing the computed solution to the prescribed analytical result.

For the particular case of interest, time-invariant solutions are found using the three-dimensional Gaussian closure for a monatomic gas between two concentric cylinders. The interior and exterior radii of the cylinders are 0.5 m and 1.0 m, respectively, and each has a height of 1.0

m. The prescribed components of the Gaussian solution for this analysis are taken to be

$$\begin{aligned}
\rho &= 2 + \sin(x+y), \\
u_x &= \cos(x+y), \\
u_y &= \sin(x-y), \\
u_z &= 0, \\
P_{xx} &= 3 - \sin(x+y), \\
P_{xy} &= \sin(y-x), \\
P_{xz} &= 0, \\
P_{yy} &= 3 + \cos(x+y), \\
P_{yz} &= 0, \\
P_{zz} &= 3 + \cos(-x-y),
\end{aligned}$$

where the $x-$ and $y-$axes lie within the plane of the circular base and the $z-$axis extends along the length of the cylinder as shown in Figure 5.2.

Boundary conditions for this case were enforced by assigning the prescribed analytical solution to appropriate ghost cells with reference to their position in three-dimensional space. The NKS algorithm developed for the solution of the three-dimensional Gaussian closure was used herein to find the time-invariant solution. The forcing nature of the manufactured residual source term towards the analytical solution and the simplified boundary conditions and flow conditions allowed the NKS solution algorithm to reach ideal convergence rates, with L_2-norm solution residual reductions of at least eight orders of magnitude.

For the grid convergence study, four nested meshes were considered. An initial coarse multi-block, hexahedral grid is used together with three grids generated by three consecutive uniform refinements of this grid. The mesh density of these four grids can be seen in Figure 5.2, and their statistics are given in Table 5.1. Each mesh block contains 8 cells in the radial direction, 8 cells in the angular direction, and 16 cells over the height of the cylinder. An example of the convergence history for the cylinder grid with 512 block grid is in Figure 5.1. The total CPU time used for this particular case is approximately 4000 minutes, that when divided over the 256 processors used for the calculation, yields a total physical time of about 17 minutes. A total of 200 Newton iterations are performed on each mesh, but as evident from Figure 5.1, a suitably converged solution is reached before this time limit is reached.

The predicted error norms based on the computed and analytical solutions with increasing mesh resolution is depicted in Figure 5.3. The L_1 and L_2 norms were calculated using the difference

Refinement Level	Blocks	Cells	Mesh Points	Processors	L_2 Norm	Time (min)
0	8	8192	9.7920×10^3	8	1.99279×10^{-12}	0.653
1	64	65536	4.2931×10^6	64	9.95513×10^{-12}	6.5
2	512	524288	2.1538×10^9	256	5.67367×10^{-11}	17
3	4096	4194304	1.0999×10^{12}	512	1.0918×10^{-8}	92.03

Table 5.1: Properties of four cylinder grids used in the method of manufactured solutions using the standard Gaussian closure.

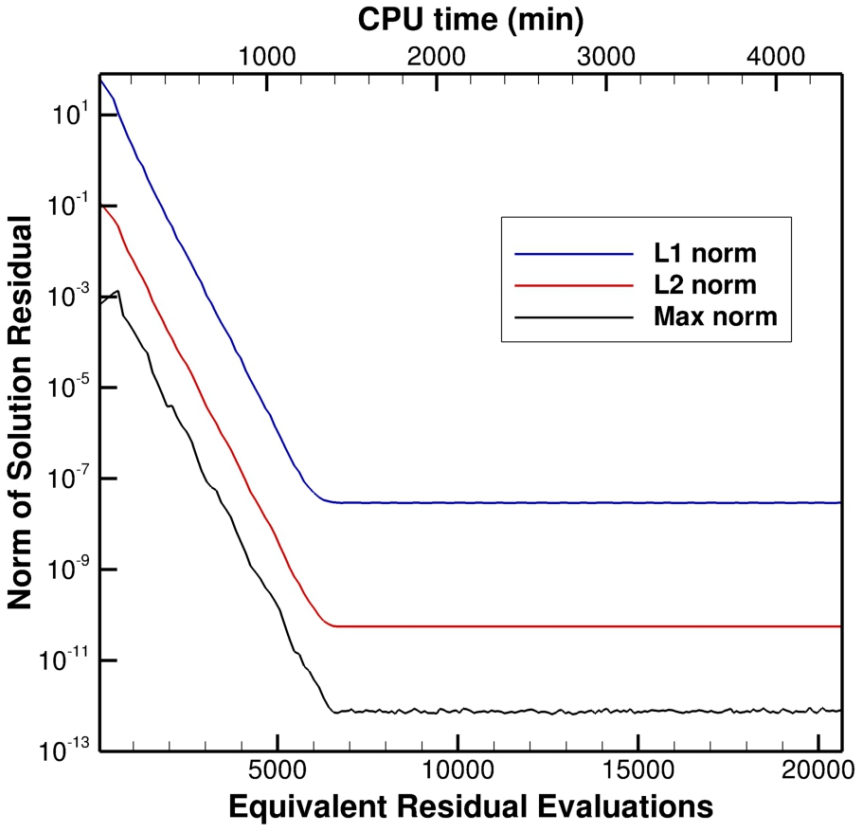

Figure 5.1: L_1, L_2, and max error norms based on the solution residual for the manufactured solution problem containing 512 computational blocks performed on 256 processors.

between computed and analytical solution at each cell center and weighted according to the volume of the cell. The three-dimensional nature of the problem prompts a comparison to the nominal mesh density given by the cube root of total number of cells, $n^{1/3}$. A reference line with a slope of -2 is included for comparison, and clearly illustrates that the formal second-order spatial accuracy of the scheme is achieved on the multi-block hexahedral mesh.

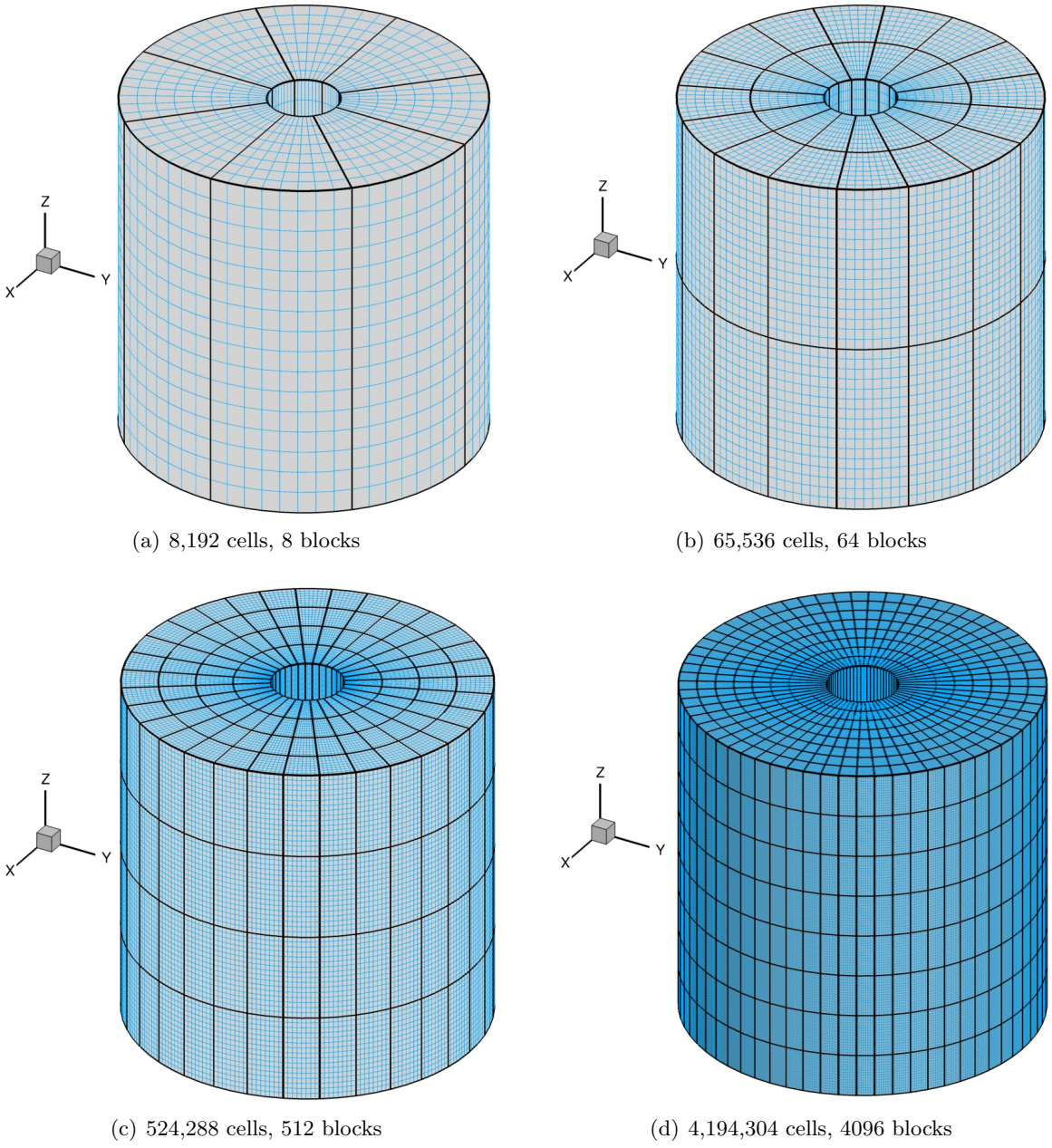

(a) 8,192 cells, 8 blocks

(b) 65,536 cells, 64 blocks

(c) 524,288 cells, 512 blocks

(d) 4,194,304 cells, 4096 blocks

Figure 5.2: Manufactured solution grids and parameters generated from consecutive uniform mesh refinements.

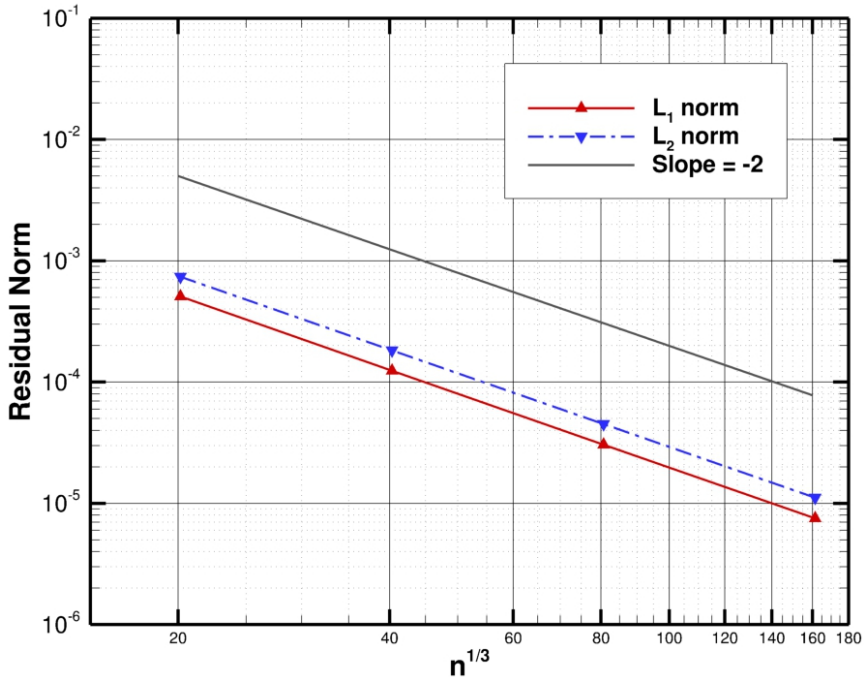

Figure 5.3: Predicted L_1 and L_2 error norms for the manufactured solution problem with increasing mesh densities using the Gaussian closure for a monatomic gas.

5.3 Planar Couette Flow with Velocity Slip

One of the main non-equilibrium characteristics of increasing Knudsen number is the appearance of velocity slip flows at solid walls. In the continuum regime, particle density at the wall is sufficiently high that a large number of particles will collide with the wall and undergo a change in velocity corresponding to the velocity of the wall. As the flows become increasingly rarefied, fewer particles will collide with the wall and undergo this velocity change, resulting in a decrease in macroscopic fluid velocity measurements at the wall. This disparity between the velocity of the wall and the velocity of the flow at the wall begins at a Knudsen number range of about $0.01 < \mathrm{Kn} < 0.1$. Accommodating velocity slip flows within the standard Navier-Stokes descriptions usually involves incorporating complex boundary conditions as an extension to the continuum-based equations [102]. The standard Gaussian closure however, requires no case-specific boundary conditions beyond those already used for specifying solid-wall boundary conditions, as slip flow effects fall out naturally from the equation set. This becomes a powerful tool for modelling flows that lie in the continuum-slip flow regime.

Having established the spatial accuracy of the proposed finite-volume scheme for the Gaussian closure, planar Couette flow is studied here to illustrate the ability of the closure to modelling

boundary layer and shear stress evolution in various flow regimes, including those with velocity slip. Figure 5.4 shows the setup for the flow modelled here, depicting the multi-block mesh configuration and a sample computed solution. For this particular problem, the two plates are moving at 30 m/s in opposite directions in argon at 288 K in standard pressure, and the setup is extruded in the $z-$direction. The plate separation is used as the characteristic length of the problem, and varies between $7.19438987 \times 10^{-5}m$ in the continuum regime to $7.19438987 \times 10^{-10}m$ in the free-molecular regime. The solution of the Gaussian closure was used with periodic boundary conditions were used at the inflow and outflow boundaries, while the solid wall boundaries described in Section 2.5 are used for the two plates. The mesh resolution with three levels of mesh refinement were used for this problem, generating a total of 43,200 cells. As the problem is relatively simple and the flow is almost one-dimensional, the use of AMR was not necessary to reach a steady solution within a reasonable amount of computational time. Flow solutions for this problem were performed using the NKS solver in parallel over eight Intel Xeon E5540 cores operating at 2.53 GHz.

Figure 5.5(a) shows the non-dimensionalized velocity u/U, where u is the fluid velocity at the wall and U is the wall velocity, versus the Knudsen number based on the separation of the two plates. The standard Navier-Stokes equations calculates the fluid velocity at the wall to be equal to the velocity of the wall regardless of Knudsen number. The free molecular solution generates an infinite slip velocity at the wall, with the fluid velocity at the wall equal to zero for all flows. Lees solution [103] provides an analytical solution to this problem that predicts the slip velocity and shear stress at the wall, gradually transitioning from the continuum result to the free-molecular. It is evident from the figure that the Gaussian solution is capable of modelling the formation of a slip velocity and follows Lees solution closely for the full range range of Knudsen numbers.

The shear pressure profile for the same problem can be seen in Figure 5.5(b). For comparison purposes, the shear stresses are normalized to the free molecular solution as $\tau_{xy}/(\rho U\sqrt{2kT/\pi m})$. Use of the continuum formulation predicts an ever-increasing shear stress with increasing Knudsen number, while the free-molecular shear stress remains constant regardless of Knudsen number. The Gaussian solution predicts a smooth transition between the continuum and free-molecular solutions and is in very close agreement with the analytical solution by Lees.

It is important to note here the constant shear stress found in the free-molecular regime, as this phenomena is clearly at odds with the continuum regime results. In the free-molecular regime, assuming no interparticle collisions and fully accommodated collisions at the walls, the non-equilibrium distribution function describing the fluid between the plates will be dependent only on the half-Maxwellian distributions emanating from the two walls. With the plates

sufficiently close such that the flow is effectively collisionless, the resulting solution for the Couette flow becomes independent of the plate separation. Based on the two half-Maxwellians, it can be shown that the shear stress between the plates is a constant non-zero value, even with zero mean velocity, and represents the forces exerted by the plates on one another due to momentum transfer occuring at the plate walls [104]. The ability of the Gaussian closure to accurately model this constant free-molecular shear stress is a highly desirable feature. At the very least, the results of Figure 5.5 provide confidence in the correctness of the slip-wall boundary condition for the Gaussian closure.

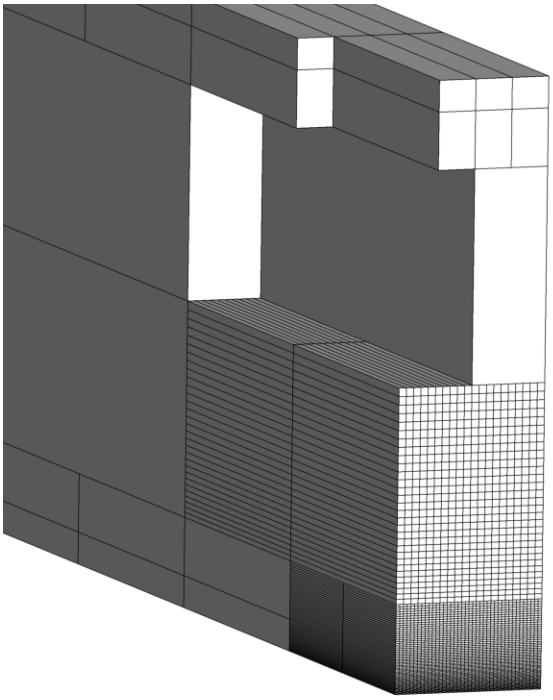

(a)

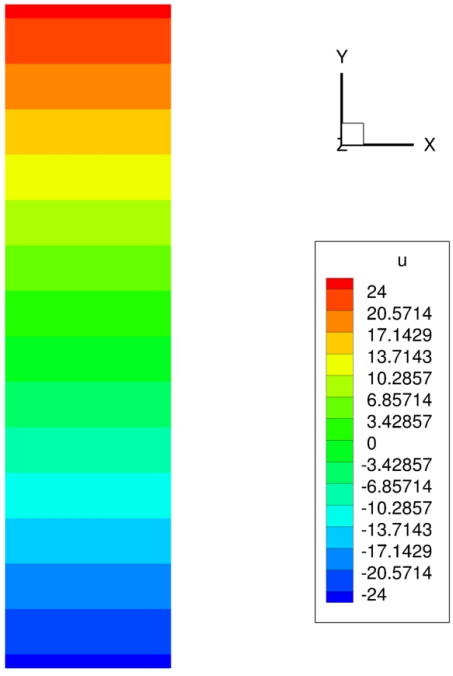

(b)

Figure 5.4: (a) Cutaway view of 3D mesh blocks for Couette flow problem with periodic boundary conditions developed using AMR. Mesh size can also be seen in the blocks in a lower half of the domain, (b) Sample result u velocity profile for Kn = 0.1. The moving walls are situated along the top and bottom edge of the domain.

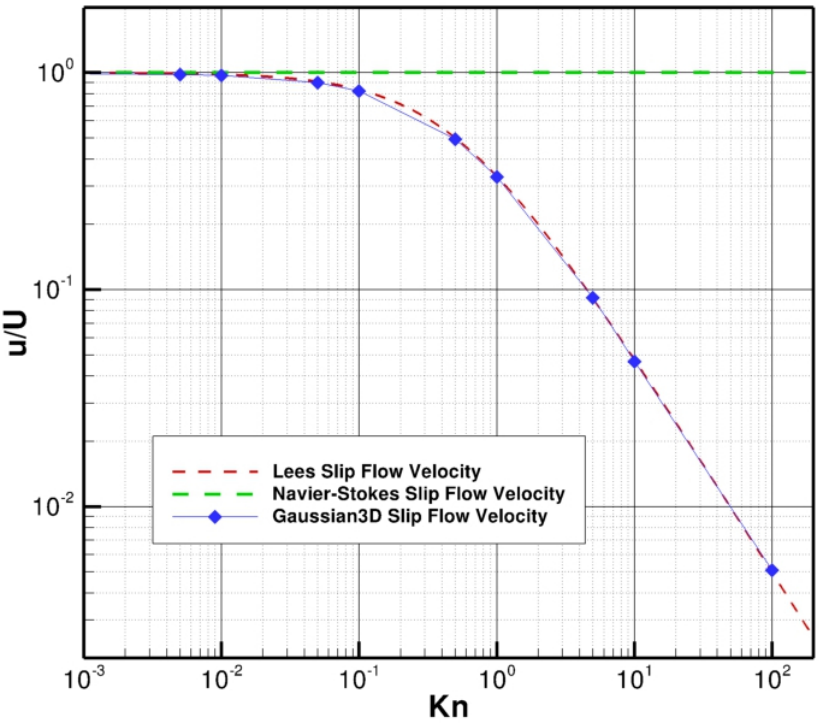

(a)

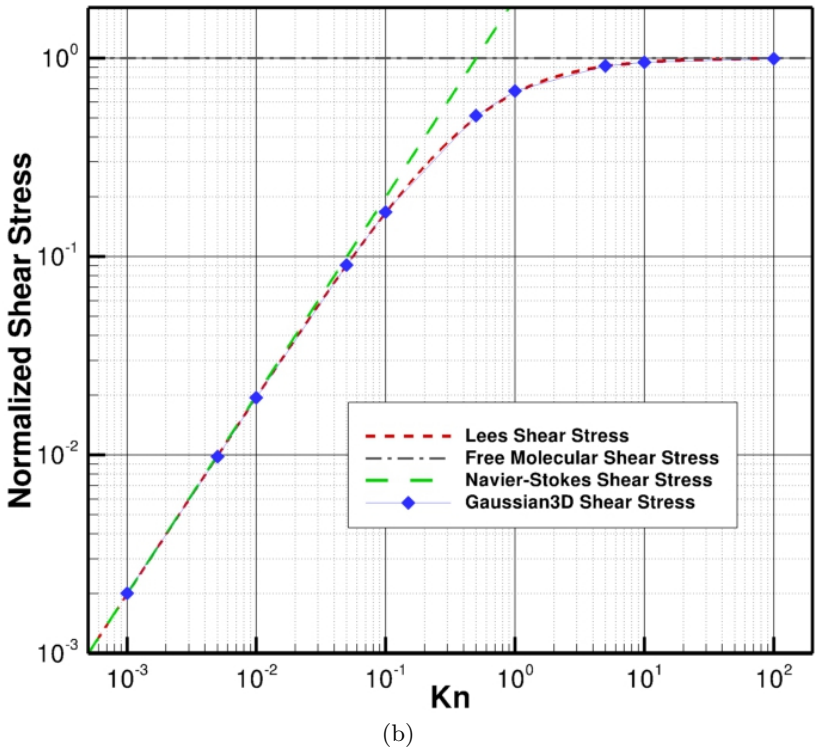

(b)

Figure 5.5: (a) Normalized fluid velocity at the wall vs. Knudsen number. Note that the free-molecular solution gives $u = 0$ at the wall regardless of Knudsen number, (b) Normalized shear stress at the wall vs. Knudsen number.

5.4 Subsonic Flat Plate Boundary Layer Flow

The Gaussian closure's ability to model slip flows and its effect on the boundary layer is further demonstrated here through the prediction of subsonic boundary layer development over a flat plate. The configuration of interest is shown in Figure 5.6, with the third spatial dimension extruded out of the page as shown in the mesh of Figure 5.7. The free stream conditions for this flow consist of air at 288 K flowing at a Mach number of 0.2 under standard atmospheric pressure. The characteristic length, and consequently the Knudsen number, is varied by sampling the boundary layer profile along different lengths along the plate downstream from the leading edge. The continuum boundary layer profile at $\mathrm{Kn} = 4.5 \times 10^{-5}$ was sampled at 1.5×10^{-3} m, while the transition regime boundary layer profile at $\mathrm{Kn} = 2.6 \times 10^{-1}$ was sampled at 2.6×10^{-7} m. The associated Reynolds number for the continuum and transition regime flows are $\mathrm{Re} = 6505$ and $\mathrm{Re} = 1.1$ respectively, well within the laminar flow regime. Solutions of the Gaussian closure for this case in two-dimensions were obtained previously by McDonald and Groth [15–18] using AMR with ten levels of refinement resulting in a very high mesh resolution at the surface of the flat plate. For the Gaussian closure solutions in three-dimensions, four levels of refinement were used, resulting mesh that contained a total of 250,000 cells. This level of mesh refinement proved satisfactory for the current purposes. The mesh is linearly varying in space such that a higher resolution is achieved closer to the plate surface. Solid wall boundary conditions were again employed for the plate, with a far field situated 10 plate lengths above the plate and inflow and outflow boundary conditions situated upstream and downstream from the plate, respectively.

Figure 5.8 compares the boundary layer profiles between the Knudsen number-independent Blasius solution [105] and solutions from the continuum ($\mathrm{Kn} = 4.5 \times 10^{-5}$) and transition ($\mathrm{Kn} = 2.6 \times 10^{-1}$) regimes. Blasius proposed a relation between a non-dimensionalized velocity u/U normalised to the free stream velocity U, and a non-dimensional number $y\sqrt{U/(\nu x)}$ relating to the development of the boundary layer at a certain position above the plate. These non-dimensionalized numbers are calculated for both the continuous and transitional case for comparison purposes.

From Figure 5.8, it is quite evident that the continuum result matches closely with the Blasius approximation with a zero slip velocity at the wall, while the transitional regime solution clearly shows a non-zero velocity at the wall. Calculations were performed with approximately 100 cells lying within the boundary layer. From the numerical results, it would seem that the Gaussian closure is equally capable of resolving the slip flow phenomena exhibited with increasing Knudsen numbers.

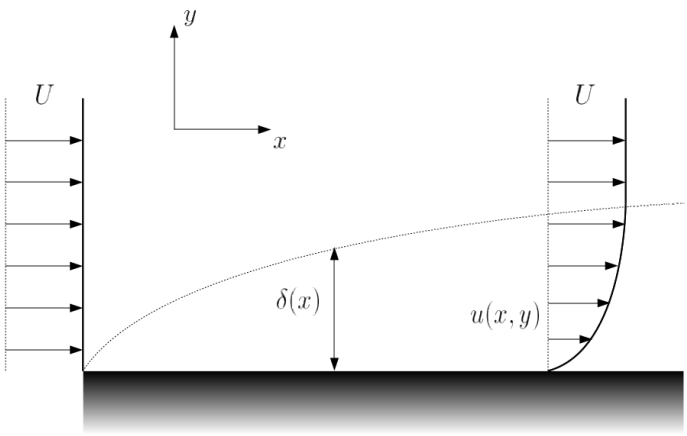

Figure 5.6: Boundary layer development along a flat plate, with boundary layer thickness $\delta(x)$, velocity profile $u(x, y)$ inside the boundary layer, and the free stream velocity U.

The convergence history of the flat plate boundary layer problem for continuum and transition regime flow for both the NKS and semi-implicit solver are shown in Figure 5.9. The solvers were performed over three Intel Core i7-980 processors operating at 3.33 Ghz. The NKS solver, performing 100 Newton iterations in this case, is capable of reaching high convergence levels at a fraction (0.3%–1%) of the computational cost of the equivalent semi-implicit solver. Beginning with uniform initial conditions, resolution of the sharp edge at the front of the plate seems to pose some problems for both solvers. The convergence rate of the NKS solver in the continuum regime does not perform as well as those from the transition regime, a phenomenon that occurs throughout most flow problems studied in this thesis. For small Knudsen numbers, the relaxation time used in the source terms becomes very small and magnifies the size of the source terms. This in turn increases the stiffness of the moment equations and reduces the efficiency of the NKS solver. However, the solutions coming from the NKS solver are still in line with results acquired from continuum-based solutions, as seen from the close agreement in boundary layer profiles shown in Figure 5.8(a).

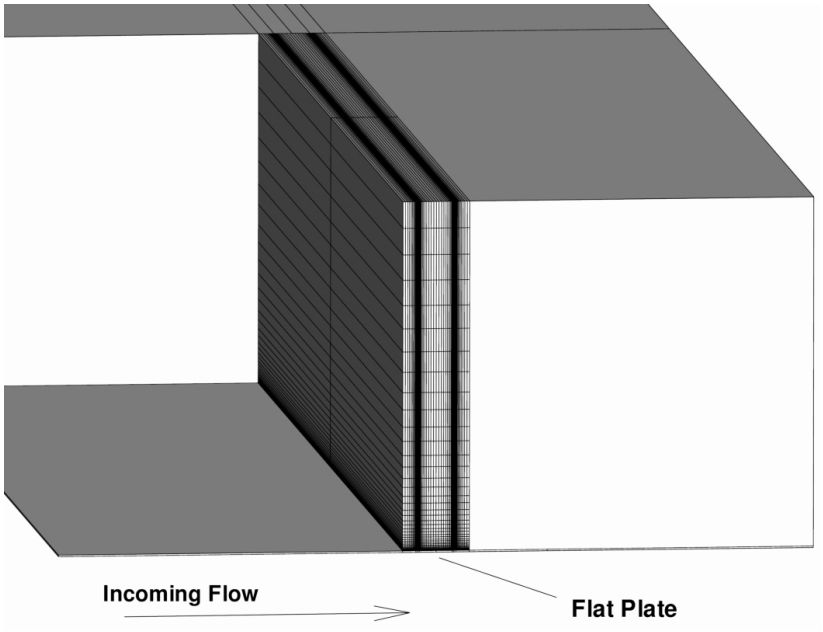

(a)

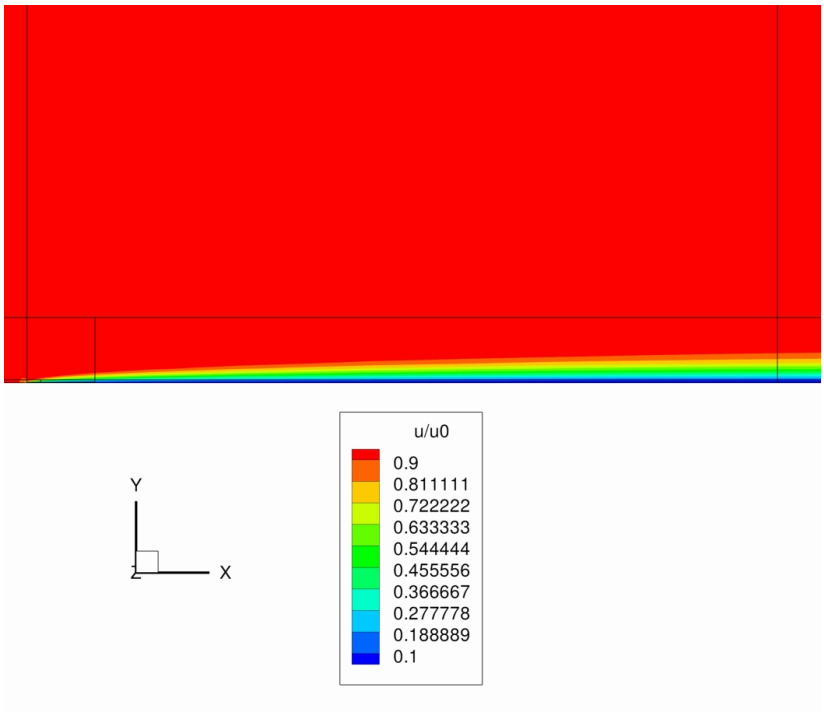

(b)

Figure 5.7: (a) Cutaway view of 3D mesh blocks for flat plate boundary layer flow problem developed using AMR. The flat plate boundary conditions are situated in the small patch of wall at the centre of the domain as indicated. The large far field extending above the plate is necessary for unimpeded boundary layer formation, (b) Sample u/U non-dimensional velocity profile for continuum regime flow. Boundary layer profiles are taken at specific points along the plate in accordance to the Knudsen number of interest.

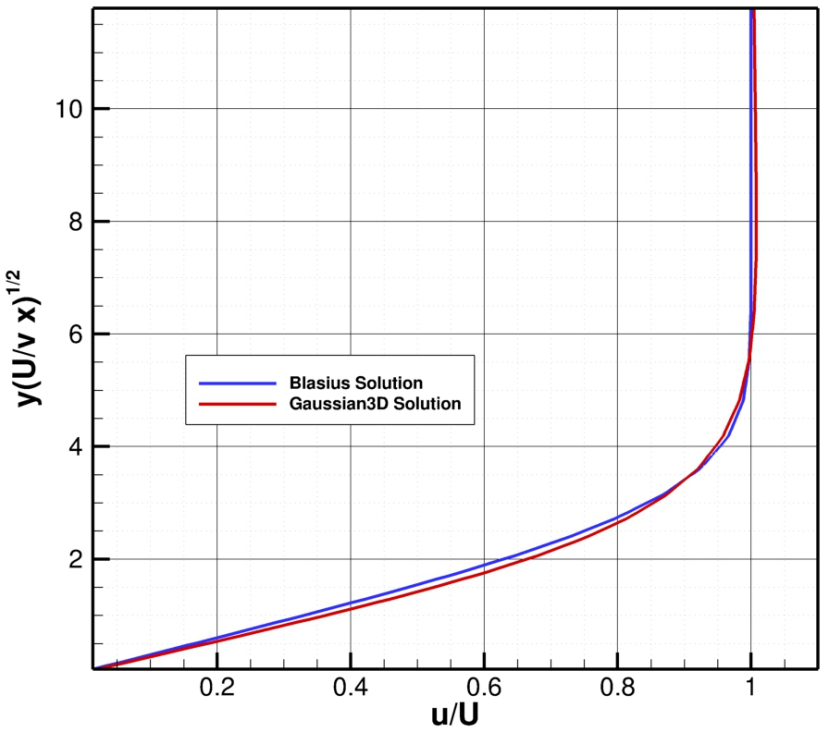

(a)

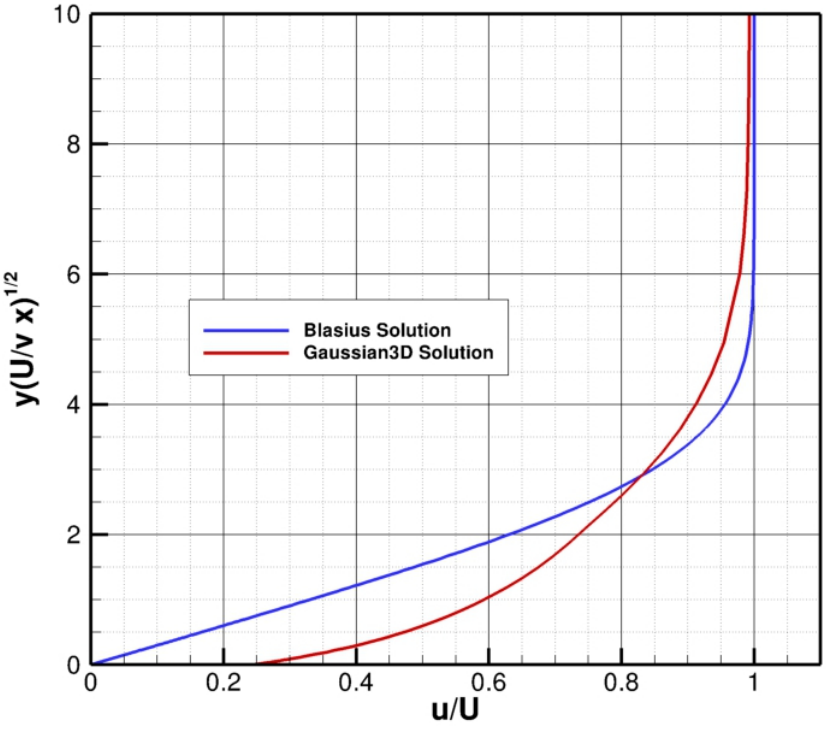

(b)

Figure 5.8: Flat plate normalised velocity distribution in developing boundary layer at varying Knudsen numbers (a) Continuum Regime, Kn $= 4.5 \times 10^{-5}$, (b) Transition Regime, Kn $= 2.6 \times 10^{-1}$.

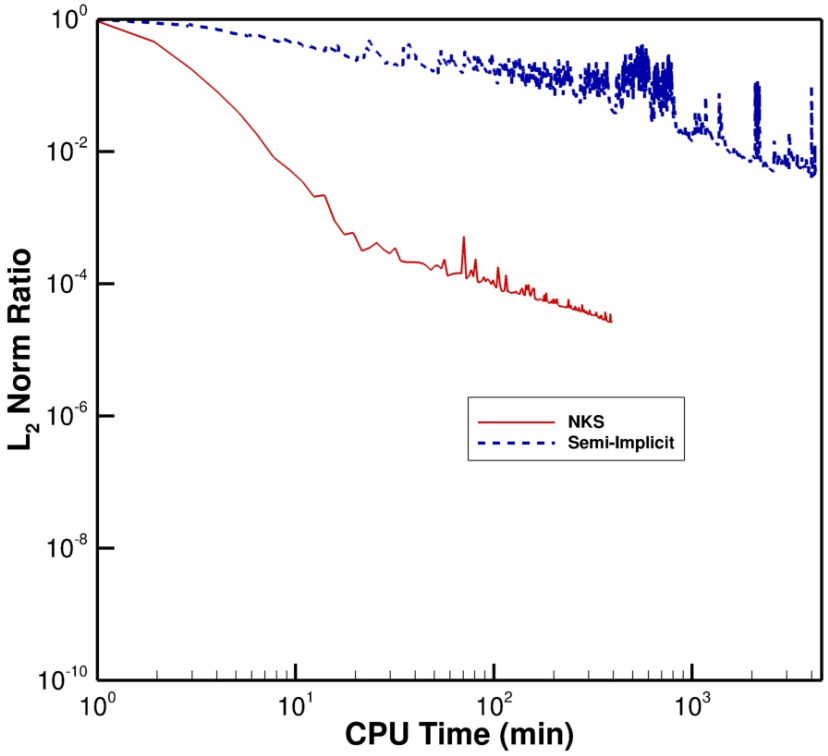

(a)

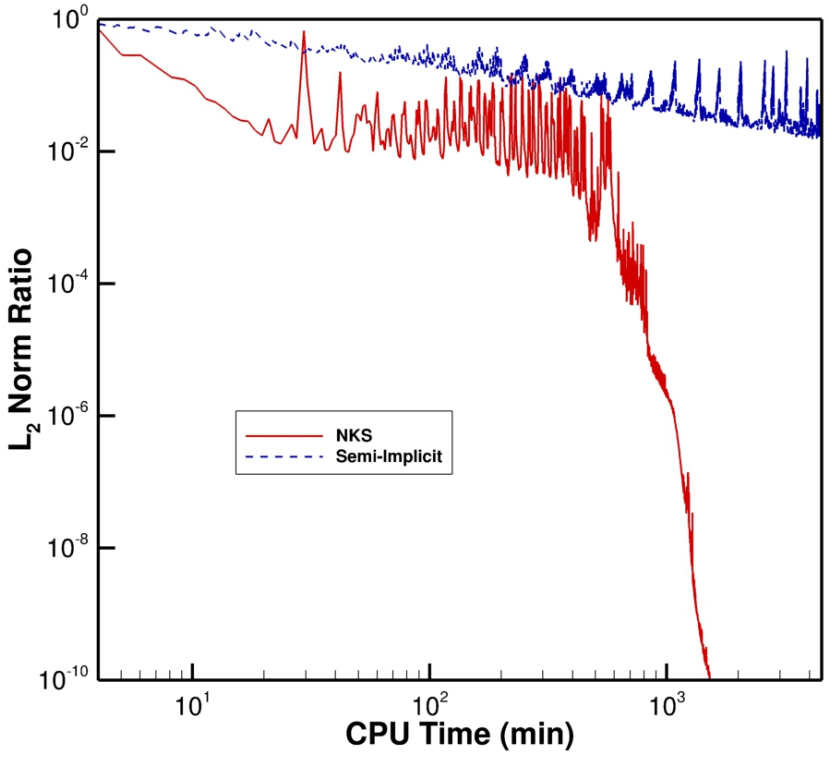

(b)

Figure 5.9: NKS and semi-implicit convergence rates for subsonic flat plate boundary layer flow in the (a) Continuum Regime, $\mathrm{Kn} = 4.5 \times 10^{-5}$, and (b) Transition Regime, $\mathrm{Kn} = 2.6 \times 10^{-1}$.

5.5 Subsonic Immersed Flow Past a Circular Cylinder

The drag forces exerted on a cylinder in an immersed flow is a well studied topic in aerodynamics and serves as an excellent platform here with which to evaluate the validity and accuracy of the Gaussian closure. The effects of laminar flow past a cylinder in both the continuum and transitional regimes have been studied experimentally by Coudeville *et al.* [106], with focus on the drag coefficient with both varying Reynolds and Knudsen numbers. Approximate solutions to the cylinder drag in the continuum and transitional regime have also been put forward by Patterson [107]. For the flow problem considered here, the cylinder radii was varied from 3.36×10^{-5} to 3.36×10^{-9} m, corresponding to a Knudsen number ranging from Kn = 0.001 to Kn = 10 using the cylinder diameter as the characteristic length. The computed Gaussian closure solutions are for air at 288 K at standard atmospheric pressure. Two speed ratios of S = 0.107 and S = 0.027 corresponding to Mach numbers of Ma = 0.128 and Ma = 0.032, repectively, were used for setting the free stream velocity, where the speed ratio is defined as the ratio between the bulk speed of the fluid to the most probable random speed of a particle, and is proportional to the Mach number. The Reynolds number for these flows ranged from Re = 0.005 up to Re = 188.

A sample of the three-dimensional computational grid with AMR implemented for this immersed cylinder flow is shown in Figure 5.10. Solid wall boundary conditions were used for the surface of the cylinder, with the far field set at 100 times the cylinder radius. However, for Kn = 0.1, the boundary layer formed around the cylinder expands considerably, and the far field boundaries were extended up to 400 times the cylinder radius to avoid any interaction with the boundary layer. Mesh resolution at the surface of the cylinder was maintained at a level similar to that of McDonald and Groth [15–18], with a final three-dimensional mesh resolution of approximately 180,000 cells. As for the flat plate problem, the mesh was stretched to create a higher concentration of cells near the cylinder surface.

The drag coefficient is plotted against the Knudsen number in Figure 5.11 for two different speed ratios S. The Gaussian closure is successful in duplicating the experimental results of Coudeville *et al.* [106] in both the continuum and transition regimes. However, the closure solution begins to over-predict the drag coefficient compared to both the experimental results and the theoretical solutions when the fluid begins to transition into the free molecular flow regime at about Kn > 0.5. While the Gaussian closure tends to over-predict the drag coefficient in this region, possibly due to the neglected heat transfer effects, it is successful in demonstrating a smooth transition of drag coefficients while moving from the continuum regime into the free molecular regime.

	NKS				Semi-Implicit		
Kn	Initial CFL	Final CFL	Time (min)	L2-norm Ratio	CFL	Time (min)	L2-norm Ratio
0.001	1×10^{2}	1×10^{9}	356.4	3.48279×10^{-7}	0.3	2871.51	7.691×10^{-6}
0.1	1×10^{1}	1×10^{10}	205.1	1.88937×10^{-6}	0.3	2782.91	1.401×10^{-6}
1	1×10^{1}	1×10^{10}	105.3	5.90163×10^{-12}	0.05	2813.25	7.630×10^{-1}

Table 5.2: Summary of NKS/semi-implicit CFL parameters and computation times for the flow problems performed in Figure 5.13.

It should be noted that as the Knudsen number increases and the flow approaches the free molecular regime, the flow structure also changes dramatically. Figure 5.12 shows the velocity profiles for the flow around the cylinder in the continuum regime (Kn = 0.001) through the transitional regime (Kn = 0.1), right up to the boundary of the free molecular regime (Kn = 1). A clear separation of the flow with a recirculation area in the wake of the cylinder can be seen in the continuum result which agrees with standard experimental results for this value of the Reynolds number. As the Knudsen number is increased, the thickness of the boundary layer increases and the flow remains attached. This thicker boundary layer disturbs the far field flow much more prominently, and numerical results for these higher Knudsen numbers required a larger domain to accommodate their effects. The increase in boundary layer thickness is in line with basic kinetic theory for rarefied flows, as the reduction in interparticle collisions comes about from larger mean free paths.

Examples of the NKS and semi-explicit solver convergence behaviour for the continuum, transition and near free-molecular regimes can be found in Figure 5.13. Both solution methods were performed in parallel over eight Intel Xeon E5540 cores operating at 2.53 GHz on the SciNet General Purpose Cluster (GPC). Table 5.2 provides a summary of the NKS and semi-implicit CFL parameters used in these cases. The NKS scheme, each running 200 Newton iterations, consistently outperforms the semi-implicit methods across all Knudsen numbers. The highly-converged results and low computation time show that the NKS scheme is both robust and efficient. The semi-implicit method requires consecutively smaller CFL numbers for convergence, ranging from CFL = 0.3 for Kn = 0.001, to CFL = 0.005 for Kn = 1, which adversely affects the amount of time required for convergence.

To further illustrate the robustness of the combined NKS and AMR schemes, the results from a mesh convergence study for immersed flow over a cylinder at Kn = 0.01 and S = 0.107 can be seen in Figure 5.14. Beginning with a coarse mesh, a converged NKS solution is computed at consecutively refined meshes using AMR. The convergence history of the NKS solution is shown in Figure 5.14(b). Rapid convergence can be seen at each refinement level and illustrates the robustness of the NKS scheme regardless of mesh refinement. Using a planar view of the

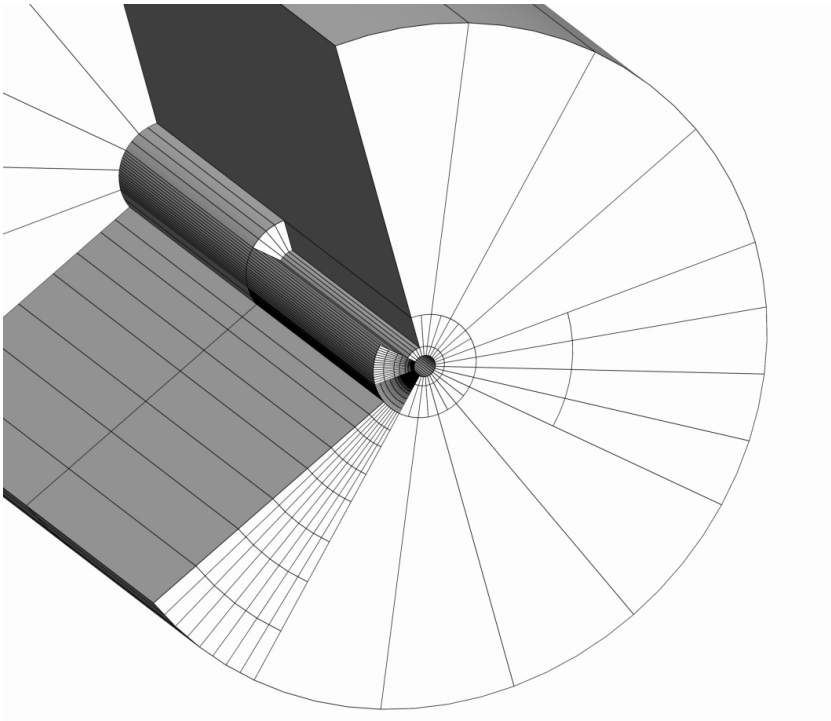

(a)

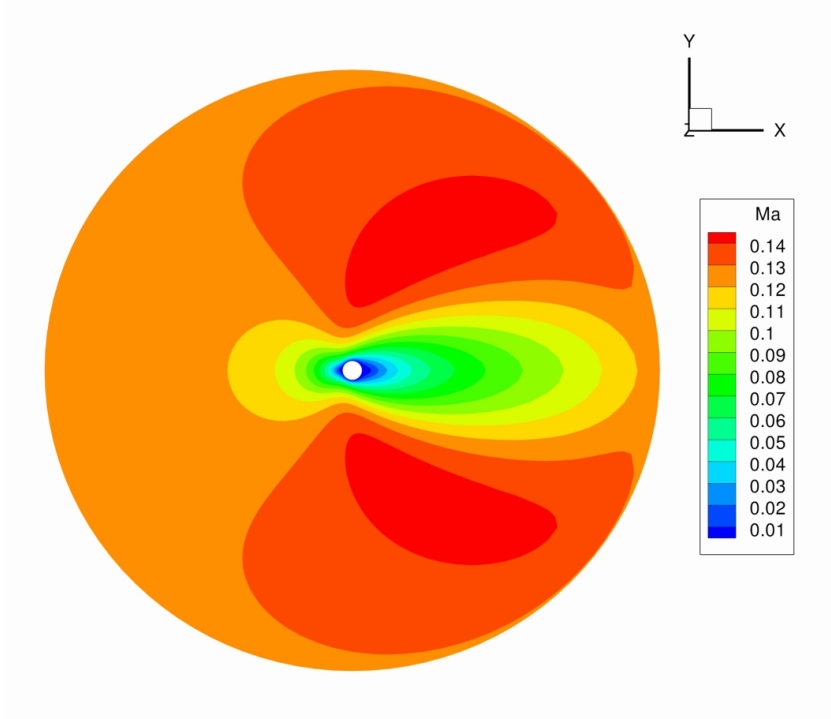

(b)

Figure 5.10: (a) A cutaway view of the radial mesh blocks created by the AMR algorithm for immersed cylinder flow, showing refined block structure at the surface of the cylinder and in the downstream regions. Mesh sizes are also shown in the lower left blocks. (b) Sample result of Mach number profile for Kn = 0.1.

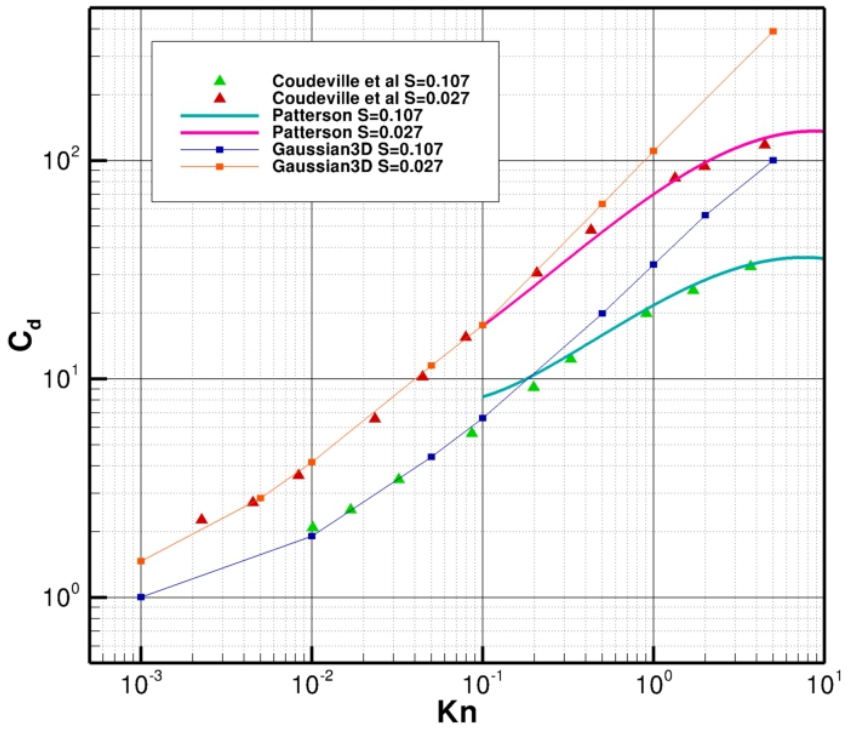

Figure 5.11: Drag coefficient for varying Knudsen numbers at two speed ratios: Gaussian closure vs. experimental results.

cylindrical grid, the meshes used at the beginning, middle and end of the the refinement study can be seen in Figure 5.15. Each mesh block contains 80 cells in the radial direction, 20 cells in the angular direction, and 2 cells over the height of the cylinder. Figure 5.14(a) shows the computed drag over the cylinder at each level of refinement, where N denotes the total number of cells in the mesh. The asymptotic behaviour of the drag with increasing refinement level shows that the accuracy of the solver is maintained and effectively becomes independent of mesh size. The experimental drag from Coudeville *et al.* [106] is plotted to show that the computed and experimental drags agree to within 1%. The results of Figure 5.14 provide confidence in the convergence accuracy of the predicted drag coefficients for the cases considered.

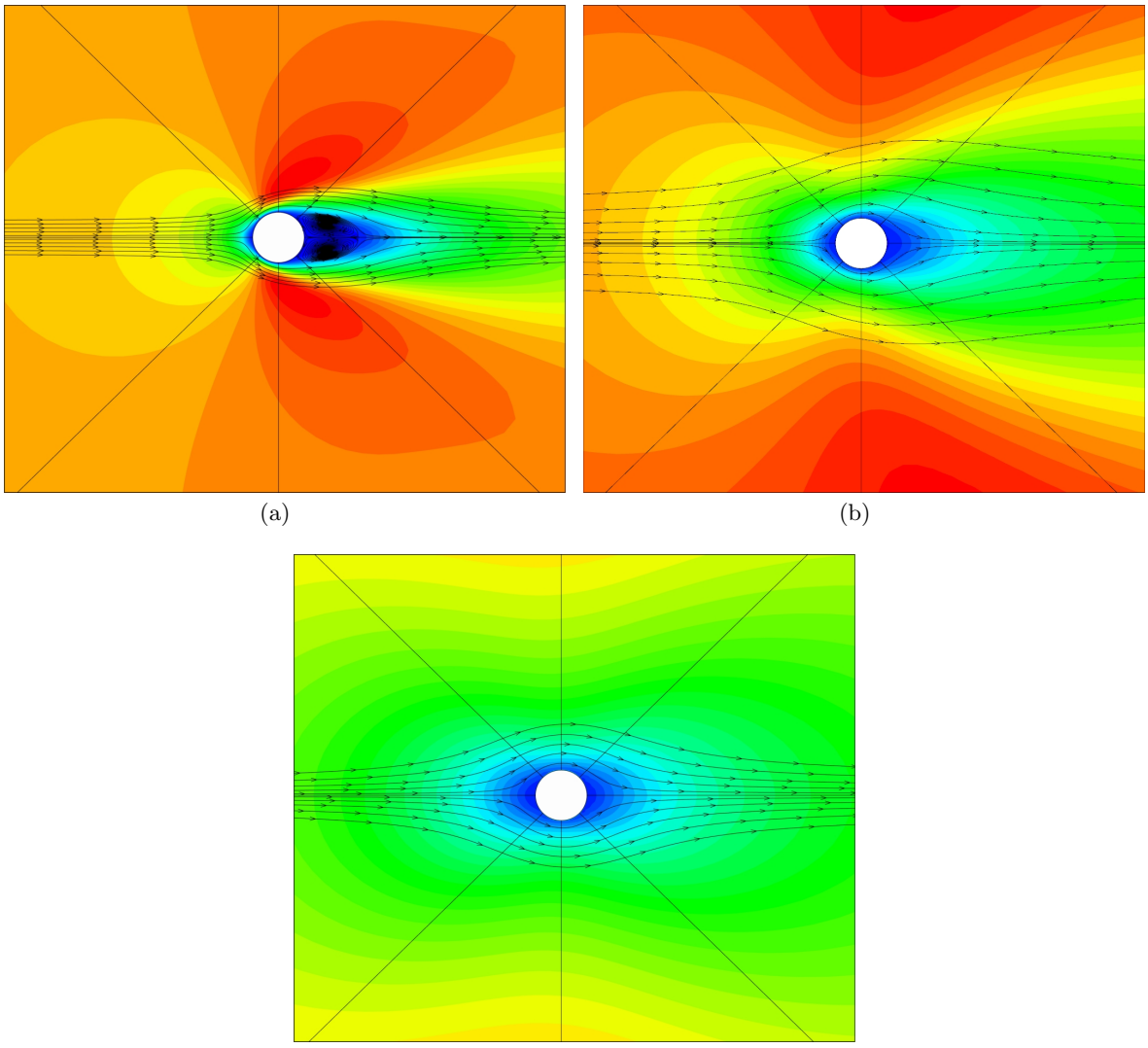

(a) (b)

(c)

Figure 5.12: Comparison of x-directional velocity profiles for immersed cylinder flow at various Knudsen numbers (a) Kn = 0.001, (b) Kn = 0.1, (c) Kn = 1.

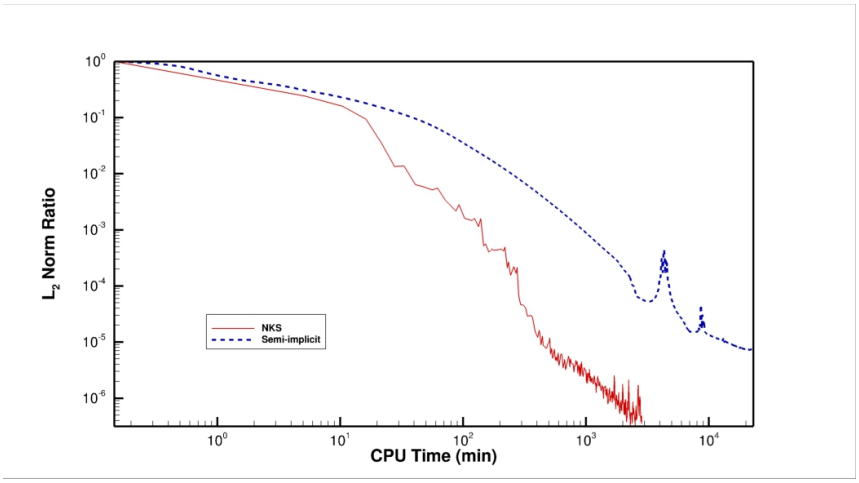

(a)

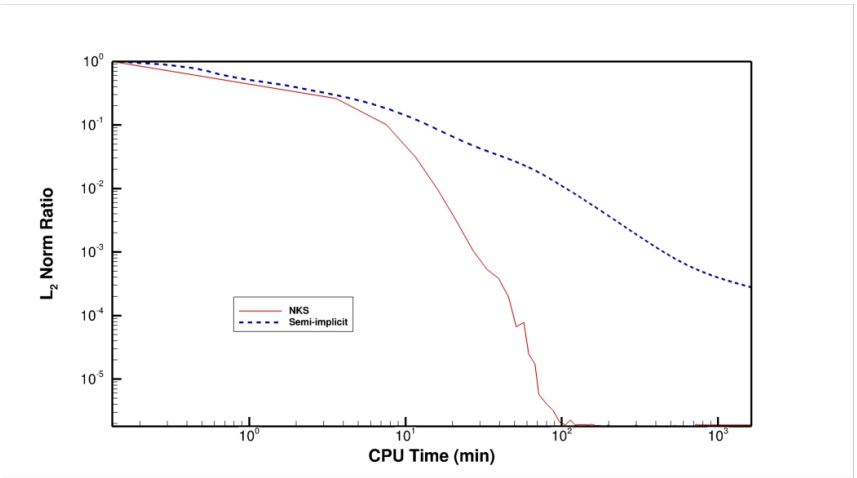

(b)

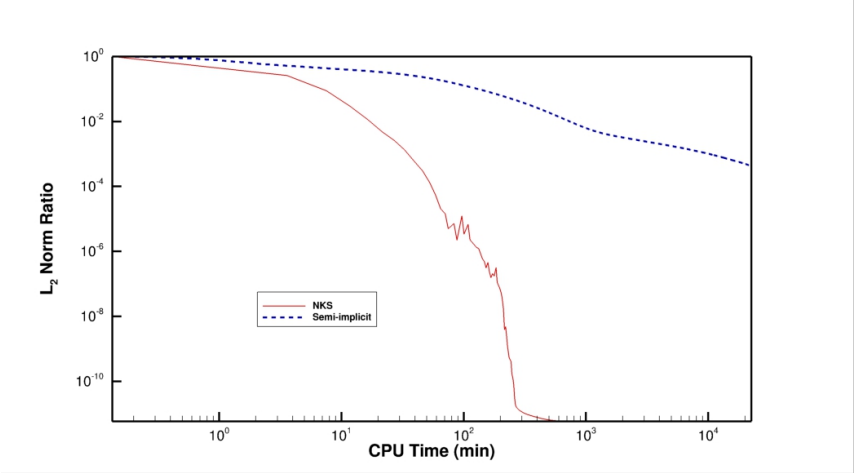

(c)

Figure 5.13: NKS and semi-implicit convergence rates for immersed subsonic flow past a cylinder using the standard Gaussian closure at (a) Kn = 0.001, (b) Kn = 0.1 and (c) Kn = 1, with S = 0.107.

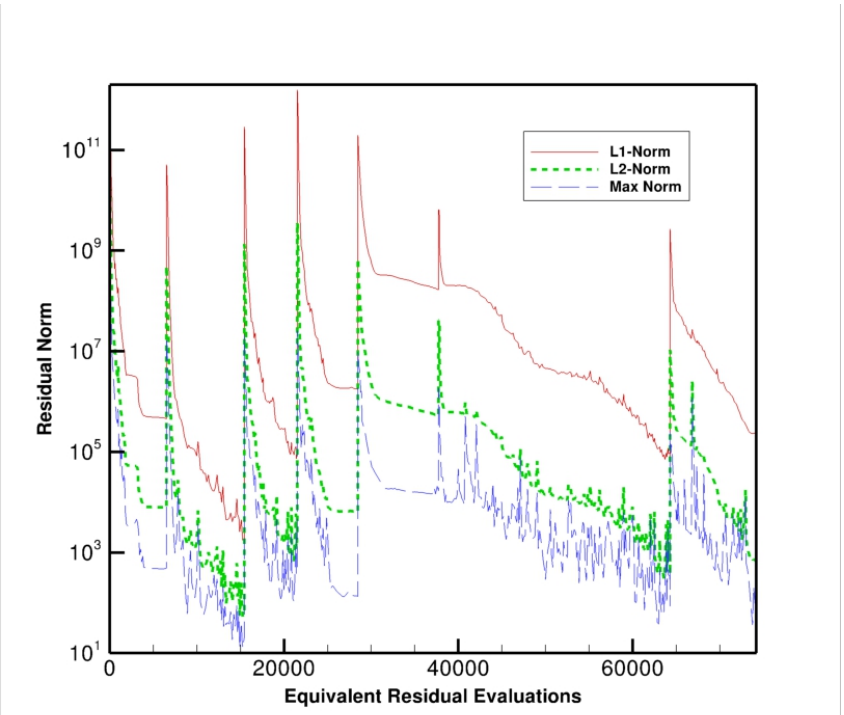

(a)

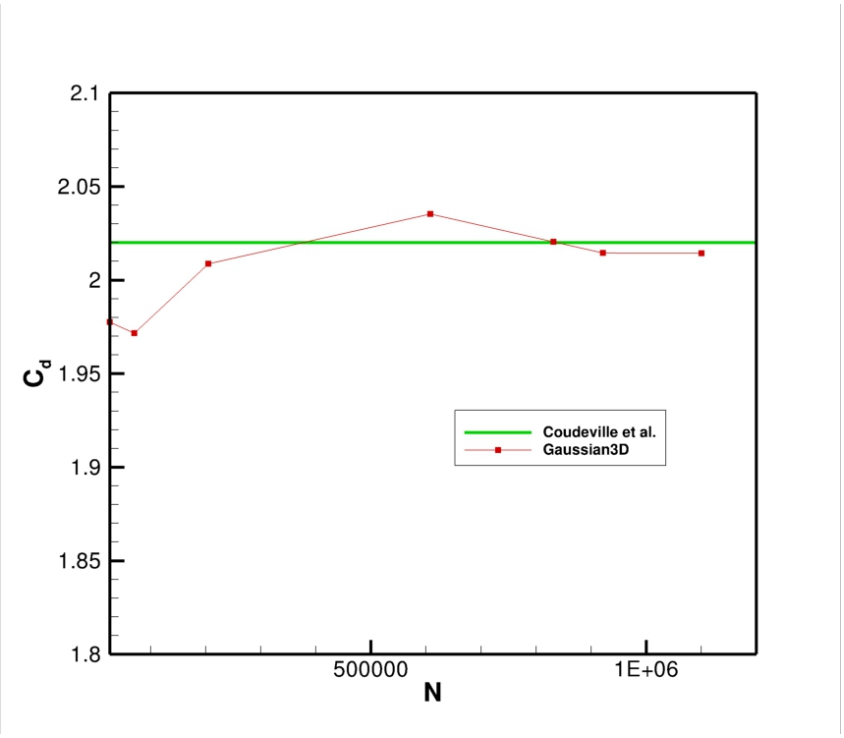

(b)

Figure 5.14: (a) Residual norm convergence over multiple applications of AMR for Kn = 0.01, (b) Drag convergence towards experimental result over the refined grids.

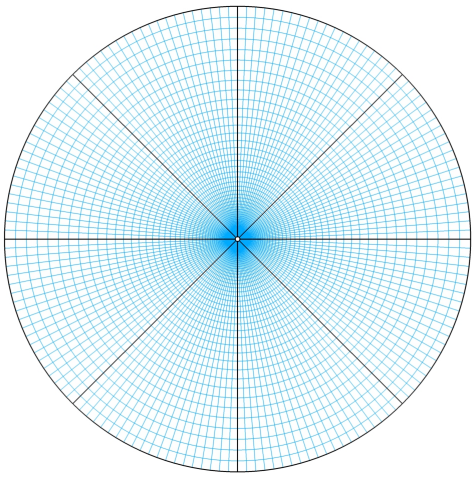

(a) 8 mesh blocks (25,600 cells)

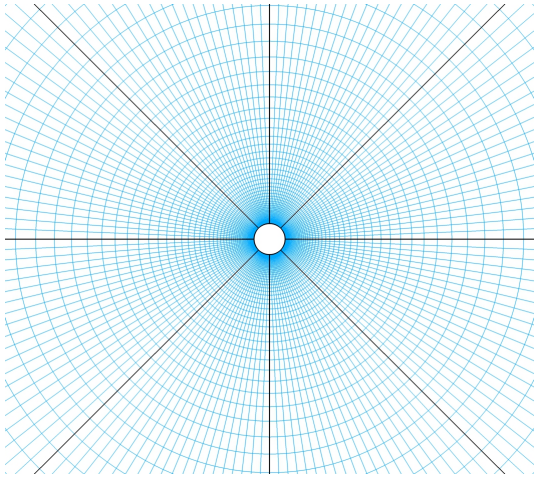

(b) 8 mesh blocks (25,600 cells), magnified

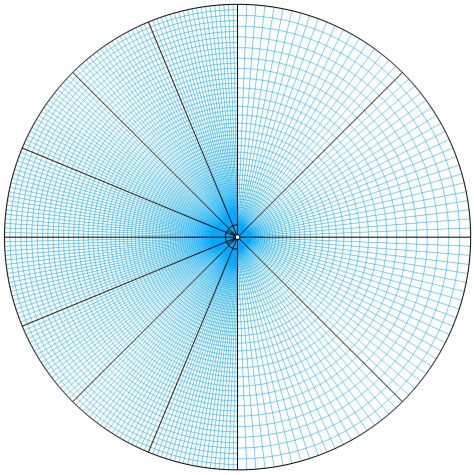

(c) 64 mesh blocks (204,800 cells)

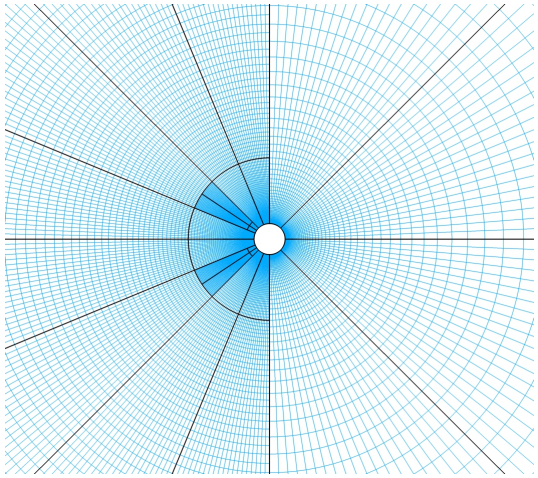

(d) 64 mesh blocks (204,800 cells), magnified

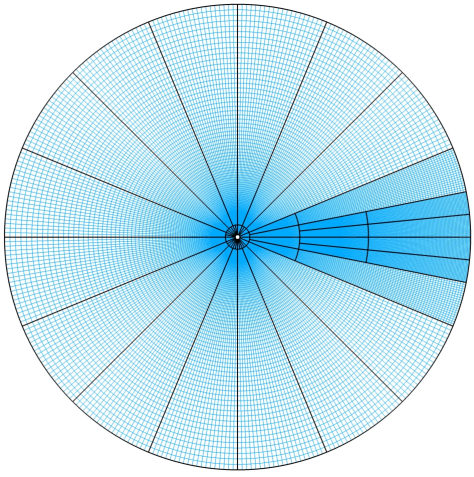

(e) 344 mesh blocks (1,100,800 cells)

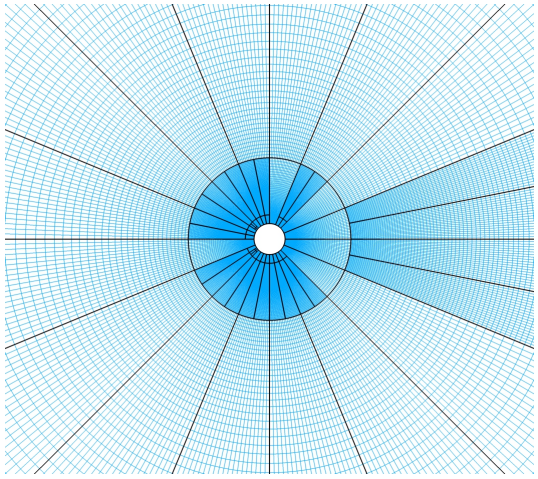

(f) 344 mesh blocks (1,100,800 cells), magnified

Figure 5.15: Sample of refined mesh blocks used for the mesh convergence study of the standard Gaussian closure.

5.6 Subsonic Immersed Flow Past a Sphere

As a final test case, flow past an immersed sphere is investigated next to demonstrate the full three-dimensional capabilities of the Gaussian closure and its solution methods. A comparison is made between the well-established values for sphere drag in low Reynolds number flows with additional considerations for increasingly rarefied flows. For the first flow of interest, the sphere radius was varied from 3.36×10^{-5} to 6.72×10^{-9} m, corresponding to a Knudsen number range of $10^{-3} \leq \text{Kn} \leq 5$ and a Reynolds number range of $1.934 \times 10^{2} \geq \text{Re} \geq 1.934 \times 10^{-1}$ using the sphere diameter as the characteristic length, and is well within the laminar regime and approaching the Stokes flow regime.

The computed Gaussian closure solutions were obtained for air at 288 K at standard atmospheric pressure. The velocity slip boundary conditions were used in all cases. A cubed sphere grid based on the work of Ivan *et al.* [62–65] for MHD flows is used, consisting of 48 blocks with 25,600 cells per block for a grand total of 1,228,800 cells. First introduced for the solution of PDEs by Ronchi *et al.* [108], hexahedral cubed-sphere grids are generated from a projection of a cube onto the surface of a sphere that divides the surface of the sphere into six identical domains. This results in a quasi-uniform grid size over the the entire domain and avoids the two computationally-restrictive poles generated in a latitudinallongitudinal grid system. The cubed-sphere mesh used herein is based on the work of Ivan *et al.* [62–65] as applied towards modelling MHD flow problems. An example of the mesh blocks and cell resolution on the cubed-sphere grid used in this thesis can be seen in Figure 5.16, with a Mach profile of a sample solution at $\text{Kn} = 0.05$ in Figure 5.17. This mesh resolution has provided sufficient accuracy in computing the drag over the sphere.

Figure 5.18 shows the convergence histories of the NKS and semi-implicit solvers applied to immersed subsonic flow past a sphere over a range of Knudsen numbers. Both NKS and semi-implicit solvers were performed over 48 Intel Xeon E5540 cores operating at 2.53 GHz. A total of 100 Newton iterations were performed for each flow problem. The NKS method clearly shows its ability to reach high levels of convergence with much better convergence rates than those from the semi-implicit solver. The small time steps required for stability in the semi-implicit method is again found to be a significant hindrance in acquiring suitably converged solutions in moderate Knudsen numbers. The CFL parameters and resulting computation times for both methods can be found in Table 5.3, where the total physical time required for the NKS method across all Knudsen numbers is orders of magnitude less than that required for the the semi-implicit method, while still reaching highly converged solutions.

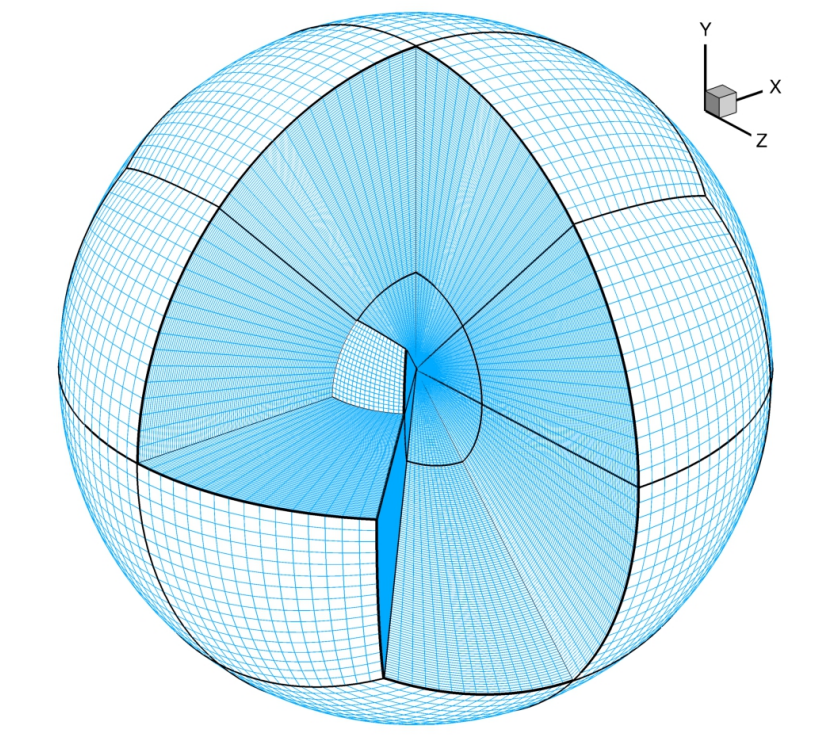

(a)

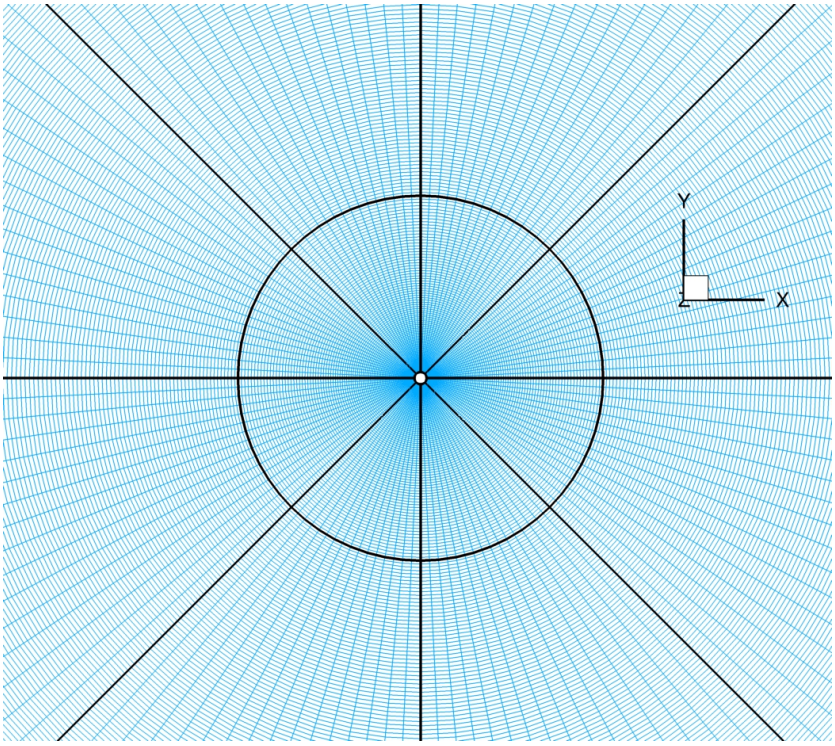

(b)

Figure 5.16: (a) A cutaway view of the 48 mesh blocks used for immersed flow over a sphere in the continuum regime, with one block illustrating the mesh density within each block, (b) Cell density on the XY-plane centered on the sphere surface.

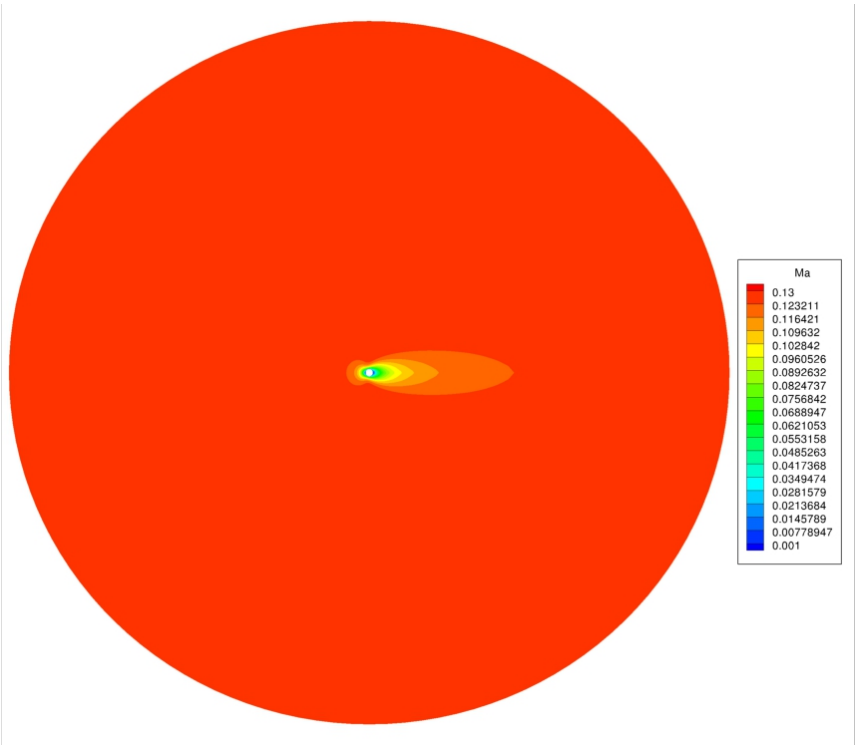

Figure 5.17: Sample result Mach number profile for Kn = 0.05.

	NKS				Semi-Implicit		
Kn	Initial CFL	Final CFL	Time (min)	L2-norm Ratio	CFL	Time (min)	L2-norm Ratio
0.001	1×10^{1}	1×10^{6}	105.6	1.6597×10^{-9}	0.1	2509.79	2.250×10^{-7}
0.05	1×10^{1}	1×10^{6}	80.69	1.19477×10^{-9}	0.1	2523.58	4.650×10^{-7}
1	1×10^{0}	1×10^{1}	59.15	2.83057×10^{-4}	0.05	1616.30	3.613×10^{-5}

Table 5.3: Summary of NKS/semi-implicit CFL parameters and computation times for the flow problems performed in Figure 5.18.

The variation of the sphere drag coefficient with respect to the Reynolds number is shown in Figure 5.19(a). Experimental data for sphere drag, such as those by Roos and Willmarth [109] and Liebster [110], and an analytical solution given by Flemmer and Banks [111], are shown here and are largely focussed on its variance with respect to the Reynolds number. Low Reynolds number flows are typically achieved in the experiments by increasing the fluid viscosity and/or lowering the free stream velocity, whereas low Reynolds number flows performed with the Gaussian closure here were achieved through a decrease in the sphere diameter only. The result is that while the range of Reynolds numbers between the sets of data remains comparable, the Gaussian closure results are subject to varying Knudsen numbers, whereas the experimental and analytical results remain firmly in the continuum regime. Noting the lines demarking

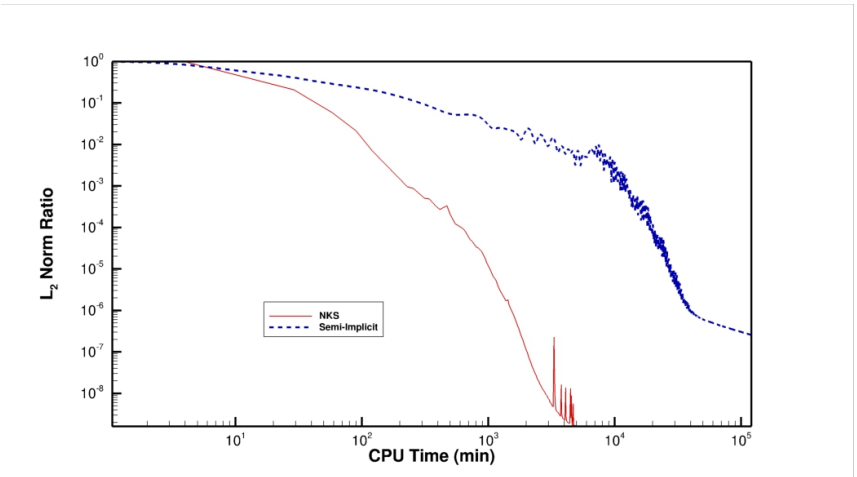

(a)

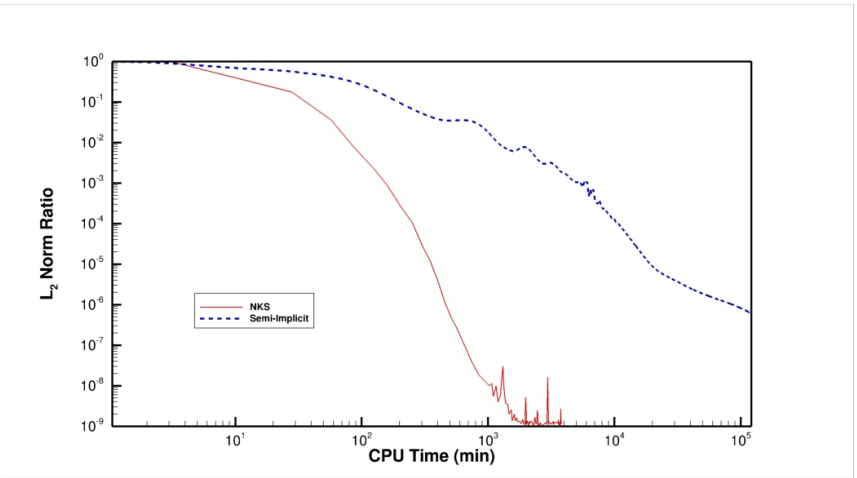

(b)

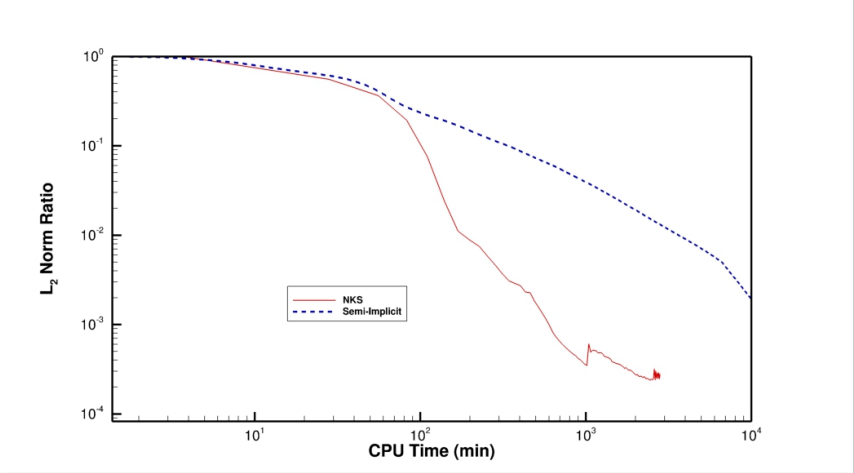

(c)

Figure 5.18: NKS and semi-implicit convergence rates for immersed subsonic flow past a sphere using the standard Gaussian closure at (a) Kn = 0.001, (b) Kn = 0.05 and (c) Kn = 1

the Knudsen number ranges for the Gaussian closure in Figure 5.19(a), the predicted drag begins to deviate from the experimental results at the lower limits of the free molecular range at about Kn = 1 due to the increased rarefication of the gas. The data comparison shown in Figure 5.19(a) is therefore more suited to showing that the Gaussian closure is capable of reproducing the continuum-type drag behaviour predicted by experimental and analytical results, and that non-continuum effects are responsible for skewing the drag coefficient away from the low Reynolds number, continuum-based near-Stokes solution.

Experimental results accounting for the rarefication of the flow over the sphere can be extracted from the oil droplet experiments of Millikan [112, 113] originally used to measure the elemental charge, with corrections by Allen and Raabe [114] using more updated values for the viscosity of air. The terminal velocity of oil droplets of varying size were measured in air with and without the presence of an electric field. Without the electric field, the terminal velocity can be directly related to the drag forces acting on the oil droplet. The advantage of comparing the Gaussian closure results to this data set is that, due to the extensive amount of recorded data by Millikan for each droplet, the computational parameters can be set such that the Knudsen and Reynolds numbers match, ensuring that neither one is affected disproportionally due to differences in rarefication. The range of Knudsen numbers covered by the investigated droplets in these experiments extend from the slip regime (Kn = 0.01) to the free molecular regime (Kn = 95). The Reynolds numbers are on the order of Re $\approx 10^{-4}$, sufficiently small to ensure Stokes flow. The Gaussian closure is used here to model a portion of these experiments, though computational convergence is difficult to achieve beyond Kn = 1. However, judging from the breakdown of the equation set in this flow regime illustrated in the above study on cylinder drags, any results gleamed from the equations in this high Knudsen number range are not expected to be in complete accordance with the experimental results.

Millikan introduced a correction factor to the Stokes sphere drag solution similar to the analytical sphere drag correction by Cunningham [115] to account for the non-continuum effects on successively smaller oil droplets and their impact on the measured drag. This factor, f_{Kn}, can be found experimentally as the ratio between the measured drag, f_{drag}, and the analytical drag predicted from Stokes flow, f_{Stokes}, and by extension is equivalent to the ratio between their respective drag coefficients. A plot of this ratio with varying Knudsen number for both the experimental and computational results with the Gaussian closure can be seen in Figure 5.19(b). The low Mach numbers and small density gradients in these flows has been found to lower the overall convergence rate of the NKS scheme, but residuals in these results shown here are on the order of at least 10^{-6} after each mesh refinement. The drag ratios from the Gaussian closure match well with the experimental results for Kn < 0.1, with an overestimation for higher

Knudsen numbers. The breakdown of the equations in this Knudsen number range is comparable to results found from a similar study on rarefied Stokes flow by Torrilhon [116], except that without the presence of heat transfer terms the calculated drag overestimates, rather than underestimates, the experimental drag. The lack of suppression on the growth of the boundary layer causing an overestimation of the drag was also seen in the study on cylinder drag outlined earlier. However, the Gaussian closure is still able to model the overall decreasing trend in the drag ratio, whereas the usual Navier-Stokes solution is firmly grounded in the continuum regime and will always return the Stokes drag (i.e., $f_{\mathrm{Kn}} = f_{\mathrm{drag}}/f_{\mathrm{Stokes}}$=1).

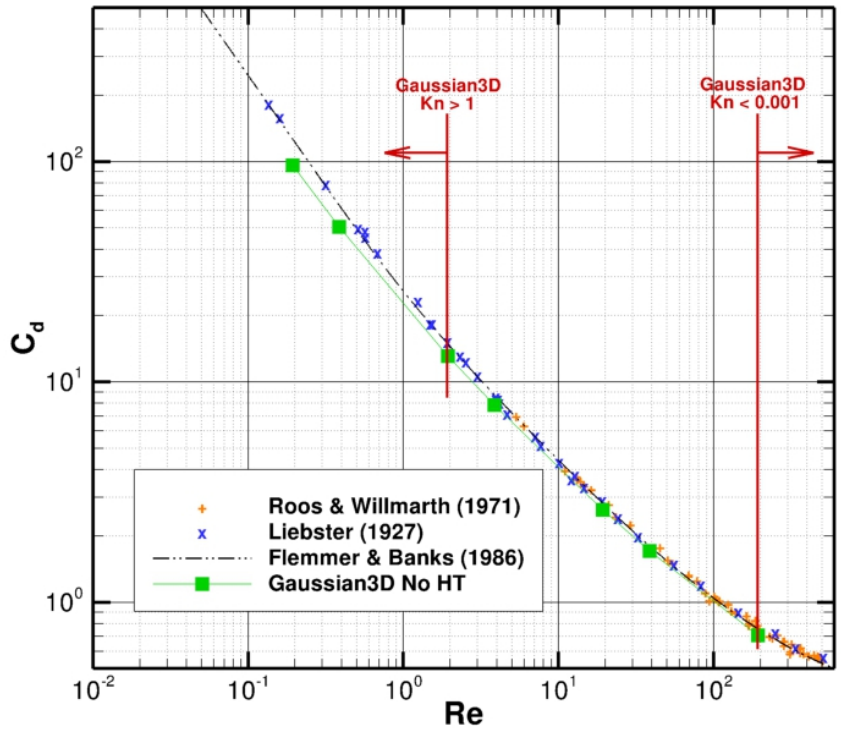

(a)

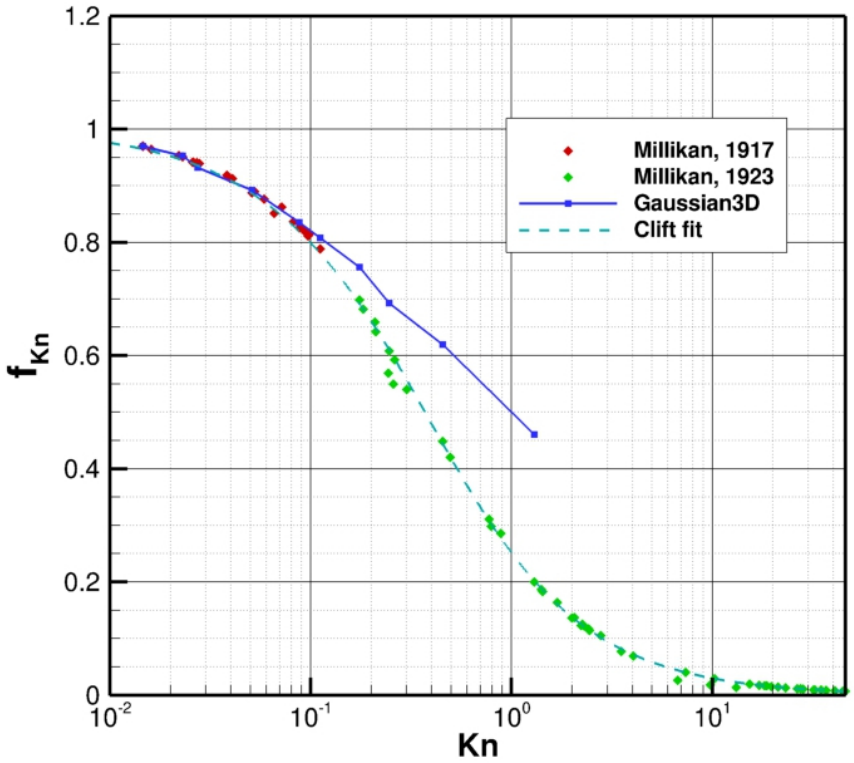

(b)

Figure 5.19: (a) Drag coefficient over a sphere: Gaussian closure vs. experimental and analytical results, (b) Stokes drag correction factor with varying Knudsen number for experimental results by Millikan [112, 113], and some corresponding data points using the Gaussian closure.

Chapter 6

Three-Dimensional Numerical Results for the Regularized Gaussian Closure

6.1 Overview

The Gaussian closure in its original form is well-adapted to modelling flows in the continuum regime as well as the velocity slip phenomenon present at moderate Knudsen numbers. While the velocity slip is modelled correctly even at high Knudsen numbers, as demonstrated in the microscale Couette flow problem, the overall performance of the closure is unable to accurately model the drag on a cylinder and sphere at comparable Knudsen numbers. This suggests that non-equilibrium drag is dependent not only on velocity slip, and that the Gaussian closure as is does not account for this phenomenon. McDonald and Groth [16] have shown that incorporating the effects of heat flux into the Gaussian closure drastically improves the predictive abilities of the closure for flow over a NACA0012 micro-airfoil and microscale cylinder. Heat transfer in non-equilibrium flow is therefore non-negligible, and its inclusion into the Gaussian closure via regularization as described in Section 2.4 of Chapter 2 should offer substantial improvements.

The improved predictive capabilities of the regularized Gaussian closure are illustrated here in a number of flow problems dedicated to evaluating non-equilibrium heat transfer effects for both monatomic and diatomic gases. The numerical predictions are compared to available analytical solutions, experimental data, and previous numerical solutions where applicable. Using the method of manufactured solutions, the second-order spatial accuracy of the solution scheme

applied to the regularized Gaussian closure is also evaluated. In addition to the velocity slip boundary conditions discussed in Section 2.5.1 of Chapter 2, the temperature slip boundary conditions from Section 2.5.2 are also applied for all flow problems discussed in this chapter. The performance of the temperature slip boundary conditions are evaluated through the energy transfer between two heated plates, and in conjunction with the velocity slip boundary conditions in pressure-driven Poiseuille flow and a lid-driven cavity. Immersed subsonic flow over a cylinder and sphere is also revisited with the regularized closure to observe changes due to the inclusion of the heat transfer terms.

6.2 Manufactured Solution

The method of manufactured solutions as described in Section 5.2 of Chapter 5 is used once again to ensure that the addition of regularized terms in the Gaussian closure does not degrade the second-order spatial accuracy in the proposed finite-volume scheme. The method follows closely that described in Section 5.2 with modifications to the residual vector accounting for the elliptic heat flux terms within the regularized Gaussian closure. The prescribed components of the regularized Gaussian solution were again set to be dependent only on the spatial coordinates, and are taken to be

$$\begin{aligned}
\rho &= 2 + \sin(x+y), \\
u_x &= \cos(x+y), \\
u_y &= \sin(x-y), \\
u_z &= 0, \\
P_{xx} &= 3 - \sin(x+y), \\
P_{xy} &= \sin(y-x), \\
P_{xz} &= 0, \\
P_{yy} &= 3 + \cos(x+y), \\
P_{yz} &= 0, \\
P_{zz} &= 3 + \cos(-x-y),
\end{aligned}$$

where the heat flux vector, Q_{ijk}, was evaluated by analytically taking derivatives of the solution state quantities given above. The residual vector associated with the chosen analytical solution defined initially in Eq. (5.2) was modified to include the elliptic heat flux terms created in the

regularized procedure, such that

$$\widehat{\mathbf{R}} = \frac{\partial \widehat{\mathbf{U}}}{\partial t} + \frac{\partial}{\partial x}(\mathbf{F}(\widehat{\mathbf{U}}) + \mathbf{F_e}(\widehat{\mathbf{U}})) + \frac{\partial}{\partial y}(\mathbf{G}(\widehat{\mathbf{U}}) + \mathbf{G_e}(\widehat{\mathbf{U}})) + \frac{\partial}{\partial z}(\mathbf{H}(\widehat{\mathbf{U}}) + \mathbf{H_e}(\widehat{\mathbf{U}})) - \mathbf{S}(\widehat{\mathbf{U}}) \quad (6.1)$$

where $\mathbf{F_e}$, $\mathbf{G_e}$, and $\mathbf{H_e}$ represent the elliptic heat transfer terms in the $x-$, $y-$, and $z-$ directions respectively. These are defined in terms of the heat flux tensor Q_{ijk} and have the form

$$\mathbf{F_e} = \begin{bmatrix} 0 \\ 0 \\ 0 \\ 0 \\ Q_{xxx} \\ Q_{xyx} \\ Q_{xzx} \\ Q_{yyx} \\ Q_{yzx} \\ Q_{zzx} \\ 0 \end{bmatrix}, \quad \mathbf{G_e} = \begin{bmatrix} 0 \\ 0 \\ 0 \\ 0 \\ Q_{xxy} \\ Q_{xyy} \\ Q_{xzy} \\ Q_{yyy} \\ Q_{yzy} \\ Q_{zzy} \\ 0 \end{bmatrix}, \quad \mathbf{H_e} = \begin{bmatrix} 0 \\ 0 \\ 0 \\ 0 \\ Q_{xxz} \\ Q_{xyz} \\ Q_{xzz} \\ Q_{yyz} \\ Q_{yzz} \\ Q_{zzz} \\ 0 \end{bmatrix}. \quad (6.2)$$

It must be noted that while Q_{ijk} is symmetric and contains at most ten unique terms, these terms are differentiated over different spatial axes, necessitating a full evaluation of all eighteen terms.

Four hierarchical grids were again used based on consecutive uniform refinements of an initially coarse mesh for a concentric cylindrical domain with interior and exterior radii of 0.5 m and 1.0 m, respectively, and a height of 1.0 m. Beginning with an 8-block description, three consecutive mesh refinements were performed with a grid converged solution acquired at each level of refinement. The mesh resolution of these grids can be found in Section 5.2 of Chapter 5, with the NKS convergence level and computation time incorporating the heat transfer effects from the regularized Gaussian closure can be found in Table 6.1. A total of 200 Newton iterations were performed on each mesh. A sample convergence history can be found in Figure 6.1 for the cylinder mesh containing 512 computational blocks.

The regularized Gaussian closure performs similarly to the original Gaussian closure in terms of convergence rate. The error norms for the regularized Gaussian closure can be found in Figure 6.2. The characteristics of a second-order spatially accurate scheme are once again reproduced and provides verification of the discretization of the elliptic terms associated with heat transfer in the regularized Gaussian closure.

Refinement Level	Blocks	Cells	Mesh Points	Processors	L_2 Norm	Time (min)
0	8	8192	9.7920×10^3	8	9.93232×10^{-12}	5.8
1	64	65536	4.2931×10^6	64	5.07717×10^{-11}	7.436
2	512	524288	2.1538×10^9	256	4.52045×10^{-10}	21.39
3	4096	4194304	1.0999×10^{12}	512	2.51864×10^{-5}	115.3

Table 6.1: Properties of four cylinder grids used in the method of manufactured solutions using the regularized Gaussian closure.

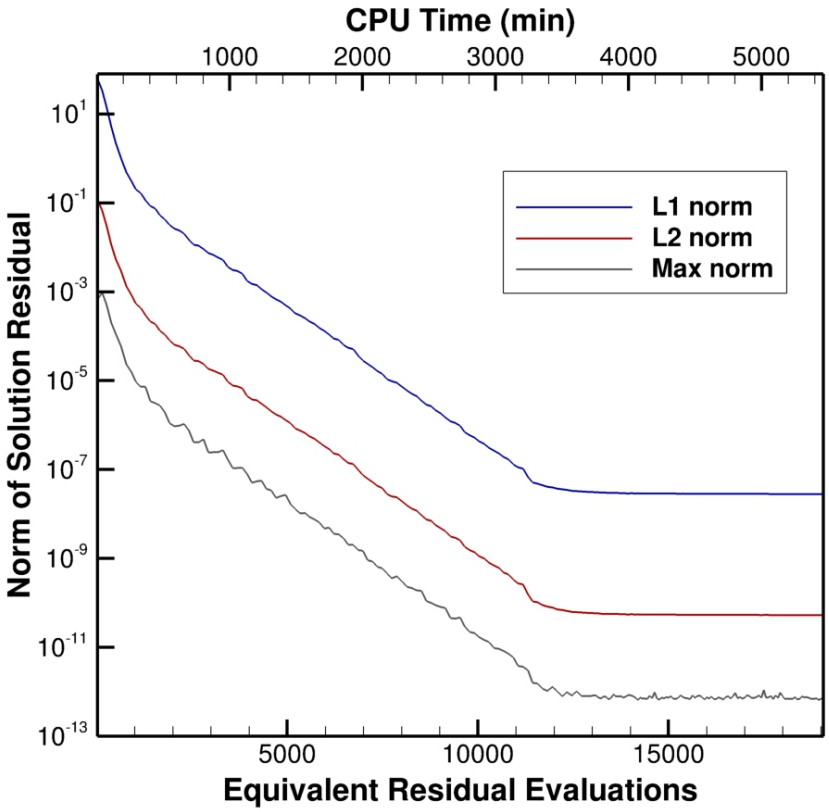

Figure 6.1: L_1, L_2, and max error norms based on the solution residual for the manufactured solution problem with heat transfer containing 512 computational blocks performed on 256 processors.

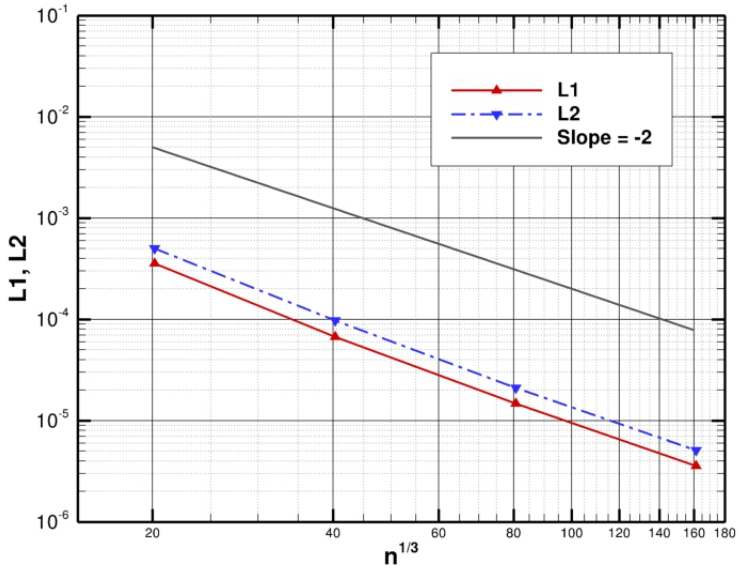

Figure 6.2: Predicted L_1, L_2 and L_∞ error norms for the manufactured solution problem with increasing mesh densities using the regularized Gaussian closure for a monatomic gas.

6.3 Energy Transfer Between Heated Plates

The regularized moment closure in combination with the slip flow boundary conditions described above have been used to model the temperature profile between two heated infinite plates over a wide range of Knudsen numbers. Argon initially at 300 K and standard pressure is placed between two isothermal plates oriented in the $x-$direction with $T_L = 290$ K and $T_R = 310$ K, separated by a distance ranging from 7.05973×10^{-4} to 7.05973×10^{-9} m (defining the characteristic length of this problem) corresponding to $10^{-4} \leq \mathrm{Kn} \leq 10$. The computational mesh can be seen in Figure 6.3, and consists of a total of 200 cells in the $x-$direction and 6 cells each in the transverse directions. The temperature profile between the plates is shown in Figure 6.4. The temperature slip phenomenon is clearly visible entering the transition regime at $\mathrm{Kn} = 0.1$ and continues well into the free molecular regime. Figure 6.5 shows the calculated normalized wall temperature at the high temperature wall and the normalized heat flux calculated between the plates. In Figure 6.5(a), the temperature is normalized using the expression

$$T^* = \frac{T - T_m}{T_w - T_m} \tag{6.3}$$

where T^* is the normalized temperature, T_m is the temperature of the gas midway between the plates, T_w is the temperature of the wall, and T is the measured temperature of the gas at

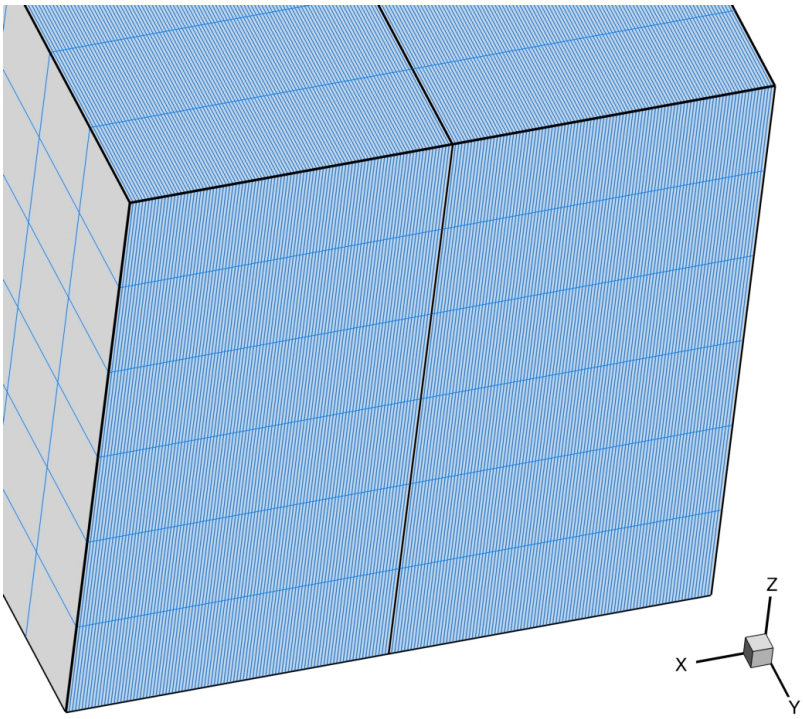

Figure 6.3: The two mesh blocks used for temperature profile calculations between two heated plates in the $x-$direction.

the wall. The figure clearly shows the temperature slip effect with increasing Knudsen number which is not captured by the Navier-Stokes. These results can be captured using the boundary conditions described in Section 2.5.2 of Chapter 2 based on work by Smoluchowski [53]. Figure 6.5(b) shows the variation of the normalized heat flux with increasing Knudsen number. The heat flux is normalized to the free molecular heat flux, q_{fm}, given by Bird [104] as

$$q_{fm} = -\rho\,(2R)^{\frac{3}{2}} \left(\frac{T_U T_L}{\pi}\right)^{\frac{1}{2}} \left(T_U^{\frac{1}{2}} - T_L^{\frac{1}{2}}\right) \tag{6.4}$$

where T_U and T_L are the temperatures of the upper and lower plate at 310 K and 290 K, respectively, and R is the specific gas constant. As discussed in Section 5.3 of Chapter 5, the lack of interparticle collisions and fully accommodated collisions at the walls produce a non-equilibrium distribution for the gas between the plates of a Couette flow that is independent of the plate separation. For the problem of heat transfer between two plates in the free-molecular flow regime, it can be shown that the heat flux between the plates has a non-zero constant value given by Eq. (6.4) above, even though the expected gas temperature between the plates is uniform and constant [104]. The heat flux between the plates in this case is produced by the energy transfer occuring at the walls as dictated by the fluxes of incoming particles arriving

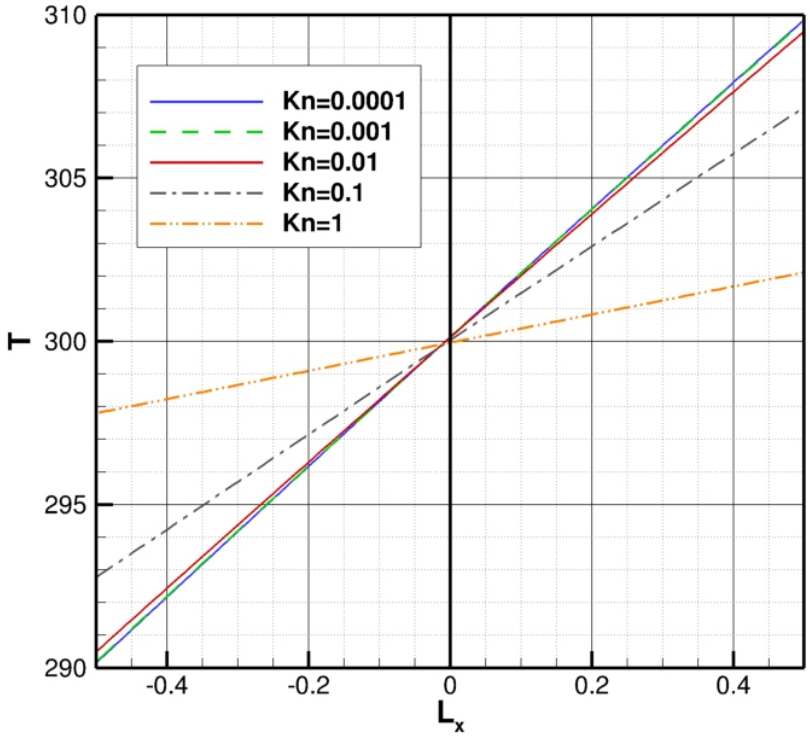

Figure 6.4: Temperature distribution between two isothermal walls over the non-dimensionalized wall separation distance L_x for a range of Knudsen numbers, with $L_x = 0$ designating the centerline between the plates.

directly from the upper and lower walls, respectively. The Gaussian closure with temperature slip boundary conditions predicts a heat flux in line with those of the Navier-Stokes in the continuum limit, and smoothly transitions to the perfect temperature slip characterized by the free-molecular limit with increasing Knudsen number. Similar to the previous Couette flow results for the velocity slip boundary conditions of the original Gaussian closure, the results for heat transfer between the heated plates of Figure 6.5 provide some confidence in the accuracy of the boundary conditions for temperature slip.

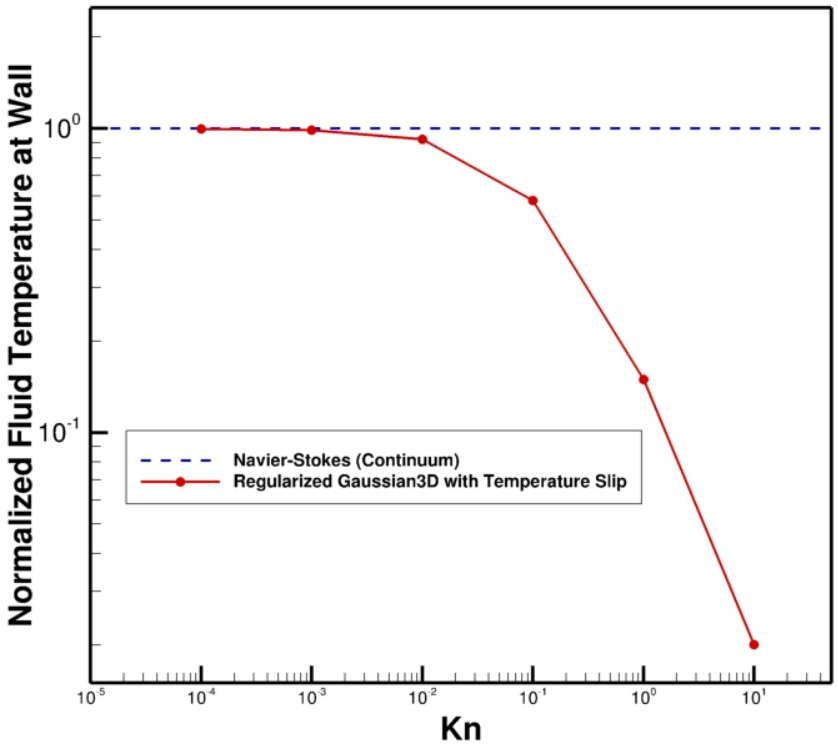

(a)

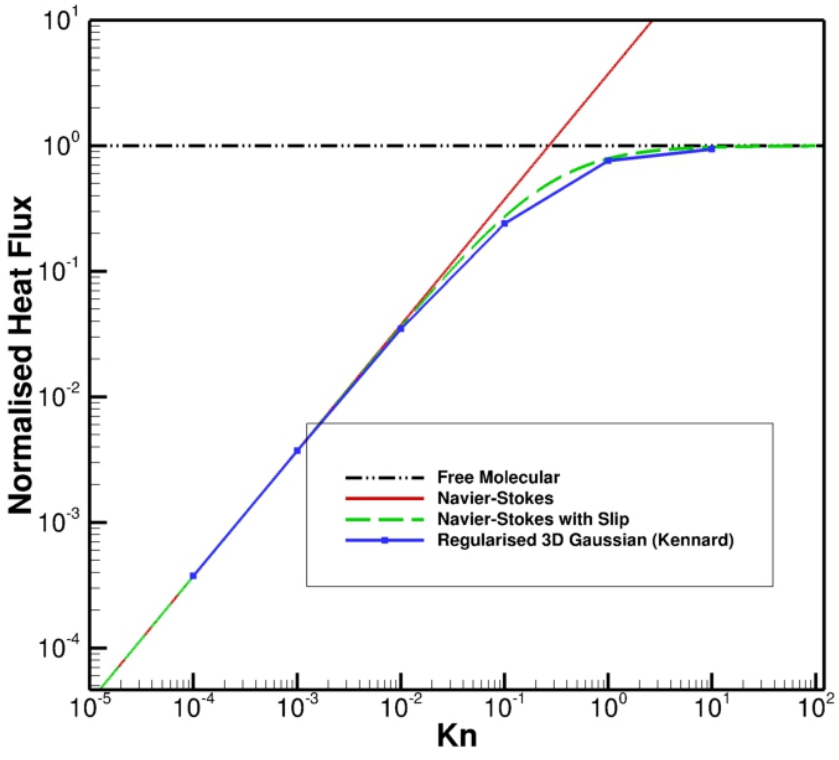

(b)

Figure 6.5: (a) Change in normalized temperature at the heated wall with increasing Knudsen number, (b) Heat flux between the plates normalized to the free-molecular solution.

6.4 Pressure-Driven Poiseuille Flow

Pressure-driven Poiseuille flows form a fundamental part of various microchannel flows commonly found in MEMS devices, and is also of interest in the study of fluid transport in animal physiology. Continuum Poiseuille flow has been well studied both analytically and experimentally, but the difficulties in acquiring accurate physical data in the rarefied regime has led to a significant lack of study of Poiseuille flow in this regime, especially in matters concerning thermal transport. It has been well established that thermal properties seen on the continuum level are not representative of those seen in rarefied flows, such as the presence of heat fluxes not enforced by a temperature gradient.

The properties of moderate Knudsen number Poiseuille flows have been investigated analytically by Taheri *et al.* [117] using the regularized 13-moment equations of Struchtrup and Torrilhon [21] and John *et al.* [118] using DSMC. One of the most interesting features of this flow is the formation of a dip in the heat flux profile coinciding with the centerline of the channel in the slip and transition regimes. This phenomenon was established analytically in literature by Tij and Santos [119] and Aoki *et al.* [120], and has been replicated by the regularized 13-moment equations and DSMC. Using the regularized Gaussian closure, pressure-driven Poiseuille flows are studied to show the capabilities of this closure under the effects of both temperature and velocity slip, aiming to reproduce the bimodal heat flux profile shown in earlier computational and analytical studies.

The initial conditions and flow geometry follow closely with those performed by John *et al.* [118]. A pressure-driven Poiseuille flow over a channel with an aspect ratio of $L/H = 5$ is studied here. Similar to the problem described earlier regarding the energy transfer between two parallel plates, argon initially at 300 K and standard pressure is placed between two isothermal plates oriented in the $x-$direction, separated by a distance ranging from 7.05973×10^{-5} to 1.41195×10^{-7} m (defining the characteristic length of this problem) corresponding to $10^{-3} \leq \mathrm{Kn} \leq 0.5$. The inlet pressure, P_i, inlet temperature, T_i, and the outlet pressure, P_o, are specified, with the wall temperature, T_w, and inlet temperature set to a reference temperature, T_0, such that $T_0 = T_w = T_i = 273\,\mathrm{K}$. Of interest is the tangential heat flux distribution across the channel height. This heat flux is non-dimensionalized against a reference heat flux, $q_0 = \mu R T_0/H$. A pressure ratio, $p' = P_i/P_o$, is defined to study the effect of the pressure gradient on the development of the heat flux profile. Values of $p' = 1.5$ and $p' = 2.0$ are studied here. For comparison purposes with the DSMC data, the heat flux profile is measured at a distance $2L/3$ from the entrance of the channel. The computational mesh uses 120 cells across the height of the channel to provide a reasonable resolution to the final results, and the complete mesh

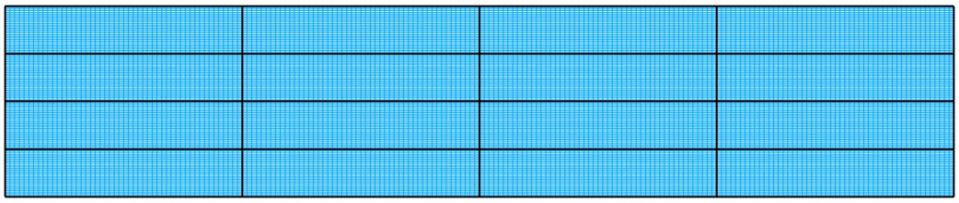

(a)

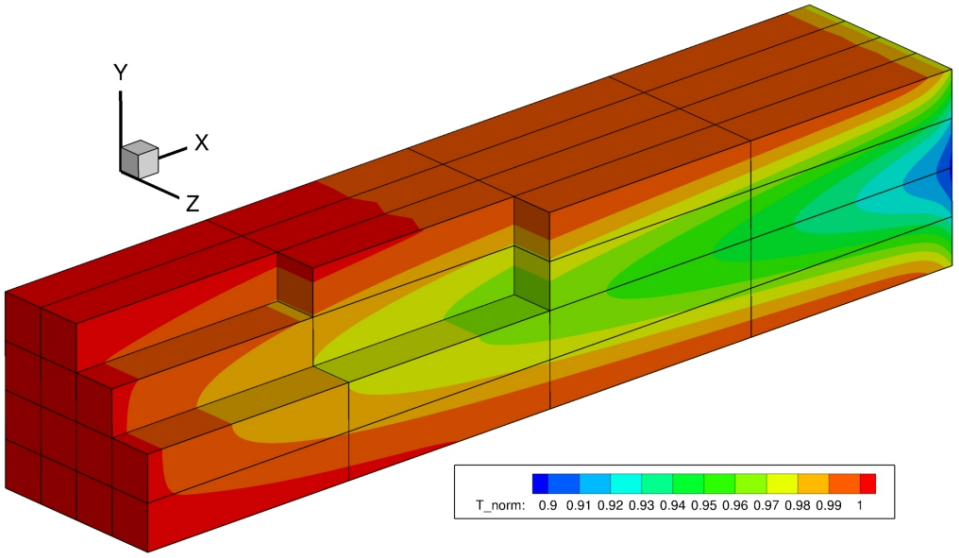

(b)

Figure 6.6: (a) Poiseuille flow mesh blocks in the XY-plane, and (b) a cutaway view of the mesh blocks with temperature contours for Kn = 0.025 and $p' = 2.0$.

contains 192,000 cells. Using the NKS algorithm, the L_2-norm residual has been reduced by up to at least six orders of magnitude. The computational mesh and a sample solution result for the Poiseuille flow problem is given in Figure 6.6.

The regularized Gaussian closure and the Navier-Stokes equations are first applied to the Poiseuille flow problem in the continuum regime with Kn = 0.001 at $p' = 1.5$, where the characteristic length is defined as the height of the channel. Figures 6.7 and 6.8 show the overall Mach number and temperature profiles compared to an equivalent flow problem solved using the Navier-Stokes equations. The Mach and temperature profiles generated by the regularized Gaussian closure are in good agreement with those from the Navier-Stokes, and shows that the closure system is capable of replicating the continuum-limit behaviour of the Poiseuille flow problem. Figure 6.9 shows the non-dimensionalized temperature, normal and transverse heat flux, and Mach number predicted from both the regularized Gaussian closure and the Navier-Stokes equations measured at 2/3 of the total channel length from the entrance of the channel.

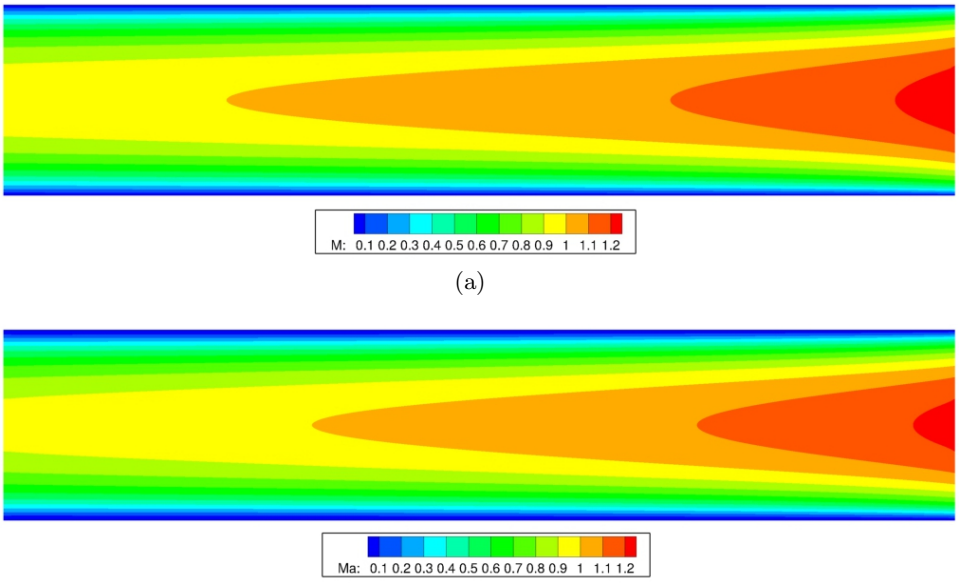

Figure 6.7: Mach number contours for Poiseuille flow, Kn = 0.001 and $p' = 1.5$ using (a) Navier-Stokes, and (b) regularized Gaussian closure

It is evident that, in the continuum regime, the regularized Gaussian closure performs well in predicting the Mach and temperature profiles, and does a reasonably good job in predicting the centerline heat fluxes. The heat flux as measured in the near-wall region leaves much to be desired. While the overall trends in heat flux generated by viscous effects at the wall are present, the regularized Gaussian closure tends to overpredict these trends. The slip temperature boundary conditions, though designed to provide the proper no-slip temperature in the continuum regime, may be insufficient in describing the full range of heat transfer phenomena that occur in the near wall regime.

The heat flux profiles obtained using the regularized Gaussian closure are compared with those from the above-mentioned DSMC analysis of John *et al.* [118] and the Navier-Stokes equations in Figure 6.10 and 6.11. The bimodal heat flux distribution is most pronounced within the early slip regime and transition regime, and is shown to occur using both DSMC and the regularized Gaussian closure. There is a distinct and general increase in magnitude for the heat flux predicted by the Gaussian closure, and a sharp reversal of the heat flux at the boundaries, while the shape of the profile is largely in agreement. Recall that the boundary conditions implemented by the Gaussian closure places no restrictions on heat flux, and the temperature slip phenomenon is modelled purely through an analytical expression, which in turn returns corrected values for the shear stress at the boundary. However, the construction of temperature

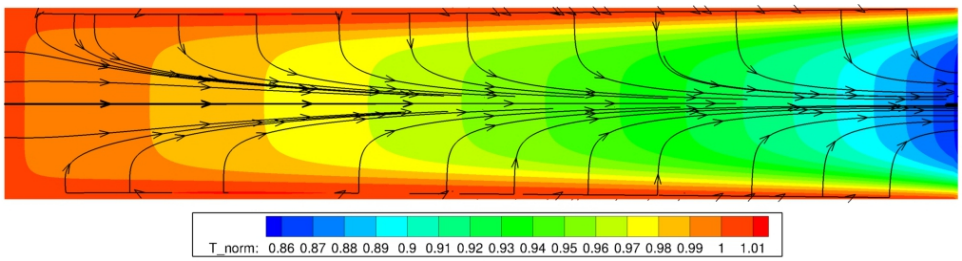

(a)

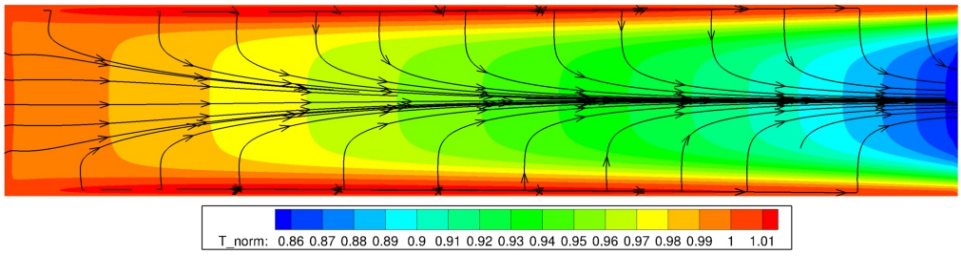

(b)

Figure 6.8: Non-dimensionalized temperature with heat flux contours for Poiseuille flow, Kn = 0.001 and $p' = 1.5$ using (a) Navier-Stokes, and (b) regularized Gaussian closure

slip boundary conditions in this manner assumes that the thermal Knudsen layer at the wall is infinitesimally thin, an assumption that carries heavy consequences with increasingly rarefied flows. From Figure 6.10 and 6.11, aside from the known physical accuracy of the DSMC method, this heat flux reversal occurs within the first few interior cells and is indicative of inadequate boundary conditions. This large shift in heat flux at the boundaries most likely effects the overall predicted heat flux in the channel and acts to increase the heat flux, shown in the figure as a shift to the left. Even with these deficiencies, it is encouraging to note that the general shape of the profile and its bimodal characteristics can be reproduced with the regularized Gaussian closure, along with its evolution with increasing Knudsen number. The pronounced bimodal profile from an increase in the pressure ratio is also properly modelled by the regularized closure. The detrimental effects of the no-slip boundary conditions in the Navier-Stokes solution become evident with increasing Knudsen number. The boundary layer that forms from the walls dominates the entire channel height and prevents particles from migrating towards the low pressure end of the channel, significantly reducing the flow velocity, temperature gradient, and transverse heat transfer. Even for a mildly rarefied flow at Kn = 0.025 the measured transverse heat flux is nearly non-existent and is independent of increasing rarefaction or pressure gradient, caused in part by this backlog of particles forming the boundary layer at the walls.

It is interesting to note that the regularized Gaussian closure maintains the bimodal behaviour in the heat flux for higher Knudsen numbers. Using DSMC, this bimodal behaviour disappears

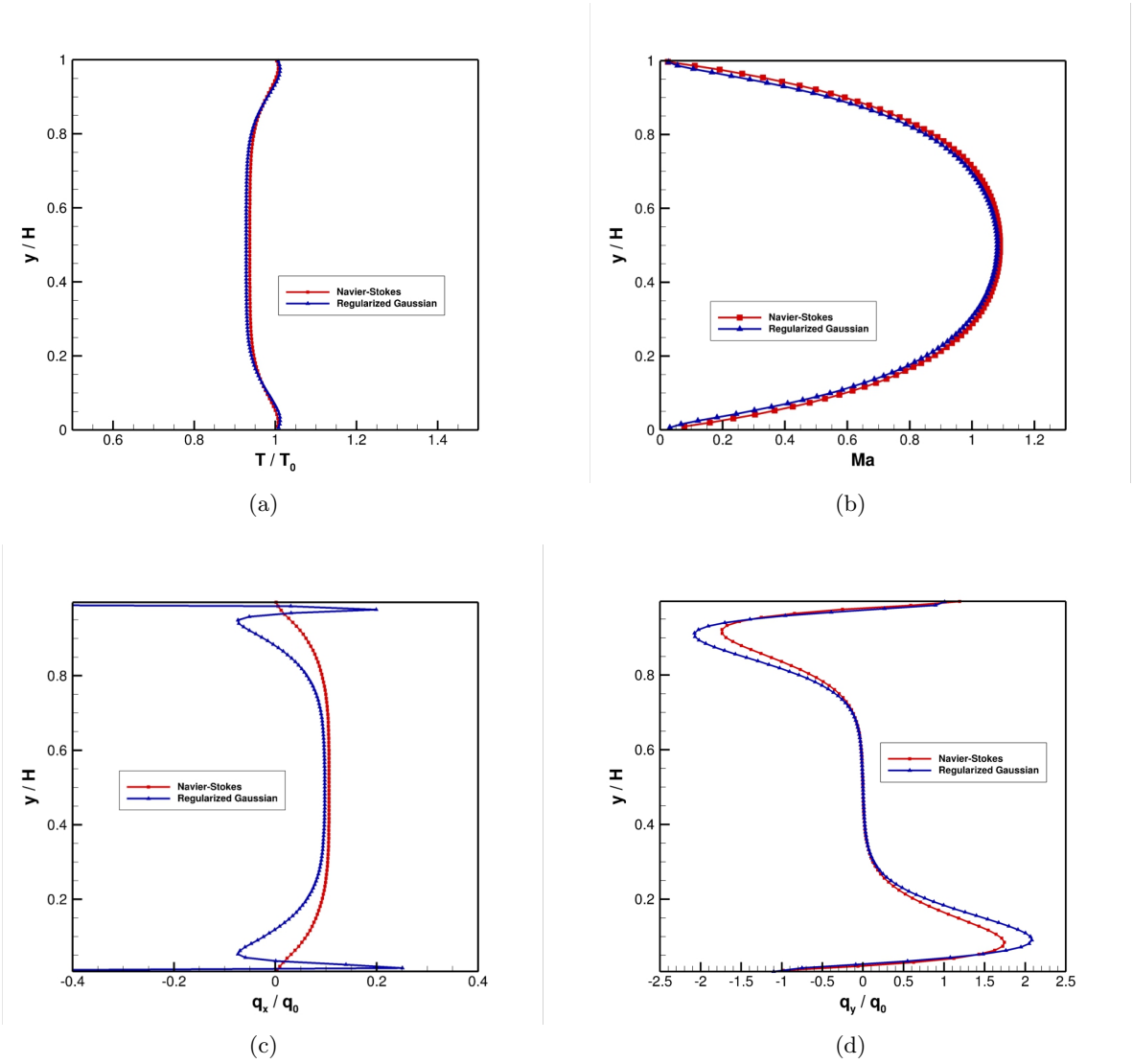

Figure 6.9: Navier-Stokes vs Regularized Gaussian Closure for Poiseuille flow, Kn = 0.001 and $p' = 1.5$, for (a) non-dimensionalized temperature, (b) Mach number, (c) non-dimensionalized transverse heat flux, and (d) non-dimensionalized normal heat flux, as measured 2/3 of the total distance from the channel entrance.

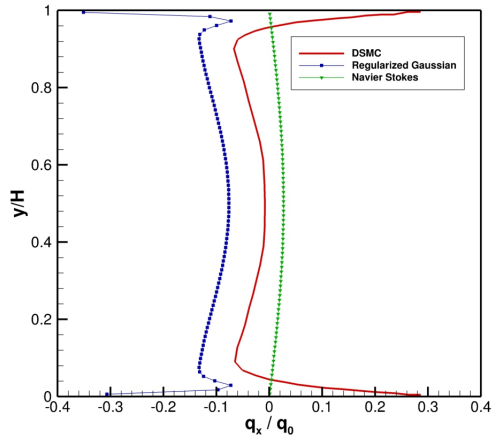

(a) Kn = 0.025, $p' = 1.5$

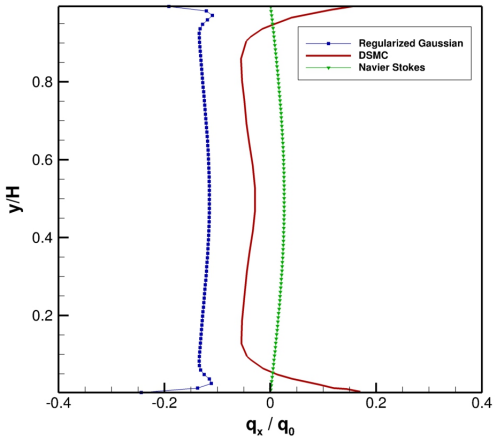

(b) Kn = 0.05, $p' = 1.5$

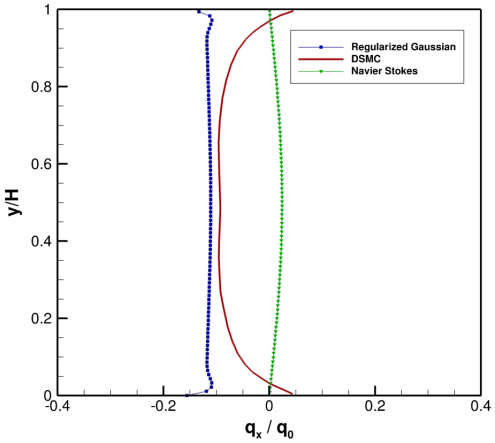

(c) Kn = 0.1, $p' = 1.5$

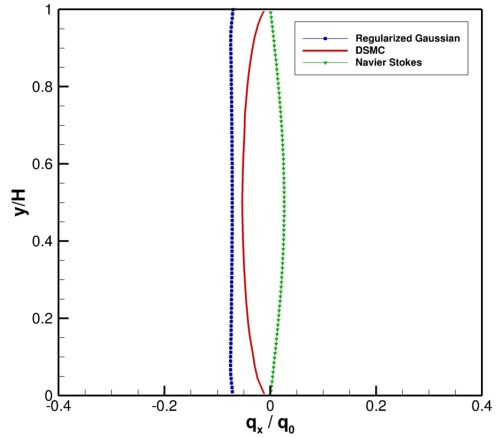

(d) Kn = 0.5, $p' = 1.5$

Figure 6.10: Non-dimensionalized heat flux profiles across the channel at various Knudsen numbers for Poiseuille flow using DSMC and the Regularized Gaussian Closure, $p' = 1.5$

at about Kn = 0.1 and takes on a parabolic profile that becomes more uniform when entering the free-molecular regime. The regularized Gaussian however predicts a small bimodal profile for flows up to Kn = 0.5. Both modelling methods generate a heat flux profile that asymptopes toward a uniform profile in the free-molecular regime.

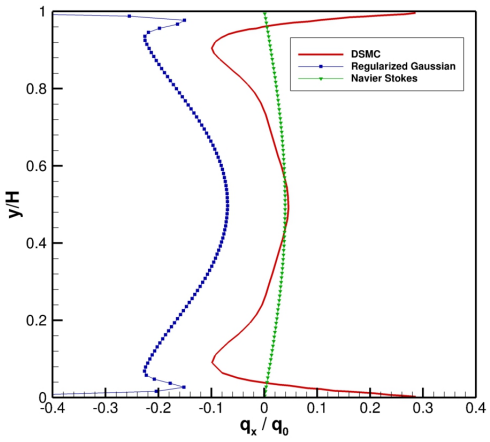

(a) Kn = 0.025, $p' = 2.0$

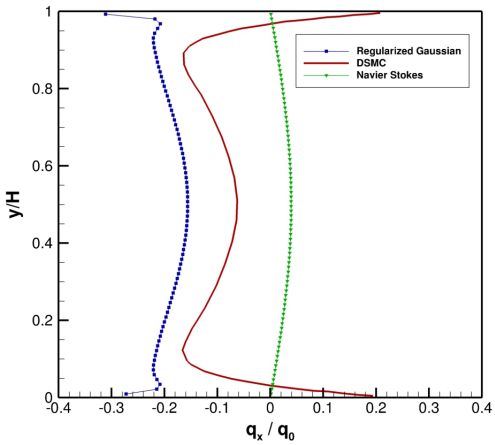

(b) Kn = 0.05, $p' = 2.0$

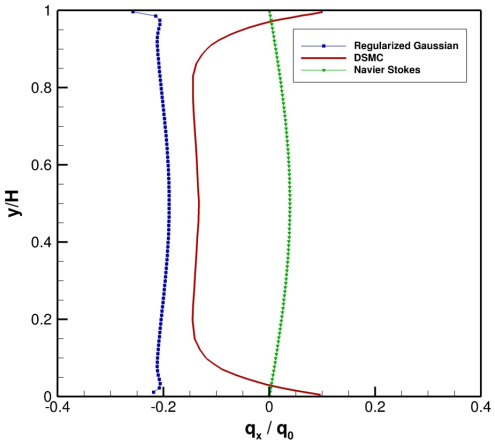

(c) Kn = 0.1, $p' = 2.0$

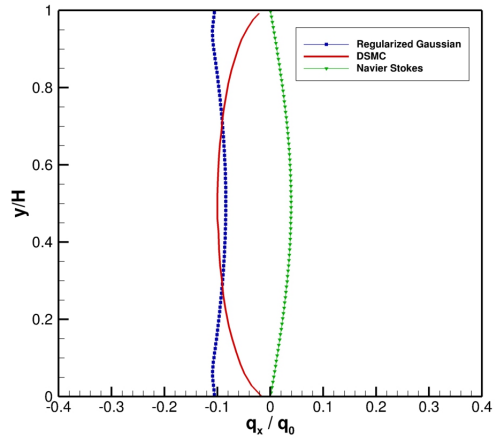

(d) Kn = 0.5, $p' = 2.0$

Figure 6.11: Non-dimensionalized heat flux profiles across the channel at various Knudsen numbers for Poiseuille flow using DSMC and the Regularized Gaussian Closure, $p' = 2.0$

6.5 Lid-Driven Cavity Flow

The capabilities of the half-Maxwellian boundary conditions in modelling temperature slip and velocity have been demonstrated separately in the parallel heated plates flow problem and the Couette flow problem respectively. The combined effect of both types of slip can be seen in the driven cavity flow problem. Channel elements and moving surfaces constitute a major portion of designs used in modern MEMS device manufacturing, such that a thorough study of its behaviour under non-equilibrium conditions is an important benchmark for validating the regularized Gaussian closure.

Continuum-based solutions to lid-driven cavity flow are widely available with a predictable velocity and heat flux profile. With increasing Knudsen number, the Navier-Stokes equations become ill-suited in demonstrating some of the phenomena that manifests itself under non-equilibrium conditions. Extensive studies by John *et al.* [121] on non-equilibrium cavity flow were performed using the DSMC method of Bird [1], with a later study on the effects of varying accommodation coefficient using the same method [122]. To the best of the author's knowledge, there exist no three-dimensional experimental studies of this problem with which an accurate comparison can be made with solutions generated from the regularized Gaussian closure. The results acquired here are instead compared to the DSMC results of John *et al.* [121, 122], given the known physical accuracy of the DSMC technique for moderate Knudsen numbers. A comparison of results from the regularized Gaussian closure and the Navier-Stokes equations for continuum-regime lid-driven cavity flow are also shown to ensure that the regularized closure is able to recover continuum-limit behaviour.

A square-shaped cavity filled with the fluid of interest is subject to shearing forces from the movement of the top face of the cavity. Figure 6.12 illustrates the setup for this problem. For the three-dimensional regularized Gaussian, periodic boundary conditions are placed in the transverse location such that a slice of the channel is comparable to the two-dimensional computational solutions available in literature. Argon under standard atmospheric conditions at 273K is placed within the cavity, and the Knudsen number is controlled by varying the dimensions of the cavity. Isothermal boundary conditions set to the initial temperature of the gas are enforced on the cavity walls, with an additional $x-$direction velocity component on the upper wall moving to the right at $u_w = 50$ m/s. The computational mesh consists of 921,600 cells concentrated in the plane of interest. A view of the computational mesh and a sample numerical result for the regularized closure can be seen in Figure 6.13.

Results from the regularized Gaussian closure for this flow problem in the continuum regime

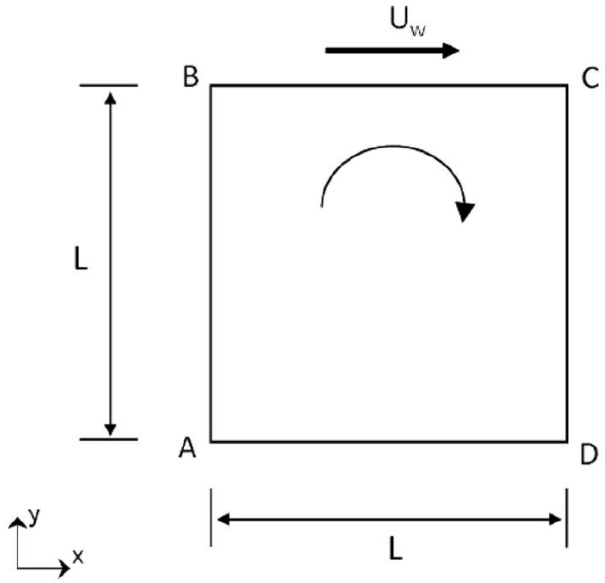

Figure 6.12: Diagram of lid-driven cavity flow by John *et al.* [121].

are first compared to those from the Navier-Stokes equations. DSMC data for these low Knudsen numbers are unavailable due to the extreme computational cost associated with the ever-increasing number of virtual particles needed per cell. These results can be seen in the Mach number and temperature contours in Figure 6.15 and Figure 6.16, respectively, for Kn = 0.001. The predicted Mach number contours are very similar for the two equation sets at this Knudsen number, but velocity slip effects are beginning to form in the upper right corner of the cavity. The computed non-dimensionalized velocity profiles along a vertical and horizontal line passing through the centre of the cavity are also shown in Figure 6.14 for both the Navier-Stokes equations and the regularized Gaussian closure. The regularized closure predicts that the speed of the recirculating flow is slightly higher than that predicted by the Navier-Stokes equations, possibly due to the small slip effect in the upper right corner, but otherwise the profiles are in good agreement.

While the actual slip values are small enough to not have any impact on the general Mach number profile of the Kn = 0.001 case, they are significant enough to affect the maximum temperature values in the predicted temperature field. The formation of the hot spot in the upper right corner of the cavity is suppressed by the slipless wall temperature in the Navier-Stokes. Although the temperature profile generated by both the regularized Gaussian closure and Navier-Stokes looks similar in shape, as seen in Figure 6.16, an examination of the temperature contour range shows that the maximum temperature acquired from the Navier-Stokes is noticeably lower than that found from the regularized closure. This shows that slip effects

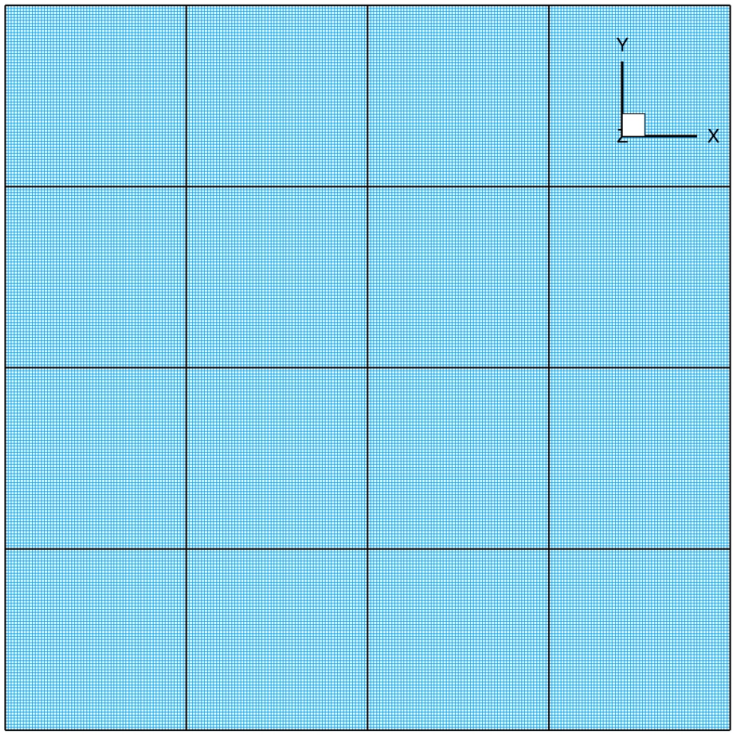

(a)

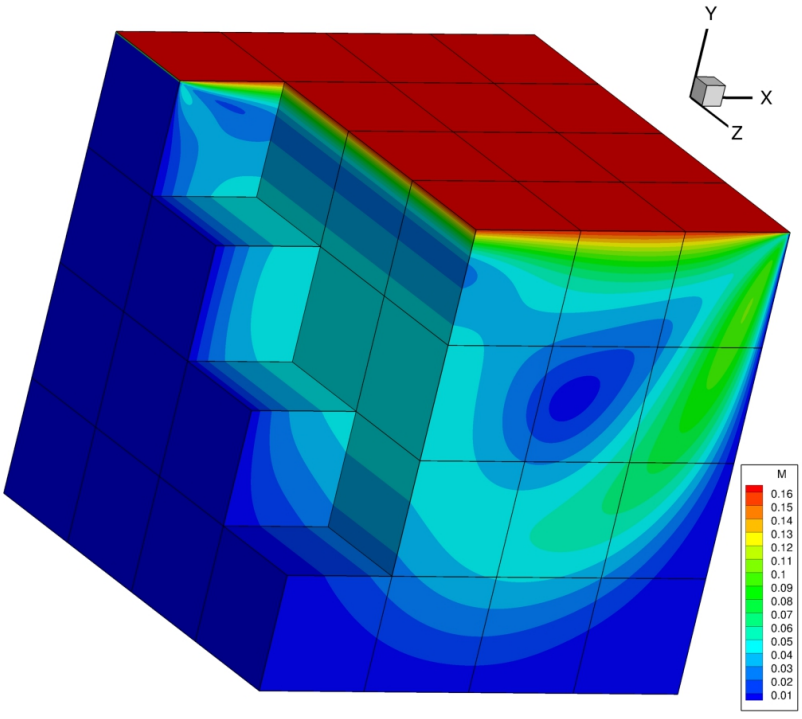

(b)

Figure 6.13: (a) Driven cavity flow mesh blocks and cells as seen on the XY plane, and (b) a cutaway view of the mesh blocks with Mach number contours for Kn = 0.001 and $u_w = 50$ m/s.

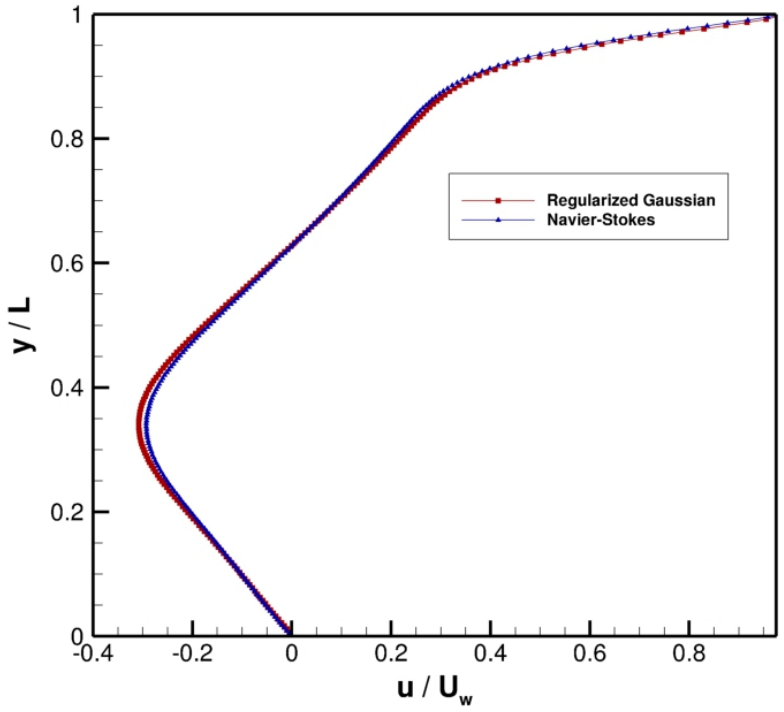

(a)

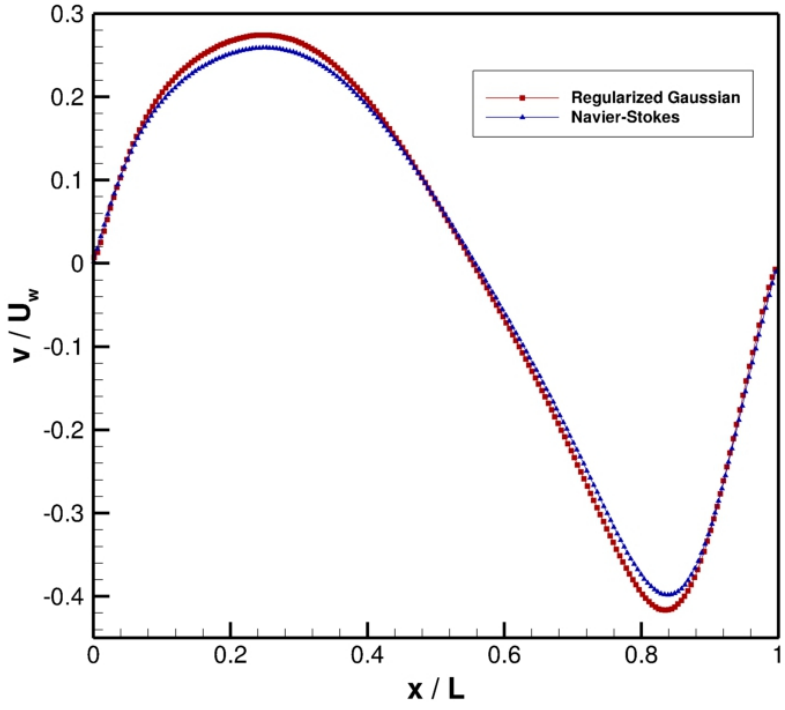

(b)

Figure 6.14: Non-dimensionalized velocity plotted against a non-dimensionalized length scale for driven cavity flow with Kn = 0.001 and $u_w = 50$ m/s showing (a) vertical velocity along a horizontal line, and (b) horizontal velocity along a vertical line. Both horizontal and vertical lines pass through the centre of the cavity.

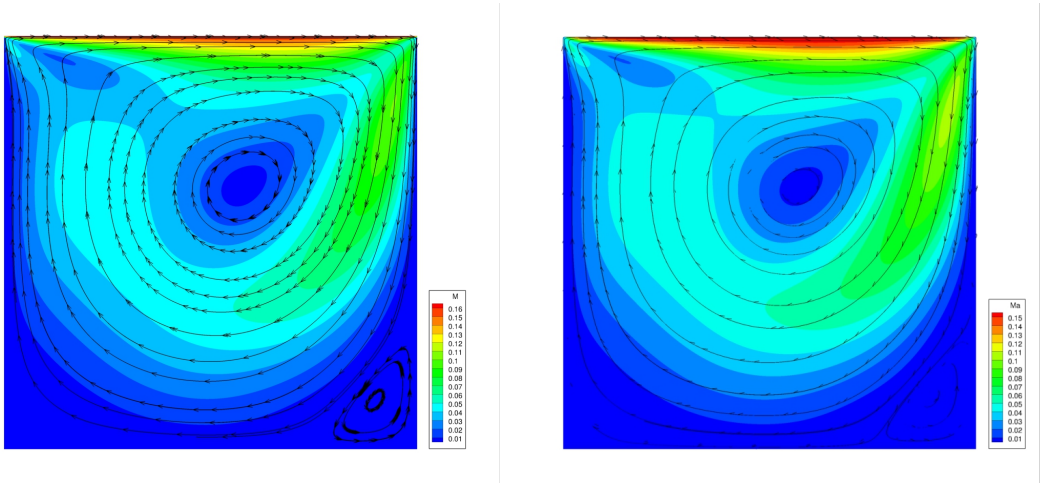

(a) (b)

Figure 6.15: Mach number profile with velocity streamlines for driven cavity flow at Kn = 0.001 and $u_w = 50$ m/s using (a) Navier-Stokes, and (b) regularized Gaussian closure

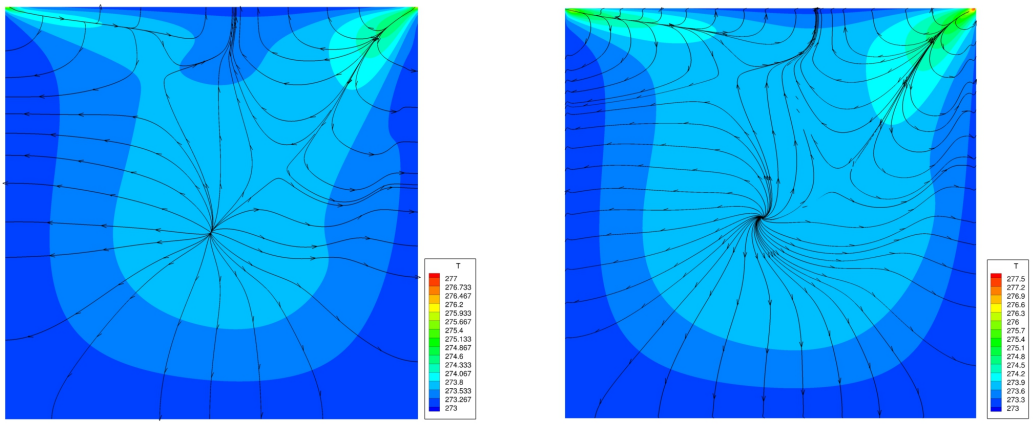

(a) (b)

Figure 6.16: Temperature profile with heat flux streamlines for driven cavity flow at Kn = 0.001 and $u_w = 50$ m/s using (a) Navier-Stokes, and (b) regularized Gaussian closure

can potentially have a significant impact even for relatively small Knudsen numbers in the continuum regime, though additional corroborating evidence from physical or computational experiments are needed to confirm this effect.

Use of the Navier-Stokes applied for the lid-driven cavity flow problem yields results that are not dependent on the Knudsen number and produces heat fluxes dictated by Fourier's Law.

While valid in the continuum regime, the Navier-Stokes alone is unable to account for the various non-equilibrium phenomena shown both experimentally and computationally by the regularized Gaussian closure and DSMC, demonstrated here through the following driven cavity flow conditions at larger Knudsen numbers. Figure 6.17 shows results of the driven cavity flow problem at Kn = 0.1 using the Navier-Stokes, along with those from the regularized Gaussian closure and DSMC. Note that the predicted range of temperatures produced by the Navier-Stokes equations is significantly more limited than those from the regularized Gaussian closure and DSMC approach. The colour scale in the temperature contour plots has been adjusted to illustrate this feature for the solutions. The lack of expansion cooling (i.e. gas temperature less than wall temperature) is clearly seen in the Navier-Stokes profile, as is the counter-gradient heat flux. Thus, while the regularized Gaussian closure is not capable of exactly reproducing the non-equilibrium phenomena described in literature and DSMC, the effects of temperature and velocity slip, expansion cooling, and a counter-gradient heat flux can still be generated. Extensive problem-based modifications to the Navier-Stokes based on empirical formulations would be necessary to adapt it to simulate these non-equilibrium phenomena, making the regularized Gaussian closure a more attractive option.

The onset of non-equilibrium effects with increasing Knudsen number can be seen in Figures 6.18 and 6.19, where the lid velocity is set at $u_w = 50$ m/s and the Knudsen number is varied within the range $0.1 \leq \text{Kn} \leq 8$. A comparison is made between the DSMC results of John *et al.* [121] and those from the regularized Gaussian closure, where the predicted temperature contours are shown overlaid with the corresponding heat flux vectors. For reference, the top boundary is the moving lid with a velocity moving to the right. The DSMC results clearly show that the heat flux near the lid is directed in the same direction as the lid velocity, but is opposite to what is implied by the temperature gradient. The regularized Gaussian closure similarly depicts this alignment of the heat flux, but the temperature profile is significantly different. As the heat flux at the wall is not strictly enforced through the current temperature slip boundary conditions, the temperature gradient at the corners of the cavity adjacent to the moving lid tries to conform to the heat flux. This results in a lowering of the temperature in the upper right corner and a raising of the temperature in the upper left corner, contrary to the expansion cooling effect depicted in the DSMC results. This discrepancy is most visible for Kn = 1. The regularized Gaussian closure recovers this expansion cooling effect for higher Knudsen numbers, but overpredicts the amount of cooling that will occur. The heat flux profiles however, maintain their directionality opposite to that of the temperature gradient. It should be mentioned that the counter-gradient heat flux predicted by the DSMC results of John *et al.* [121] arises due to a combination of expansion cooling and heating due to viscous dissipation,

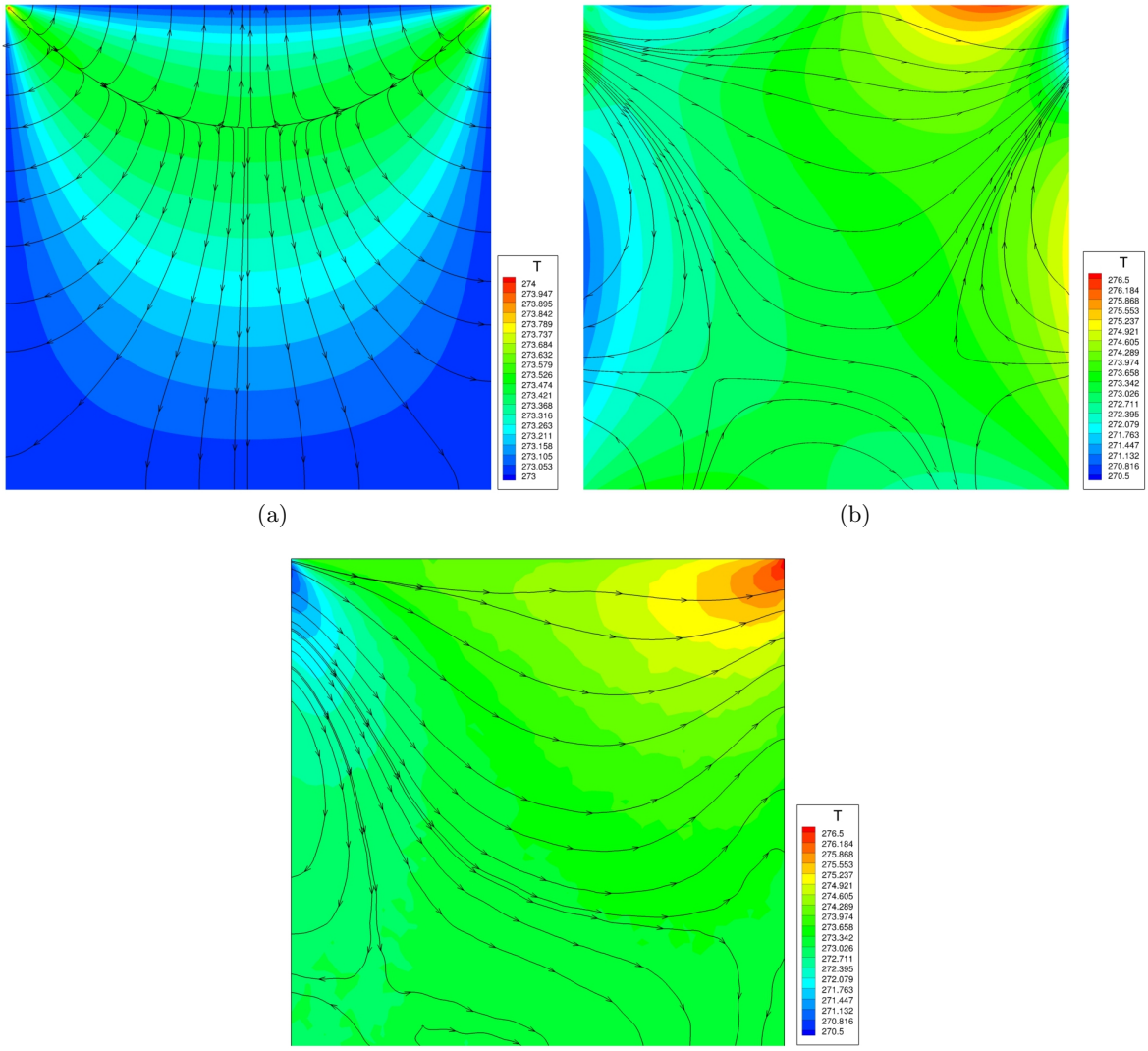

Figure 6.17: Temperature profile with heat flux streamlines for driven cavity flow at Kn = 0.1 and $u_w = 50$ m/s using (a) Navier-Stokes, (b) regularized Gaussian closure, and (c) DSMC.

and results in a heat flux that is in a direction from low to high temperatures.

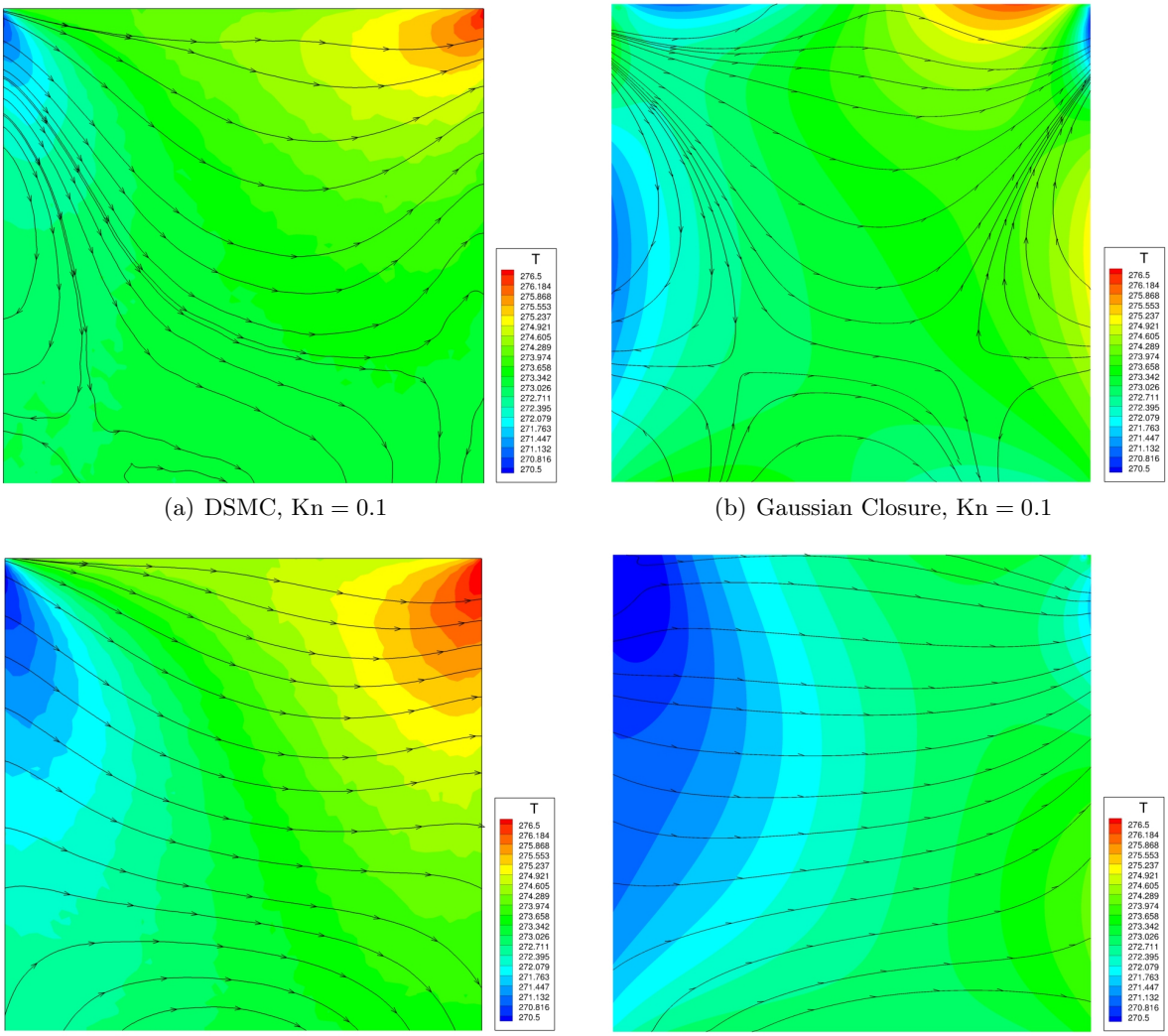

(a) DSMC, Kn = 0.1

(b) Gaussian Closure, Kn = 0.1

(c) DSMC, Kn = 0.5

(d) Gaussian Closure, Kn = 0.5

Figure 6.18: DSMC vs Regularized Gaussian Closure for driven cavity flow, $u_w = 50$ m/s at Kn = 0.1 and Kn = 0.5

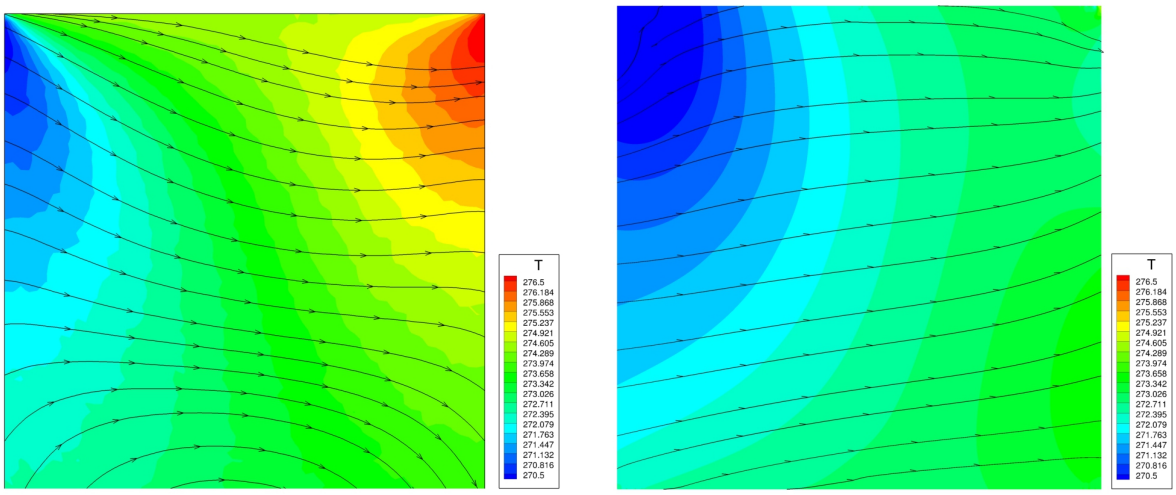

(a) DSMC, Kn = 1

(b) Gaussian Closure, Kn = 1

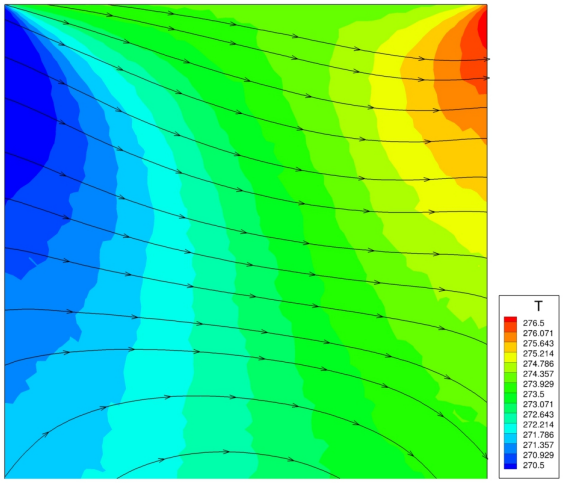

(c) DSMC, Kn = 8

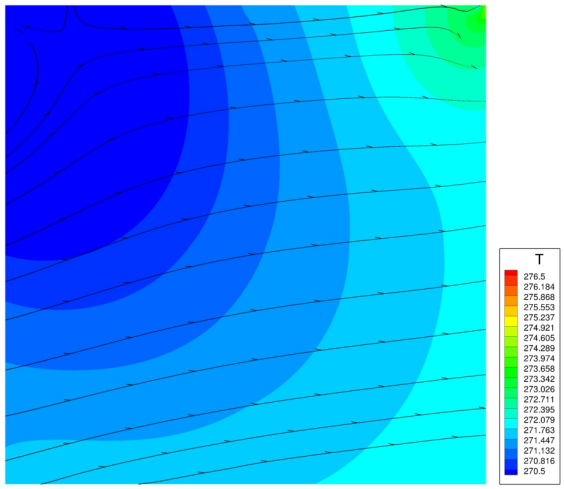

(d) Gaussian Closure, Kn = 8

Figure 6.19: DSMC vs Regularized Gaussian Closure for driven cavity flow, $u_w = 50$ m/s at Kn = 1 and Kn = 8

6.6 Subsonic Immersed Flow Past a Circular Cylinder

Immersed flow over a cylinder is re-considered here to examine the effects of heat transfer on drag coefficients over a range of Knudsen numbers. The results are compared to the previous three-dimensional results for the standard Gaussian closure of Chapter 5, that do not include heat transfer. The proposed NKS solution method is employed with the temperature slip boundary conditions of Smoluchowski [53] as described in Section 2.5.2 of Chapter 2. Isothermal boundary conditions were used on the surface of the cylinder and set to the free stream temperature of 288 K. As a result, the heat flux from the wall into the fluid is not large and the temperature slip phenomena should manifest itself only in higher Knudsen number regimes.

As noted previously, the effects of laminar flow past a cylinder in both the continuum and transitional regimes has been studied experimentally by Coudeville *et al.* [106], with focus on the drag coefficient with varying Reynolds and Knudsen numbers. As in Chapter 5, the cylinder radii was varied from 3.36×10^{-5} to 6.72×10^{-9} m, corresponding to $10^{-3} \leq \mathrm{Kn} \leq 5$ using the cylinder diameter as the characteristic length. A speed ratio of $\mathrm{S} = 0.107$ is used here and corresponds to a Mach number of $\mathrm{Ma} = 0.128$, where the speed ratio is defined as the ratio between the bulk speed of the fluid and the most probable random speed of a particle. The Reynolds numbers for these flows ranges from $0.005 \leq \mathrm{Re} \leq 188$, well within the laminar regime. The far field boundary was set at 32 times the cylinder radius, however, for $\mathrm{Kn} = 0.1$, the boundary layer formed around the cylinder expands considerably, and the far field boundaries were extended up to 300 times the cylinder radius to avoid any interaction with the boundary layer. Final three-dimensional mesh resolution ranges from 83,200 to 166,400 cells.

A comparison can be made between the predictions of the Gaussian closure with and without heat transfer and the Navier-Stokes equations pertaining to the immersed flow over a cylinder with varying Knudsen number. Figure 6.20 shows the performance of these three descriptions compared to the experimental measurements by Coudeville *et al.* [106] and an analytical solution valid for the free molecular regime of Patterson [107]. The addition of heat transfer maintains physical accuracy up till about $\mathrm{Kn} = 1$ but drops off for higher Knudsen numbers. Interestingly, the Gaussian closure without heat transfer and the Navier-Stokes equations predict similar overestimated drag coefficients even though the Navier-Stokes model includes heat transfer, but not slip. This suggests that boundary conditions that account for temperature slip are most likely required for an accurate depiction of high Knudsen number flows.

To get a sense of the structure of the boundary layer predicted by these methods, the Mach number profiles for a transition regime problem ($\mathrm{Kn} = 0.1$) and free molecular regime problem

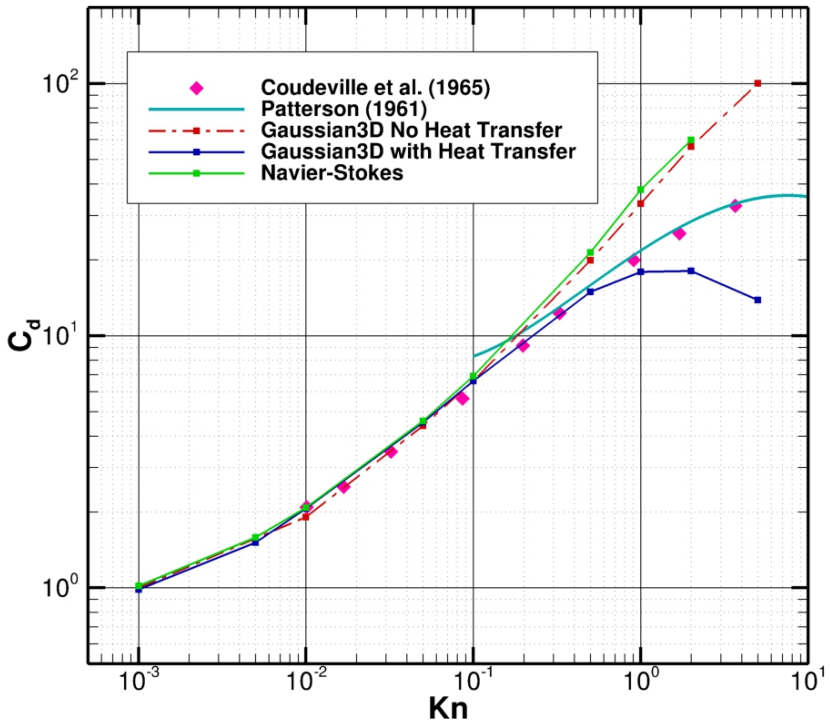

Figure 6.20: Drag coefficient over a cylinder vs. Knudsen number for a speed ratio $S = 0.107$.

(Kn = 1) are shown in Figures 6.21 and 6.22, respectively. In the transition regime, all three methods produce similar drag coefficients and boundary layer thicknesses, but the lack of velocity slip at the cylinder boundaries in the Navier-Stokes is already evident. Adding heat transfer in the regularized Gaussian closure does not produce any noticeable effects at this point. At Kn = 1, the overestimation of the cylinder drag by the Navier-Stokes and the Gaussian closure without heat transfer can be related to an overestimation of the boundary layer thickness as evidenced by Figures 6.22(a) and 6.22(b). The addition of heat transfer in Figure 6.22(c) suppresses the growth of the boundary layer and results in a cylinder drag more in line with experimental and analytical data. However, for Kn > 1, the suppressed boundary layer gives way to an underestimation of the drag which becomes worse with increasing Kn. This limit may represent a point at which the current form of the equations breaks down and can be also seen in the results of other moment techniques [116]. Further study into the physical phenomena occurring in this regime will be subject of future follow-on research to this thesis.

As for the standard Gaussian closure, it is useful at this point to illustrate the advantages

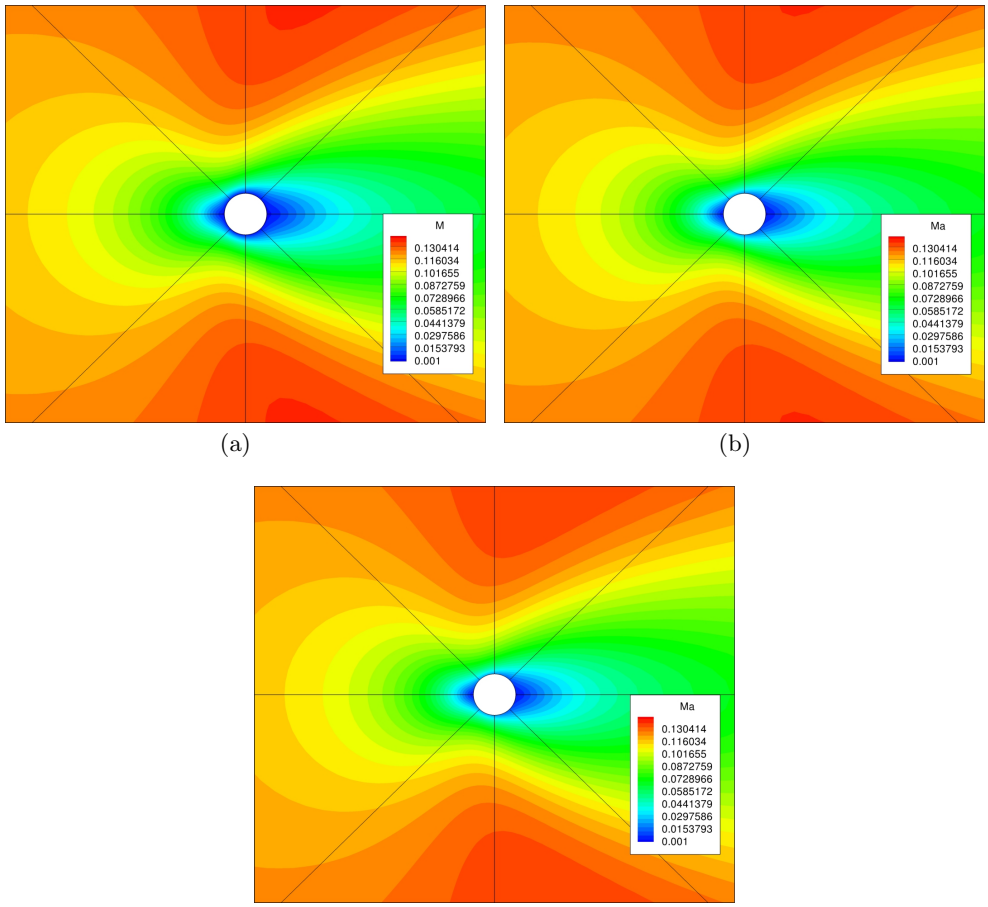

Figure 6.21: Mach number profile of flow over a cylinder at Kn = 0.1 as calculated by (a) Navier-Stokes, (b) standard Gaussian closure with no heat transfer, and (c) regularized Gaussian closure with heat transfer.

in computational cost provided by the AMR and NKS algorithm for solutions to the three-dimensional regularized Gaussian closure. For Kn = 0.01, the AMR algorithm was used to produce a cylinder mesh with up to four levels of refinement. A close-up view of the mesh blocks produced from the AMR procedure is given in Figure 6.23. At each mesh refinement, the drag over the cylinder was calculated and compared to the experimental result from Coudeville *et al.* [106] for the same flow conditions. Figure 6.24(a) shows the mesh convergence of the solution method with reference to the calculated drag over the cylinder. The strength of the AMR/NKS solution method is even more pronounced as the converged computational drag approaches the experimental drag to within 0.6%. The convergence history of the NKS solution method with consecutive mesh refinements from the AMR algorithm can be seen in Figure 6.24(b), showing rapid convergence can be seen at each mesh level. The grid refinement is set to occur every 60

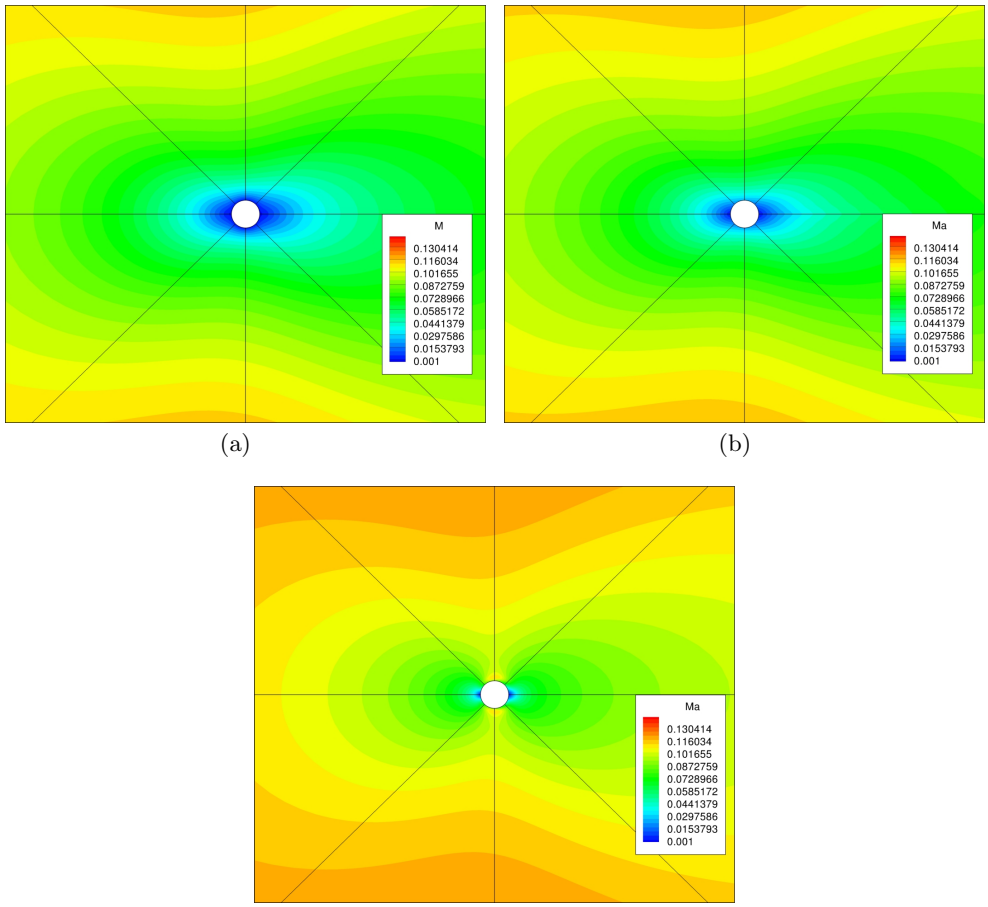

Figure 6.22: Mach number profile of flow over a cylinder at Kn = 1 as calculated by (a) Navier-Stokes, (b) standard Gaussian closure with no heat transfer, and (c) regularized Gaussian closure with heat transfer.

Newton iterations, though if allowed to proceed further the norm can be reduced by more than the approximately five orders of magnitude shown here. Using a planar view of the cylindrical grid, the meshes used at the beginning, middle and end of the the refinement study can be seen in Figure 6.25. Each mesh block contains 40 cells in the radial direction, 10 cells in the angular direction, and 2 cells over the height of the cylinder.

The advantages offered by the NKS include a vast saving in computational costs. Figure 6.26 depicts the convergence history of the immersed cylinder flow in a range of Knudsen numbers without AMR on a eight block mesh with a total of 179,200 cells using NKS and the semi-implicit solver. Both schemes were performed over eight Intel Xeon E5540 cores at 2.53 GHz. Additionally, Table 6.2 provides a summary of the NKS and semi-implicit CFL parameters and computation time for the three convergence cases considered here. As seen in the figures, the

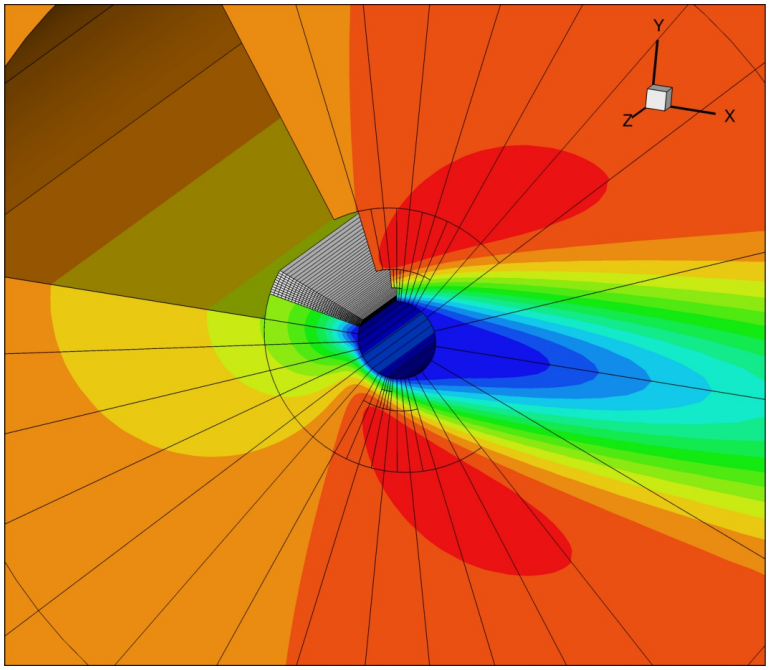

Figure 6.23: Mesh blocks created with the AMR algorithm for flow over a cylinder at Kn = 0.01. The uncolored block shows the individual cells residing within that particular mesh block to illustrate the resolution acquired.

	NKS				Semi-Implicit		
Kn	Initial CFL	Final CFL	Time (min)	L2-norm Ratio	CFL	Time (min)	L2-norm Ratio
0.001	1×10^2	1×10^9	268.9	8.54167×10^{-11}	0.2	2868.06	1.825×10^{-6}
0.1	1×10^3	1×10^9	208.6	9.58762×10^{-7}	0.05	2870.8	5.332×10^{-4}
1	1×10^2	1×10^6	218.9	6.70304×10^{-5}	0.005	2744.1	4.28×10^{-4}

Table 6.2: Summary of NKS/semi-implicit CFL parameters and computation times for the flow problems performed in Figure 6.26.

NKS scheme for these flow problems require 4 hours to reach a suitably converged solution, while the explicit method requires 48 hours providing a reduction in the overall computational costs of the simulations by approximately a factor of 12. The convergence history also shows that the NKS solution method is capable of reducing the residual by almost eleven orders of magnitude in the continuum case. The ability to reach a highly converged solution, the enormous savings in computational time, and the accuracy of the method shown in the examples above illustrate the potential that these moment closures have for both research and industrial applications.

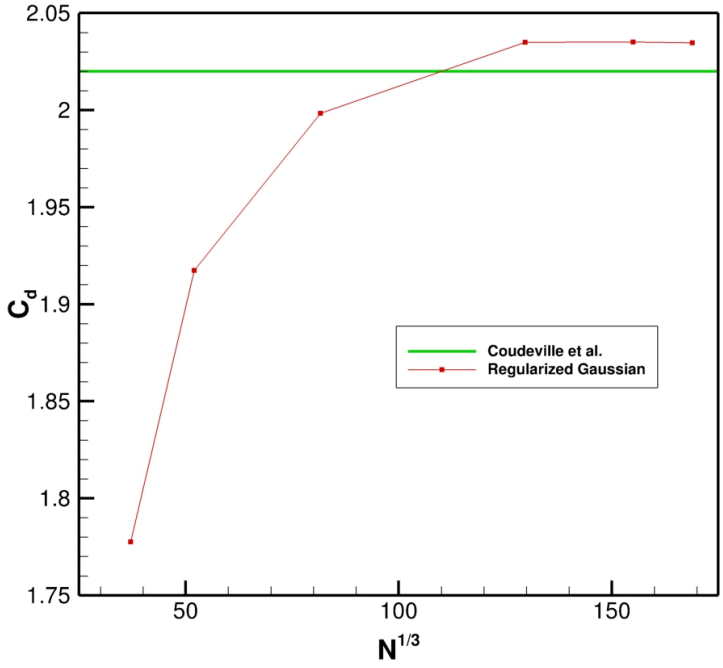

(a)

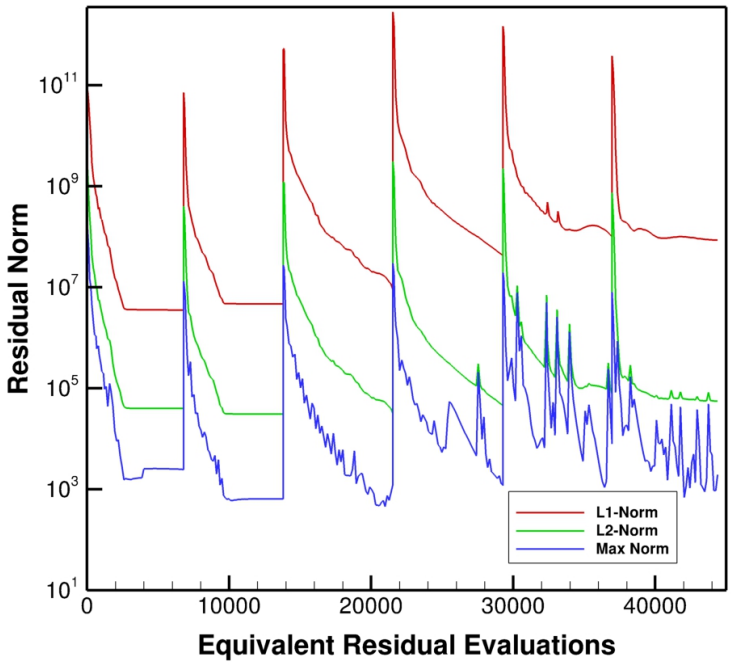

(b)

Figure 6.24: (a) Cylinder drag for Kn = 0.01 with increasing number of cells, showing mesh-convergent behavior approaching the experimental data of Coudeville *et al.* [106], (b) Error norm evolution over multiple mesh refinements.

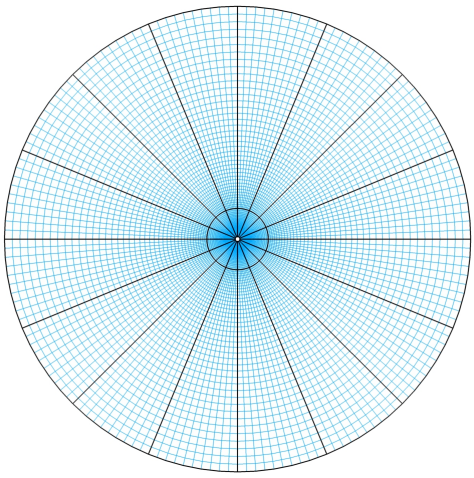

(a) 64 mesh blocks (51,200 cells)

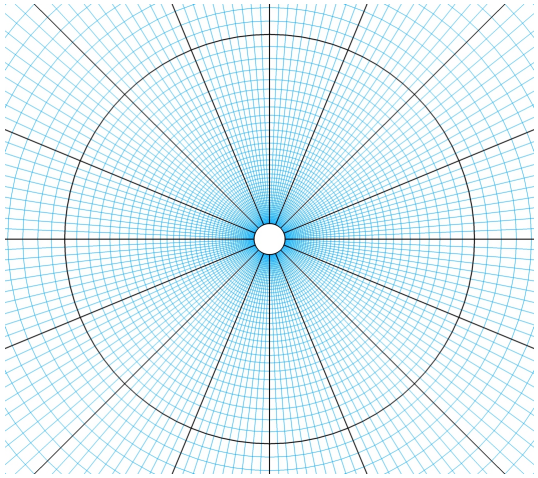

(b) 64 mesh blocks (51,200 cells), magnified

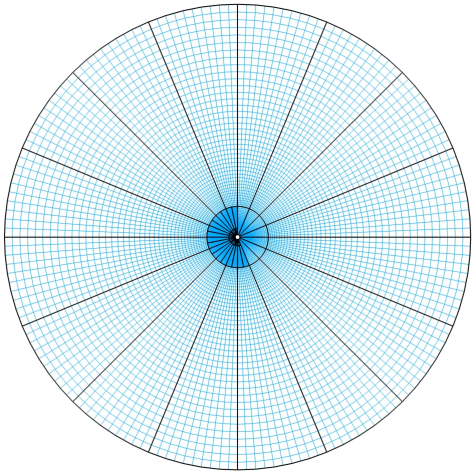

(c) 302 mesh blocks (241,600 cells)

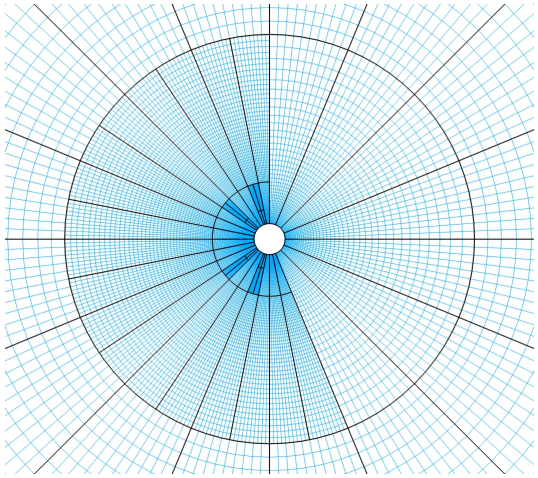

(d) 302 mesh blocks (241,600 cells), magnified

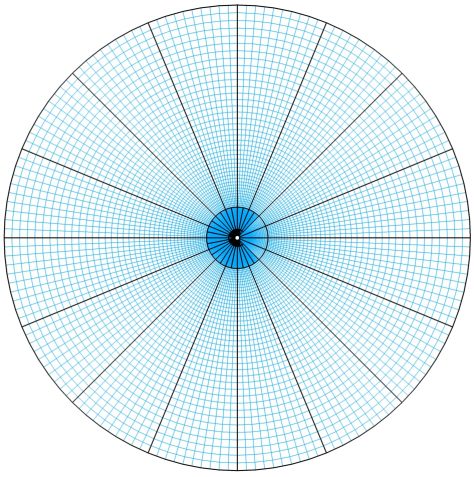

(e) 2192 mesh blocks (1,753,600 cells)

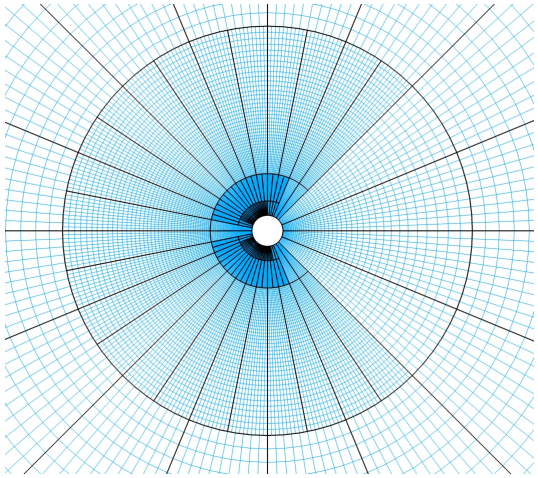

(f) 2192 mesh blocks (1,753,600 cells), magnified

Figure 6.25: Sample of refined mesh blocks used for the mesh convergence study of the regularized Gaussian closure.

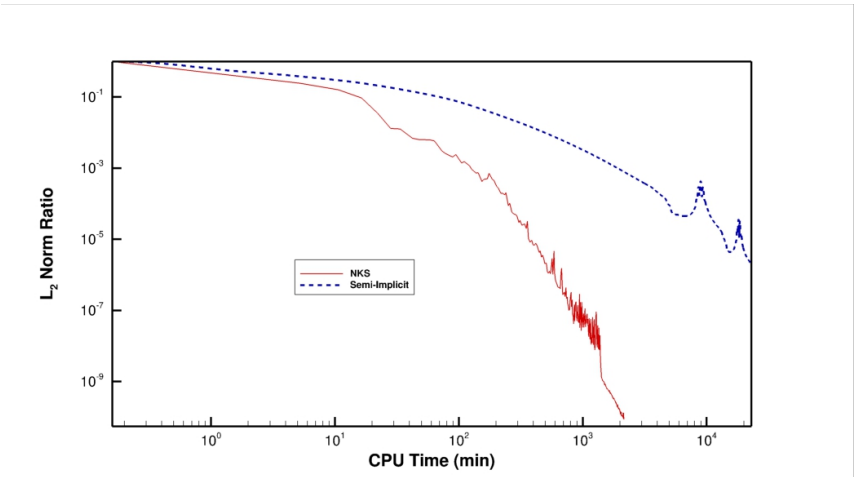

(a)

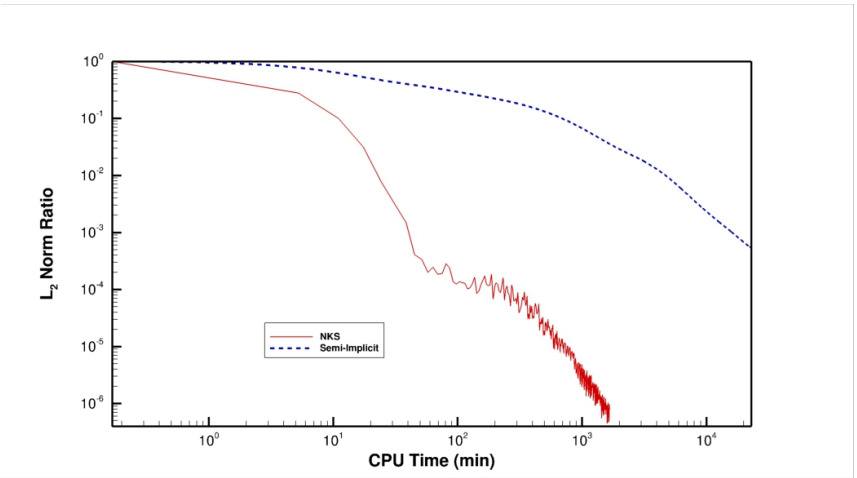

(b)

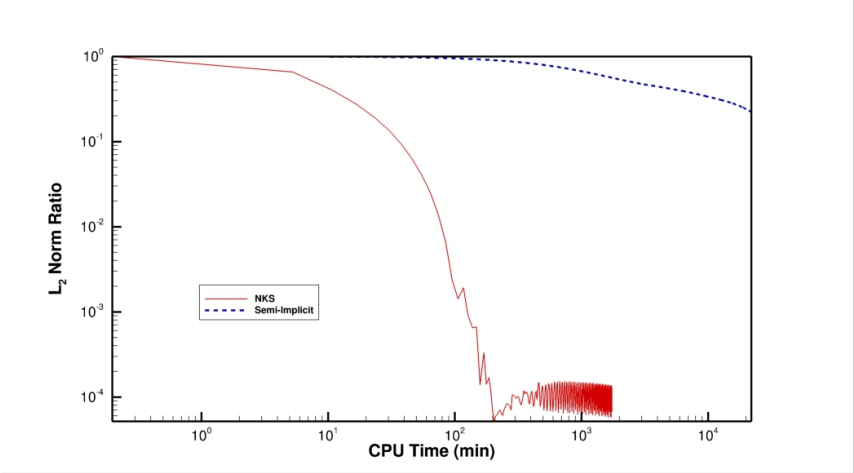

(c)

Figure 6.26: NKS and semi-implicit convergence rates for immersed subsonic flow past a cylinder using the regularized Gaussian closure at (a) Kn = 0.001, (b) Kn = 0.1 and (c) Kn = 1.

6.7 Subsonic Immersed Flow Past a Sphere

Under the same physical parameters as those described in Section 5.6 of Chapter 5, the drag on a sphere is also again studied here using the regularized Gaussian closure. Using the same grid and NKS parameters as summarized earlier, the sphere drag is once again compared to the experimental results of Roos and Willmarth [109], Liebster [110], and Millikan [112,113], as well as an analytical solution given by Flemmer and Banks [111]. Use of the regularized Gaussian closure and its associated heat term is expected to improve the accuracy of the sphere drag predictions in the transition regime as was seen in the improvement of cylinder drag prediction studied earlier in Section 6.6.

The NKS and semi-explicit convergence histories for this flow problem using the regularized Gaussian closure are shown in Figure 6.27 for a range of Knudsen numbers, with Table 6.3 showing the CFL parameters and physical computational times used by each method. Using only 100 Newton iterations in each case, the NKS method is clearly superior in providing converged solutions within all flow regimes. While the semi-implicit method can be highly converged in the continuum regime, the computational time needed to account for the additional heat transfer terms in the regularized Gaussian closure increases dramatically even for moderately rarefied flows compared to the standard Gaussian closure (see Table 5.3 in Chapter 5). The robust nature of the regularized Gaussian closure with the NKS solution method for this fully three-dimensional flow makes it an attractive option for more complex geometries and flow conditions.

Figure 6.28(a) shows the change in sphere drag with Reynolds number, compared with an analytical solution by Flemmer and Banks [111], and experimental results from Roos and Willmarth [109] and Liebster [110]. Once again it must be noted that the Reynolds number in these experimental and analytical results are obtained by varying the flow velocity and fluid viscosity, and are therefore firmly entrenched in the continuum regime. The Gaussian closure sphere drags shown previously in Figure 5.19 are also included here for reference. The computed

	NKS				Semi-Implicit		
Kn	Initial CFL	Final CFL	Time (min)	L2-norm Ratio	CFL	Time (min)	L2-norm Ratio
0.001	1×10^{1}	1×10^{7}	97.24	3.089×10^{-8}	0.1	2877	3.821×10^{-13}
0.05	1×10^{1}	1×10^{5}	82.92	4.276×10^{-6}	0.0001	2877.29	3.528×10^{-1}
1	1×10^{1}	1×10^{5}	98.25	5.618×10^{-7}	0.0001	2877.54	3.613×10^{-5}

Table 6.3: Summary of NKS/semi-implicit CFL parameters and computation times for the flow problems performed in Figure 6.27.

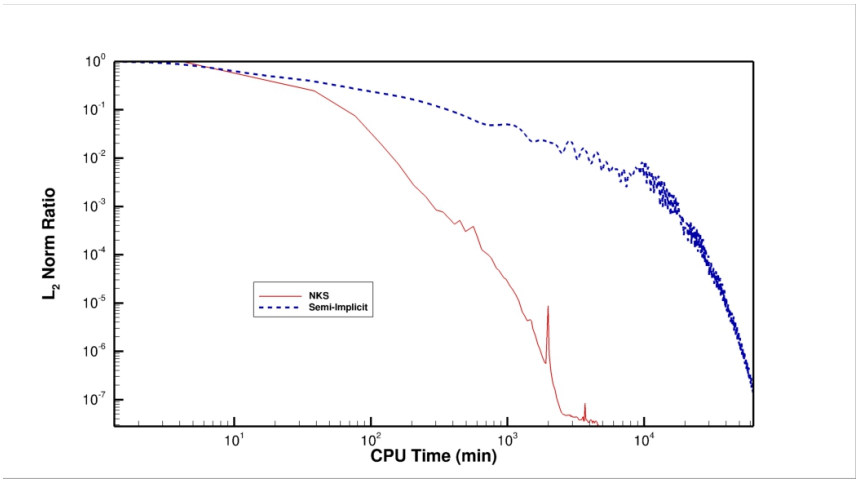

(a)

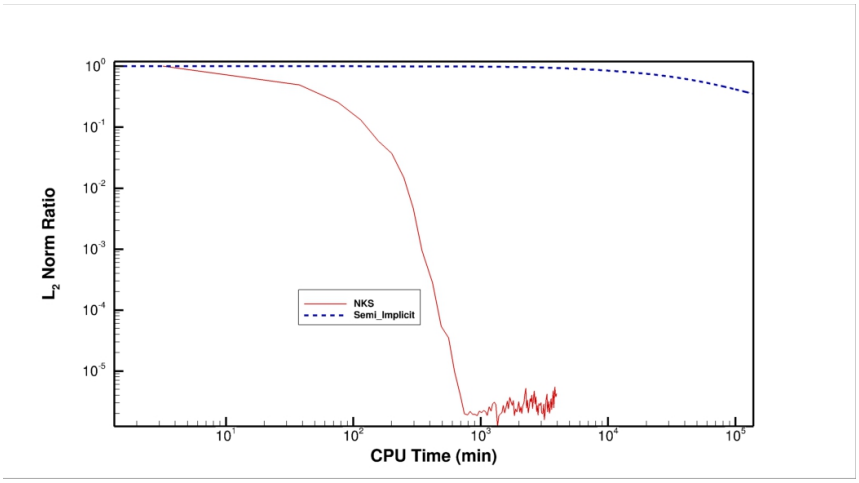

(b)

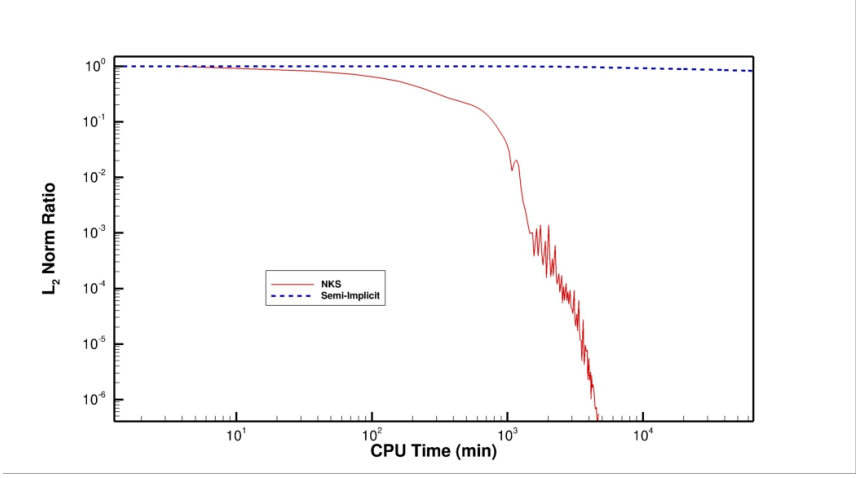

(c)

Figure 6.27: NKS and semi-implicit convergence rates for immersed subsonic flow past a sphere using the regularized Gaussian closure at (a) Kn = 0.001, (b) Kn = 0.05 and (c) Kn = 1

sphere drag from the regularized Gaussian closure in the continuum limit agrees closely with those from the analytical and experimental results. For Kn > 1, the drag reaches a maximum and begins to decrease as the flow becomes increasingly rarefied. This behaviour is similar to that found in the cylinder drag flow problems summarized in Section 6.6 above at about the same Knudsen number.

Experimental data by Millikan [112, 113], as corrected by Allen and Raabe [114], and an analytical solution by Clift *et al.* [123] showing the relationship between Knudsen number and sphere drag correction coefficient, is shown with the results from the Gaussian closure and the regularized Gaussian closure in Figure 6.28(b). Due to Millikan's extensive collection of data, this particular problem is known to possess no significant initial temperature gradients. It can be clearly seen, however, that taking into account a heat flux term produces significant improvements in the predictive abilities of the Gaussian closure in the transition and early free-molecular regimes. While both Gaussian closures predict similar drags in the continuum regime, the regularized closure follows the decreasing trend much closer to the experimental and analytical results, and only begins to deviate from them for Kn > 0.4. A similar behaviour of sphere drag can be found from an analytical solution [116] to the regularized 13-moment equations by Struchtrup and Torrilhon [21, 22]. The overprediction of drag for the Gaussian closure is once again reminiscent of its behaviour for cylinder drag, and can be attributed to the overpredicted growth of the Knudsen layer.

Using the linearized Boltzmann equation, Takata *et al.* [124] have found that a thermal polarization effect develops on the surface of the sphere. Furthermore, Torrilhon [116] has recently studied low-speed non-equilibrium flow over a sphere using the regularized 13-moment Grad closure on a two-dimensional grid with axisymmetric boundary conditions and found a similar temperature polarization effect. The temperature of the gas near the leading surface of the sphere rises while the trailing surface drops. However, similar to the lid-driven cavity flow discussed previously, the heat flux vectors from the results of both Takata *et al.* [124] and Torrilhon [116] originate from the back of the sphere towards the front, contrary to the heat flux / temperature gradient relationship dictated by Fourier's Laws. This can be seen in Figure 6.29(a) from Torrilhon [116], showing the temperature contours and heat flux vectors for flow over a sphere at Kn $= 0.3$. The counter-gradient heat flux effect is clearly evident, with the heat flux vectors forming a recirculation region above and below the sphere.

The regularized Gaussian solution for the same Knudsen number can be found in Figure 6.29(b). While the heat flux vectors are oriented in the same direction as those from the regularized 13-moment closure, the temperature profile is flipped to accommodate the heat flux vectors. This shows that, while the regularized Gaussian closure can predict the correct heat flux in this

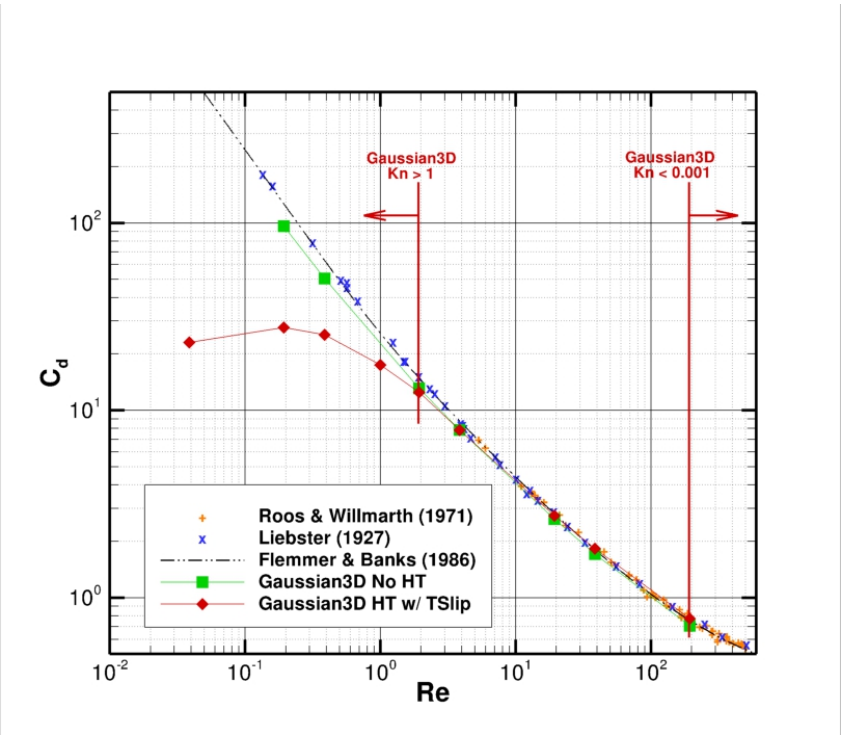

(a)

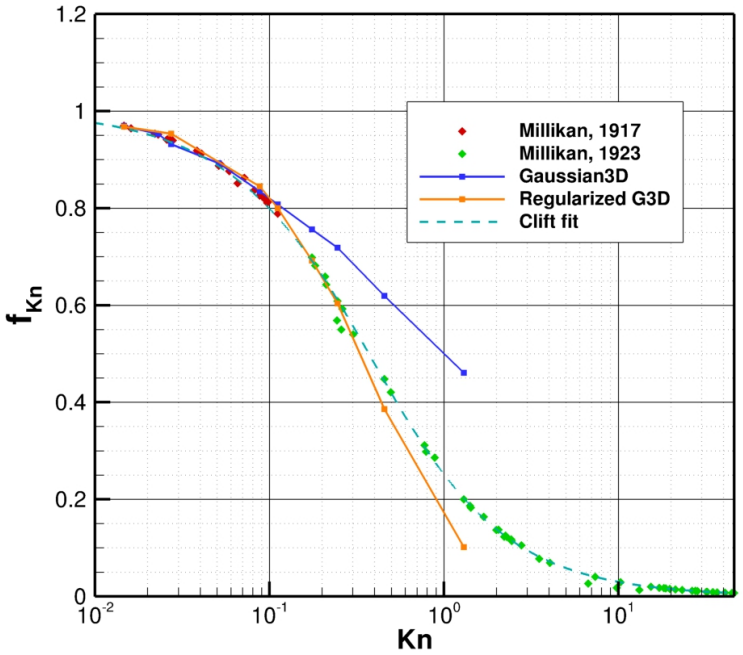

(b)

Figure 6.28: (a) Drag coefficient over a sphere: Regularized Gaussian closure vs. experimental and analytical results, (b) Stokes drag correction factor with varying Knudsen number for experimental results by Millikan [112,113], and some corresponding data points using the regularized Gaussian closure.

flow regime, the temperature profile is not decoupled from the heat flux and therefore cannot generate the counter-gradient behaviour predicted by Takata *et al.* [124] and Torrilhon [116].

At higher Knudsen numbers (Kn = 0.9), a similar analysis on the regularized 13-moment equations in Figure 6.29(a) reveals that the counter-gradient behaviour of the temperature profile has disappeared. The regularized Gaussian closure at this Knudsen number in Figure 6.29(b) similarly shows no counter-gradient effect. Torrilhon [116] has attributed this to the loss of validity of the regularized 13-moment closures for this higher range of Knudsen numbers. In contrast it appears, however, that the regularized Gaussian closure is never able to reproduce this counter-gradient behaviour regardless of Knudsen number. In particular, the boundary conditions used for the regularized Gaussian closure do not account for thermal transpiration effects that are important for accurately modelling counter-gradient heat fluxes in these flow regimes. Counter-gradient heat fluxes must take into account thermal stresses generated by temperature gradients within the bulk mass of the gas, and transpiration effects in the near-wall regime created by temperature gradients at the wall. While the strong coupling between temperature gradients and heat flux direction within the first-order correction in the regularized Gaussian closure remains as a primary source of error in modelling general counter-gradient effects, transpiration effects will directly affect how this counter-gradient behaviour evolves in the near-wall regime and is vital towards modelling this non-equilibrium flow phenomenon.

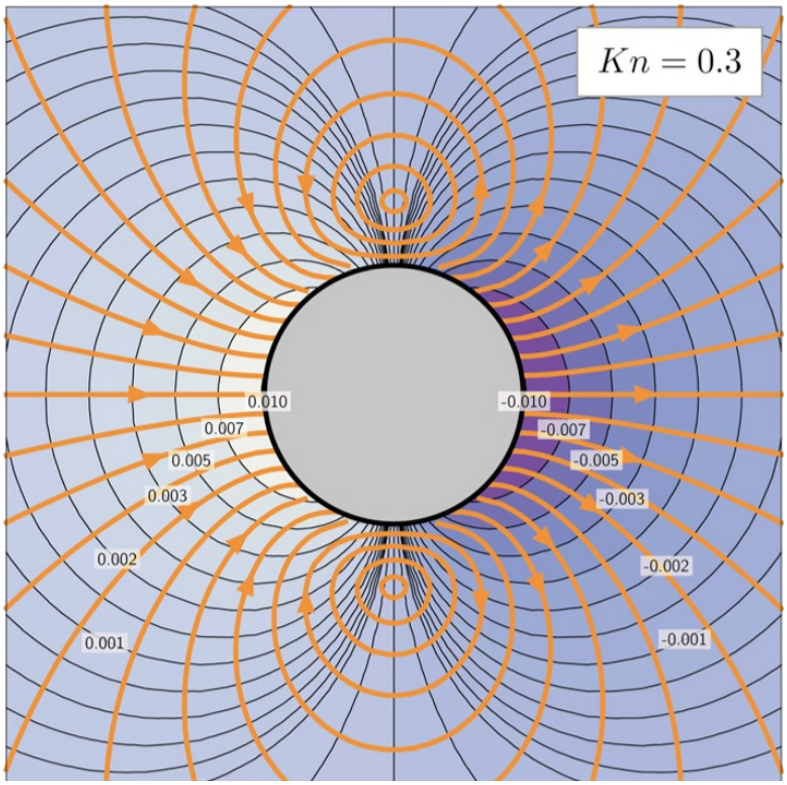

(a)

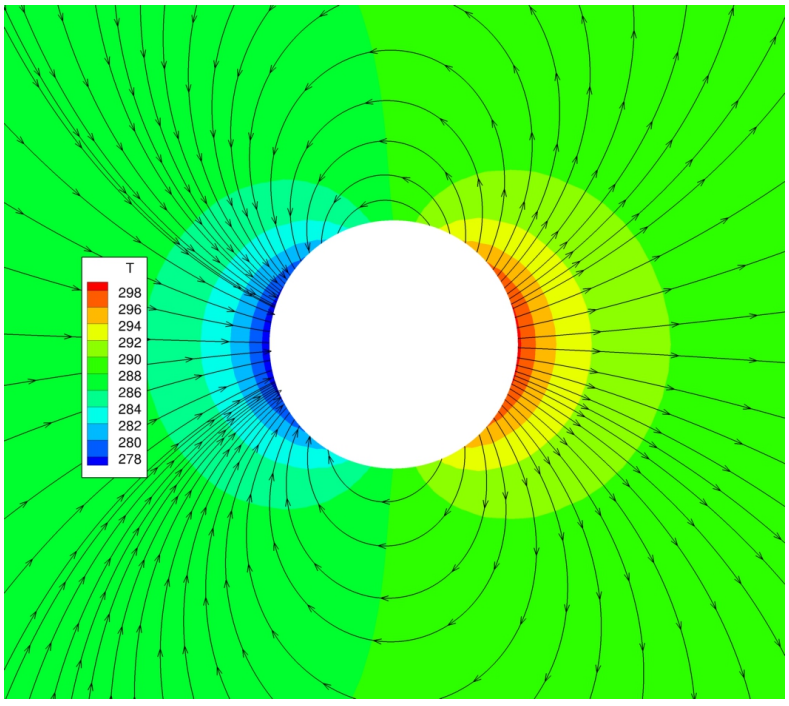

(b)

Figure 6.29: Temperature contours with heat flux vector streamlines for flow over a sphere at Kn = 0.3 calculated from a) the regularized Grad 13-moment closure performed by Torrilhon [116] and b) the regularized Gaussian closure.

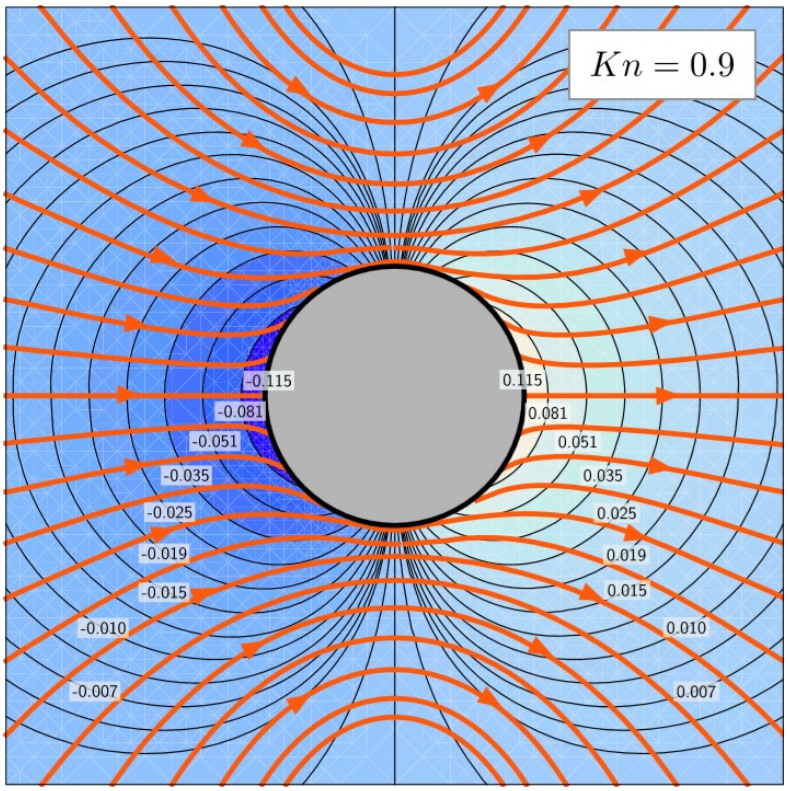

(a)

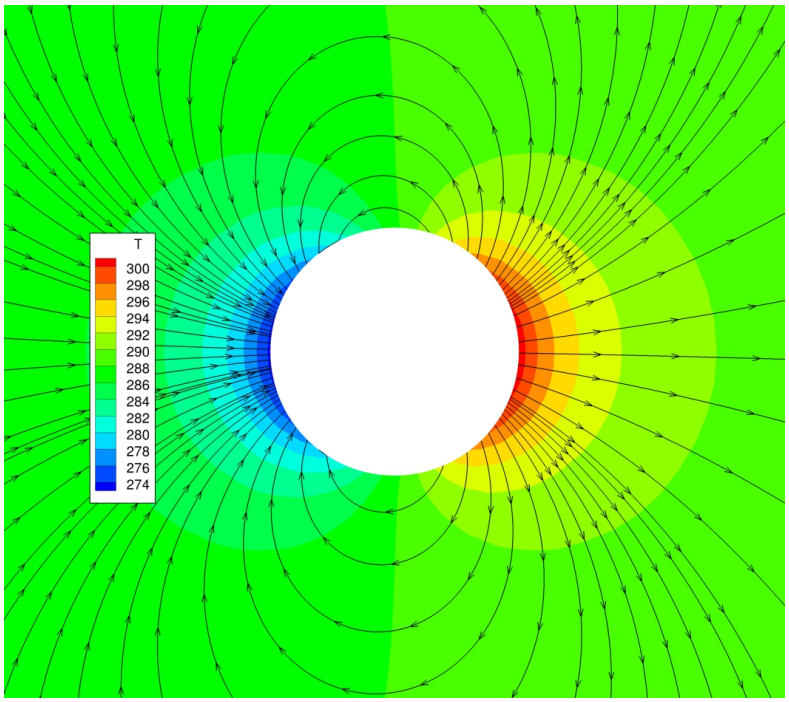

(b)

Figure 6.30: Temperature contours with heat flux vector streamlines for flow over a sphere at Kn = 0.9 calculated from a) the regularized Grad 13-moment closure performed by Torrilhon [116] and b) the regularized Gaussian closure.

Chapter 7

Conclusions and Future Research

7.1 Conclusions

The development of a parallel, implicit finite-volume method for the solution of the standard and regularized Gaussian closure for both monatomic and diatomic gases on three-dimensional, body-fitted, hexahedral mesh with block-based AMR and its subsequent application for a range of micro-scale flows has been considered in this thesis. This has yielded the first fully three-dimensional numerical solutions of the Gaussian closure for non-equilibrium gases, and some of the first moment closure solutions for geometries and flow conditions of more practical interest. Unlike the continuum-based Euler and Navier-Stokes equations, the Gaussian closures allow for an anisotropic pressure tensor directly, even in the absence of solution gradients. This and other considerations allow for the modelling of not only the continuum regimes, but also higher-Knudsen number regimes approaching free molecular flow. The inclusion of regularized terms describing heat flux have been incorporated into the original Gaussian system, and allows for a reasonably accurate depiction of none-equilibrium thermal phenomena, including the presence of a counter-gradient heat flux and suppressed boundary layer growth. Suitable boundary conditions describing velocity and temperature slip have also been developed that show agreement with both empirical and analytical results, though due to the regularization of the system, boundary conditions cannot be directly implemented on the heat flux. Nevertheless, the system of equations has been shown to possess certain computational advantages that have been exploited through the use of the implicit NKS solution method. The proposed finite-volume and NKS solution methods have been shown to maintain second-order spatial accuracy and reach highly converged states with drastically reduced computational cost.

The efficiency, robustness and accuracy of the Gaussian closures used in combination with the

NKS solution scheme have been clearly demonstrated through the application of the closure to various canonical flow problems which has yielded physically-realistic results over a wide range of Knudsen numbers. Numerical results for Couette flow have shown a smooth transition in the shear stress and slip velocities between continuum and free-molecular regimes, while a flat plate boundary layer profile solved with the Gaussian closure agrees closely with the Blasius solution and the slip velocity phenomenon is again clearly identified. The evolution of the boundary layers through the transition regime is shown through the modelling of immersed flow past a cylinder and a sphere, and a further comparison of drag coefficients of the cylinder in this regime agrees closely with experimental results.

The inclusion of heat flux terms through the regularization procedure has enabled the Gaussian closure to explore the effects of heat flux in high-Knudsen number regimes. A simple heated plate problem demonstrates the accuracy of the temperature slip boundary conditions and its effect on overall temperature profile between the plates. More complex problems involving high-Knudsen number heat flux in driven cavity flow and Poiseuille flow have shown that while the regularized heat flux terms effect the flow in the correct manner, the magnitude of the effects can be incorrect. The expansion cooling demonstrated in the driven cavity flow, while encouraging in the fact that the effect is absent in the Navier-Stokes solution, is much stronger than that predicted by the DSMC results. The bimodal heat flux profile in microscale Poiseuille flow is likewise duplicated, but incorrect in magnitude. Since heat flux is not calculated directly as a moment quantity, there exist no boundary conditions on it, and the resulting temperature slip effect is added in via a Knudsen layer treatment and empirical expression.

The regularized closure is applied again to immersed cylinder and sphere drag flow problems. These problems possess no significant initial temperature gradients, but it has been shown that the inclusion of heat flux terms significantly improves the performance of the Gaussian closure. While the original Gaussian closure tends to create excessively thick boundary layers that contribute to an overestimation of the drag at high Knudsen numbers, the heat flux terms of the regularized closures suppress that growth and maintain agreement with experimental and analytical results up to conditions approaching the free-molecular regime.

The performance of the NKS and semi-implicit scheme for the standard and regularized Gaussian closure for both monatomic and diatomic gases has been evaluated throughout for the flow problems considered in the thesis. The fully-implicit NKS method has been shown to consistently perform better than the time-marching approach from the semi-implicit method, requiring far less computational time given the same resources, and reaching a high level of convergence. This performance is maintained for a wide range of Knudsen numbers, though the convergence rate degrades somewhat for high Knudsen number flows. While computation-

ally cheaper on a per-iteration cost, the semi-implicit solver requires extremely small time steps even for transition regime flows carries heavy penalties in convergence rate. The proposed NKS solution scheme for the Gaussian closures is therefore shown to be both a robust and computationally efficient tool for analyzing three-dimensional non-equilibrium flow behaviour.

7.2 Future Recommendations

This study represents a first step for planned moment closure research pertaining to three-dimensional non-equilibrium gaseous flows. While the potential of such techniques has been demonstrated, a more thorough study for fully three-dimensional flows is certainly warranted and will be the focus of future research. It is worthwhile to note that moment methods in general have the capability to simulate a broader range of non-equilibrium fluid flow phenomena than what is afforded by the standard Navier-Stokes equations, such as velocity and temperature slip as shown in this thesis and counter-gradient heat fluxes as found by Takata *et al.* [124] and Torrilhon [116]. The development of higher-order moment closures methods therefore would provide more insight into flow behaviour under varying conditions, though computational considerations for cost and hyperbolicity will need to be addressed. Continuing work by Tensuda *et al.* [13, 14] on a set of interpolative closures based on Levermore's hierarchy of maximum-entropy closures [8] and its near-hyperbolic description of heat transfer provides another avenue of exploration into modelling higher-order moments at moderate Knudsen numbers.

Since the Gaussian closure does not handle heat flux directly as a moment quantity, there is no transport equation for heat flux and consequently there is also no boundary condition on it either. One method of possibly incorporating heat flux into the boundary conditions is to consider a half-Maxwellian type integration for the heat flux. While a full integration through the entire velocity space of this moment quantity will be zero, as dictated by the construction of the assumed non-equilibrium distribution function, a half-Maxwellian integration will provide non-zero boundary conditions. The problem then lies in equating this heat flux boundary condition with that from the heat flux term in the regularized closure. This leaves unknowns in the pressure gradient that need to be addressed. Some preliminary tests with this type boundary conditions briefly considered here but not reported, did not yield favourable results for moderate Knudsen numbers, though this approach may be feasible with the use of more appropriate expressions for the pressure gradient at the boundaries.

The lack of thermal transpiration in the boundary conditions constructed for the regularized Gaussian closure is a contributing factor that prevents it from accurately modelling counter-

gradient heat flux behaviour shown in the DSMC results by John *et al.* [118] and the regularized Grad 13-moment closure results by Torrilhon [116]. However, it may be possible to incorporate thermal transpiration terms to the velocity slip boundary conditions by using the boundary conditions derived from higher-order moment closures, such as those within the regularized Grad 13-moment closure, or the 14-moment closure by Tensuda *et al.* [13, 14]. This approach could also provide a better boundary conditions for the heat flux at the wall and alleviate the issues seen in the regularized Gaussian closure.

The Gaussian closures studied here have been subjected to tests concerning its computational and physical accuracy over problems with relatively simple geometries. The problems are solved over a fully three-dimensional grid, but the solutions with which they are compared to are largely limited to two-dimensional geometries. There are really no experiments conducted with fully non-axisymmetric three-dimensional microscale geometries with which to gauge the full potential of the Gaussian closures. Setting up and quantifying such problems in a physical environment is understandably difficult, and fully three-dimensional DSMC solutions can be very costly. Future research may provide solutions to such problems, in which case the evaluation of the regularized Gaussian closure can be taken into more detail. A direct application to industrial problems is certainly possible, given the feasibility of the proposed accelerated Newton-Krylov solver developed herein, and the closures' subsequent successes and failures can then point along new lines of inquiry.

Appendix A

Half-Maxwellian Integration for Solid Wall Boundaries

As described in Section 2.1.3, macroscopic properties can be found from the phase space distribution function by multiplying them with some chosen velocity functionals and integrating throughout all of phase space. The limits on the velocity components are taken to extend from $-\infty < \{v_x, v_y, v_z\} < +\infty$. Solid boundaries limit the movement of particles in certain directions depending on its orientation, and the limits of this integration must be modified accordingly. The derivation shown here considers a solid wall with a normal vector pointing in the $+x-$ direction into the fluid. Wall normals pointing in different directions are handled in the computational calculations by rotating the cell states into the $+x-$ direction to limit the complexity of the integration procedure.

The phase space distribution function at the wall is given as

$$\mathcal{F}_{\mathrm{Kn}} = \mathcal{F}_{-} + \mathcal{F}_{+}\,, \tag{A.1}$$

where $\mathcal{F}_{-}$ and $\mathcal{F}_{+}$ are given by

$$\mathcal{F}_{-} = \begin{cases} \mathcal{G}_{\mathrm{e}}(v_x, v_y, v_z) & \text{for} \quad v_x < 0\,, \\ 0 & \text{for} \quad v_x > 0\,, \end{cases} \tag{A.2}$$

$$\mathcal{F}_{+} = \begin{cases} \alpha\mathcal{M}_{\mathrm{w}}(v_x, v_y, v_z) + (1-\alpha)\mathcal{G}_{\mathrm{e}}(-v_x, v_y, v_z) & \text{for} \quad v_x > 0\,, \\ 0 & \text{for} \quad v_x < 0\,, \end{cases} \tag{A.3}$$

where $\mathcal{G}_{\mathrm{e}}$ represents the Gaussian particle distribution at the interior edge of the boundary and $\mathcal{M}_{\mathrm{w}}$ is a Maxwell-Boltzmann distribution defined by the solid wall properties.

Boundary conditions on the shear pressure are given here to show how to manage weighting factors with multiple velocity components. However, a similar half-Maxwellian integration process is required to find values for the bulk velocities (via a velocity weighting representing momentum) and density within the Knudsen layer. These lower order weights simplify the integration procedure shown here and are left as an exercise for the reader. Expressions for the bulk velocity and density within the Knudsen layer can be found in Eqs.(2.85) and (2.87).

Since particles cannot pass through the wall in the $-x$ direction, the limits on the integration of particle velocities in the $x-$direction are changed. The shear pressure P_{xy} is then formulated as

$$u_{x\,\mathrm{Kn}} = \overline{u}_x = 0, \tag{A.4}$$

$$\begin{aligned} P_{xy\,\mathrm{Kn}} = & \; m \int_0^\infty dv_x \int_{-\infty}^\infty dv_y \int_{-\infty}^\infty dv_z v_x \left(v_y - \overline{u}_y\right) \left[(1-\alpha)\,\mathcal{G}\left(-v_x, v_y, v_z\right) + \alpha \mathcal{M}\left(v_x, v_y, v_z\right)\right] \\ & + \; m \int_{-\infty}^0 dv_x \int_{-\infty}^\infty dv_y \int_{-\infty}^\infty dv_z v_x \left(v_y - \overline{u}_y\right) \left[\mathcal{G}\left(v_x, v_y, v_z\right)\right] \\ = & \; m \int_0^\infty dv_x \int_{-\infty}^\infty dv_y \int_{-\infty}^\infty dv_z v_x \left(v_y - \overline{u}_y\right) \left[-\alpha \mathcal{G}\left(-v_x, v_y, v_z\right) + \alpha \mathcal{M}\left(v_x, v_y, v_z\right)\right]. \end{aligned} \tag{A.5}$$

The Gaussian portion of the integrand is considered first. The Gaussian distribution function is given as

$$\begin{aligned} \mathcal{G}(t, x_i, c_i) &= \frac{(\rho/m)}{(2\pi)^{3/2} \left(\det \boldsymbol{\Theta}\right)^{1/2}} \exp\left(-\frac{1}{2}\Theta_{ij}^{-1} c_i c_j\right) \\ &= \mathbf{A} \exp\left(-\frac{1}{2}\left(\Theta_{xx}^{-1}c_x^2 + \Theta_{yy}^{-1}c_y^2 + \Theta_{zz}^{-1}c_z^2 + 2\Theta_{xy}^{-1}c_x c_y + 2\Theta_{xz}^{-1}c_x c_z + 2\Theta_{yz}^{-1}c_y c_z\right)\right) \end{aligned} \tag{A.6}$$

where

$$\mathbf{A} = \frac{(\rho/m)}{(2\pi)^{3/2} \left(\det \boldsymbol{\Theta}\right)^{1/2}}, \tag{A.7}$$

and Θ represents a pseudo-temperature tensor shown in Eq. (2.23), with an inverse defined in Eq. (2.25).

Substituting, the Gaussian portion of the integration becomes,

$$\begin{aligned} P_{xy,G} = & -\alpha m \int_0^\infty \mathrm{d}v_x \int_{-\infty}^\infty \mathrm{d}v_y \int_{-\infty}^\infty \mathrm{d}v_z \, v_x \left(v_y - \overline{u}_y\right) \left[\mathcal{G}\left(-v_x, v_y, v_z\right)\right] \\ = & -\alpha m \int_0^\infty \mathrm{d}v_x \int_{-\infty}^\infty \mathrm{d}v_y \int_{-\infty}^\infty \mathrm{d}v_z \, v_x \left(v_y - \overline{u}_y\right) \\ & \left[\mathbf{A} \exp\left(-\frac{1}{2}\left(\Theta_{xx}^{-1}v_x^2 + \Theta_{yy}^{-1}v_y^2 + \Theta_{zz}^{-1}v_z^2 + 2\Theta_{xy}^{-1}\left(-v_x\right)\left(v_y - u_{G_y}\right)\right.\right.\right. \\ & \left.\left.\left. + 2\Theta_{xz}^{-1}\left(-v_x\right)\left(v_z - u_{G_z}\right) + 2\Theta_{yz}^{-1}\left(v_y - u_{G_y}\right)\left(v_z - u_{G_z}\right)\right)\right)\right] \end{aligned} \tag{A.8}$$

where the substitution $v_x = \overline{u}_x + c_x, v_y = \overline{u}_y + c_y, v_z = \overline{u}_z + c_z$ has been made to express the integral purely in terms of the random velocities c_i, with $u_{x\,\mathrm{Kn}} = \overline{u}_x = 0$. Values for $\overline{u}_i$ represent the bulk velocities of the Knudsen layer and are addressed later.

This type of exponential integration can be performed with a series of integrations of the form

$$\int_{-\infty}^{\infty} e^{\left(-Ax^2+Bx\right)}\mathrm{d}x \tag{A.9}$$

where the mapping $x = X + \frac{B}{2A}$ is used such that

$$\int_{-\infty}^{\infty} e^{\left(-Ax^2+Bx\right)}\mathrm{d}x = \int_{-\infty}^{\infty} e^{\left(-AX^2+\frac{B}{4A}\right)}\mathrm{d}X = \sqrt{\frac{\pi}{A}}e^{\frac{B}{4A}} \tag{A.10}$$

When applied to the Gaussian integrand, the mapping

$$v_z - u_{G_z} = V_z - \frac{\Theta_{xz}^{-1}}{\Theta_{zz}^{-1}}\left(-v_x\right) - \frac{\Theta_{yz}^{-1}}{\Theta_{zz}^{-1}}\left(v_y - u_{G_y}\right) \tag{A.11}$$

is used to eliminate the $z-$direction dependency of the integration. The terms in the integration from Eq. (A.8) that contain $(v_z - u_{G_z})$ can be re-expressed as follows:

$$\begin{aligned}
\Theta_{zz}^{-1}\left(v_z - u_{G_z}\right) =& \Theta_{zz}^{-1}V_z^2 - 2\Theta_{xz}^{-1}V_z\left(-v_x\right) - 2\Theta_{yz}^{-1}V_z\left(v_y - u_{G_y}\right) + \frac{\left(\Theta_{xz}^{-1}\right)^2}{\Theta_{zz}^{-1}}\left(-v_x\right)^2 \\
&+ \frac{\left(\Theta_{yz}^{-1}\right)^2}{\Theta_{zz}^{-1}}\left(v_y - u_{G_y}\right)^2 + 2\frac{\Theta_{xz}^{-1}\Theta_{yz}^{-1}}{\Theta_{zz}^{-1}}\left(-v_x\right)\left(v_y - u_{G_y}\right) \\
2\Theta_{xz}^{-1}\left(-v_x\right)\left(v_z - u_{G_z}\right) =& 2\Theta_{xz}^{-1}\left(-v_x\right)V_z - 2\frac{\left(\Theta_{xz}^{-1}\right)^2}{\Theta_{zz}^{-1}}\left(-v_x\right)^2 - 2\frac{\Theta_{xz}^{-1}\Theta_{yz}^{-1}}{\Theta_{zz}^{-1}}\left(-v_x\right)\left(v_y - u_{G_y}\right) \\
2\Theta_{xz}^{-1}\left(v_y - u_{G_y}\right)\left(v_z - u_{G_z}\right) =& 2\Theta_{yz}^{-1}\left(v_y - u_{G_y}\right)V_z - 2\frac{\left(\Theta_{yz}^{-1}\right)^2}{\Theta_{zz}^{-1}}\left(v_y - u_{G_y}\right)^2 \\
&- 2\frac{\Theta_{xz}^{-1}\Theta_{yz}^{-1}}{\Theta_{zz}^{-1}}\left(-v_x\right)\left(v_y - u_{G_y}\right)
\end{aligned} \tag{A.12}$$

Note that in order to successfully apply this new mapping from v_z to V_z the limits of integration must also match. It is simple to see that as $v_z : -\infty \to +\infty$, so too does $V_z : -\infty \to +\infty$, evident from a rearranging of the mapping Eq. (A.11) into

$$V_z = \left(v_z - u_{G_z}\right) + \textit{independent terms.} \tag{A.13}$$

Substituting Eqs.(A.12) into the integral from Eq. (A.8) yields

$$\begin{aligned}
P_{xy,G} = &-\alpha m \int_0^\infty \mathrm{d}v_x \int_{-\infty}^\infty \mathrm{d}v_y \int_{-\infty}^\infty \mathrm{d}V_z \, v_x \left(v_y - \overline{u}_y\right) \\
&\left[\mathbf{A} \exp\left(-\frac{1}{2}\left(\Theta_{xx}^{-1} v_x^2 + \Theta_{yy}^{-1} v_y^2 + \Theta_{zz}^{-1} V_z^2 + 2\Theta_{xy}^{-1}\left(-v_x\right)\left(v_y - u_{G_y}\right)\right.\right.\right. \\
&\left.\left.\left. - \frac{\left(\Theta_{xz}^{-1}\right)^2}{\Theta_{zz}^{-1}}\left(-v_x\right)^2 - \frac{\left(\Theta_{yz}^{-1}\right)^2}{\Theta_{zz}^{-1}}\left(v_y - u_{G_y}\right)^2 - 2\frac{\Theta_{xz}^{-1}\Theta_{yz}^{-1}}{\Theta_{zz}^{-1}}\left(-v_x\right)\left(v_y - u_{G_y}\right)\right)\right)\right] \\
= &-\alpha m \mathbf{A} \left(\frac{2\pi}{\Theta_{zz}^{-1}}\right)^{\frac{1}{2}} \int_0^\infty \mathrm{d}v_x \int_{-\infty}^\infty \mathrm{d}v_y \, v_x \left(v_y - \overline{u}_y\right) \\
&\left[\exp\left(-\frac{1}{2}\left(A v_x^2 - 2B v_x \left(v_y - u_{G_y}\right) + C\left(v_y - u_{G_y}\right)^2\right)\right)\right], \qquad \text{(A.14)}
\end{aligned}$$

where the V_z terms have been integrated out, and

$$A = \frac{1}{\Theta_{zz}^{-1}}\left(\Theta_{xx}^{-1}\Theta_{zz}^{-1} - \left(\Theta_{xz}^{-1}\right)^2\right) \qquad \text{(A.15)}$$

$$B = \frac{1}{\Theta_{zz}^{-1}}\left(\Theta_{xy}^{-1}\Theta_{zz}^{-1} - \Theta_{xz}^{-1}\Theta_{yz}^{-1}\right) \qquad \text{(A.16)}$$

$$C = \frac{1}{\Theta_{zz}^{-1}}\left(\Theta_{yy}^{-1}\Theta_{zz}^{-1} - \left(\Theta_{yz}^{-1}\right)^2\right) \qquad \text{(A.17)}$$

As these terms are independent of velocity they may be treated as constants. This new integrand is once again in the same exponential form and a similar mapping procedure can be performed. By setting

$$v_y - u_{G_y} = V_y + \frac{B}{C} v_x, \qquad \text{(A.18)}$$

the remaining terms in the integrand can be re-expressed as

$$-2B v_x \left(v_y - u_{G_y}\right) = -2B v_x \left(V_y + \frac{B}{C} v_x\right) \qquad \text{(A.19)}$$

$$C\left(v_y - u_{G_y}\right)^2 = C V_y^2 + 2B v_x V_y + \frac{B^2}{C} v_x^2 \qquad \text{(A.20)}$$

and substituted into the integrand to reveal

$$\begin{aligned}
A v_x^2 - 2B v_x \left(v_y - u_{G_y}\right) + C\left(v_y - u_{G_y}\right)^2 &= \left(A - \frac{B^2}{C}\right) v_x^2 + C V_y^2 \\
&= \left(\frac{1}{C\Theta_{zz}^{-1} \det \boldsymbol{\Theta}}\right) v_x^2 + C V_y^2 \qquad \text{(A.21)}
\end{aligned}$$

Substituting this expression back into Eq. (A.14) transforms it into a separable form

$$\begin{aligned}
P_{xy,G} = &-\alpha m\mathbf{A}\left(\frac{2\pi}{\Theta_{zz}^{-1}}\right)^{\frac{1}{2}}\int_0^\infty \mathrm{d}v_x \int_{-\infty}^\infty \mathrm{d}V_y \\
&\quad v_x\left(V_y + \frac{B}{C}v_x + u_{G_y} - \overline{u}_y\right)\exp\left(-\frac{1}{2C\Theta_{zz}^{-1}\det\boldsymbol{\Theta}}\right)\exp\left(-\frac{1}{2}CV_y^2\right) \\
= &-\alpha m\mathbf{A}\left(\frac{2\pi}{\Theta_{zz}^{-1}}\right)^{\frac{1}{2}}\left[\int_0^\infty \mathrm{d}v_x\, v_x \exp\left(-\frac{1}{2C\Theta_{zz}^{-1}\det\boldsymbol{\Theta}}v_x^2\right)\int_{-\infty}^\infty \mathrm{d}V_y\, V_y \exp\left(-\frac{1}{2}CV_y^2\right)\right. \\
&\left. + \int_0^\infty \mathrm{d}v_x \left(\frac{B}{C}v_x + u_{G_y} - \overline{u}_y\right)\exp\left(-\frac{1}{2C\Theta_{zz}^{-1}\det\boldsymbol{\Theta}}v_x^2\right)\int_{-\infty}^\infty \mathrm{d}V_y \exp\left(-\frac{1}{2}CV_y^2\right)\right]
\end{aligned} \tag{A.22}$$

The first term in the integrand containing the integrand $V_y \exp\left(-\frac{1}{2}CV_y^2\right)$ is an odd function when integrated over the entire V_y velocity space and is by definition equivalent to zero. The remaining integral is separable and can be evaluated using expressions for definite integrals over exponential functions that can be found in a general integral table. Referring to Eqs.(2.23) and (2.25), the shear pressure can be further simplified to give

$$\begin{aligned}
P_{xy,G} = &-\alpha m\mathbf{A}\left(\frac{2\pi}{\Theta_{zz}^{-1}}\right)^{\frac{1}{2}}\left(\frac{2\pi}{C}\right)^{\frac{1}{2}}\left[\left(\frac{B\pi^{\frac{1}{2}}}{4C}\left(2C\Theta_{zz}^{-1}\det\boldsymbol{\Theta}\right)^{\frac{3}{2}}\right) + \left(u_{G_y} - \overline{u}_y\right)\left(C\Theta_{zz}^{-1}\det\boldsymbol{\Theta}\right)\right] \\
= &-\alpha m\left(\frac{n_G}{(2\pi)^{3/2}\left(\det\boldsymbol{\Theta}\right)^{1/2}}\right)\left(\frac{2\pi}{\Theta_{zz}^{-1}}\right)^{\frac{1}{2}}\left(\frac{2\pi\Theta_{zz}^{-1}}{\Theta_{yy}^{-1}\Theta_{zz}^{-1} - \left(\Theta_{yz}^{-1}\right)^2}\right)^{\frac{1}{2}}\left(\Theta_{yy}^{-1}\Theta_{zz}^{-1} - \left(\Theta_{yz}^{-1}\right)^2\right) \\
&\left(\det\boldsymbol{\Theta}\right)\left[\left(\frac{\pi\det\boldsymbol{\Theta}}{2}\right)^{\frac{1}{2}}\left(\frac{\Theta_{xy}^{-1}\Theta_{zz}^{-1} - \Theta_{xz}^{-1}\Theta_{yz}^{-1}}{\Theta_{yy}^{-1}\Theta_{zz}^{-1} - \left(\Theta_{yz}^{-1}\right)^2}\right)\left(\Theta_{yy}^{-1}\Theta_{zz}^{-1} - \left(\Theta_{yz}^{-1}\right)^2\right)^{\frac{1}{2}} + \left(u_{G_y} - \overline{u}_y\right)\right] \\
= &-\alpha m n_G\left[\left(\frac{\det\boldsymbol{\Theta}}{2\pi}\right)\left(\Theta_{yy}^{-1}\Theta_{zz}^{-1} - \left(\Theta_{yz}^{-1}\right)^2\right)\right]^{\frac{1}{2}} \\
&\left[\left(\frac{\Theta_{xy}^{-1}\Theta_{zz}^{-1} - \Theta_{xz}^{-1}\Theta_{yz}^{-1}}{\Theta_{yy}^{-1}\Theta_{zz}^{-1} - \left(\Theta_{yz}^{-1}\right)^2}\right)\left(\frac{\pi\det\boldsymbol{\Theta}}{2}\right)^{\frac{1}{2}} + \left(u_{G_y} - \overline{u}_y\right)\right] \\
= &\,\alpha\left[\frac{P_{xy}}{2} - \sqrt{\frac{\rho P_{xx}}{2\pi}}\left(u_{G_y} - \overline{u}_y\right)\right]
\end{aligned} \tag{A.23}$$

The Maxwellian portion of the integration is substantially simpler due to the structure of the Maxwell-Boltzmann distribution function. With the limitations on the $x-$directional velocities in place, the integration of the Maxwellian portion becomes

$$\begin{aligned}
P_{xy,M} = mn_w\alpha &\int_0^\infty \mathrm{d}v_x\, v_x\left(\frac{\beta}{\pi}\right)^{\frac{1}{2}}\exp\left[-\beta v_x^2\right] \\
&\int_{-\infty}^\infty \mathrm{d}v_y\ \left(v_y - \overline{u}_y\right)\left(\frac{\beta}{\pi}\right)^{\frac{1}{2}}\exp\left[-\beta\left(v_y - u_{wy}\right)^2\right] \\
&\int_{-\infty}^\infty \mathrm{d}v_z\left(\frac{\beta}{\pi}\right)^{\frac{1}{2}}\exp\left[-\beta v_z^2\right]
\end{aligned} \tag{A.24}$$

where u_{wy} and u_{wz} represent the bulk velocity of the wall. The even function integration over v_z is by definition equal to 1. Using a variable substitution $V_y = v_y - u_{wy}$,

$$\begin{aligned} P_{xy,M} &= mn_w\alpha\left(\frac{\beta}{\pi}\right)\left(\frac{1}{2\beta}\right)\left[\int_{-\infty}^{\infty} \mathrm{d}V_y \left(V_y + (u_{wy} - \overline{u}_y)\right) \exp\left[-\beta V_y^2\right]\right] \\ &= mn_w\alpha\left(\frac{1}{2\pi}\right)(u_{wy} - \overline{u}_y)\left(\frac{\pi}{\beta}\right)^{\frac{1}{2}} \\ &= \alpha\sqrt{\frac{P_{xx}\rho}{2\pi}}\,(u_{wy} - \overline{u}_y) \end{aligned} \tag{A.25}$$

Combining both the Gaussian and Maxwellian portions of the integration yields the shear pressure $P_{xy_{Kn}}$ within the Knudsen layer for a wall normal in the $+x$-direction:

$$\begin{aligned} P_{xy_{Kn}} &= P_{xy,G} + P_{xy,M} \\ &= \alpha\left[\frac{P_{xy}}{2} - \sqrt{\frac{\rho P_{xx}}{2\pi}}\left(u_{G_y} - \overline{u}_y\right)\right] + \alpha\sqrt{\frac{P_{xx}\rho}{2\pi}}\,(u_{wy} - \overline{u}_y) \end{aligned} \tag{A.26}$$

Appendix B

Flux Jacobians for the Gaussian Closure

The construction of the flux Jacobians specific for the 10-moment Gaussian closure needed for the Newton-Krylov implicit solver is a straightforward affair and is included here for reference. Evaluation of the viscous flux Jacobian for the regularized terms requires care, as the flux vector for the heat transfer terms is described in terms of the cell face solution state, as opposed to the cell center solution used in the hyperbolic fluxes. This comes about from the finite-volume treatment of elliptic fluxes using the centrally-weighted method for cell face gradients described by Mathur and Murphy [58].

For the 10-moment Gaussian closure for diatomic gases, the conserved state vector, $\mathbf{U}$, and primitive state vector, $\mathbf{W}$, is given by

$$\mathbf{U} = \begin{bmatrix} \rho \\ \rho u \\ \rho v \\ \rho w \\ \rho u^2 + P_{xx} \\ \rho uv + P_{xy} \\ \rho uw + P_{xz} \\ \rho v^2 + P_{yy} \\ \rho vw + P_{yz} \\ \rho w^2 + P_{zz} \\ E_{rot} \end{bmatrix}, \quad \mathbf{W} = \begin{bmatrix} \rho \\ u \\ v \\ w \\ P_{xx} \\ P_{xy} \\ P_{xz} \\ P_{yy} \\ P_{yz} \\ P_{zz} \\ E_{rot} \end{bmatrix}. \tag{B.1}$$

The Jacobian $\partial\mathbf{U}/\partial\mathbf{W}$ is then found to be

$$\frac{\partial \mathbf{U}}{\partial \mathbf{W}} = \begin{bmatrix} 1 & 0 & 0 & 0 & 0 & 0 & 0 & 0 & 0 & 0 & 0 \\ u & \rho & 0 & 0 & 0 & 0 & 0 & 0 & 0 & 0 & 0 \\ v & 0 & \rho & 0 & 0 & 0 & 0 & 0 & 0 & 0 & 0 \\ w & 0 & 0 & \rho & 0 & 0 & 0 & 0 & 0 & 0 & 0 \\ u^2 & 2\rho u & 0 & 0 & 1 & 0 & 0 & 0 & 0 & 0 & 0 \\ uv & \rho v & \rho u & 0 & 0 & 1 & 0 & 0 & 0 & 0 & 0 \\ uw & \rho w & 0 & \rho u & 0 & 0 & 1 & 0 & 0 & 0 & 0 \\ v^2 & 0 & 2\rho v & 0 & 0 & 0 & 0 & 1 & 0 & 0 & 0 \\ vw & 0 & \rho w & \rho v & 0 & 0 & 0 & 0 & 1 & 0 & 0 \\ w^2 & 0 & 0 & 2\rho w & 0 & 0 & 0 & 0 & 0 & 1 & 0 \\ 0 & 0 & 0 & 0 & 0 & 0 & 0 & 0 & 0 & 0 & 1 \end{bmatrix} \tag{B.2}$$

.

The Jacobian $\partial\mathbf{W}/\partial\mathbf{U}$ is simply the inverse of the matrix in Eq. (B.2), and is calculated as

$$\frac{\partial \mathbf{W}}{\partial \mathbf{U}} = \begin{bmatrix} 1 & 0 & 0 & 0 & 0 & 0 & 0 & 0 & 0 & 0 & 0 \\ -u/\rho & 1/\rho & 0 & 0 & 0 & 0 & 0 & 0 & 0 & 0 & 0 \\ -v/\rho & 0 & 1/\rho & 0 & 0 & 0 & 0 & 0 & 0 & 0 & 0 \\ -w/\rho & 0 & 0 & 1/\rho & 0 & 0 & 0 & 0 & 0 & 0 & 0 \\ u^2 & -2u & 0 & 0 & 1 & 0 & 0 & 0 & 0 & 0 & 0 \\ uv & -v & -u & 0 & 0 & 1 & 0 & 0 & 0 & 0 & 0 \\ uw & -w & 0 & -u & 0 & 0 & 1 & 0 & 0 & 0 & 0 \\ v^2 & 0 & -2v & 0 & 0 & 0 & 0 & 1 & 0 & 0 & 0 \\ vw & 0 & -w & -v & 0 & 0 & 0 & 0 & 1 & 0 & 0 \\ w^2 & 0 & 0 & -2w & 0 & 0 & 0 & 0 & 0 & 1 & 0 \\ 0 & 0 & 0 & 0 & 0 & 0 & 0 & 0 & 0 & 0 & 1 \end{bmatrix} \tag{B.3}$$

.

Orienting the cell states of two neighbouring cells such that the interface cell face normal is aligned in the $+x$-direction eliminates the need to account for any fluxes in the transverse direction along the cell face as they are equivalently zero. The construction of flux Jacobian is therefore only necessary for the $+x$-direction. The x-direction flux vector for the 10-moment

Gaussian closure is given in Section 2.3.3 as

$$\mathbf{F_x} = \begin{bmatrix} \rho u \\ \rho u^2 + P_{xx} \\ \rho uv + P_{xy} \\ \rho uw + P_{xz} \\ \rho u^3 + 3uP_{xx} \\ \rho u^2 v + 2uP_{xy} + vP_{xx} \\ \rho u^2 w + 2uP_{xz} + wP_{xx} \\ \rho uv^2 + uP_{yy} + 2vP_{xy} \\ \rho uvw + uP_{yz} + vP_{xz} + wP_{xy} \\ \rho w^2 u + uP_{zz} + 2wP_{xz} \\ uE_{rot} \end{bmatrix} \tag{B.4}$$

.

The Jacobian of this flux vector with respect to the primitive variables is found to be

$$\frac{\partial \mathbf{F}_x}{\partial \mathbf{W}} = \begin{bmatrix} u & \rho & 0 & 0 & 0 & 0 & 0 & 0 & 0 & 0 & 0 \\ u^2 & 2\rho u & 0 & 0 & 1 & 0 & 0 & 0 & 0 & 0 & 0 \\ uv & \rho v & \rho u & 0 & 0 & 1 & 0 & 0 & 0 & 0 & 0 \\ uw & \rho w & 0 & \rho u & 0 & 0 & 1 & 0 & 0 & 0 & 0 \\ u^3 & 3\rho u^2 + 3P_{xx} & 0 & 0 & 3u & 0 & 0 & 0 & 0 & 0 & 0 \\ u^2 v & 2\rho uv + 2P_{xy} & \rho u^2 + P_{xx} & 0 & v & 2u & 0 & 0 & 0 & 0 & 0 \\ u^2 w & 2\rho uw + 2P_{xz} & 0 & \rho u^2 + P_{xx} & w & 0 & 2u & 0 & 0 & 0 & 0 \\ uv^2 & \rho v^2 + P_{yy} & 2\rho uv + 2P_{xy} & 0 & 0 & 2v & 0 & u & 0 & 0 & 0 \\ uvw & \rho vw + P_{yz} & \rho uw + P_{xz} & \rho uv + P_{xy} & 0 & w & v & 0 & u & 0 & 0 \\ w^2 u & \rho w^2 + P_{zz} & 0 & 2\rho uw + 2P_{xz} & 0 & 0 & 2w & 0 & 0 & u & 0 \\ 0 & E_{rot} & 0 & 0 & 0 & 0 & 0 & 0 & 0 & 0 & u \end{bmatrix}. \tag{B.5}$$

The Jacobian of the flux vector with respect to the conserved solution state necessary for the Newton-Krylov solver can be found from the product of the Jacobian of the flux vector with respect the primitive state multiplied by the Jacobian in Eq. (B.3) as described in Eq. (4.13).

Performing this chain rule yields

$$\frac{\partial \mathbf{F}_x}{\partial \mathbf{U}} = \left(\frac{\partial \mathbf{F}_x}{\partial \mathbf{W}}\right)\left(\frac{\partial \mathbf{W}}{\partial \mathbf{U}}\right) =$$

$$\begin{bmatrix}
0 & 1 & 0 & 0 & 0 & 0 & 0 & 0 & 0 & 0 & 0 \\
0 & 0 & 0 & 0 & 1 & 0 & 0 & 0 & 0 & 0 & 0 \\
0 & 0 & 0 & 0 & 0 & 1 & 0 & 0 & 0 & 0 & 0 \\
0 & 0 & 0 & 0 & 0 & 0 & 1 & 0 & 0 & 0 & 0 \\
-\frac{u\left(-\rho u^2+3P_{xx}\right)}{\rho} & \frac{3\left(-\rho u^2+P_{xx}\right)}{\rho} & 0 & 0 & 0 & 3u & 0 & 0 & 0 & 0 & 0 \\
\frac{-\left(-\rho u^2 v+2uP_{xy}+vP_{xx}\right)}{\rho} & \frac{2(-\rho uv+P_{xy})}{\rho} & \frac{-\rho u^2+P_{xx}}{\rho} & 0 & v & 2u & 0 & 0 & 0 & 0 & 0 \\
\frac{-\left(-\rho u^2 w+2uP_{xz}+wP_{xx}\right)}{\rho} & \frac{2(-\rho uw+P_{xz})}{\rho} & 0 & \frac{-\rho u^2+P_{xx}}{\rho} & w & 0 & 2u & 0 & 0 & 0 & 0 \\
\frac{-\left(-\rho uv^2+uP_{yy}+2vP_{xy}\right)}{\rho} & \frac{-\rho v^2+P_{yy}}{\rho} & \frac{2(-\rho uv+P_{xy})}{\rho} & 0 & 0 & 2v & 0 & u & 0 & 0 & 0 \\
\frac{-(-\rho uvw+uP_{yz}+vP_{xz}+wP_{xy})}{\rho} & \frac{-\rho vw+P_{yz}}{\rho} & \frac{-\rho uw+P_{xz}}{\rho} & \frac{-\rho uv+P_{xy}}{\rho} & 0 & w & v & 0 & u & 0 & 0 \\
\frac{-\left(-\rho w^2 u+uP_{zz}+2wP_{xz}\right)}{\rho} & \frac{-\rho w^2+P_{zz}}{\rho} & 0 & \frac{2(-\rho uw+P_{xz})}{\rho} & 0 & 0 & 2w & 0 & 0 & u & 0 \\
\frac{E_{rot}u}{\rho} & \frac{E_{rot}}{\rho} & 0 & 0 & 0 & 0 & 0 & 0 & 0 & 0 & u
\end{bmatrix}. \tag{B.6}$$

For the regularized Gaussian closure, orienting the cell interface normal in the $+x$-direction does not eliminate the need to evaluate the Jacobians in the transverse directions since the elliptic fluxes are dependent on non-zero gradients at the cell face. As an example, the x-direction heat flux term shown in Eq. (2.62) can be written as

$$\mathbf{F}_{\mathbf{E},\mathbf{x}} = [0,\ 0,\ 0,\ 0,\ Q_{xx_x},\ Q_{xy_x},\ Q_{xz_x},\ Q_{yy_x},\ Q_{yz_x},\ Q_{zz_x},\ E_{rot}]^{\mathrm{T}}\ , \tag{B.7}$$

where

$$
\begin{aligned}
Q_{xx_x} &= 3\tau\left[\frac{P_{xx}}{\rho}\left(\frac{\partial P_{xx}}{\partial x}-\frac{P_{xx}}{\rho}\frac{\partial \rho}{\partial x}\right)+\frac{P_{xy}}{\rho}\left(\frac{\partial P_{xx}}{\partial y}-\frac{P_{xx}}{\rho}\frac{\partial \rho}{\partial y}\right)+\frac{P_{xz}}{\rho}\left(\frac{\partial P_{xx}}{\partial z}-\frac{P_{xx}}{\rho}\frac{\partial \rho}{\partial z}\right)\right]\\
Q_{xy_x} &= \tau\left[\frac{2P_{xx}}{\rho}\left(\frac{\partial P_{xy}}{\partial x}-\frac{P_{xy}}{\rho}\frac{\partial \rho}{\partial x}\right)+\frac{2P_{xy}}{\rho}\left(\frac{\partial P_{xy}}{\partial y}-\frac{P_{xy}}{\rho}\frac{\partial \rho}{\partial y}\right)+\frac{2P_{xz}}{\rho}\left(\frac{\partial P_{xy}}{\partial z}-\frac{P_{xy}}{\rho}\frac{\partial \rho}{\partial z}\right)\right.\\
&\quad\left.+\frac{P_{xy}}{\rho}\left(\frac{\partial P_{xx}}{\partial x}-\frac{P_{xx}}{\rho}\frac{\partial \rho}{\partial x}\right)+\frac{P_{yy}}{\rho}\left(\frac{\partial P_{xx}}{\partial y}-\frac{P_{xx}}{\rho}\frac{\partial \rho}{\partial y}\right)+\frac{P_{yz}}{\rho}\left(\frac{\partial P_{xx}}{\partial z}-\frac{P_{xx}}{\rho}\frac{\partial \rho}{\partial z}\right)\right]\\
Q_{xz_x} &= \tau\left[\frac{2P_{xx}}{\rho}\left(\frac{\partial P_{xz}}{\partial x}-\frac{P_{xz}}{\rho}\frac{\partial \rho}{\partial x}\right)+\frac{2P_{xy}}{\rho}\left(\frac{\partial P_{xz}}{\partial y}-\frac{P_{xz}}{\rho}\frac{\partial \rho}{\partial y}\right)+\frac{2P_{xz}}{\rho}\left(\frac{\partial P_{xz}}{\partial z}-\frac{P_{xz}}{\rho}\frac{\partial \rho}{\partial z}\right)\right.\\
&\quad\left.+\frac{P_{xz}}{\rho}\left(\frac{\partial P_{xx}}{\partial x}-\frac{P_{xx}}{\rho}\frac{\partial \rho}{\partial x}\right)+\frac{P_{yz}}{\rho}\left(\frac{\partial P_{xx}}{\partial y}-\frac{P_{xx}}{\rho}\frac{\partial \rho}{\partial y}\right)+\frac{P_{zz}}{\rho}\left(\frac{\partial P_{xx}}{\partial z}-\frac{P_{xx}}{\rho}\frac{\partial \rho}{\partial z}\right)\right]\\
Q_{yy_x} &= \tau\left[\frac{P_{xx}}{\rho}\left(\frac{\partial P_{yy}}{\partial x}-\frac{P_{yy}}{\rho}\frac{\partial \rho}{\partial x}\right)+\frac{P_{xy}}{\rho}\left(\frac{\partial P_{yy}}{\partial y}-\frac{P_{yy}}{\rho}\frac{\partial \rho}{\partial y}\right)+\frac{P_{xz}}{\rho}\left(\frac{\partial P_{yy}}{\partial z}-\frac{P_{yy}}{\rho}\frac{\partial \rho}{\partial z}\right)\right.\\
&\quad\left.+\frac{2P_{xy}}{\rho}\left(\frac{\partial P_{xy}}{\partial x}-\frac{P_{xy}}{\rho}\frac{\partial \rho}{\partial x}\right)+\frac{2P_{yy}}{\rho}\left(\frac{\partial P_{xy}}{\partial y}-\frac{P_{xy}}{\rho}\frac{\partial \rho}{\partial y}\right)+\frac{2P_{yz}}{\rho}\left(\frac{\partial P_{xy}}{\partial z}-\frac{P_{xy}}{\rho}\frac{\partial \rho}{\partial z}\right)\right]\\
Q_{yz_x} &= \tau\left[\frac{P_{xx}}{\rho}\left(\frac{\partial P_{yz}}{\partial x}-\frac{P_{yz}}{\rho}\frac{\partial \rho}{\partial x}\right)+\frac{P_{xy}}{\rho}\left(\frac{\partial P_{yz}}{\partial y}-\frac{P_{yz}}{\rho}\frac{\partial \rho}{\partial y}\right)+\frac{P_{xz}}{\rho}\left(\frac{\partial P_{yz}}{\partial z}-\frac{P_{yz}}{\rho}\frac{\partial \rho}{\partial z}\right)\right.\\
&\quad+\frac{P_{xz}}{\rho}\left(\frac{\partial P_{xy}}{\partial x}-\frac{P_{xy}}{\rho}\frac{\partial \rho}{\partial x}\right)+\frac{P_{yz}}{\rho}\left(\frac{\partial P_{xy}}{\partial y}-\frac{P_{xy}}{\rho}\frac{\partial \rho}{\partial y}\right)+\frac{P_{zz}}{\rho}\left(\frac{\partial P_{xy}}{\partial z}-\frac{P_{xy}}{\rho}\frac{\partial \rho}{\partial z}\right)\\
&\quad\left.+\frac{P_{xy}}{\rho}\left(\frac{\partial P_{xz}}{\partial x}-\frac{P_{xz}}{\rho}\frac{\partial \rho}{\partial x}\right)+\frac{P_{yy}}{\rho}\left(\frac{\partial P_{xz}}{\partial y}-\frac{P_{xz}}{\rho}\frac{\partial \rho}{\partial y}\right)+\frac{P_{yz}}{\rho}\left(\frac{\partial P_{xz}}{\partial z}-\frac{P_{xz}}{\rho}\frac{\partial \rho}{\partial z}\right)\right]\\
Q_{zz_x} &= \tau\left[\frac{2P_{xz}}{\rho}\left(\frac{\partial P_{xz}}{\partial x}-\frac{P_{xz}}{\rho}\frac{\partial \rho}{\partial x}\right)+\frac{2P_{yz}}{\rho}\left(\frac{\partial P_{xz}}{\partial y}-\frac{P_{xz}}{\rho}\frac{\partial \rho}{\partial y}\right)+\frac{2P_{zz}}{\rho}\left(\frac{\partial P_{xz}}{\partial z}-\frac{P_{xz}}{\rho}\frac{\partial \rho}{\partial z}\right)\right.\\
&\quad\left.+\frac{P_{xx}}{\rho}\left(\frac{\partial P_{zz}}{\partial x}-\frac{P_{zz}}{\rho}\frac{\partial \rho}{\partial x}\right)+\frac{P_{xy}}{\rho}\left(\frac{\partial P_{zz}}{\partial y}-\frac{P_{zz}}{\rho}\frac{\partial \rho}{\partial y}\right)+\frac{P_{xz}}{\rho}\left(\frac{\partial P_{zz}}{\partial z}-\frac{P_{zz}}{\rho}\frac{\partial \rho}{\partial z}\right)\right]
\end{aligned}
$$

Note that the above fluxes are the negative of those found from Eq. (2.62), as the Newton-Krylov solver pertaining to the implementation of second-order 'viscous' fluxes uses the inward-facing face normal, instead of the outward-facing normals used in other flux calculations. This methodology is reproduced for the Gaussian closures to maintain congruity with other solvers and equation sets in the group code.

The primitive solution state at the cell face, $\mathbf{W_f}$, contains the variables present in the cell center primitive solution state, $\mathbf{W_c}$, but also includes the derivatives of those variables with respect to each axial direction. This creates three Jacobians $\partial\mathbf{W_f}/\partial\mathbf{W_c}$, one for each direction applied respectively to a corresponding flux vector. Simplifications to the Jacobian can be made by realizing that the heat flux tensor contains no velocity terms or their corresponding derivatives, thus reducing the size of the primitive solution states and the resulting Jacobian matrix. The primitive solution state at the cell face can then be written in tensor notation as

$$
\mathbf{W_f} = \left[\rho,\ P_{ij},\ E_{rot},\ \frac{\partial \rho}{\partial x_i},\ \frac{\partial P_{ij}}{\partial x_i},\ \frac{\partial E_{rot}}{\partial x_i}\right]^{\mathrm{T}}, \tag{B.8}
$$

The vector contains 32 distinct terms, such that the Jacobian $\partial \mathbf{F}_{\mathbf{E},\mathbf{x}} / \partial \mathbf{W}_{\mathbf{f}}$ is of dimension 11×32. This largely sparse matrix is somewhat large for inclusion in print, but is sufficiently simple to generate with symbolic mathematics software. The required flux Jacobian with respect to the conserved variables is found by multiplying this Jacobian with the Jacobian found in Eq. (B.3).

References

[1] Bird, G. A., *Molecular Gas Dynamics and the Direct Simulation of Gas Flows*, Clarendon Press, Oxford, 1994.

[2] Hellman, A. N., Kaustubh, R. R., Yoon, H. H., Bae, S., Palmer, J. F., Phillips, K. S., Allbritton, N. L., and Venugopalan, V., "Laser-Induced Mixing in Microfluidic Channels," *Analytical Chemistry*, Vol. 79, 2007, pp. 4484–4492.

[3] Maxwell, J. C., "On the Dynamical Theory of Gases," *Philosophical Transactions of the Royal Society of London*, Vol. 157, 1867, pp. 49–88.

[4] Boltzmann, L., "Weitere Studien über das Wärmegleichgewicht unter Gasmolekülen," *Sitzungsberichte der Akademie der Wissenschaften*, Vol. 66, 1872, pp. 275–370.

[5] Grad, H., "On the Kinetic Theory of Rarefied Gases," *Communications on Pure and Applied Mathematics*, Vol. 2, 1949, pp. 331–407.

[6] Dreyer, W., "Maximisation of the entropy in non-equilibrium," *Journal of Physics A: Mathematical and General*, Vol. 20, 1987, pp. 6505–6517.

[7] Müller, I. and Ruggeri, T., *Extended Thermodynamics*, Springer-Verlag, New York, 1993.

[8] Levermore, C. D., "Moment Closure Hierarchies for Kinetic Theories," *Journal of Statistical Physics*, Vol. 83, 1996, pp. 1021–1065.

[9] Junk, M., "Domain of Definition of Levermore's Five-Moment System," *Journal of Statistical Physics*, Vol. 93, No. 5/6, 1998, pp. 1143–1167.

[10] Godunov, S. K., "Finite-Difference Method for Numerical Computations of Discontinuous Solutions of the Equations of Fluid Dynamics," *Matematicheskii Sbornik*, Vol. 47, 1959, pp. 271–306.

[11] McDonald, J. G. and Groth, C. P. T., "Towards Realizable Hyperbolic Moment Closures for Viscous Heat-Conducting Gas Flows Based on a Maximum-Entropy Distribution," Vol. 25, 2013, pp. 573–603.

[12] McDonald, J. G. and Torrilhon, M., "Affordable Robust Moment Closures for CFD Based on the Maximum-Entropy Hierarchy," *Journal of Computational Physics*, Vol. 251, 2013, pp. 500–523.

[13] Tensuda, B., McDonald, J., and Groth, C., "Numerical Solution of a Maximum-Entropy-Based 14-Moment Closure for Multi-Dimensional Flows," *Proceedings of the Eighth International Conference on Computational Fluid Dynamics, ICCFD8, Chengdu, China, July 14–18, 2014*, edited by H. Zhang, X. Deng, and Z. Fans, 2014, pp. 1491–1507.

[14] Tensuda, B., McDonald, J., and Groth, C. P. T., "Application of a Maximum-Entropy-Based 14-Moment Closure for Multi-Dimensional Non-Equilibrium Flows," Paper 2015-3420, AIAA, June 2015.

[15] McDonald, J. G. and Groth, C. P. T., "Numerical Modeling of Micron-Scale Flows Using the Gaussian Moment Closure," Paper 2005-5035, AIAA, June 2005.

[16] McDonald, J. and Groth, C. P. T., "Extended Fluid-Dynamic Model for Micron-Scale Flows Based on Gaussian Moment Closure," Paper 2008-691, AIAA, January 2008.

[17] Groth, C. P. T. and McDonald, J. G., "Towards Physically-Realizable and Hyperbolic Moment Closures for Kinetic Theory," *Continuum Mechanics and Thermodynamics*, Vol. 21, 2010, pp. 467–493.

[18] McDonald, J. G., *Extended Fluid-Dynamic Modelling for Numerical Solution of Micro-Scale Flows*, Ph.D. thesis, University of Toronto, 2010.

[19] Hittinger, J. A., *Foundations for the Generalization of the Godunov Method to Hyperbolic Systems with Stiff Relaxation Source Terms*, Ph.D. thesis, University of Michigan, 2000.

[20] Struchtrup, H., *Macroscopic Transport Equations for Rarefied Gas Flows*, Springer-Verlag, Berlin, 2005.

[21] Struchtrup, H. and Torrilhon, M., "Regularization of Grad's 13 Moment Equations: Derivation and Linear Analysis," *Physics of Fluids*, Vol. 15, No. 9, 2003, pp. 2668–2680.

[22] Struchtrup, H. and Torrilhon, M., "H Theorem, Regularization, and Boundary Conditions for the Linearized 13 Moment Equations," *Physical Review Letters*, Vol. 99, 2007, pp. 014502.

[23] Torrilhon, M. and Struchtrup, H., "Boundary Conditions for Regularized 13 Moment Equations for Micro-Channel-Flows," *Journal of Computational Physics*, Vol. 227, 2008, pp. 1982–2011.

[24] Brown, S. L., Roe, P. L., and Groth, C. P. T., "Numerical Solution of a 10-Moment Model for Nonequilibrium Gasdynamics," Paper 95-1677, AIAA, June 1995.

[25] Brown, S. L., *Approximate Riemann Solvers for Moment Models of Dilute Gases*, Ph.D. thesis, University of Michigan, 1996.

[26] Barth, T. J., "On Discontinuous Galerkin Approximations of Boltzmann Moment Systems with Levermore Closure," *Computer Methods in Applied Mechanics and Engineering*, Vol. 195, 2006, pp. 3311–3330.

[27] Levermore, C. D. and Morokoff, W. J., "The Gaussian Moment Closure for Gas Dynamics," *SIAM Journal on Applied Mathematics*, Vol. 59, No. 1, 1999, pp. 72–96.

[28] Groth, C. P. T. and Northrup, S. A., "Parallel Implicit Adaptive Mesh Refinement Scheme for Body-Fitted Multi-Block Mesh," Paper 2005-5333, AIAA, June 2005.

[29] Charest, M. R. J., Groth, C. P. T., and Gülder, Ö. L., "A Parallel Solution Adaptive Method for Radiative Heat Transfer Using a Newton-Krylov Approach," *Proceedings of the 18th Annual Conference of the CFD Society of Canada, London, Ontario, Canada, May 18-19, 2010*, 2010.

[30] Hicken, J. E. and Zingg, D. W., "Parallel Newton-Krylov Solver for the Euler Equations Discretized Using Simultaneous-Approximation Terms," *AIAA Journal*, Vol. 46, No. 11, 2008, pp. 2773–2786.

[31] Osusky, L., Buckley, H., Reist, T., and Zingg, D. W., "Drag Minimization Based on the Navier-Stokes Equations Using a Newton-Krylov Approach," *AIAA Journal*, Vol. 53, No. 6, 2015, pp. 1555–1577.

[32] Gao, X. and Groth, C. P. T., "Parallel Adaptive Mesh Refinement Scheme for Three-Dimensional Turbulent Non-Premixed Combustion," Paper 2008-1017, AIAA, January 2008.

[33] Gao, X. and Groth, C. P. T., "A Parallel Solution-Adaptive Method for Three-Dimensional Turbulent Non-Premixed Combusting Flows," *Journal of Computational Physics*, Vol. 229, No. 5, 2010, pp. 3250–3275.

[34] Gao, X., *A Parallel Solution-Adaptive Method for Turbulent Non-Premixed Combusting Flows*, Ph.D. thesis, University of Toronto, August 2008.

[35] Gombosi, T. I., *Gaskinetic Theory*, Cambridge University Press, Cambridge, 1994.

[36] Chapman, S. and Cowling, T. G., *The Mathematical Theory of Non-Uniform Gases*, Cambridge University Press, Cambridge, 1960.

[37] Burgers, J. M., *Flow Equations for Composite Gases*, Academic Press, New York, 1969.

[38] Bobylev, A. V. and Cercignani, C., "Exact Eternal Solutions of the Boltzmann Equation," *Journal of Statistical Physics*, Vol. 106, No. 5, 2002, pp. 1019–1038.

[39] Bobylev, A. V. and Cercignani, C., "Self-Similar Solutions of the Boltzmann Equation and Their Applications," *Journal of Statistical Physics*, Vol. 106, No. 6, 2002, pp. 1039–1071.

[40] Bhatnagar, P. L., Gross, E. P., and Krook, M., "A Model for Collision Processes in Gases. I. Small Amplitude Processes in Charged and Neutral One-Component Systems," *Physical Review*, Vol. 94, No. 3, 1954, pp. 511–525.

[41] Holway, L. H., "New Statistical Models for Kinetic Theory: Methods of Construction," *Physics of Fluids*, Vol. 9, No. 9, 1966, pp. 1658–1673.

[42] Andries, P. and Perthame, B., "The ES-BGK Model Equation with Correct Prandtl Number," *Rarefied Gas Dynamics*, edited by T. J. Bartel and M. A. Gallis, Vol. I, American Institute of Physics, New York, 2001, pp. 30–36.

[43] Andries, P., Le Tallec, P., Perlat, J.-P., and Perthame, B., "The Gaussian-BGK model of Boltzmann Equation with Small Prandtl Number," *European Journal of Mechanics B — Fluids*, Vol. 19, 2000, pp. 813–830.

[44] Junk, M., "Maximum Entropy Moment Systems and Galilean Invariance," Vol. 14, 2002, pp. 563–576.

[45] Hertweck, F., "Allgemeine 13-Momenten-Näherung zur Fokker-Planck-Gleichung eines Plasmas," *Zeitschrift für Naturforschung*, Vol. 20a, 1965, pp. 1243–1255.

[46] Oraevskii, V., Chodura, R., and Feneberg, W., "Hydrodynamic Equations for Plasmas in Strong Magnetic Fields — I Collisionless Approximation," *Plasma Physics*, Vol. 10, 1968, pp. 819–828.

[47] Holway, L. H., *Approximation Procedures for Kinetic Theory*, Ph.D. thesis, Harvard University, 1963.

[48] Holway, L. H., "Kinetic Theory of Shock Structure Using an Ellipsoidal Distribution Function," *Rarefied Gas Dynamics*, edited by J. H. e Leeuw, Vol. I, Academic Press, New York, 1966, pp. 193–215.

[49] Holway, L. H., "The Effect of Collisional Models upon Shock Wave Structure," *Rarefied Gas Dynamics*, edited by C. L. Brundin, Vol. I, Academic Press, New York, 1967, pp. 759–784.

[50] McDonald, J. G., Sachdev, J. S., and Groth, C. P. T., "Application of Gaussian Moment Closure to Micro-Scale Flows with Moving and Embedded Boundaries," Vol. 52, No. 9, 2014, pp. 1839–1857.

[51] Hadjiconstantinou, N. G., "The limits of Navier-Stokes theory and kinetic extensions for describing small-scale gaseous hydrodynamics," *Physics of Fluids*, Vol. 18, No. 11, 2006, pp. 111301.

[52] Lauga, E. and Stone, H. A., "Effective slip in pressure-driven Stokes flow," *Journal of Fluid Mechanics*, Vol. 489, 2003, pp. 55–77.

[53] Kennard, E. H., *Kinetic Theory of Gases*, McGraw-Hill, New York, 1938.

[54] Gao, X. and Groth, C. P. T., "Parallel Adaptive Mesh Refinement Scheme for Turbulent Non-Premixed Combusting Flow Prediction," Paper 2006-1448, AIAA, January 2006.

[55] Gao, X. and Groth, C. P. T., "A Parallel Adaptive Mesh Refinement Algorithm for Predicting Turbulent Non-Premixed Combusting Flows," *International Journal of Computational Fluid Dynamics*, Vol. 20, No. 5, 2006, pp. 349–357.

[56] Gao, X. and Groth, C. P. T., "A Parallel Solution-Adaptive Method for Three-Dimensional Turbulent Non-Premixed Combusting Flows," *Journal of Computational Physics*, Vol. 229, No. 5, 2010, pp. 3250–3275.

[57] Gao, X., Northrup, S. A., and Groth, C. P. T., "Parallel Solution-Adaptive Method for Two-Dimensional Non-Premixed Combusting Flows," Vol. 11, No. 2, 2011, pp. 76–95.

[58] Mathur, S. R. and Murthy, J. Y., "A Pressure-Based Method for Unstructured Meshes," Vol. 31, 1997, pp. 191–215.

[59] Northrup, S. A., *A Parallel Implicit Adaptive Mesh Refinement Algorithm for Predicting Unsteady Fully-Compressible Reactive Flows*, Ph.D. thesis, University of Toronto, 2014.

[60] Charest, M. R. J., Groth, C. P. T., and Gülder, Ö. L., "A Parallel Solution Adaptive Method for Radiative Heat Transfer Using a Newton-Krylov Approach," *Proceedings of the 18th Annual Conference of the CFD Society of Canada, London, Ontario, Canada, May 18-19, 2010*, 2010.

[61] Lam, C., *Application of Gaussian Moment Closure Methods to Three-Dimensional Micro-Scale Flows*, Master's thesis, University of Toronto, June 2011.

[62] Susanto, A., Ivan, L., Sterck, H. D., and Groth, C. P. T., "High-order central ENO finite-volume scheme for ideal MHD," *Journal of Computational Physics*, Vol. 250, 2013, pp. 141–164.

[63] Ivan, L., Sterck, H. D., Northrup, S. A., and Groth, C. P. T., "Three dimensional MHD on cubed-sphere grids: parallel solution-adaptive simulation framework," Paper 2011-3382, AIAA, January 2011.

[64] Ivan, L., Sterck, H. D., Northrup, S. A., and Groth, C. P. T., "Multi-dimensional finite-volume scheme for hyperbolic conservation laws on three-dimensional solution-adaptive cubed-sphere grids," *Journal of Computational Physics*, Vol. 255, 2013, pp. 205–22758.

[65] Ivan, L., Northrup, S. A., Groth, C. P. T., and Sterck, H. D., "Adaptive cubed-sphere simulation framework for space physics flows," *Proceedings of the 18th Annual Conference of the CFD Society of Canada, London, Ontario, Canada, May 18-19, 2010*, 2010.

[66] Groth, C. P. T. and McDonald, J. G., "Towards Physically-Realizable and Hyperbolic Moment Closures for Kinetic Theory," Vol. 21, No. 6, 2009, pp. 467–493.

[67] Lomax, H., Pulliam, T. H., and Zingg, D. W., *Fundamentals of Computational Fluid Dynamics*, Springer-Verlag, New York, 2001.

[68] Hirsch, C., *Numerical Computation of Internal and External Flows, Volume 1, Fundamentals of Numerical Discretization*, John Wiley & Sons, Toronto, 1989.

[69] Hirsch, C., *Numerical Computation of Internal and External Flows, Volume 2, Computational Methods for Inviscid and Viscous Flows*, John Wiley & Sons, Toronto, 1990.

[70] Barth, T. J., "Recent Developments in High Order K-Exact Reconstruction on Unstructured Meshes," Paper 93-0668, AIAA, January 1993.

[71] Venkatakrishnan, V., "On the Accuracy of Limiters and Convergence to Steady State Solutions," Paper 93-0880, AIAA, January 1993.

[72] Roe, P. L., "Approximate Riemann Solvers, Parameter Vectors, and Difference Schemes," *Journal of Computational Physics*, Vol. 43, 1981, pp. 357–372.

[73] Gottlieb, J. J. and Groth, C. P. T., "Assessment of Riemann Solvers for Unsteady One-Dimensional Inviscid Flows of Perfect Gases," *Journal of Computational Physics*, Vol. 78, 1988, pp. 437–458.

[74] Harten, A., "High Resolution Schemes for Hyperbolic Conservation Laws," *Journal of Computational Physics*, Vol. 49, 1983, pp. 357–393.

[75] Einfeldt, B., "On Godunov-Type Methods for Gas Dynamics," *SIAM Journal on Numerical Analysis*, Vol. 25, 1988, pp. 294–318.

[76] Linde, T., "A Practical, General-Purpose, Two-State HLL Riemann Solver for Hyperbolic Conservation Laws," *International Journal for Numerical Methods in Fluids*, Vol. 40, 2002, pp. 391–402.

[77] Barth, T. J. and Jespersen, D. C., "The Design and Application of Upwind Schemes on Unstructured Meshes," Paper 89-0366, AIAA, January 1989.

[78] Sachdev, J. S., Groth, C. P. T., and Gottlieb, J. J., "A Parallel Solution-Adaptive Scheme for Predicting Multi-Phase Core Flows in Solid Propellant Rocket Motors," *International Journal of Computational Fluid Dynamics*, Vol. 19, No. 2, 2005, pp. 159–177.

[79] Northrup, S. A. and Groth, C. P. T., "Solution of Laminar Diffusion Flames Using a Parallel Adaptive Mesh Refinement Algorithm," Paper 2005–0547, AIAA, January 2005.

[80] Charest, M. R. J., Groth, C. P. T., and Gülder, O. L., "A Computational Framework for Predicting Laminar Reactive Flows with Soot Formation," *Combustion Theory and Modelling*, Vol. 14, No. 6, 2011, pp. 793–825.

[81] Charest, M. R. J., Joo, H. I., Groth, C. P. T., and Gülder, O. L., "Experimental and Numerical Study of Soot Formation in Laminar Ethylene Diffusion Flames at Elevated Pressures from 10 to 35 atm," Vol. 33, 2011, pp. 549–557.

[82] Charest, M. R. J., Groth, C. P. T., and Gülder, O. L., "Effects of Gravity and Pressure on Laminar Co-flow Methane-Air Diffusion Flames at Pressures from 1 to 60 Atmospheres," Vol. 158, No. 5, 2011, pp. 860–875.

[83] Sachdev, J. S., Groth, C. P. T., and Gottlieb, J. J., "Parallel AMR Scheme for Turbulent Multi-Phase Rocket Motor Core Flows," Paper 2005-5334, AIAA, June 2005.

[84] Charest, M. R. J., Groth, C. P. T., and Gülder, O. L., "Solution of the Equation of Radiative Transfer Using a Newton-Krylov Approach and Adaptive Mesh Refinement," *Journal of Computational Physics*, Vol. 231, 2012, pp. 3023–3040.

[85] Sachdev, J. S. and Groth, C. P. T., "A Mesh Adjustment Scheme for Embedded Boundaries," Vol. 2, No. 6, 2007, pp. 1095–1124.

[86] Zhang, Z. J. and Groth, C. P. T., "Parallel High-Order Anisotropic Block-Based Adaptive Mesh Refinement Finite-Volume Scheme," Paper 2011-3695, AIAA, June 2011.

[87] Williamschen, M. J. and Groth, C. P. T., "Parallel anisotropic block-based adaptive mesh refinement algorithm for three-dimensional flows," Paper 2013-2442, AIAA, June 2013.

[88] Jameson, A., "Solution of the Euler Equations by a Multigrid Method," *Applied Mathematics and Computation*, Vol. 13, 1983, pp. 327–356.

[89] Groth, C. P. T., De Zeeuw, D. L., Powell, K. G., Gombosi, T. I., and Stout, Q. F., "A Parallel Solution-Adaptive Scheme for Ideal Magnetohydrodynamics," Paper 99-3273, AIAA, June 1999.

[90] Tai, C., Sheu, J., and van Leer, B., "Optimal Multistage Schemes for Euler Equations with Residual Smoothing," *AIAA Journal*, Vol. 33, No. 6, 1995, pp. 1008–1016.

[91] Dembo, R. S., Eisenstat, S. C., and Steihaug, T., "Inexact Newton Methods," *SIAM Journal on Numerical Analysis*, Vol. 19, No. 2, 1982, pp. 400–408.

[92] Brown, P. N. and Saad, Y., "Hybrid Krylov Methods for Nonlinear Systems of Equations," *SIAM Journal for Scientific and Statistical Computing*, Vol. 11, No. 3, 1990, pp. 450–481.

[93] Saad, Y., *Iterative Methods for Sparse Linear Systems*, PWS Publishing Company, Boston, 1996.

[94] Saad, Y. and Schultz, M. H., "GMRES: A Generalized Minimal Residual Algorithm for Solving Nonsymmetric Linear Equations," *SIAM Journal for Scientific and Statistical Computing*, Vol. 7, No. 3, 1986, pp. 856–869.

[95] McHugh, P. R. and Knoll, D. A., "Comparison of Standard and Matrix-Free Implementations of Several Newton-Krylov Solvers," *AIAA Journal*, Vol. 32, No. 12, 1994, pp. 2394–2400.

[96] Schwarz, H. A., "Gesammelte Mathematische Abhandlungen," *Vierteljahrsschrift der Naturforschenden Gesellschaft in Zürich*, Vol. 15, 1870, pp. 272–286.

[97] Mulder, W. A. and van Leer, B., "Experiments with Implicit Upwind Methods for the Euler Equations," *Journal of Computational Physics*, Vol. 59, 1985, pp. 232–246.

[98] Northrup, S. A. and Groth, C. P. T., "Prediction of Unsteady Laminar Flames Using a Parallel Implicit Adaptive Mesh Refinement Algorithm," *Proceedings of the U. S. National Combustion Meeting, Ann Arbor, Michigan, U.S.A., May 17–20, 2009*, 2009, p. 23H3.

[99] Nielsen, E. J., Anderson, W. K., Walters, R. W., and Keyes, D. E., "Application of Newton-Krylov Methodology to a Three-Dimensional Unstructured Euler Code," Paper 95-1733-CP, AIAA, June 1995.

[100] Sachdev, J. S., *Parallel Solution-Adaptive Method for Predicting Solid Propellant Rocket Motor Core Flows*, Ph.D. thesis, University of Toronto, April 2007.

[101] Vedovotoa, J. M. and A. da Silveira Netoa, A. Murab, L. F. F. d. S., "Application of the method of manufactured solutions to the verification of a pressure-based finite-volume numerical scheme," *Computers & Fluids*, Vol. 51, 2011, pp. 85–99.

[102] Zhang, T., Jia, L., and Wang, Z., "Validation of Navier-Stokes equations for slip flow analysis within transition region," *International Journal of Heat and Mass Transfer*, Vol. 51, No. 25-26, 2008, pp. 6323–6327.

[103] Vincenti, W. G. and Kruger, C. H., *Introduction to Physical Gas Dynamics*, R. E. Krieger Publishing, Huntington, NY, 1975.

[104] Bird, G. A., *Molecular Gas Dynamics*, Clarendon Press, Oxford, 1976.

[105] Granger, R. A., *Fluid Mechanics*, Dover, New York, 1995.

[106] Coudeville, H., Trepaud, P., and Brun, E. A., "Drag Measurements in Slip and Transition Flow," *Rarefied Gas Dynamics*, edited by J. H. de Leeuw, Vol. I, Academic Press, New York, 1965, pp. 444–466.

[107] Patterson, G. N., *Introduction to the Kinetic Theory of Gas Flows*, University of Toronto Press, Toronto, 1961.

[108] Ronchi, C., Iacono, R., and Paolucci, P. S., "The "Cubed Sphere": A New Method for the Solution of Partial Differential Equations in Spherical Geometry," *Journal of Computational Physics*, Vol. 124, 1996, pp. 94–114.

[109] Roos, F. W. and Willmarth, W. W., "Some Experimental Results on Sphere and Disk Drag," *AIAA Journal*, Vol. 9, 1971, pp. 285–291.

[110] Liebster, M., "Uber den Widerstand von Kugeln," *Annalen der Physik*, Vol. 83, 1927, pp. 541–562.

[111] Flemmer, R. L. C. and Banks, C. L., "On the drag coefficient of a sphere," *Powder Technology*, Vol. 48, 1986, pp. 217–221.

[112] Millikan, R. A., "A New Determination of e, N, and Related Constants," *Philosophical Magazine*, Vol. 34, No. 1, 1917, pp. 1–30.

[113] Millikan, R. A., "The General Low of Fall of a Small Spherical Body Through a Gas, and its Bearing upon the Nature of Molecular Reflection from Surfaces," *Physical Review*, Vol. 22, No. 1, 1923, pp. 1–23.

[114] Allen, M. D. and Raabe, O. G., "Re-Evaluation of Millikan's Oil Drop Data for the Motion of Small Particles in Air," *Journal of Aerosol Science*, Vol. 13, No. 6, 1982, pp. 537–547.

[115] Cunningham, E., "On the Velocity of Steady Fall of Spherical Particles through Fluid Medium," *Proceedings of the Royal Society of London A*, Vol. 83, 1910, pp. 357–365.

[116] Torrilhon, M., "Slow gas microflow past a sphere: Analytical solution based on moment equations," *Physics of Fluids*, Vol. 22, No. 7, 2010, pp. 072001.

[117] Taheri, P., Torrilhon, M., and Struchtrup, H., "Couette and Poiseuille microflows: Analytical solutions for the regularized 13 moment equations," *Physics of Fluids*, Vol. 21, No. 1, 2009, pp. 017102.

[118] John, B., Gu, X., and Emerson, D. R., "Nonequilibrium gaseous heat transfer in pressure-driven plane Poiseuille flow," *Physical Review E*, Vol. 88, 2013, pp. 013018.

[119] Tij, M. and Santos, A., "Perturbation Analysis of a Stationary Nonequilibrium Flow Generated by an External Force," *Journal of Statistical Physics*, Vol. 76, 1994, pp. 1399–1414.

[120] Aoki, K., Takata, S., and Nakanishi, T., "Poiseuille-type flow of a rarefied gas between two parallel plates driven by a uniform external force," *Physical Review E*, Vol. 65, 2002, pp. 026315.

[121] John, B., Gu, X., and Emerson, D. R., "Investigation of Heat and Mass Transfer in a Lid-Driven Cavity Under Non-equilibrium Flow Conditions," *Numerical Heat Transfer, Part B: Fundamentals: An International Journal of Computation and Methodology*, Vol. 58, 2010, pp. 287–303.

[122] John, B., Gu, X., and Emerson, D. R., "Effects of incomplete surface accommodation on non-equilibrium heat transfer in cavity flow: A parallel DSMC study," *Computers & Fluids*, Vol. 45, 2011, pp. 197–201.

[123] Clift, R., Grace, J. R., and Weber, M. E., *Bubbles, Drops, and Particles*, Academic Press, New York, 1978.

[124] Takata, S., Sone, Y., and Aoki, K., "Numerical analysis of a uniform flow of a rarefied gas past a sphere on the basis of the Boltzmann equation for hard-sphere molecules," *Physics of Fluids*, Vol. 5, 1993, pp. 716–737.